DAMAGE PROCESSES IN RUTHENIUM THIN FILMS INDUCED BY ULTRASHORT LASER PULSES

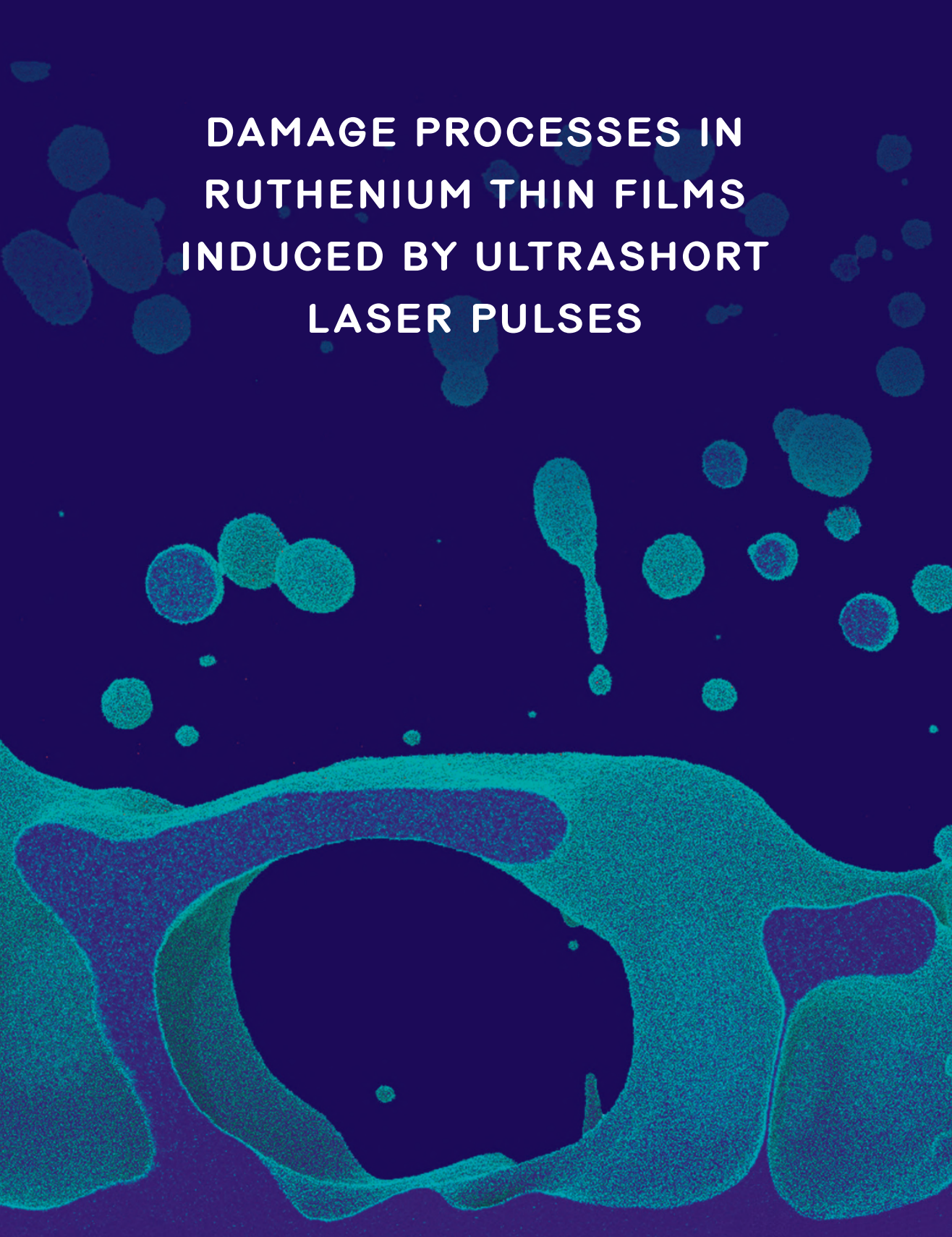

IGOR MILOV

DAMAGE PROCESSES IN RUTHENIUM THIN FILMS INDUCED BY ULTRASHORT LASER PULSES

Igor DMITRIEVICH MILOV

DAMAGE PROCESSES IN RUTHENIUM THIN FILMS INDUCED BY ULTRASHORT LASER PULSES

DISSERTATION

to obtain
the degree of doctor at the University of Twente,
on the authority of the rector magnificus,
prof.dr. T. T. M. Palstra,
on acoount of the decision of the Doctorate Board,
to be publicly defended
on Wednesday 9th of September 2020 at 16:45 hours

by

Igor DMITRIEVICH MILOV

born on the 16th of June 1990
in Tver, Russian Federation.

This dissertation has been approved by

supervisor: Prof.dr. F. Bijkerk
co-supervisor: Dr. E. Louis
co-supervisor: Dr.ir. I.A. Makhotkin

Graduation Committee

Chairman & secretary:	
Prof.dr. J.L. Herek	University of Twente
Supervisor:	
Prof.dr. F. Bijkerk	University of Twente
Co-Supervisor:	
Dr.ir. I.A. Makhotkin	University of Twente
Dr. E. Louis	University of Twente
Members:	
Prof.dr. H.C. Chapman	Center for Free-Electron Laser Science, Deutsches Elektronen-Synchrotron DESY, Universität Hamburg
Prof.dr. A.V. Kimel	Radboud University
Prof.dr. P.C.M. Planken	Advanced Research Center for Nanolithography (ARCNL), University of Amsterdam
Prof.dr. C. Filippi	University of Twente
Dr. G.H.L.A. Brocks	University of Twente

Keywords: Laser ablation, free-electron laser, extreme ultraviolet, thin films, ruthenium, two-temperature model, two-temperature hydrodynamics, molecular dynamics, Monte Carlo

Cover: Laser ablation of ruthenium simulated with molecular dynamics by Igor Milov; design by Layla Celegato (https://www.behance.net/laylayla)

Printed by: Ipskamp Printing, Enschede
ISBN: 978-90-365-5053-6
DOI: 10.3990/1.9789036550536

Acknowledgements
This work is part of the research programme MiLiMiD with project number 14HTSM05, which is financed by the Netherlands Organisation for Scientific Research (NWO) and Carl Zeiss SMT. We acknowledge the support of the Industrial Focus Group XUV Optics being part of the MESA+ Institute for Nanotechnology and the University of Twente, notably the industrial partners ASML and Malvern Panalytical, as well as the Province of Overijssel.

UNIVERSITY OF TWENTE. | MESA+ INSTITUTE

ASML

List of Publications

This thesis is based on the following publications:

Chapter 2: I. Milov, I.A. Makhotkin, R. Sobierajski, N. Medvedev, V. Lipp, J. Chalupský, J.M. Sturm, K. Tiedtke, G. de Vries, M. Störmer, F. Siewert, R. van de Kruijs, E. Louis, I. Jacyna, M. Jurek, L. Juha, V. Hájková, V. Vozda, T. Burian, K. Saksl, B. Faatz, B. Keitel, E. Plönjes, S. Schreiber, S. Toleikis, R. Loch, M. Hermann, S. Strobel, H.-K. Nienhuys, G. Gwalt, T. Mey, H. Enkisch, and F. Bijkerk, "Mechanism of single-shot damage of Ru thin films irradiated by femtosecond extreme UV free-electron laser." *Opt. Express* **26**, 19665-19685 (2018)

Chapter 3: I. Milov, V. Lipp, N. Medvedev, I. A. Makhotkin, E. Louis, and F. Bijkerk, "Modeling of XUV-induced damage in Ru films: the role of model parameters." *J. Opt. Soc. Am. B* **35**, B43-B53 (2018)

Chapter 4: I. Milov, V. Lipp, D. Ilnitsky, N. Medvedev, K. Migdal, V. Zhakhovsky, V. Khokhlov, Yu. Petrov, N. Inogamov, S. Semin, A. Kimel, B. Ziaja, I. A. Makhotkin, E. Louis, and F. Bijkerk, "Similarity in ruthenium damage induced by photons with different energies: from visible light to hard X-rays." *Appl. Surf. Sci.* **501**, 143973 (2020)

Chapter 5: I. Milov, V. Zhakhovsky, D. Ilnitsky, K. Migdal, V. Khokhlov, Yu. Petrov, N. Inogamov, V. Lipp, N. Medvedev, B. Ziaja, V. Medvedev, I. Makhotkin, E. Louis, and F. Bijkerk, "Two-level ablation and damage morphology of Ru films under femtosecond extreme UV irradiation." *Appl. Surf. Sci.* **528**, 146952 (2020)

Chapter 6: I.A. Makhotkin, I. Milov, J. Chalupský, K. Tiedtke, H. Enkisch, G. de Vries, F. Scholze, F. Siewert, J.M. Sturm, K.V. Nikolaev, R. van de Kruijs, M.A. Smithers, H. van Wolferen, E. Keim, E. Louis, I. Jacyna, M. Jurek, D. Klinger, J. Pelka, L. Juha, V. Hájková, V. Vozda, T. Burian, K. Saksl, B. Faatz, B. Keitel, E. Plönjes, S. Schreiber, S. Toleikis, R. Loch, M. Hermann, S. Strobel, R. Donker, T. Mey, and R. Sobierajski, "Damage accumulation in thin ruthenium films induced by repetitive exposure to femtosecond XUV pulses below the single-shot ablation threshold." *J. Opt. Soc. Am. B* **35**, 2799-2805 (2018)

Co-authored publications:

1. I.A. Makhotkin, R. Sobierajski, J. Chalupský, K. Tiedtke, G. de Vries, M. Störmer, F. Scholze, F. Siewert, R.W.E. van de Kruijs, I. Milov, E. Louis, I. Jacyna, M. Jurek, D. Klinger, L. Nittler, Y. Syryanyy, L. Juha, V. Hájková, V. Vozda, T. Burian, K. Saksl, B. Faatz, B. Keitel, E. Plönjes, S. Schreiber, S. Toleikis, R. Loch, M. Hermann, S. Strobel, H.-K. Nienhuys, G. Gwalt, T. Mey, and H. Enkisch, "Experimental study of EUV mirror radiation damage resistance under long-term free-electron laser exposures below the single-shot damage threshold." *J. Synchrotron Radiat.* **25**, 77-84 (2018)

2. G. Mercurio, I.A. Makhotkin, I. Milov, Y.Y. Kim, I.A. Zaluzhnyy, S. Dziarzhytski, L. Wenthaus, I.A. Vartanyants, and W. Wurth, "Surface structure determination by x-ray standing waves at a free-electron laser." *New J. Phys.* **21**, 033031 (2019)

3. Yu. Petrov, K. Migdal, N. Inogamov, V. Khokhlov, D. Ilnitsky, I. Milov, N. Medvedev, V. Lipp, and V. Zhakhovsky, "Ruthenium under ultrafast laser excitation: model and dataset for equation of state, conductivity, and electron-ion coupling." *Data in Brief* **28**, 104980 (2020)

4. N. Medvedev, and I. Milov, "Nonthermal phase transitions in metals." *Sci. Rep.* **10**, 12775 (2020)

5. N. Medvedev, and I. Milov, "Electron-phonon coupling in metals at high electronic temperatures." *Phys. Rev. B* **102**, 064302 (2020)

CONTENTS

1

INTRODUCTION

1.1. HIGH INTENSITY LIGHT-MATTER INTERACTION

"The 2018 Nobel Prize in Physics was awarded for groundbreaking inventions in the field of laser physics with one half to Arthur Ashkin for the optical tweezers and their application to biological systems, the other half jointly to Gérard Mourou and Donna Strickland for their method of generating high-intensity, ultrashort optical pulses." [1] It is hard to overestimate the impact of these inventions on the scientific world, with the first one providing a possibility to manipulate atoms, viruses and other living cells with laser beams, whereas the second one creates a powerful tool for investigating unexplored properties of matter at extreme conditions on an ultrashort timescale. This thesis focuses on one of the outcomes of Gérard Mourou's and Donna Strickland's discovery: damage in materials exposed to ultrashort hight intensity laser pulses.

One of the typical damage phenomena is *laser ablation*, which is the process of removing material from a solid or liquid surface by irradiating it with a laser beam. The history of laser ablation probably started when the first lens or window was burned by a ruby laser in the 1960's. Among the first major applications of laser ablation one should mention microanalysis of solid samples using laser microprobe emission and mass spectroscopy, and laser deposition of thin films for the studies of high-temperature superconductivity. The significant improvement in accuracy, control and range of laser systems in the eighties resulted in tremendous growth of laser ablation applications. Among them are surface micromachining and nanostructuring, laser surgery, laser mass spectroscopy for the studies of biomolecules, and the development of X-ray lasers exploiting the emission of a laser produced plasma. High-power lasers were even considered as energy weapons.

The early concepts of laser ablation continue their non-stop development with the new fields of applications constantly emerging. The pulsed laser deposition technique has become a powerful tool for the growth of high quality thin films with complex stoichiometry [2]. Other notable applications are laser printing using the principal of laser induced forward transfer [3], surface cleaning [4], production of laser induced periodic surface structures [5] and laser propulsion for launching small satellites into space [6]. Laser ablation is used to produce chemically clean nanoparticles of various size, shape and structure for numerous applications in plasmonics, catalysis and biomedicine [7]. The latter includes drug delivery technology and cancer treatment.

Apart from numerous applications, high intensity ultrashort light-matter interaction is also a fundamentally interesting topic. When a high dose of radiation is absorbed by a material in an extremely short time, the properties of the excited material can change dramatically. A new non-equilibrium transient state of matter, also referred to as warm dense matter, can be created. In this state material is at an extremely high temperature up to several eV (tens of thousands of Kelvin), while still at nearly solid state density, which makes it something in between condensed matter and plasma. Such a peculiar state is of great interest and challenge for fundamental science, since neither standard quantum mechanics nor semi-classical plasma formalisms can be directly applied to study it [8, 9]. New theoretical models and their computational implementations must be developed to describe properties of matter at extreme conditions, which is essential, for example, in the fields of nuclear and thermonuclear engineering or synthesis of new materials. Apart from materials irradiated with ultrashort laser pulses, warm dense matter can be found in the cores of giant planets, brown dwarfs, and small stars, or created

in inertial confinement fusion.

Having ultrashort optical lasers at hand, further development of laser systems moved into the direction of expanding the wavelength range to shorter values. Such light sources as synchrotrons and X-ray free-electron lasers (XFELs) were created to combine ultrahigh time resolution with sub-nanometer scale spatial resolution of X-rays. Such a combination opens up a possibility to produce a movie of chemical reactions on an atomic scale. Getting access to such intrinsic details of, for example, catalysis processes is crucial to push the progress in that field.

A very ambitions and fascinating idea of using an XFEL as a source for extreme ultraviolet lithography (EUVL) was considered [10]. Despite several key advantages of XFELs, such as a tunable wavelength, "clean" photons (no unwanted wavelengths in the spectrum) and high power, the latter one has a flip side. XFELs generate the light in femtosecond pulses and these pulses have an extremely high peak power density compared to the standard nanosecond pulses from laser produced plasma sources. The intensity in the femtosecond pulses can be too high for the optical elements in EUVL machines to survive. Damage issues can become real show stoppers, and addressing them served as one of the motivations of this thesis.

Apart from industrial interest, damage issues occupy a much broader scope of science and technology. The general trend of increasing the intensity of different types of light sources for various applications keeps the topic of damage relevant. One of the reasons of increased intensity is a need to decrease the beam spot size for some applications. A small beam size is required, for example, in coherent X-ray imaging of single particles [11]. Focusing the light down to a ~ 10nm spot size one can create an enormous intensity (more than 10^{20} W/cm^2) on the sample surface.

This trend of increasing intensity of a laser pulse creates the risk of optical elements, such as mirrors, lenses, gratings, and beam-stoppers to be modified or even severely damaged. It goes without saying that such a scenario has to be avoided in order to achieve robust operation of complex and delicate machines such as XFELs and synchrotrons.

Many experimental studies of damage induced in different types of materials exposed to XFELs were performed in recent years in order to identify the conditions of material failure [12–17]. Although a significant amount of data has been already accumulated, many of the performed experiments aimed only at obtaining the damage threshold values for different materials and irradiation parameters in order to draw "safe lines" for real application conditions. In many cases there is still a lack of fundamental understanding of what actually happens in materials exposed to an extreme amount of X-ray radiation on a very small temporal and spatial timescale.

Although damage of materials with optical lasers has been extensively studied in the past, this expertise can not be directly transferred to the X-ray regime. Due to a high energy of X-ray photons, the absorption process and the following energy distribution within the target is different compared to the optical case. Therefore, different mechanisms of damage can potentially be expected. Citing the recently published textbook [18]: "It is anticipated but not yet clear if a similar [to optical] short-pulse ablation mechanism is going to be observed in the X-ray regime". This sentence emphasizes one of the key objectives of this thesis, which can be formulated as building fundamental understanding of laser-induced processes in materials over a wide range of photon en-

ergies.

Whereas optical lasers are easily accessible in the labs, the high intensity ultrashort XUV and X-ray sources are more unique. Beam time at XFEL facilities is expensive, which limits the opportunity to perform numerous damage experiments for various materials and irradiation conditions. That is why it is so important to have a reliable predictive theoretical model that can serve as a tool to investigate damage phenomena in a wide space of parameters. The main achievement of this thesis is the construction of such a model and its application for various experimental conditions.

1.2. MODELING OF LIGHT-MATTER INTERACTION

Theoretical studies of the interaction of laser light with matter have been developing for several decades. The variety of available models is vast and depends on the particular choice of materials and irradiation conditions. To narrow it down to those that are closely related to the work performed in this thesis, one has to set some borders for the key parameters. This thesis focuses on the interaction of ultrashort, moderate intensity laser pulses in a wide range of wavelengths with metals in vacuum in single- and multi-shot regimes. Below, each parameter is defined more accurately.

By definition, *ultrashort* pulses are those with a duration in the sub-picosecond domain. Such a short time is typically smaller than the characteristic electron-phonon interaction time. It means that when a solid absorbs such a pulse, it switches to a two-temperature (2T) state, when electrons and phonons (lattice) have different temperatures. In this thesis pulses with a full width at half maximum duration from 20 to 100 fs were considered. One should note, that the specifics of longer (nanosecond) pulses interaction with matter are largely distinct from pico- and femtosecond ones, involving different mechanisms of damage. Due to the relatively long heating time, there are no significant stresses generated in the target during nanosecond laser irradiation. Therefore, the ablation mechanism is purely thermal in nature. The metal target melts first, and when the absorbed energy becomes larger than the specific heat of evaporation, significant evaporation occurs. Detailed modeling of nanosecond laser ablation is complicated by the fact that, unlike in the femtosecond regime, the timescale of most of the processes involved is within the pulse duration, which means that one would have to model photoabsorption in a constantly changing system. Nanosecond pulses are out of the focus of this work.

Moderate intensity defines a regime when a laser pulse is sufficiently intense to cause significant material modifications such as melting and ablation, but not too intense to strongly ionize the material. The typical laser intensity used was in the order of 10^{12} W/cm^2. All the experiments considered in this thesis were performed in *high vacuum*, except for the one with an optical laser, where air was used as an environment. The ionization of air was avoided in the latter case. Therefore, the effects of plasma formation and expansion and its interaction with sample surfaces are considered to be negligible.

A wide range of *photon energies* (wavelengths) is considered in this thesis: from visible light to hard X-rays. Studying the dependence of damage on this parameter is an essential part of this thesis, with Chapter 4 purely dedicated to this topic.

The computational formalism developed in this work is generally applicable to any

metal, if the required material parameters are known. Nevertheless, all the following chapters are dedicated to one particular metal - *ruthenium* (Ru). Such a specific interest to Ru will be discussed in the following section.

Finally, both *single-* and *multi-shot* irradiation regimes are considered. The main focus has been put into the single-shot regime. Interaction of a single pulse with a metal is already a complex multiphysical and multiscale problem, requiring fundamental studies of the processes involved. It serves as a perfect foundation of the detailed theoretical studies. The multi-shot regime is even more complex for reliable simulations, especially when the energy of each pulse is below the single-shot damage threshold. In this regime each pulse can introduce only minor, barely or even not detectable modifications in a target that will only become visible in a long-term exposure. The first steps towards understanding such accumulation effects are performed in this work only with experimental studies.

After such a definition of the parameter space that this thesis focuses on, it is important to briefly describe several existing models that are developed for this domain and the necessity to improve or combine the existing solutions. A more detailed overview of different simulations techniques to model ultrashort light-matter interaction can be found elsewhere [8, 18, 19].

A classical way to simulate the response of a metal to ultrashort optical laser irradiation is the two-temperature model (TTM), that was developed more than 50 years ago [20–22]. It takes into account absorption of light by conduction band electrons, transport of absorbed energy by electron thermal diffusion and heating of the lattice via electron-phonon interaction. The detailed description of the TTM and the limits of its applicability can be found in Chapters 2 and 3. Here it is important to specify that the TTM works quantitatively accurate only for relatively low fluences below the melting threshold, when density variations of the material can be neglected.

For high fluences, when there is significant expansion and compaction involved, together with possible phase transitions, a more general two-temperature hydrodynamics (2T-HD) approach must be used [23, 24]. To take into account the thermodynamics of irradiated material in different phases (solid, liquid and gas), 2T-HD is usually supplemented with the material equation of state [25]. The 2T-HD approach can be used to calculate the material density, temperature, pressure and mass velocity evolution after laser irradiation. Having this information about material behaviour one can study different mechanisms responsible for damage, such as melting, ablation, spallation and even high fluence (intensity) effects such as critical-point phase separation (also referred to as explosive boiling or phase explosion).

If one is interested in the detailed atomistic picture and morphological features of material evolution induced by different damage processes, a classical molecular dynamics (MD) approach can be used. However, since classical MD only considers interaction of neutral atoms or molecules, it is not directly applicable to metals, which consist of free electrons and an ionic lattice. A combination of the TTM with classical MD is one of the ways to overcome that difficulty [26].

Despite the fact that two-temperature-based models can be successfully applied to simulate interaction of optical or infrared lasers with matter, they fail when the photon energy increases. The absorption of XUV or X-ray light induces non-equilibrium electron kinetics, that has to be taken into account. The X-ray induced electron cascades in

matter can be efficiently simulated with the Monte-Carlo-based (MC) models [27–29]. Such models provide a description of the excited electronic system, but do not simulate atomistic evolution.

To have a more complete understanding of how X-ray irradiated materials evolve, including both electronic and atomic systems, one may use hybrid approaches. Hybrid simulation techniques combine several models into a unified approach to efficiently describe various sub-problems within the complex problem studied. They include, for example, multiscale techniques [30, 31] and similar approaches [32].

For instance, in work [33] the authors used the X-RIM code to model the X-ray FEL (XFEL) interaction with ruthenium and silicon at the damage threshold intensity. The code links the calculations of the radiation field in the material with the hydrodynamics (HD) simulations. The HD part of the model is limited to the elastoplastic regime only. Hence, a quantitative description of damage at moderate intensity is not possible. As another example, a hybrid approach XTANT (X-ray-induced Thermal And Non-thermal Transition) [32] simulates material evolution taking into account non-equilibrium electron distribution, non-adiabatic electron-ion energy exchange, transient electron band structure, atomic potential energy surface evolution, and atomic motion, all within one interconnected model. The complexity of parallel calculations of various physical processes restricts the model to a timescale up to ~ 100 ps and a system size up to ~ 1000 atoms.

The complex nature of light-matter interaction dictates the necessity to use hybrid approaches if one needs to obtain detailed information regarding the damage processes on a broad temporal scale. As one can see, the existing models either are not applicable in a wide range of irradiation parameters or do not cover all stages of material evolution or are computationally too heavy to get close to experimental spatial and temporal scales. The central place in this thesis is dedicated to the development of a hybrid model that overcomes some of the limits listed above, making a further step into reliable predictive computations of light-matter interaction. The model combines Monte Carlo, hydrodynamics and molecular dynamics techniques, and the steps performed to develop such a model will be extensively described in the following chapters.

1.3. RUTHENIUM AND ITS PROPERTIES

Having briefly introduced the main computational tool that will be used throughout this thesis to study fundamentals of laser induced damage, this section will describe the main research object - Ru thin films.

As discussed above, one of the main motivations for this work is to study damage effects in materials relevant for synchrotrons and XFEL applications. In that respect, Ru thin films can be used as grazing incidence mirrors to reflect XUV and X-ray radiation. The reflection in that case is based on the principal of total external reflection. The high free electron density in Ru increases the range of grazing incidence angles in which Ru performs a high reflectance up to 27 degrees, making it more flexible to operate with. Ru is also a favourable material in the context of optical performance due to its low oxidation properties. The thickness of a native oxide stabilizes at about 1-2 nm. For this reason, Ru is routinely used as a capping layer to protect materials from a harsh external environment. Altogether it makes Ru a suitable material for XUV and X-ray optics.

In the field of laser-induced damage, apart from optical, thermo-mechanical properties play a crucial role. It is important to distinguish between equilibrium and nonequilibrium states. Here the word equilibrium denotes thermal equilibrium between electrons and lattice ions (both systems have equal temperature). Such situation is typical when the laser pulse duration is longer than the characteristic electron-phonon interaction time. Contrarily, absorption of an ultrashort pulse brings material into a nonequilibrium state, that we will refer to as the two-temperature (2T) state, where electrons and ions have a significantly different temperature. The material properties in this 2T state can be considerably different from those in the equilibrium one-temperature (1T) state. For example, metals exhibit a sharp increase of the thermal conductivity after the transition into the 2T state [34].

Ru is a barely studied material in that context. Almost no information regarding Ru 2T state properties was available in the literature. Ru in a solid phase differs from crystals with a cubic symmetry - aluminum, gold, copper, nickel - that are more often studied in laser ablation problems. Ru has a hexagonal close-packed structure with two atoms in a unit cell, which creates additional difficulties for calculating its properties. A huge theoretical effort was dedicated to obtain the missing information about Ru to be able to perform the computer simulations. Part of this work is described in the Chapters 2, 3 and 5. An extensive *ab initio* study of the Ru thermo-mechanical properties in the 1T and 2T states was done in a collaborative work [35] that is not included into this thesis.

Calculating the material properties at such extreme conditions is challenging and largely depends on the particular model applied. The results of the calculations should be benchmarked by comparison with the experiment. Unfortunately, the direct measurements of material non-equilibrium properties at the conditions of high temperature, pressure and varying density are very complex if possible at all. Different types of pump-probe experiments can be applied. Although, one should take into account that each pump pulse will, in general, be able to destroy the target surface, so complicated experimental schemes should be used to prepare a pristine target surface for each pump pulse. Such types of experiments are outside the focus of this thesis.

Nevertheless, the Ru properties calculated and used in the following chapters are validated via comparison of the damage experimental results with the corresponding simulations. A good agreement was achieved, which guaranties the adequate description of Ru as a material in the context of laser-induced damage. As a result, the understanding of Ru properties under ultrashort laser irradiation has been significantly deepened. The combination of the Ru thermo-mechanical properties obtained, namely a relatively low thermal conductivity, a large electron-phonon coupling factor and a strong surface tension results in ablation dynamics which is not typical for previously studied metals, see Chapter 5.

1.4. STRUCTURE OF THIS THESIS

The chapter structure of this thesis follows the steps made towards fundamental understanding of physical processes in laser irradiated Ru at various conditions. The development of a computational tool - a hybrid multiscale model of light-metal interaction - is synchronized with these steps.

Chapter 2 describes the single-shot damage experiment with Ru thin films carried

out at the FLASH facility (Free-electron LASer in Hamburg). The detailed analysis of the damage morphologies was performed, together with the measurements of the single-shot damage thresholds. The first iteration in the model development is also reported, namely a combination of the Monte Carlo code XCASCADE(3D) with the TTM. Such a particular combination, applied for the first time, enables one to study the XUV induced electron cascades and the temperature evolution in Ru. Both the quantitative results and the qualitative discussion regarding the mechanisms of XUV damage are reported. The applicability of the TTM limited the quantitative analysis to low fluences near the melting threshold and to the timescale covering the initial stage of Ru evolution only.

Chapter 3 studies the role of model parameters in the XCASCADE(3D)+TTM scheme with respect to the XUV induced damage. It was found that the results of the simulations are not very sensitive to the XCASCADE(3D) parameters, since electron cascading induced by XUV photon absorption is not significant. As for the thermal parameters, the electron-phonon coupling factor and electron thermal conductivity in the 2T regime play a key role in the heat dynamics in Ru, which defines the eventual damage.

Chapter 4 occupies the central and most important part of the thesis. Two crucial steps were made. First, the damage analysis was expanded to other laser wavelengths, namely to the visible and the hard X-ray range. The puzzling similarity in the Ru ablation observed in the whole wide range of wavelengths was detected and explained. Such a discovery provides an opportunity to scale the extensive existing studies of laser ablation with optical lasers to the hard X-ray regime, which currently is very relevant in the field of rapidly developing XFELs. Second, as a computational tool to enable such a study, a combination of the XCASCADE(3D) code and two-temperature hydrodynamics was realized. The 2T-HD substituted the TTM and provided a way to calculate not only the temperature evolutions, but also the pressure. The latter is crucial to quantitatively understand ultrashort laser ablation mechanisms.

Chapter 5 focuses on the XUV regime only, but deepens our understanding of all the physical processes involved in Ru damage. A final step in the model development is introduced, namely adding classical molecular dynamics. With this step the model is complete, covering the full timescale of material evolution: from photoabsorption to complete relaxation of the Ru target. The MD part provides the detailed description of Ru ablation on an atomistic level. The simulations can be carried out until the complete recrystallization of the Ru after the ablation process, providing access to a direct comparison with single-shot damage experiments. Special attention is given to the explanation of the damage morphology dependence on the locally absorbed fluence.

Chapter 6 makes a step in the damage studies towards the multi-shot irradiation regime, setting a possible future direction of damage research. The multi-shot regime below the single-shot damage threshold is very interesting for industrial applications. When a single pulse is not capable to induce noticeable changes in the material, different accumulation effects can still induce degradation and eventual failure of the material. This chapter reports the experimental analysis of the multi-shot damage experiments with Ru performed at the FLASH facility. Damage morphologies and thresholds are determined. A qualitative discussion regarding the damage mechanisms is provided, although more experiments and simulations are needed to continue research in that direction.

REFERENCES

[1] *The Nobel Prize in Physics 2018. NobelPrize.org. Nobel Media AB 2020. Wed. 1 Apr 2020.* https://www.nobelprize.org/prizes/physics/2018/summary/.

[2] D. H. Lowndes, D. Geohegan, A. Puretzky, D. Norton, and C. Rouleau, *Synthesis of novel thin-film materials by pulsed laser deposition,* Science **273**, 898 (1996).

[3] C. W. Visser, R. Pohl, C. Sun, G.-W. Römer, B. Huis in 't Veld, and D. Lohse, *Toward 3d printing of pure metals by laser-induced forward transfer,* Adv. Mater. **27**, 4087 (2015).

[4] A. C. Tam, W. P. Leung, W. Zapka, and W. Ziemlich, *Laser-cleaning techniques for removal of surface particulates,* J. Appl. Phys. **71**, 3515 (1992).

[5] J. Bonse, J. Krüger, S. Höhm, and A. Rosenfeld, *Femtosecond laser-induced periodic surface structures,* J. Laser Appl. **24**, 042006 (2012).

[6] C. Phipps, C. Bonnal, F. Masson, and P. Musumeci, *Launching swarms of microsatellites using a 100 kW average power pulsed laser,* J. Opt. Soc. Am. B **35**, B20 (2018).

[7] D. Zhang, B. Gökce, and S. Barcikowski, *Laser synthesis and processing of colloids: fundamentals and applications,* Chem. Rev. **117**, 3990 (2017).

[8] F. Graziani, M. P. Desjarlais, R. Redmer, and S. B. Trickey, *Frontiers and challenges in warm dense matter*, Vol. 96 (Springer Science & Business, 2014).

[9] N. Medvedev and B. Ziaja, *Multistep transition of diamond to warm dense matter state revealed by femtosecond X-ray diffraction,* Sci. Rep. **8**, 5284 (2018).

[10] E. R. Hosler and O. R. Wood, *EUV free-electron laser requirements for semiconductor manufacturing,* in *X-Ray Lasers 2016*, edited by T. Kawachi, S. V. Bulanov, H. Daido, and Y. Kato (Springer International Publishing, Cham, 2018) pp. 351–359.

[11] C. G. Schroer, P. Boye, J. Feldkamp, J. Patommel, A. Schropp, A. Schwab, S. Stephan, M. Burghammer, S. Schöder, and C. Riekel, *Coherent X-ray diffraction imaging with nanofocused illumination,* Phys. Rev. Lett. **101**, 090801 (2008).

[12] S. P. Hau-Riege, R. A. London, R. M. Bionta, M. A. McKernan, S. L. Baker, J. Krzywinski, R. Sobierajski, R. Nietubyc, J. B. Pelka, M. Jurek, L. Juha, J. Chalupský, J. Cihelka, V. Hájková, A. Velyhan, J. Krása, J. Kuba, K. Tiedtke, S. Toleikis, T. Tschentscher, H. Wabnitz, M. Bergh, C. Caleman, K. Sokolowski-Tinten, N. Stojanovic, and U. Zastrau, *Damage threshold of inorganic solids under free-electron-laser irradiation at 32.5 nm wavelength,* Appl. Phys. Lett. **90**, 173128 (2007).

[13] J. Chalupský, V. Hájková, V. Altapova, T. Burian, A. J. Gleeson, L. Juha, M. Jurek, H. Sinn, M. Störmer, R. Sobierajski, K. Tiedtke, S. Toleikis, T. Tschentscher, L. Vyšín, H. Wabnitz, and J. Gaudin, *Damage of amorphous carbon induced by soft X-ray femtosecond pulses above and below the critical angle,* Appl. Phys. Lett. **95**, 1 (2009).

[14] J. Pelka, R. Sobierajski, D. Klinger, W. Paszkowicz, J. Krzywinski, M. Jurek, D. Zymierska, A. Wawro, A. Petroutchik, L. Juha, V. Hajkova, J. Cihelka, J. Chalupsky, T. Burian, L. Vysin, S. Toleikis, K. Sokolowski-Tinten, N. Stojanovic, U. Zastrau, R. London, S. Hau-Riege, C. Riekel, R. Davies, M. Burghammer, E. Dynowska, W. Szuszkiewicz, W. Caliebe, and R. Nietubyc, *Damage in solids irradiated by a single shot of XUV free-electron laser: Irreversible changes investigated using X-ray microdiffraction, atomic force microscopy and nomarski optical microscopy,* Radiat. Phys. Chem. **78**, S46 (2009).

[15] A. R. Khorsand, R. Sobierajski, E. Louis, S. Bruijn, E. D. van Hattum, R. W. E. van de Kruijs, M. Jurek, D. Klinger, J. B. Pelka, L. Juha, T. Burian, J. Chalupsky, J. Cihelka, V. Hajkova, L. Vysin, U. Jastrow, N. Stojanovic, S. Toleikis, H. Wabnitz, K. Tiedtke, K. Sokolowski-Tinten, U. Shymanovich, J. Krzywinski, S. Hau-Riege, R. London, A. Gleeson, E. M. Gullikson, and F. Bijkerk, *Single shot damage mechanism of Mo/Si multilayer optics under intense pulsed XUV-exposure,* Opt. Express **18**, 700 (2010).

[16] T. Koyama, H. Yumoto, Y. Senba, K. Tono, T. Sato, T. Togashi, Y. Inubushi, T. Katayama, J. Kim, S. Matsuyama, H. Mimura, M. Yabashi, K. Yamauchi, H. Ohashi, and T. Ishikawa, *Investigation of ablation thresholds of optical materials using 1-μm-focusing beam at hard X-ray free electron laser,* Opt. Express **21**, 15382 (2013).

[17] J. Krzywinski, D. Cocco, S. Moeller, and D. Ratner, *Damage threshold of platinum coating used for optics for self-seeding of soft X-ray free electron laser,* Opt. Express **23**, 5397 (2015).

[18] S. P. Hau-Riege, *High-Intensity X-rays-Interaction with Matter: Processes in Plasmas, Clusters, Molecules and Solids* (John Wiley & Sons, 2012).

[19] B. Rethfeld, D. S. Ivanov, M. E. Garcia, and S. I. Anisimov, *Modelling ultrafast laser ablation,* J. Phys. D: Appl.Phys. **50**, 193001 (2017).

[20] M. Kaganov, I. Lifshitz, and L. Tanatarov, *Relaxation between electrons and crystalline lattice,* Sov. Phys. JETP **4**, 173 (1957).

[21] S. Anisimov, A. Bonch-Bruevich, M. El'yashevich, Y. Imas, N. Pavlenko, and G. Romanov, *Effect of powerful light (laser) fluxes on metals,* Zh. Tekh. Fiz **36**, 1273 (1966).

[22] S. Anisimov, B. Kapeliovich, and T. Perelman, *Electron emission from metal surfaces exposed to ultrashort laser pulses,* Zh. Eksp. Teor. Fiz **66**, 776 (1974).

[23] S. Anisimov, N. Inogamov, Y. V. Petrov, V. Khokhlov, V. Zhakhovskii, K. Nishihara, M. Agranat, S. Ashitkov, and P. Komarov, *Interaction of short laser pulses with metals at moderate intensities,* Appl. Phys. A **92**, 939 (2008).

[24] M. E. Povarnitsyn and T. E. Itina, *Hydrodynamic modeling of femtosecond laser ablation of metals in vacuum and in liquid,* Appl. Phys. A **117**, 175 (2014).

[25] M. E. Povarnitsyn, T. E. Itina, M. Sentis, K. Khishchenko, and P. Levashov, *Material decomposition mechanisms in femtosecond laser interactions with metals,* Phys. Rev. B **75**, 235414 (2007).

[26] D. S. Ivanov and L. V. Zhigilei, *Combined atomistic-continuum modeling of short-pulse laser melting and disintegration of metal films,* Phys. Rev. B **68**, 064114 (2003).

[27] J. Sempau, E. Acosta, J. Baro, J. Fernández-Varea, and F. Salvat, *An algorithm for Monte Carlo simulation of coupled electron-photon transport,* Nucl. Instrum. Meth. B **132**, 377 (1997).

[28] N. Medvedev, *Femtosecond X-ray induced electron kinetics in dielectrics: application for fel-pulse-duration monitor,* Appl. Phys. B **118**, 417 (2015).

[29] V. Lipp, N. Medvedev, and B. Ziaja, *Classical Monte-Carlo simulations of X-ray induced electron cascades in various materials,* Proc. SPIE, Damage to VUV, EUV, and X-ray Optics VI **10236**, 102360H (2017).

[30] K. Nordlund, C. Björkas, T. Ahlgren, A. Lasa, and A. E. Sand, *Multiscale modelling of plasma–wall interactions in fusion reactor conditions,* J. Phys. D: Appl. Phys. **47**, 224018 (2014).

[31] Y. Rong, P. Ji, M. He, Y. Zhang, and Y. Tang, *Multiscale investigation of femtosecond laser pulses processing aluminum in burst mode,* Nanosc. Microsc. Therm. **22**, 324 (2018).

[32] N. Medvedev, V. Tkachenko, V. Lipp, Z. Li, and B. Ziaja, *Various damage mechanisms in carbon and silicon materials under femtosecond X-ray irradiation,* 4open **1**, 3 (2018).

[33] O. Peyrusse, J.-M. André, P. Jonnard, and J. Gaudin, *Modeling of the interaction of an X-ray free-electron laser with large finite samples,* Phys. Rev. E **96**, 043205 (2017).

[34] J. Hohlfeld, S.-S. Wellershoff, J. Güdde, U. Conrad, V. Jähnke, and E. Matthias, *Electron and lattice dynamics following optical excitation of metals,* Chem. Phys. **251**, 237 (2000).

[35] Y. Petrov, K. Migdal, N. Inogamov, V. Khokhlov, D. Ilnitsky, I. Milov, N. Medvedev, V. Lipp, and V. Zhakhovsky, *Ruthenium under ultrafast laser excitation: Model and dataset for equation of state, conductivity, and electron-ion coupling,* Data Brief **28**, 104980 (2020).

2

MECHANISM OF SINGLE-SHOT DAMAGE OF RU THIN FILMS IRRADIATED BY FEMTOSECOND EXTREME UV FREE-ELECTRON LASER

Ruthenium is a perspective material to be used for XUV mirrors at free-electron laser facilities. Yet, it is still poorly studied in the context of ultrafast laser-matter interaction. In this work, we present single-shot damage studies of thin Ru films irradiated by femtosecond XUV free-electron laser pulses at FLASH. Ex-situ analysis of the damaged spots, performed by different types of microscopy, shows that the weakest detected damage is surface roughening. For higher fluences we observe ablation of Ru. Combined simulations using Monte-Carlo code XCASCADE(3D) and the two-temperature model reveal that the damage mechanism is thermo-mechanical in nature, similar to the case of irradiating the target with optical lasers. The analogy with the optical damage studies enables us to explain the observed damage morphologies.

2.1. INTRODUCTION

Radiation parameters of extreme ultraviolet (XUV) free-electron laser (FEL) light sources such as FLASH [1] or FERMI [2] create challenges for the optical elements operating at such facilities. High-peak power femtosecond pulses generated by FELs induce ultrafast and highly non-equilibrium processes in the irradiated material. Such processes may lead to degradation and significant damage of the material, strongly reducing its optical performance. In order to prevent optics from being damaged and, thus, to increase its lifetime, fundamental understanding of the nature of XUV laser-induced damage formation is required.

Previous studies of XUV-induced damage focused on various materials that are of interest for XUV optics. Mo/Si-based multilayers are commonly used as normal incidence mirrors optimized for a wavelength of 13.5 nm. Thermally-induced compaction of the multilayer due to energetically stable silicide formation was found to be the leading damage mechanism for both nanosecond pulses generated with a table-top laser produced plasma (LPP) source [3] and femtosecond pulses at FLASH [4], with the latter damage threshold being several factors lower than in the ns case. In order to increase the damage threshold value, Mo/Si multilayers with different capping layers [5, 6], diffusion barriers [5] or thermodynamically stable compounds [7] were also considered.

Other materials used in XUV optics as grazing incidence mirrors are metal or carbon-based films that work on the principle of total external reflection. For B_4C and SiC samples it was found that the damage threshold strongly depends on the photon energy. In the range of 38 - 830 eV it was typically of the order of the fluence required for thermal melting [8–10]. Another damage mechanism, namely solid-solid phase transition (graphitization), was reported when irradiating a-C samples with femtosecond pulses with 91.8 and 177.1 eV photon energies [11, 12]. For gold films surface melting with subsequent complete removal of the film was observed when exposed to XUV light from an LPP source [3]. Similar damage morphologies showing a step-like complete removal of the gold film were reported for a femtosecond pulse case [13].

Ablation of metals with optical lasers was extensively studied in the literature [14–18]. However, the interaction of XUV light with metals is fundamentally different. The photons with higher energy can create strongly non-equilibrium states of the electronic system and also excite deep shells of target atoms, not only the conduction band. Additionally, since in our experiments grazing incidence conditions are applied, the energy is absorbed in a very thin (few nanometers) layer. This may result in realization of more extreme conditions in the material compared to the excitation with optical lasers having the same amount of absorbed energy. In this work, we investigate whether these differences have a significant impact on the single-shot damage process.

We study the nature of single-shot damage induced in ruthenium (Ru) thin films by femtosecond XUV pulses generated by FLASH. Ru is chosen as optically favorable material, since it has a high XUV reflectance in a wide range of grazing incidence angles [19] and is relatively resistant to oxidation [20]. Ru is also a standard material for grazing incidence hard X-ray optics [21].

In order to understand the mechanisms responsible for the observed damage, we perform simulations of the interaction of femtosecond XUV laser pulses with the Ru target. Generally for metals, such interaction proceeds in three characteristic stages. (i) The absorption of XUV photons induces non-equilibrium electron kinetics in the

near surface region of the metal. During that stage, photo- and secondary electrons travel ballistically with velocities high above the Fermi velocity. After several collisions these electrons thermalize to a Fermi-Dirac distribution with an elevated electron temperature, while the lattice remains cold. (ii) The second stage is characterized by thermal non-equilibrium between electrons and the lattice. During that stage thermalized electrons diffuse into the depth of the metal, while simultaneously heating up the lattice via electron-phonon interaction, until electron and lattice temperatures are equal. (iii) Equilibrium thermal diffusion proceeds in the third stage. When the laser pulse fluence is sufficiently high, various damage processes such as melting and resolidification, mechanical fracture or phase explosion may occur after the interaction with the laser pulse [17].

In the present work, apart from the experimental study, we use a combined computational approach to describe the interaction of XUV FEL femtosecond pulses with a Ru film. The first stage mentioned above, non-equilibrium electron kinetics induced by XUV light, is simulated with the classical Monte Carlo code XCASCADE(3D) [22]. The code models the absorption of XUV photons by the target and follows the temporal and spatial evolution of the electron cascades produced upon photoabsorption.

The second and third stages are described using the two-temperature model (TTM) [23]. Typically, the TTM is used to simulate the interaction of optical lasers with solids [14, 15, 24–27]. It assumes that the electronic system is always in thermal equilibrium, so it can be described with a temperature. Contrarily to visible light, XUV photons have sufficient energy to ionize core shells of the target atoms, creating highly non-equilibrium electronic states, which is not possible to describe with the TTM alone.

For that reason, the XCASCADE(3D) calculations are performed prior to the TTM, so that XUV-induced non-equilibrium electron kinetics is taken into account. Coupling of the two models is realized in the following way: the transient energy density depth profiles of thermalized electrons obtained from XCASCADE(3D) are used to calculate the heat source term for the TTM.

Our calculations give detailed information about the ultrafast heating of the Ru lattice, which is of crucial importance for understanding the mechanisms responsible for the observed damage phenomena.

2.2. EXPERIMENT

We performed single-shot damage experiments with Ru thin films at FLASH. The FEL in the configuration used in the experiment provided single pulses of 100 fs duration (FWHM) at 13.5 nm wavelength with 1% spectral bandwidth. The FEL beam was p-polarized with respect to the sample surface and focused using a carbon coated ellipsoidal mirror. The experiment was performed in a high vacuum experimental chamber with a base pressure better than 10^{-6} mbar. The samples, clamped on a sample holder that was controlled by a motorized manipulator, were exposed to FEL radiation at 20° grazing incidence angle. For each single shot pristine material was exposed. Sample position monitoring and *in-situ* investigation of strongly damaged spots were performed using an optical microscope mounted onto the vacuum chamber. The energy of each pulse was attenuated with gas and/or solid attenuators with calibrated transmission factors and was measured with a gas monitor detector [28]. The energy range of 0.2-

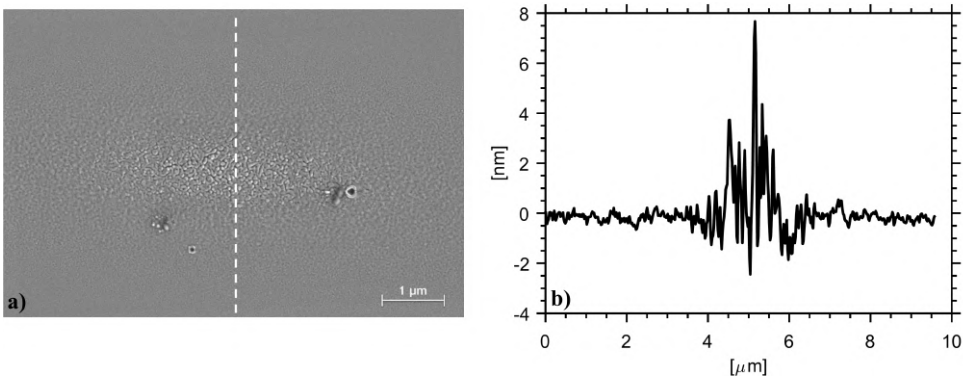

Figure 2.1: (a) HR-SEM image of the damaged spot produced by the 100 fs XUV FEL pulse with an incident peak fluence of $F = 213\,\mathrm{mJ/cm^2}$. The dashed vertical line indicates where the AFM line profile is made. (b) Line profile in the center of the spot extracted from the AFM scan.

46 μJ per pulse was chosen so that the highest values create heavily damaged surfaces, while for the lowest values no damage was observed by means of the *in-situ* optical microscope. More details about the experimental set-up and procedures can be found elsewhere [19, 29].

The spatial energy distribution of FEL beams is typically non-Gaussian. Therefore, the beam profile should be characterized prior to laser-matter interaction experiments. The fluence scan method [30, 31], based on single-shot ablative imprints on PMMA, was used to measure the effective area of the beam, A_{eff}. In this experiment A_{eff} was measured to be 41 $\mu\mathrm{m}^2$ in the normal incidence condition, which corresponds to 120 $\mu\mathrm{m}^2$ at 20° grazing incidence. The peak fluence F of each pulse can be calculated from the pulse energy E_p, which is directly measured in the experiment, and the effective area A_{eff} as $F = E_p / A_{\mathrm{eff}}$. The total error for the peak fluence determination is estimated to be ~ 20%. This value represents a combined error of pulse energy measurements and determination of the effective area of the beam.

A Ru polycrystalline metal film of 50 nm thickness was used as a target. The sample was prepared by depositing Ru on a naturally oxidized superpolished silicon substrate using the magnetron sputtering technique. The thickness of the film was determined with X-ray reflectivity measurements.

Ex-situ analysis of the damage morphologies was performed by means of differential interference contrast microscopy (DIC) with a Nomarski prism, high-resolution scanning electron microscopy (HR-SEM), transmission electron microscopy (TEM) and atomic force microscopy (AFM).

2.2.1. EX-SITU ANALYSIS OF DAMAGED SPOTS

We report a detailed analysis of the damage morphologies in the energy range of ~ 0.2 – 0.6 μJ per pulse, which corresponds to a peak fluence range of ~ 190 – 500 $\mathrm{mJ/cm^2}$. By applying higher fluences we start to damage the Si substrate underneath Ru, studying which is beyond the focus of the present work.

HR-SEM image of the damaged spot produced by the laser pulse with an incident flu-

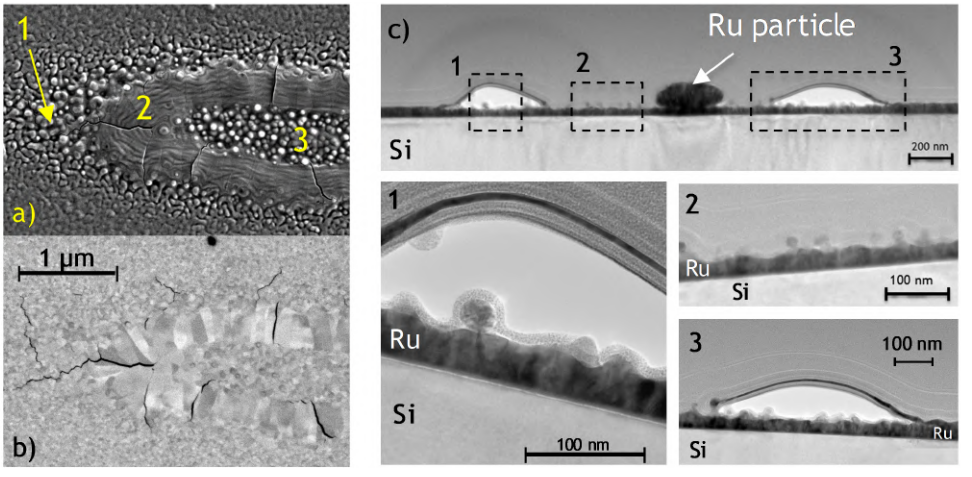

Figure 2.2: (a) HR-SEM image of the damaged spot produced by the 100 fs XUV FEL pulse with an incident peak fluence $F = 234\,\mathrm{mJ/cm^2}$. (b) HR-SEM image of the same spot obtained with the ESB detector. (c) TEM cross-section made at the center along the short axis of the damaged spot produced by the 100 fs XUV FEL pulse with an incident peak fluence of $F = 232\,\mathrm{mJ/cm^2}$. The spot has a similar morphology as the one shown in (a) and (b).

ence of $F = 213\,\mathrm{mJ/cm^2}$ is shown in Fig. 2.1 (a). This is the minimal damage detectable by means of HR-SEM. Note that DIC microscopy is not able to resolve such minor surface changes. A damaged spot with a lateral size of about 4.5 μm is observed and can be characterized as increased surface roughness and cracks. The roughness gradually decreases from the center of the spot towards the edge, which is confirmed with the AFM line profile taken in the center along the short axis of the spot, Fig. 2.1 (b). No other signatures of damage such as compaction of Ru layer were detected.

Different morphology is observed when irradiating the target with slightly higher fluences. The damaged spot produced with an incident fluence of $F = 234\,\mathrm{mJ/cm^2}$ is shown in Fig. 2.2 (a). Three distinct regions can be identified: nanoroughness and cracks at the edge (region 1), similar to that observed in Fig. 2.1 (a), a smooth "ring" structure with cracks (region 2) and spherical nanofeatures in the center of the spot (region 3). The lateral size of the nanofeatures varies in the range of $\sim 20-70\,\mathrm{nm}$. The HR-SEM image obtained with an energy selective backscattered (ESB) detector is shown in Fig. 2.2 (b). This detector enables one to resolve the elemental composition of the surface of the material under investigation. Since the difference in atomic number between Si and Ru is large, these elements result in a very different contrast. The ESB image shows that the surface consists of Ru only, while the cracks reach down to the Si substrate. The grain structure of the damaged spot happened to be better resolved with the ESB detector, since this detector is also sensitive to the atomic planes orientation. Interestingly, the grains in region 2, having an increased size and asymmetrical shape, are different from the grains in region 1 and 3 and in the non-irradiated region.

TEM cross-section is made in one of the spots that have a similar morphology as the spot in Fig. 2.2(a,b). The cross-section is made in the center along the short axis of the spot. During sample preparation, a layer of Pt was deposited on top of Ru to protect the

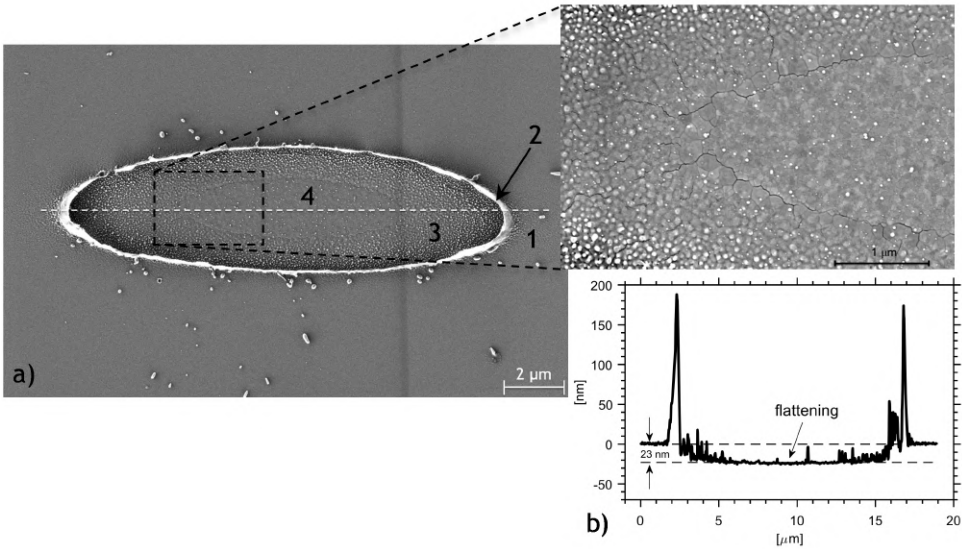

Figure 2.3: (a) HR-SEM image of the damaged spot produced by the 100 fs XUV FEL pulse with an incident peak fluence of $F = 374\,\mathrm{mJ/cm^2}$. The dashed horizontal line indicates where the AFM line profile is made. (b) AFM line profile illustrating the flat bottom in the central part of the damage crater.

surface from focused ion beam cycles. The results are shown in Fig. 2.2 (c), revealing the in-depth structure of the damaged spot. The TEM image shows that the smooth "ring" region observed with HR-SEM is a delaminated top layer of Ru. The thickness of that layer varies from 5 to 16 nm being the thickest in the part where it is still connected to the sample and decreasing towards the far end. At the center of the spot, where the local fluence is higher than at the edge, the delaminated layer is either completely removed (as in the spot shown in Fig. 2.2 (a), region 3) or remained at the surface in the form of a large Ru particle, Fig. 2.2 (c). Spherical nanofeatures in the center of the spot and below the delaminated layer seem to be droplets of molten and resolidified Ru. The remaining thickness of the Ru in the central part is measured to be roughly 35 nm, which corresponds to the thickness of the delaminated layer in this part to be ~ 15 nm.

Figure 2.3 illustrates a typical damage spot produced by laser pulses with an incident peak fluence in the range of $327 - 458\,\mathrm{mJ/cm^2}$. Same morphologies (nanoroughness 1, delaminated layer 2 and spherical nanofeatures 3) as in the previous stages of damage, Fig. 2.2, are observed with a new feature in the center of the spot (region 4). This region has a well-defined border in the form of a crack, see Fig. 2.3 (a) magnification, and appears to be more flat compared to region 3. A line cross-section extracted from the AFM scan of the spot illustrates the flattening in the center, see Fig. 2.3 (b). It also shows that the depth of the crater does not extend into the Si substrate. The thickness of the delaminated layer in the center of the spot is estimated to be ~ 23 nm. Low density of nanofeatures in region 4 (white dots in the HR-SEM images) enables one to resolve the grain structure of the surface in this region. Separate grains are clearly observed and are larger than the grains in the non-irradiated part of Ru surface.

Ablation induced by ultra-short laser pulses in metal targets is a phenomenon that

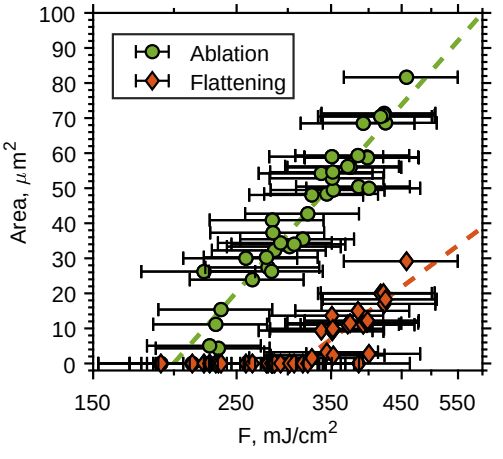

Figure 2.4: Liu's plot for the two damage threshold processes: ablation (circles) and flattening in the center of the crater (diamonds). The dashed lines represent the best fit of the experimental data.

was extensively studied in literature, but in case of irradiation with optical lasers [18, 32]. The damage morphologies in Ru that we observe in our experiments with XUV light resemble the same features. In the discussion part, based on our calculations, we suggest that the mechanism responsible for the XUV single-shot ablation of Ru is the same as was previously reported for the case of damage with optical lasers, and its nature is thermo-mechanical.

2.2.2. DAMAGE THRESHOLD DETERMINATION

Two types of morphologies detected during *ex-situ* analysis of the damaged spots exhibit clear threshold behavior: ablation and flattening of the surface in the center of the spot. The damage threshold values for both processes are obtained using the Liu's plot method [33], where the dependence of the damaged area on the peak fluence is plotted on a semilogarithmic scale, Fig. 2.4. The ablated areas are measured using DIC microscopy. For the second type of morphology the HR-SEM images are used to measure the areas surrounded by the crack, region 4 in Fig. 2.3 (a), since DIC microscopy was not accurate enough to resolve such fine features of the damage morphology. By extrapolating the linear fit of the experimental data to zero damaged area, we determine the ablation and flattening thresholds to be $F_{\text{th}}^{\text{abl}} = 200 \pm 40\,\text{mJ/cm}^2$ and $F_{\text{th}}^{\text{flat}} = 311 \pm 62\,\text{mJ/cm}^2$ respectively. Data points with zero damage area are not taken into account in the fitting procedure. The uncertainty of the presented approach is mostly determined by the error of peak fluence determination since the uncertainty of the damage area measurement is much lower (~ 1.5%).

2.3. SIMULATIONS

In this part we describe the XCASCADE(3D) [22] and the TTM [23] that are used to simulate the interaction of the XUV femtosecond laser pulse with a thin Ru film. Within the XCASCADE(3D) approach, the target is assumed to be a homogeneous arrangement

of atoms (atomic approximation) with a density corresponding to the chosen material. The code uses an event-by-event Monte Carlo simulation scheme. For simulations of photoabsorption, the cross sections are taken from the EPDL97 database [34]. A photoelectron receives an amount of energy equal to the difference between the photon energy and the ionization potential of the corresponding atomic shell, extracted from the EADL database [35].

Electron propagation is simulated using atomic binary-encounter-Bethe (BEB) cross sections of the impact ionization [36] and Mott's atomic cross sections for the elastic collisions [37]. In an impact ionization event, an incident electron triggers emission of a secondary electron from an atomic shell chosen according to relative cross sections [38]. In an elastic scattering event, an incident electron scatters on an atom without energy loss, so only the direction of electron propagation changes. The scattering angle of an incident electron in both scattering processes is calculated using the anisotropic scattering scheme, described in [22]. The scattering angle of the impact-ionized electron follows from the momentum conservation law.

The XCASCADE(3D) code provides a good description of electron cascades in the regime of "low" fluence. The latter means that: (i) the electrons are non-interacting and the electron cascades develop independently, i.e. the density of high-energy electrons participating in the cascading is at least ten times less than the atomic density and (ii) the material properties are not affected during the electron cascading, i.e. the photoionization and impact ionization cross sections do not change significantly. Correspondingly, cross sections for the unexcited material are applied.

The holes created in atomic core-levels recombine via an Auger decay process releasing an Auger electron, which is the dominant recombination channel for outer atomic shells. When impact ionization or a core hole decay generates a valence hole, its energy and position are recorded. Within the atomic approximation we consider that the energy stored in the valence holes corresponds to the energy of thermalized electrons in the conduction band in a real metal system.

Polarization of light is known to affect the direction of photoelectrons. Separate XCASCADE(3D) calculations were performed to estimate the influence of polarization on the development of electron cascades. Two limiting cases were compared. In the first one, the direction of photoelectrons was chosen to be isotropic (no polarization assumed). In the second case, we chose the direction of photoelectrons to be perpendicular to the surface (up and down, mimicking p-polarization under grazing incidence). The results showed only insignificant difference proving that the role of the polarization is small for the conditions considered in this work.

All photo- as well as secondary electrons are traced until their energy falls below a cut-off energy, which is chosen to be 10 eV [22, 38]. As soon as an electron loses its energy below this cut-off, it is considered as a slow electron thermalized in the conduction band of the material. The Monte Carlo simulations are repeated $> 10^5$ times for sufficient statistics to provide reliable results.

To calculate the energy density depth profiles we first perform simulations for bulk material assuming all photons are absorbed at z = 0 ("surface"). Here and further z denotes the in-depth direction. Then the realistic absorption positions are taken into account by applying a convolution with the Lambert-Beer's law taking the light penetration depth corresponding to the particular angle of incidence. Here we treat the region

z ≥ 0 as Ru, while region z < 0 is considered as vacuum above the Ru surface. This approach enables one to estimate the total energy emitted from the sample, but not the actual distribution of energy above the surface.

As a result, we obtain the energy density of the thermalized electrons, $U_e(\boldsymbol{r}, t)$, and valence holes, $U_h(\boldsymbol{r}, t)$, as functions of space and time. The time derivative of the total energy density $U = U_e + U_h$ is used to calculate the source term for the TTM.

The TTM is formulated as a set of two coupled nonlinear differential equations, which describe the spatial and temporal evolution of electron (T_e) and lattice (T_l) temperatures:

$$\begin{cases} C_e(T_e)\dfrac{\partial T_e}{\partial t} = \dfrac{\partial}{\partial \mathrm{z}}\left(k_e(T_e, T_l)\dfrac{\partial T_e}{\partial \mathrm{z}}\right) - G(T_e)(T_e - T_l) + S(\mathrm{z}, t) \\ C_l(T_l)\dfrac{\partial T_l}{\partial t} = G(T_e)(T_e - T_l), \end{cases} \tag{2.1}$$

where C_e and C_l are the electron and lattice heat capacities, respectively, k_e is the electron thermal conductivity, G is the electron-phonon coupling factor, which describes the energy exchange rate between electrons and the lattice, and $S(\mathrm{z}, t)$ is the heat source. All thermal parameters are temperature-dependent (see Appendix for details). The problem is formulated in only one, in-depth, dimension, since the laser spot size (∼ μm) is much larger than the penetration depth of the radiation (∼ nm), which makes the temperature gradients in lateral direction much smaller than in the in-depth direction.

As a source term, we use the time derivative of the total energy density U inside the Ru film, projected into the in-depth direction z:

$$S(\mathrm{z}, t) = \frac{\partial U(\mathrm{z}, t)}{\partial t}, \quad 0 \le \mathrm{z} \le L, \tag{2.2}$$

where L is the film thickness. To evaluate the importance of the non-equilibrium electron kinetics stage, we also perform the TTM calculations without XCASCADE(3D) using a standard source term, representing heating of the electronic system with a temporally Gaussian laser pulse with exponential decay of the absorbed energy:

$$S(\mathrm{z}, t) = \sqrt{\frac{4\ln 2}{\pi}}\frac{F(1-R)}{\delta \tau_p} e^{-\mathrm{z}/\delta} e^{-4\ln 2(t/\tau_p)^2}, \tag{2.3}$$

where F is the incident fluence, R is the surface reflectivity, δ is the light penetration depth and τ_p is the pulse duration. With this standard TTM approach it is assumed that electrons are always in thermal equilibrium during the heating process.

We neglect the lattice thermal conductivity since electrons are considered as the main heat carriers in metals. The system (3.1) is solved numerically using the finite-difference method with Neumann boundary conditions (no heat flux at both interfaces). Both electrons and lattice are at room temperature $T_0 = 300$ K at the beginning of the simulations. The choice of thermal and optical parameters is described in Appendix.

Melting of the Ru film is simulated within the TTM taking the latent heat of melting H_m into account using the enthalpy method [39]. The lattice temperature is reconstructed from the relationship between enthalpy and lattice temperature, taken from

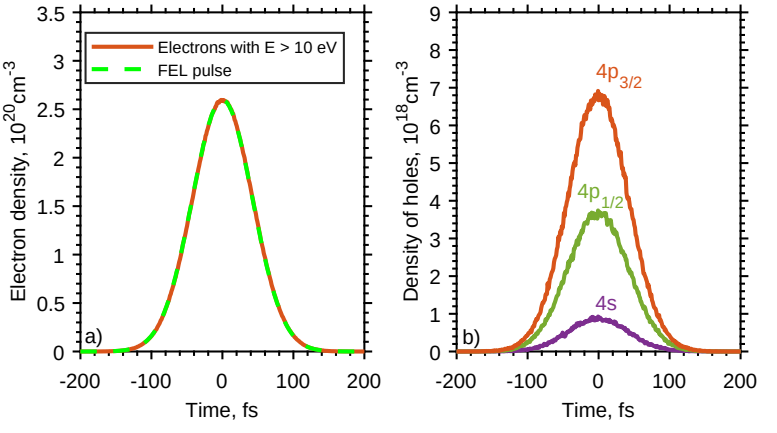

Figure 2.5: (a) Transient integral density of excited electrons with energy above the cut off threshold of 10 eV (solid line). The Gaussian temporal profile of a 100 fs FEL pulse is shown schematically with a dashed line. (b) Transient integral density of holes created in $4s$, $4p_{1/2}$ and $4p_{3/2}$ levels of Ru. The incident fluence is $F = 200\,\mathrm{mJ/cm^2}$.

[40]. Here for simplicity we neglect the difference in thermal properties between the liquid and solid phase.

In the following two sections we present the results of the XCASCADE(3D) and TTM calculations. The incident fluence level used in most of the calculations in this work is chosen to be $F = 200\,\mathrm{mJ/cm^2}$, which is the ablation threshold measured in the experiment.

2.3.1. RESULTS OF THE XCASCADE(3D) CALCULATIONS

Transient number and energy densities of electrons and deep-shell holes generated in Ru with 92 eV photons and $200\,\mathrm{mJ/cm^2}$ incident fluence are calculated with the XCASCADE(3D) code. Figure 2.5 presents the integral densities of (a) cascading electrons and (b) deep-shell holes. We assume a Gaussian temporal profile of the laser pulse in the simulations of photoabsorption. Here and further, $t = 0$ corresponds to the moment of time when the maximum of the laser pulse intensity is at the surface of the Ru film. The density of electrons participating in the cascading, i.e. those with an energy above the cut off threshold of 10 eV, follows closely the Gaussian temporal profile of the FEL pulse with 100 fs FWHM, Fig. 2.5 (a), which shows that there is virtually no cascading after the laser pulse. The duration of electron cascades in Ru at this photon energy, defined as FWHM of the electron density increase [38], is found to be < 1 fs. Please note, that the density of cascading electrons is much lower than the atomic density of Ru ($7.4 \cdot 10^{22}\,\mathrm{cm^{-3}}$), ensuring the applicability of the XCASCADE(3D) code.

A photon with an energy of 92 eV is capable of ionizing 4s, 4p, 4d and 5s electrons in Ru. The 4d and 5s valence levels in our atomic approximation represent the conduction band of the material, and, thus, photoabsorption by these electrons is considered simply as heating of the conduction band electronic system. The holes, created in those levels do not recombine via Auger processes, and the energy stored in these holes is treated as the energy of electrons thermalized in the conduction band.

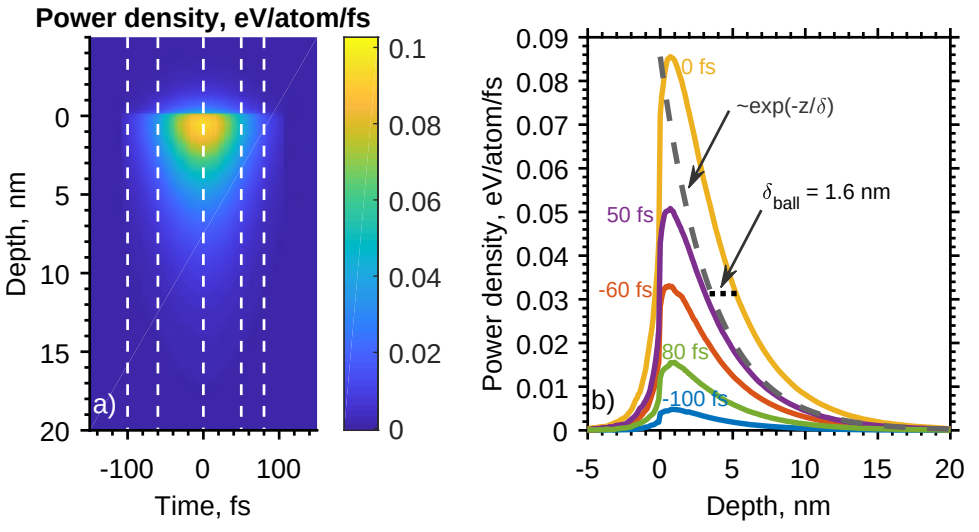

Figure 2.6: (a) 2D map of temporal and spatial evolution of the power density $\partial U(z,t)/\partial t$ of thermalized electrons and valence holes obtained from XCASCADE(3D) calculations with an incident fluence of F = 200 mJ/cm^2. The top 20 nm of the total 50 nm thick Ru film are shown. The surface of the Ru film is at z = 0, and the region z < 0 corresponds to the vacuum above the surface. (b) Power density depth profiles at different times (solid lines). For comparison, the Lambert-Beer's exponent is shown schematically with a dashed line.

The 4s-, $4p_{1/2}$- and $4p_{3/2}$-level holes have characteristic Auger or Coster-Kronig decay times of 0.04 fs, 0.13 fs and 0.12 fs, respectively [35]. Thus, they are quickly decaying into the conduction band within the pulse duration, see Fig. 2.5 (b).

For the heat source in the TTM, we need the spatiotemporal distributions of the energy density of thermalized electrons, $U_e(z,t)$, and valence holes, $U_h(z,t)$, which are obtained from the XCASCADE(3D) calculations. The time derivative of the total energy density $\partial U(z,t)/\partial t = \partial(U_e(z,t)+U_h(z,t))/\partial t$ is used to generate the heat source. The resulting 2D map of the power density $\partial U(z,t)/\partial t$ is shown in Fig. 2.6 (a). The first 20 nm of the 50 nm thick Ru film are shown together with 5 nm of vacuum above the Ru surface. One can see that most of the energy (92%) stays inside the Ru, while 8% escapes from the surface via electron emission. The values are obtained by integrating the power density below and above the surface, respectively. The energy escapes via photo- and secondary electrons that have sufficient energy to travel to the surface and overcome the work function of Ru (4.7 eV).

Figure 2.6 (b) illustrates the depth profiles of the power density $\partial U(z,t)/\partial t$ at different moments of time, indicated with vertical dashed lines in Fig. 2.6 (a). The average distance electrons travel before thermalization (electron ballistic range) can be extracted. The spatial profiles in Fig. 2.6 (b) are the result of convolution with the Lambert-Beer's exponent $\exp(-z/\delta)$ with light penetration depth δ = 3.5 nm (20° grazing incidence). Therefore, the actual electron ballistic range δ_{ball} is obtained as the difference between the final profile (solid lines) and the Lambert-Beer's exponent (dashed line) at $1/e$ level. Following this procedure, the electron ballistic range in Ru is found to be 1.6 nm in case of irradiation with 92 eV photons.

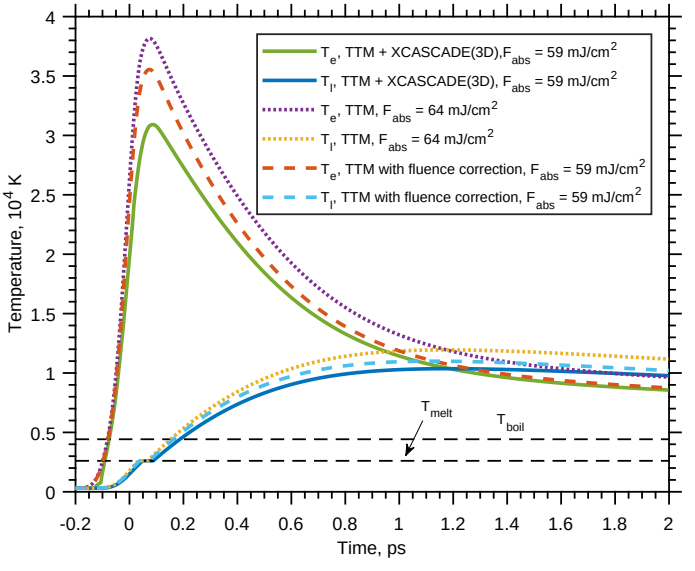

Figure 2.7: Temporal evolution of electron (T_e) and lattice (T_l) surface temperatures of a 50 nm Ru film irradiated by a 100 fs XUV pulse with an incident fluence of $F = 200\,\mathrm{mJ/cm^2}$, calculated with different approaches. Solid lines are the results of the TTM calculations with the XCASCADE(3D) heat source. Dotted and dashed lines show the results of the TTM calculations with a standard heat source without and with the 8% fluence correction taking into account the electron emission, respectively. Black dashed horizontal lines indicate the melting (2607 K) and boiling (4423 K) temperatures of Ru under normal conditions.

In summary, our XCASCADE(3D) calculations show a small electron cascading effect in Ru under XUV exposure. Excited electrons thermalize within < 1 fs and travel only 1.6 nm ballistically before thermalization. About 8% of the absorbed energy escapes from the surfaces due to high-energy electron emission. Note, however, that we expect longer cascading times and electron ranges with increase of the photon energy.

2.3.2. RESULTS OF THE TWO-TEMPERATURE MODEL CALCULATIONS

In this section we present the results of the TTM calculations of electron and lattice temperature evolution, Eq. (3.1). As a heat source for the TTM we use the time derivative of the total energy density $U(z, t)$ inside the Ru film, Eq. (3.2) with $L = 50$ nm. In that way, only the energy that stays inside the Ru film is taken into account in the TTM calculations. The results are compared with the TTM calculations with a standard heat source, Eq. (3.3).

Figure 2.7 shows the temporal evolution of electron and lattice temperatures at the front surface of the Ru film. Solid lines are the results of the TTM calculations with the XCASCADE(3D) heat source, Eq. (3.2). There is strong thermal non-equilibrium between electrons and lattice just after the absorption of the FEL pulse, with electrons having significantly higher temperature than the lattice. The non-equilibrium occurs since the pulse duration of 100 fs is shorter than the electron-phonon thermalization time $\tau_{\text{e-ph}}$ [24]. The latter is calculated from the TTM results as the time when the difference between electron and lattice temperatures at the surface decreases to the $1/e$ level

and is equal to $\tau_{\text{e-ph}} \sim 0.5$ ps. The incident fluence level of $F = 200\,\text{mJ/cm}^2$ corresponds to the absorbed fluence of $F_{\text{abs}} = F(1-R)(1-\alpha) = 59\,\text{mJ/cm}^2$, where α is the fraction of energy emitted from the surface obtained from the XCASCADE(3D) calculations (8%).

The dotted lines are the results of the TTM calculations with a standard heat source, Eq. (3.3). The absorbed fluence in that case is $F_{\text{abs}} = F(1-R) = 64\,\text{mJ/cm}^2$, since electron emission from the surface is not taken into account in the standard TTM approach. As expected, the temperatures are overestimated since the absorbed fluence is higher compared to the TTM + XCASCADE(3D) calculations.

In order to take into account the electron emission within the TTM, we decrease the absorbed fluence by 8% in the TTM calculations with a standard heat source (dashed lines). The results are closer to the ones obtained with the TTM + XCASCADE(3D) approach. The 13% difference at the electron temperature peak is due to the fact that in the TTM + XCASCADE(3D) calculations, before thermalization, electrons travel ballistically for a distance of 1.6 nm, see Fig. 2.6, which effectively increases the volume where the energy was absorbed. This results in a lower peak value of the electron temperature compared to the standard TTM calculations where ballistic transport is not taken into account. The difference becomes smaller with time (2% at $t = 2$ ps), since the diffusion of thermalized electrons dominates the ballistic transport of electrons before thermalization. The diffusion length L_c, which is the distance electrons travel diffusively before thermal equilibration with the lattice at the surface, can be extracted from the electron temperature profile at $t = \tau_{\text{e-ph}}$ as the depth where the temperature decreases to $1/e$ level. It is found to be ~ 10 nm, which is ~ 6 times larger than the ballistic range. The difference in the lattice temperatures at the surface between the TTM calculations with the fluence correction and those with the XCASCADE(3D) source term stays below 10%.

This comparison suggests that although using the XCASCADE(3D) source term we obtain lower electron temperatures just after the absorption of the laser pulse compared to the standard TTM calculations due to the effects of electron emission from the surface and electron ballistic transport, neither of these effects has a significant impact on the dynamics of the lattice heating, which is the crucial process in the damage mechanism, as will be shown in the discussion section.

The lattice temperature plateau at $T_l = 2607$ K, Fig. 2.7, corresponds to the melting process. The surface of Ru reaches the melting temperature at the beginning and becomes liquid at the end of the plateau. The melting threshold can thus be determined as the incident fluence required to melt the front surface of Ru. With a separate set of TTM + XCASCADE(3D) calculations we determine the melting threshold to be $F_{\text{th}}^{\text{melt}} = 44\,\text{mJ/cm}^2$, corresponding to the absorbed fluence of $F_{\text{abs}} = 13\,\text{mJ/cm}^2$, which is 5 times lower than the ablation threshold, observed in the experiment. That suggests that melting occurs before ablation, which is also supported by our experimental observations. Figure 2.8 illustrates the onset of melting showing the evolution of electron and lattice surface temperatures for an absorbed fluence of $F_{\text{abs}} = 14\,\text{mJ/cm}^2$.

Further, we present the lattice temperature evolution on a longer timescale compared to Fig. 2.7, in order to illustrate the melting dynamics of the top part of the Ru film. The corresponding TTM + XCASCADE(3D) simulations are performed for a 100 nm thick film. The thickness is increased compared to the 50 nm Ru used in the experiment, so that the heat flux into the thick Si substrate is also modeled, albeit in a simplified way, where the bottom 50 nm of Ru in the calculations represent the substrate. In order to se-

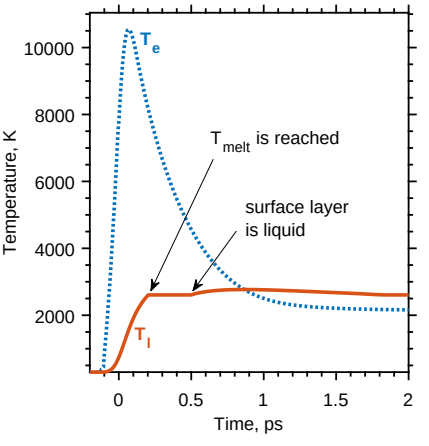

Figure 2.8: Temporal evolution of electron (dotted line) and lattice (solid line) surface temperatures of a 50 nm Ru film irradiated by a 100 fs XUV pulse with an absorbed fluence of $F_{\text{abs}} = 14\,\text{mJ/cm}^2$, calculated with the TTM + XCASCADE(3D) approach.

lect the optimal thickness of the film we perform calculations with increasing thickness until convergence of the results is reached.

The 2D map of the lattice temperature as a function of depth and time calculated for the absorbed fluence of $F_{\text{abs}} = 59\,\text{mJ/cm}^2$ is shown in Fig. 2.9. This fluence level corresponds to the onset of ablation observed in the experiment. Thus, the lattice temperature behavior presented in Fig. 2.9 can be treated as melting of the top Ru layer that occurs just before ablation (in terms of fluence). The black solid line marks the border between the liquid and the solid phases of Ru. Fast melting of the top 10 nm during the first 1.2 ps is followed by a much slower propagation of the melting front into the depth of the material. Similar two-step melting dynamics was previously reported for other metals [17, 27]. The melting starts at 0.08 ps and the maximum melted depth of 17 nm is reached at 30 ps after the laser pulse. The vertical white dashed line, plotted at the moment of time when $T_e = T_l$ at the surface, see Fig. 2.7, separates the two melting regimes. Hence, the fast melting of the top 10 nm is due to the diffusion of hot electrons and transfer of their energy to the lattice during the thermal non-equilibrium stage, while the second melting stage is a slow propagation of the solid-liquid interface after electrons and lattice equilibration. The calculated maximum melted depth (17 nm) is larger than the estimated thickness of the ablated layer observed in the experiment at a comparable fluence ($\sim 5-16$ nm), see Fig. 2.2 (c), which indicates that the ablation occurs inside the liquid layer.

2.4. DISCUSSION

The experimentally observed features of XUV-induced damage of the Ru film resemble the phenomenon of thermo-mechanical ablation (also referred to as spallation) in metal targets induced by optical lasers. It was shown that the generation of a thermo-induced compressive stress wave followed by a tensile stress wave propagating in the irradiated target is the cause of ablation [17, 18, 32, 41, 42]. Large stresses are generated because

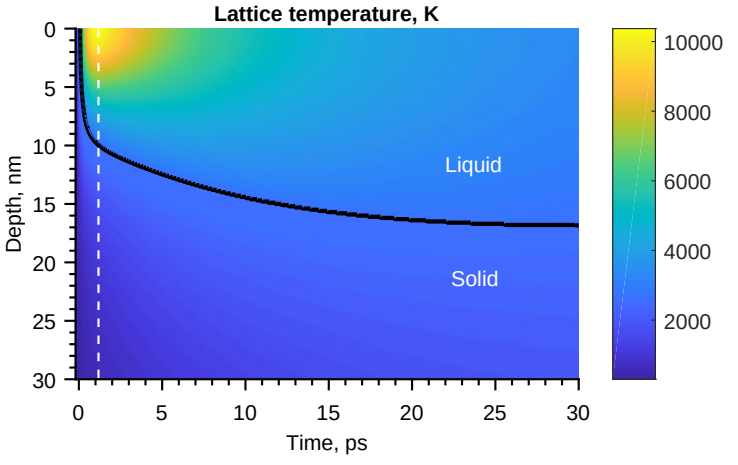

Figure 2.9: 2D map of temporal and spatial evolution of the lattice temperature of a 100 nm thick Ru film calculated with the TTM + XCASCADE(3D) approach for an absorbed fluence of $F_{\text{abs}} = 59\,\text{mJ/cm}^2$. Black solid line shows the interface between solid and liquid Ru. The top 30nm of the total 100nm thick Ru film are shown. The white dashed line plotted at the moment of time when $T_e = T_l$ at the surface separates the two melting regimes: fast melting of the top 10 nm of Ru and subsequent slow propagation of the solid-liquid interface for another 7 nm.

the heating of the lattice is faster than the time needed for the system to mechanically react to that ultrafast heating by expanding. This situation is referred to as the *stress confinement regime*, which occurs under the following conditions: $\tau_{\text{e-ph}} \leq \tau_a$, where $\tau_{\text{e-ph}}$ is the electron-phonon thermalization time which represents the characteristic time of lattice heating and τ_a is the acoustic relaxation time. From our calculations we obtain that $\tau_{\text{e-ph}} = 0.5\,\text{ps}$, see Fig. 2.7). Acoustic relaxation time can be estimated as $\tau_a \sim L_c/C_s$, where $L_c \sim 10\,\text{nm}$ is the diffusion length described above, and C_s is the bulk speed of sound. The latter is calculated as $C_s = \sqrt{B/\rho} \sim 5000\,\text{m/s}$, where B is the bulk modulus and ρ is the density of Ru. Thus, $\tau_a \sim 2$ ps and the condition of the stress confinement regime is satisfied. Therefore, we conclude that the mechanism responsible for the XUV induced single-shot crater formation of Ru is thermo-mechanical ablation in the stress confinement regime.

As one can see from Fig. 2.7, the incident fluence level of $200\,\text{mJ/cm}^2$ is sufficient not only to melt the surface of Ru, but also to heat the resulting liquid up to ~ 2.5 times above the boiling temperature at atmospheric pressure ($T_{\text{boil}} = 4423\,\text{K}$). Although such high temperatures are reached, boiling is not considered here as a damage mechanism since homogeneous explosive boiling with a vapor bubble nucleation rate of the order of $J \sim 10^{36}\,\text{m}^{-3}\text{s}^{-1}$ is only possible in close vicinity of the critical point of the material [43, 44]. The bubble nucleation rate is determined using the heated depth of about $L_c \sim 10\,\text{nm}$ and the acoustic time of $\tau_a \sim 2\,\text{ps}$, which were determined above, as $J = 1/(L_c^3 \tau_a)$. The morphology of damage craters also does not support the idea of boiling to be the damage mechanism.

Our XCASCADE(3D) calculations support the hypothesis that XUV-induced ablation in Ru has the same nature as ablation in metals induced by optical lasers. Namely, the electron cascading effect is found to be small: electrons thermalize very quickly within

the pulse duration and travel ballistically for a short distance before thermalization. Only a small part of the absorbed energy escapes from Ru via electron emission.

Electron thermal diffusion length is found to dominate both the light penetration depth and the electron ballistic range. Therefore, despite the difference in the light penetration depth between XUV used in our experiment and optical lasers, electrons should diffuse the absorbed energy over comparable volumes, which should result in the same damage process – thermo-mechanical ablation. Hence, according to our investigations, XUV light does not introduce any other significant effects into the single-shot damage process compared to visible light.

Within the proposed damage mechanism, we suggest the explanation of some of the damage morphologies observed in our experiment, using the analogy with the optical damage studies. The absorption of the high fluence femtosecond laser pulse first results in the ultrafast melting of the top part of the Ru film. The depth of melting depends on the incident fluence and is equal to 17 nm for $F = 200\,\mathrm{mJ/cm^2}$ according to our calculations, Fig. 2.9. If the fluence of the pulse is below the ablation threshold of $F_{\mathrm{th}}^{\mathrm{abl}} = 200 \pm 40\,\mathrm{mJ/cm^2}$, the melted layer of Ru cools down and recrystallizes, which may result into increased surface roughness. The fact that we did not observe compaction of Ru layer can be supported by the argument that Ru is magnetron deposited on top of a wafer, so the sample already has near bulk density.

During this pre-ablation stage cavitation below the surface typically occurs as a result of propagation of a tensile stress wave in the melted material [18, 32, 41, 45]. When the absorbed energy is not sufficient to cause complete ablation, the cavities in the cavitation zone collapse due to the surface tension. If the recrystallization front from the depth of the metal arrives before the collapse, the cavities may remain frozen below the surface [46–48]. The existence of such frozen cavities may also explain the nanoroughness observed in the pre-ablation stage, Fig. 2.1 and region 1 in Figs. 2.2 (a) and 2.3 (a), although detailed atomistic calculations are required to confirm this hypothesis.

When the incident fluence overcomes the ablation threshold, ejection of the top 6 – 23 nm of Ru occurs, see Figs. 2.2 and 2.3. Increased grain size in the ablated layer, that remained attached to the surface, see Fig. 2.2 (b), compared to the grains outside the damage spot, shows that the ablated layer was melted and resolidified having a different grain structure in the final state. During the ablation process the cavitation zone that is formed in the liquid layer by the tensile stress is stretched until it finally breaks [45]. Part of the liquid material between the ablated layer and the rest of the film is drawn into the ablated layer and the other part is attracted back to the bottom of the damage crater by the surface tension. As a result, spherical nanoparticles of Ru are observed at the bottom of the crater, Figs. 2.2 and 2.3.

The flattening in the centre of the spot at even higher fluences, Fig. 2.3, can be explained as the interplay between two processes: rupture of the cavitation zone and arrival of the recrystallization front that propagates from the depth to the surface of the material. In the central part of the spot, where the local fluence is higher, the recrystallization front arrives much later than the rupture of the cavitation zone and subsequent ablation of the top part of the film, “freezing” the remaining liquid layer that had sufficient time to equilibrate into a smooth surface. At the edge of the spot, where the fluence is lower, the rupture of the cavitation zone occurs later, while the recrystallization front arrives earlier. As a result, the rough surface, that is formed just after ablation, is

frozen. The existence of a similar flat central region in the damage crater of Al irradiated by 800 nm light [47], again, illustrates the similarities between XUV and optical damage of metals.

The fact that the calculated melting threshold of Ru is 5 times lower than the ablation threshold supports the assumption that melting takes place before ablation. A similar trend was reported for other metals damaged by optical lasers. It was calculated [17] that the melting threshold of bulk Ni irradiated with a 1 ps laser pulse is ~ 5 times lower than the ablation threshold. Ablation starts inside the liquid layer of melted Ni with the thickness of the ablated layer smaller than the melted depth. The experimentally measured melting threshold of epitaxial Ag(001) [27] is ~ 6 times lower than the fluence at which surface swelling of single-crystal Ag(001) was observed [48], which can be considered as the onset of ablation.

In our experiments we detect the surface modifications (roughening and cracks, see Fig. 2.1) that happen before ablation in the fluence range from 190 to 213 mJ/cm^2. No exposures were performed with lower fluences. The minimum damage induced by 190 mJ/cm^2 pulses could only be detected by AFM measurements. Hence, we suggest that AFM is the most accurate microscopy technique to detect minor surface modifications produced by laser pulses.

In future work, we plan to supplement our model with detailed molecular dynamics simulations of melting, cavitation, ablation and possibly recrystallization processes. This would allow tracing the entire material evolution and benchmarking our model with the experimental data.

2.5. SUMMARY AND CONCLUSIONS

We performed single-shot damage experiments at the free-electron laser FLASH, where 50 nm Ru films were exposed to 100 fs XUV (13.5 nm) pulses with varying fluences. The *ex-situ* analysis of the damaged spots revealed the following picture of damage development with increasing fluence. The first observable damage at the lowest applied fluence is roughening of the top surface of the Ru film. Melting and resolidification together with the possible existence of subsurface voids produced by a tensile stress wave propagating in the melted material are suggested as the processes responsible for increased surface roughness. The melting threshold is calculated as the incident fluence required to melt the top surface of Ru and is equal to $F_{\rm th}^{\rm melt} = 44$ mJ/cm^2. Spallation of the top 5–23 nm of Ru was observed for fluences above the ablation threshold, which was measured to be $F_{\rm th}^{\rm abl} = 200 \pm 40$ mJ/cm^2. There are two types of morphologies observed inside the damage craters: spherical nanofeatures and flattening in the central part of the crater. The flattening occurs when the incident fluence is above the flattening threshold $F_{\rm th}^{\rm flat} = 311 \pm 62$ mJ/cm^2. The interplay between the rupture of the cavitation zone that is formed during the ablation process and the dynamics of resolidification may explain the observed morphologies inside the damage crater.

For better understanding of the observed damage morphologies we performed simulations of the interaction of the 100 fs XUV FEL pulse with a Ru target using the combined TTM + XCASCADE(3D) approach. We modeled the absorption of the laser pulse and the non-equilibrium electron kinetics with the Monte Carlo code XCASCADE(3D), while the diffusion of thermalized electrons and heating of the lattice were calculated

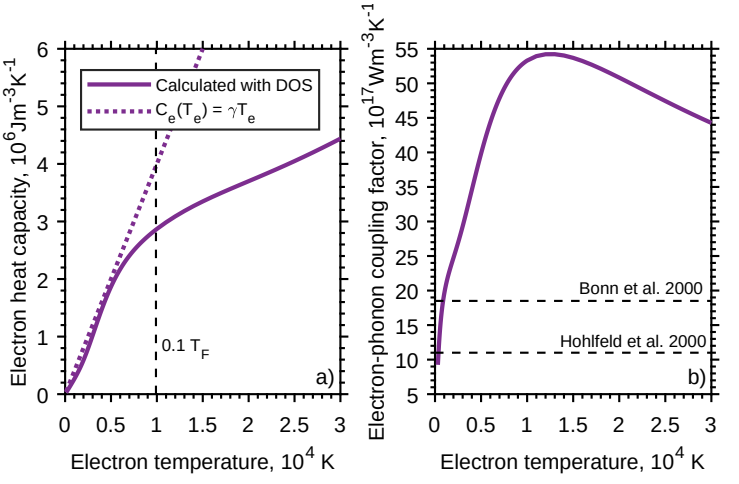

Figure 2.10: Electron temperature dependence of the electron heat capacity (a) and electron-phonon coupling factor (b) calculated with the DOS of Ru taken into account (solid lines). Linear approximation for the electron heat capacity is shown with the dotted line in (a). The vertical dashed line at $T_e = 0.1 T_F$ approximately marks the limit of validity of the linear approximation for the electron heat capacity. The constant values of the electron-phonon coupling factor available in the literature are shown with dashed lines in (b).

with the two-temperature model. The results of the XCASCADE(3D) calculations were used as the heat source for the TTM. Based on our calculations we suggest that the ablation observed in Ru under XUV exposure occurs in the stress confinement regime, similar to what was previously reported in studies of damage of metals with optical lasers. The results of XCASCADE(3D) calculations support the similarities between XUV- and optically-induced ablation, showing only a small electron cascading effect in Ru induced by XUV (92 eV) photons. Excited electrons thermalize within < 1 fs and travel ballistically over a distance of 1.6nm before thermalization takes place. We calculated that ~ 8% of the absorbed energy escapes from the surface due to electron emission. Together with ballistic transport it affects the electron temperature just after the absorption of the FEL pulse, although both effects were found to have a small impact on the lattice temperature evolution, with the latter being crucial in understanding the single-shot damage mechanism. The presented computational analysis of non-equilibrium electron kinetics and ultrafast lattice heating can be applied to describe material response in a wide range of photon energies, provided that other conditions of applicability are met, which makes it a promising tool to study performance of materials under XUV and X-ray irradiation.

2.6. APPENDIX. THERMAL PARAMETERS

The accuracy of TTM depends on the proper choice of the thermal parameters of the material under investigation, especially in the regime of high electron temperatures, where these properties can significantly differ from their room temperature values. In our TTM calculations we reach the maximum values of electron temperature of the order of $3.5 \cdot 10^4$ K, which is only ~ 3 times lower than the Fermi temperature $T_F = \epsilon_F / k_B$ ~

Table 2.1: Parameter values used in calculations.

Electron specific heat constant[a]	$\gamma = 400\,\mathrm{J/m^3/K^2}$
Latent heat of melting[b]	$H_m = 4.7 \cdot 10^9\,\mathrm{J/m^3}$
Surface reflectivity[c]	$R = 68\%$
Light penetration depth[c]	$\delta = 3.5\,\mathrm{nm}$
Pulse duration	$\tau_p = 100\,\mathrm{fs}$
Bulk modulus[d]	$B = 310\,\mathrm{GPa}$
Density[b]	$\rho = 12.3\,\mathrm{g/cm^3}$

[a] Ref. [50]

[b] Ref. [40]

[c] Ref. [51], at 13.5 nm wavelength, 20° grazing incidence

[d] Ref. [52]

$9.9 \cdot 10^4$ K of Ru [49], where k_B and ϵ_F are the Boltzmann constant and the Fermi energy, respectively. Therefore, the parameters that we use in the TTM calculations should be valid in the regime of high electron temperatures.

The dependencies of the electron heat capacity and electron-phonon coupling factor on the electron temperature are calculated using the formalism described in [53] within the effective one-band approximation and are shown in Fig. 2.10. The Ru density of states (DOS) is taken from [49]. The electron-phonon coupling factor is calculated within the harmonic approximation [53].

The calculated electron heat capacity is compared with the linear approximation $C_e(T_e) = \gamma T_e$, with the electron specific heat constant γ taken from [50], see Fig. 2.10 (a). A significant difference is observed in the high electron temperature region where the linear approximation is no longer valid. The latter is limited to the electron temperature range $0 < T_e < 0.1 T_F$ [54, 55].

Electron-phonon coupling G is strong in Ru, which is typical for transition metals. The calculated dependence of G on the electron temperature is shown in Fig. 2.10 (b). The strong enhancement is followed by a decrease with a maximum value reached at $T_e \sim 1.2 \cdot 10^4$ K. A similar behavior of G with increasing electron temperature was previously reported for titanium [56]. Both metals have hcp crystal structure and relatively low DOS at the Fermi level, which can explain the similar behavior. Our calculations are in a good agreement with previously reported values of G at room temperature [25, 26].

The electron thermal conductivity is expressed as

$$k_e(T_e, T_l) = K \cdot \frac{(\vartheta^2 + 0.16)^{5/4}(\vartheta^2 + 0.44)\vartheta}{(\vartheta^2 + 0.092)^{1/2}(\vartheta^2 + b\,\vartheta_l)}, \tag{2.4}$$

where $\vartheta = k_B T_e/\epsilon_F$ and $\vartheta_l = k_B T_l/\epsilon_F$ [16, 57]. K and b are material dependent constants. This expression is valid in a wide range of electron temperatures up to the temperatures considerably larger than the Fermi temperature. In order to determine K and b for Ru we fit Eq. (3.4) to the experimental curve of equilibrium thermal conductivity from [58] with K and b as fitting parameters, taking $T_e = T_l = T$ in Eq. (3.4). Values of thermal conductivity measured between 300 and 2500 K are used in the fitting procedure. Following this scheme we find $K = 35\,\mathrm{W/m/K}$ and $b = 0.04$. Here we neglect phonon thermal con-

ductivity in the metal and consider electron thermal conductivity to be equal to the total thermal conductivity.

The dependence of the lattice heat capacity on lattice temperature and the relationship between enthalpy and lattice temperature are taken from [40]. Surface reflectivity and light penetration depth are calculated using IMD software [51]. The summary of thermal and optical parameters used in this work is shown in Table 2.1.

ACKNOWLEDGEMENTS

I gratefully acknowledge the support of the operators of the FLASH facility. I thank Mark Smithers, Enrico Keim and Henk van Wolferen for their help in performing the HR-SEM and TEM analysis, as well as Chris J. Lee, Frank Scholze, Vasily Zhakhovsky, Nail Inogamov, Viacheslav Medvedev, Cristina Sfiligoj, Joost Frenken, and Beata Ziaja for fruitful discussions.

REFERENCES

[1] W. Ackermann *et al.*, *Operation of a free-electron laser from the extreme ultraviolet to the water window,* Nat. Photonics **1**, 336 (2007).

[2] E. Allaria *et al.*, *Highly coherent and stable pulses from the FERMI seeded free-electron laser in the extreme ultraviolet,* Nat. Photonics **6**, 699 (2012).

[3] F. Barkusky, A. Bayer, S. Doring, P. Grossmann, and K. Mann, *Damage threshold measurements on EUV optics using focused radiation from a table-top laser produced plasma source,* Opt. Express **18**, 4346 (2010).

[4] A. R. Khorsand, R. Sobierajski, E. Louis, S. Bruijn, E. D. van Hattum, R. W. E. van de Kruijs, M. Jurek, D. Klinger, J. B. Pelka, L. Juha, T. Burian, J. Chalupsky, J. Cihelka, V. Hajkova, L. Vysin, U. Jastrow, N. Stojanovic, S. Toleikis, H. Wabnitz, K. Tiedtke, K. Sokolowski-Tinten, U. Shymanovich, J. Krzywinski, S. Hau-Riege, R. London, A. Gleeson, E. M. Gullikson, and F. Bijkerk, *Single shot damage mechanism of Mo/Si multilayer optics under intense pulsed XUV-exposure,* Opt. Express **18**, 700 (2010).

[5] M. Muller, F. Barkusky, T. Feigl, and K. Mann, *EUV damage threshold measurements of Mo/Si multilayer mirrors,* Appl. Phys. A **108**, 263 (2012).

[6] A. Jody Corso, P. Zuppella, F. Barkusky, K. Mann, M. Müller, P. Nicolosi, M. Nardello, and M. Guglielmina Pelizzo, *Damage of multilayer optics with varying capping layers induced by focused extreme ultraviolet beam,* J. Appl. Phys. **113**, 203106 (2013).

[7] R. Sobierajski, S. Bruijn, A. Khorsand, E. Louis, R. E. van de Kruijs, T. Burian, J. Chalupsky, J. Cihelka, A. Gleeson, J. Grzonka, E. Gullikson, V. Hajkova, S. Hau-Riege, L. Juha, M. Jurek, D. Klinger, J. Krzywinski, R. London, J. B. Pelka, T. Płociński, M. Rasiński, K. Tiedtke, S. Toleikis, L. Vysin, H. Wabnitz, and F. Bijkerk, *Damage mechanisms of MoN/SiN multilayer optics for next-generation pulsed XUV light sources,* Opt. Express **19**, 193 (2011).

[8] S. P. Hau-Riege, R. A. London, R. M. Bionta, M. A. McKernan, S. L. Baker, J. Krzywinski, R. Sobierajski, R. Nietubyc, J. B. Pelka, M. Jurek, L. Juha, J. Chalupský, J. Cihelka,

V. Hájková, A. Velyhan, J. Krása, J. Kuba, K. Tiedtke, S. Toleikis, T. Tschentscher, H. Wabnitz, M. Bergh, C. Caleman, K. Sokolowski-Tinten, N. Stojanovic, and U. Zastrau, *Damage threshold of inorganic solids under free-electron-laser irradiation at 32.5 nm wavelength,* Appl. Phys. Lett. **90**, 173128 (2007).

[9] S. P. Hau-Riege, R. A. London, R. M. Bionta, D. Ryutov, R. Soufli, S. Bajt, M. A. McKernan, S. L. Baker, J. Krzywinski, R. Sobierajski, R. Nietubyc, D. Klinger, J. B. Pelka, M. Jurek, L. Juha, J. Chalupský, J. Cihelka, V. Hájková, A. Velyhan, J. Krása, K. Tiedtke, S. Toleikis, H. Wabnitz, M. Bergh, C. Caleman, and N. Timneanu, *Wavelength dependence of the damage threshold of inorganic materials under extreme-ultraviolet free-electron-laser irradiation,* Appl. Phys. Lett. **95**, 111104 (2009).

[10] S. P. Hau-Riege, R. A. London, A. Graf, S. L. Baker, R. Soufli, R. Sobierajski, T. Burian, J. Chalupsky, L. Juha, J. Gaudin, J. Krzywinski, S. Moeller, M. Messerschmidt, J. Bozek, and C. Bostedt, *Interaction of short X-ray pulses with low-Z X-ray optics materials at the LCLS free-electron laser,* Opt. Express **18**, 23933 (2010).

[11] J. Chalupský, V. Hájková, V. Altapova, T. Burian, A. J. Gleeson, L. Juha, M. Jurek, H. Sinn, M. Störmer, R. Sobierajski, K. Tiedtke, S. Toleikis, T. Tschentscher, L. Vyšín, H. Wabnitz, and J. Gaudin, *Damage of amorphous carbon induced by soft X-ray femtosecond pulses above and below the critical angle,* Appl. Phys. Lett. **95**, 1 (2009).

[12] S. Dastjani Farahani, J. Chalupsky, T. Burian, H. Chapman, A. Gleeson, V. Hajkoya, L. Juha, M. Jurek, D. Klinger, H. Sinn, R. Sobierajski, M. Störmer, K. Tiedtke, S. Toleikis, T. Tschentscher, H. Wabnitz, and J. Gaudin, *Damage threshold of amorphous carbon mirror for 177 eV FEL radiation,* Nucl. Instrum. Meth. A **635**, S39 (2011).

[13] J. Pelka, R. Sobierajski, D. Klinger, W. Paszkowicz, J. Krzywinski, M. Jurek, D. Zymierska, A. Wawro, A. Petroutchik, L. Juha, V. Hajkova, J. Cihelka, J. Chalupsky, T. Burian, L. Vysin, S. Toleikis, K. Sokolowski-Tinten, N. Stojanovic, U. Zastrau, R. London, S. Hau-Riege, C. Riekel, R. Davies, M. Burghammer, E. Dynowska, W. Szuszkiewicz, W. Caliebe, and R. Nietubyc, *Damage in solids irradiated by a single shot of XUV free-electron laser: irreversible changes investigated using X-ray microdiffraction, atomic force microscopy and Nomarski optical microscopy,* Radiat. Phys. Chem. **78**, S46 (2009).

[14] S. Nolte, C. Momma, H. Jacobs, A. Tünnermann, B. N. Chichkov, B. Wellegehausen, and H. Welling, *Ablation of metals by ultrashort laser pulses,* J. Opt. Soc. Am. B **14**, 2716 (1997).

[15] J. Yang, Y. Zhao, N. Zhang, Y. Liang, and M. Wang, *Ablation of metallic targets by high-intensity ultrashort laser pulses,* Phys. Rev. B **76**, 165430 (2007).

[16] B. Rethfeld, D. S. Ivanov, M. E. Garcia, and S. I. Anisimov, *Modelling ultrafast laser ablation,* J. Phys. D: Appl. Phys. **50**, 193001 (2017).

[17] L. V. Zhigilei, Z. Lin, and D. S. Ivanov, *Atomistic modeling of short pulse laser ablation of metals: connections between melting, spallation, and phase explosion,* J. Phys. Chem. C **113**, 11892 (2009).

[18] B. J. Demaske, V. V. Zhakhovsky, N. A. Inogamov, and I. I. Oleynik, *Ablation and spallation of gold films irradiated by ultrashort laser pulses,* Phys. Rev. B **82**, 064113 (2010).

[19] I. A. Makhotkin, R. Sobierajski, J. Chalupský, K. Tiedtke, G. de Vries, M. Störmer, F. Scholze, F. Siewert, R. W. E. van de Kruijs, I. Milov, E. Louis, I. Jacyna, M. Jurek, D. Klinger, L. Nittler, Y. Syryanyy, L. Juha, V. Hájková, V. Vozda, T. Burian, K. Saksl, B. Faatz, B. Keitel, E. Plönjes, S. Schreiber, S. Toleikis, R. Loch, M. Hermann, S. Strobel, H.-K. Nienhuys, G. Gwalt, T. Mey, and H. Enkisch, *Experimental study of EUV mirror radiation damage resistance under long-term free-electron laser exposures below the single-shot damage threshold,* J. Synchrotron Radiat. **25**, 77 (2018).

[20] T. Tsarfati, E. Zoethout, R. van de Kruijs, and F. Bijkerk, *Growth and sacrificial oxidation of transition metal nanolayers,* Surf. Sci. **603**, 1041 (2009).

[21] A. Aquila, R. Sobierajski, C. Ozkan, V. Hájková, T. Burian, J. Chalupský, L. Juha, M. Störmer, S. Bajt, M. T. Klepka, P. Dłużewski, K. Morawiec, H. Ohashi, T. Koyama, K. Tono, Y. Inubushi, M. Yabashi, H. Sinn, T. Tschentscher, a. P. Mancuso, and J. Gaudin, *Fluence thresholds for grazing incidence hard X-ray mirrors,* Appl. Phys. Lett. **106**, 241905 (2015).

[22] V. Lipp, N. Medvedev, and B. Ziaja, *Classical Monte-Carlo simulations of X-ray induced electron cascades in various materials,* Proc. SPIE, Damage to VUV, EUV, and X-ray Optics VI **10236**, 102360H (2017).

[23] S. Anisimov, B. Kapeliovich, and T. Perelman, *Electron emission from metal surfaces exposed to ultrashort laser pulses,* Zh. Eksp. Teor. Fiz **66**, 776 (1974).

[24] T. Qiu and C. Tien, *Heat transfer mechanisms during short-pulse laser heating of metals,* J. Heat Trans. **115**, 835 (1993).

[25] J. Hohlfeld, S.-S. Wellershoff, J. Güdde, U. Conrad, V. Jähnke, and E. Matthias, *Electron and lattice dynamics following optical excitation of metals,* Chem. Phys. **251**, 237 (2000).

[26] M. Bonn, D. N. Denzler, S. Funk, M. Wolf, S.-S. Wellershoff, and J. Hohlfeld, *Ultrafast electron dynamics at metal surfaces: competition between electron-phonon coupling and hot-electron transport,* Phys. Rev. B **61**, 1101 (2000).

[27] W.-L. Chan, R. S. Averback, D. G. Cahill, and A. Lagoutchev, *Dynamics of femtosecond laser-induced melting of silver,* Phys. Rev. B **78**, 214107 (2008).

[28] K. Tiedtke, J. Feldhaus, U. Hahn, U. Jastrow, T. Nunez, T. Tschentscher, S. V. Bobashev, A. A. Sorokin, J. B. Hastings, S. Möller, L. Cibik, A. Gottwald, A. Hoehl, U. Kroth, M. Krumrey, H. Schöppe, G. Ulm, and M. Richter, *Gas detectors for X-ray lasers,* J. Appl. Phys. **103**, 094511 (2008).

[29] R. Sobierajski, M. Jurek, J. Chalupsky, J. Krzywinski, T. Burian, S. D. Farahani, V. Hajkova, M. Harmand, L. Juha, D. Klinger, R. a. Loch, C. Ozkan, J. B. Pelka, K. Sokolowski-Tinten, H. Sinn, S. Toleikis, K. Tiedtke, T. Tschentscher, H. Wabnitz,

and J. Gaudin, *Experimental set-up and procedures for the investigation of XUV free electron laser interactions with solids,* J. Instrum. **8**, P02010 (2013).

[30] J. Chalupsky, J. Krzywinski, L. Juha, V. Hajkova, J. Cihelka, T. Burian, L. Vysin, J. Gaudin, A. Gleeson, M. Jurek, a. R. Khorsand, D. Klinger, H. Wabnitz, R. Sobierajski, M. Stormer, K. Tiedtke, and S. Toleikis, *Spot size characterization of focused non-Gaussian X-ray laser beams,* Opt. Express **18**, 27836 (2010).

[31] J. Chalupský, T. Burian, V. Hájková, L. Juha, T. Polcar, J. Gaudin, M. Nagasono, R. Sobierajski, M. Yabashi, and J. Krzywinski, *Fluence scan: an unexplored property of a laser beam,* Opt. Express **21**, 26363 (2013).

[32] C. Wu and L. V. Zhigilei, *Microscopic mechanisms of laser spallation and ablation of metal targets from large-scale molecular dynamics simulations,* Appl. Phys. A **114**, 11 (2014).

[33] J. Liu, *Simple technique for measurements of pulsed gaussian-beam spot sizes,* Opt. Lett. **7**, 196 (1982).

[34] D. E. Cullen, J. H. Hubbell, and L. Kissel, *EPDL97: the Evaluated Photon Data Library, '97 version*, Tech. Rep. (Lawrence Livermore National Lab., CA (United States), 1997).

[35] S. Perkins, D. Cullen, M. Chen, J. Rathkopf, J. Scofield, and J. Hubbell, *Tables and graphs of atomic subshell and relaxation data derived from the LLNL Evaluated Atomic Data Library (EADL), Z= 1–100*, Tech. Rep. (Lawrence Livermore National Lab., CA (United States), 1991).

[36] Y.-K. Kim and M. E. Rudd, *Binary-encounter-dipole model for electron-impact ionization,* Phys. Rev. A **50**, 3954 (1994).

[37] I. Plante and F. A. Cucinotta, *Cross sections for the interactions of 1 eV–100 MeV electrons in liquid water and application to Monte-Carlo simulation of HZE radiation tracks,* New J. Phys. **11**, 063047 (2009).

[38] N. Medvedev, *Femtosecond X-ray induced electron kinetics in dielectrics: application for FEL-pulse-duration monitor,* Appl. Phys. B **118**, 417 (2015).

[39] H. Hu and S. A. Argyropoulos, *Mathematical modelling of solidification and melting: a review,* Model. Simul. Mater. Sci. **4**, 371 (1996).

[40] A. E. Morris, H. A. Fine, and G. Geiger, *Handbook on Material and Energy Balance Calculations in Material Processing* (John Wiley Sons, 2011).

[41] E. Leveugle, D. Ivanov, and L. Zhigilei, *Photomechanical spallation of molecular and metal targets: molecular dynamics study,* Appl. Phys. A **79**, 1643 (2004).

[42] N. Nedialkov, S. Imamova, P. Atanasov, P. Berger, and F. Dausinger, *Mechanism of ultrashort laser ablation of metals: molecular dynamics simulation,* Appl. Surf. Sci. **247**, 243 (2005).

[43] V. P. Skripov, *Metastable liquids* (Wiley, New York, 1974).

[44] C. F. Delale, J. Hruby, and F. Marsik, *Homogeneous bubble nucleation in liquids: the classical theory revisited,* J. Chem. Phys. **118**, 792 (2003).

[45] V. V. Zhakhovskii, N. A. Inogamov, and K. Nishihara, *New mechanism of the formation of the nanorelief on a surface irradiated by a femtosecond laser pulse,* JETP Lett. **87**, 423 (2008).

[46] S. I. Ashitkov, N. a. Inogamov, V. V. Zhakhovskii, Y. N. Emirov, M. B. Agranat, I. I. Oleinik, S. I. Anisimov, and V. E. Fortov, *Formation of nanocavities in the surface layer of an aluminum target irradiated by a femtosecond laser pulse,* JETP Lett. **95**, 176 (2012).

[47] J.-M. Savolainen, M. S. Christensen, and P. Balling, *Material swelling as the first step in the ablation of metals by ultrashort laser pulses,* Phys. Rev. B **84**, 193410 (2011).

[48] C. Wu, M. S. Christensen, J.-M. Savolainen, P. Balling, and L. V. Zhigilei, *Generation of subsurface voids and a nanocrystalline surface layer in femtosecond laser irradiation of a single-crystal Ag target,* Phys. Rev. B **91**, 035413 (2015).

[49] D. A. Papaconstantopoulos, *Handbook of the Band Structure of Elemental Solids: From Z=1 To Z=112* (Springer, 2016).

[50] C. Kittel, *Introduction to Solid State Physics* (Wiley, 1996).

[51] D. L. Windt, *IMD—software for modeling the optical properties of multilayer films,* Computers in Physics **12**, 360 (1998).

[52] R. Ramji Rao and A. Ramanand, *Lattice dynamics, thermal expansion, and bulk modulus of ruthenium,* J. Low Temp. Phys. **27**, 837 (1977).

[53] S. Gorbunov, N. Medvedev, P. Terekhin, and A. Volkov, *Electron–lattice coupling after high-energy deposition in aluminum,* Nucl. Instrum. Meth. B **354**, 220 (2015).

[54] L. Jiang and H.-l. Tsai, *Improved two-temperature model and its application in ultrashort laser heating of metal films,* J. Heat Trans. **127**, 1167 (2005).

[55] N. Ashcroft and N. Mermin, *Solid State Physics*, HRW international editions (Holt, Rinehart and Winston, 1976).

[56] Z. Lin, L. V. Zhigilei, and V. Celli, *Electron-phonon coupling and electron heat capacity of metals under conditions of strong electron-phonon nonequilibrium,* Phys. Rev. B **77**, 075133 (2008).

[57] S. I. Anisimov and B. Rethfeld, *Theory of ultrashort laser pulse interaction with a metal,* Proc. SPIE, Nonresonant Laser-Matter Interaction (NLMI-9) **3093**, 192 (1997).

[58] C. Y. Ho, R. W. Powell, and P. E. Liley, *Thermal conductivity of the elements,* J. Phys. Chem. Ref. Data **1**, 279 (1972).

3

MODELING OF XUV-INDUCED DAMAGE IN RU FILMS: THE ROLE OF MODEL PARAMETERS

We perform a computational study of damage formation in XUV-irradiated ruthenium thin films by means of a combined Monte Carlo – two temperature model approach. The model predicts that the damage formation is most affected by ultrafast heating of the lattice by hot electrons, and is not very sensitive to the initial stage of the material excitation. Numerical parameters of the model, as well as different approximations for the thermal parameters were analyzed, showing the importance of the temperature dependence of the electron thermal conductivity and the electron-phonon coupling factor. Our analysis reveals that the details of photoabsorption and ultrafast non-equilibrium electron kinetics play only a minor role in the XUV irradiation regime.

3.1. INTRODUCTION

Survivability of optical elements exposed to ultrafast (femtosecond) high peak power free-electron laser (FEL) pulses becomes more and more important in the context of rapidly developing XUV and X-ray FEL light sources [1–5]. Such sources are capable of generating pulses with energies sufficiently high to cause a significant damage of the optics used at these facilities. Fundamental understanding and accurate description of the processes responsible for the degradation of optics are required in order to increase its lifetime.

The quality of modeling of the interaction of ultrafast high intensity laser pulses with matter strongly depends on the proper choice of model parameters. Despite the fact that the field of ultrafast laser-matter interaction has been extensively developing in the last decades, reliable thermal parameters such as electron heat capacity, electron thermal conductivity and electron-phonon coupling factor are still unknown for many materials relevant for XUV and X-ray optics. The knowledge of such parameters and, especially, their electron temperature dependence in the regime of strong laser excitation is crucial in order to get a quantitatively correct description of the processes involved. In the regime of high electron temperature all mentioned parameters can significantly differ from their room-temperature values [6]. The use of temperature-dependent thermal parameters for simulations of the electron temperature evolution in a highly excited gold target [7] led to a good agreement with experimental findings, while low-temperature values of the parameters failed to reproduce experimental data. In another work, a modification of the common expression for thermal conductivity in order to take into account d-band excitation enabled authors to explain the details of melting dynamics in silver [8]. Measuring and calculating material properties in the regime of strong laser excitation when the electron temperature reaches values much higher than the Fermi temperature is challenging and requires separate dedicated studies.

Our work focuses on ruthenium (Ru) as a perspective material for XUV [9] and X-ray [10–12] grazing incidence reflective mirrors. The relatively high value of its critical angle (27° at 92 eV photon energy) allows operation in a wide range of grazing incidence angles. In our recent study [13] we investigated femtosecond XUV-induced single-shot damage of a 50 nm thick Ru film on a Si substrate. The experiment was performed at FLASH (Free-electron LASer in Hamburg) [1]. Experimental analysis of the damaged morphologies together with simulations of photoabsorption and ultrafast evolution of electron and lattice temperatures showed that the nature of single-shot damage is thermo-mechanical ablation (also referred to as spallation), a phenomenon that was previously studied in case of irradiation of solids with optical [14–19] and XUV [20–23] lasers. The ablation threshold for Ru was measured to be $F_{\mathrm{abl}} = 200 \pm 40\,\mathrm{mJ/cm^2}$ [13].

In this paper we analyze the model parameters of Ru as a material that is still poorly studied in the field of ultrafast laser-matter interaction, despite its promising applications as mentioned above. The evolution of electron and lattice temperatures is calculated with our combined approach using the XCASCADE(3D) Monte Carlo (MC) code [24, 25] and the two temperature model (TTM) [26, 27]. The influence of a particular choice of model parameters on the results of our calculations is investigated in order to determine which parameters play the most important role in the phenomenon of XUV single-shot damage.

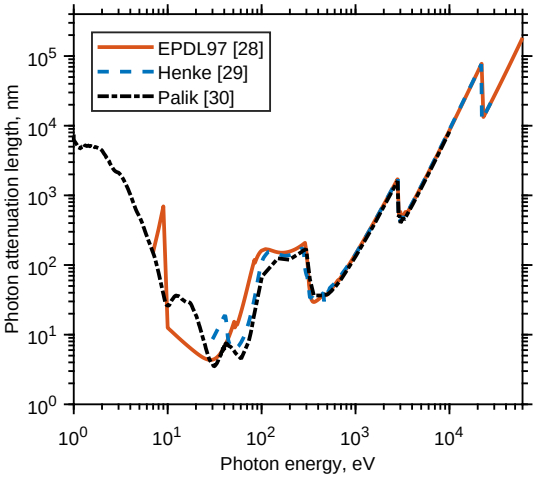

Figure 3.1: Dependence of photon attenuation length on photon energy in Ru at normal incidence conditions.

3.2. MODEL

The interaction of a femtosecond XUV laser pulse with a metal starts with photoabsorption. Depending on the photon energy and the atomic constituents of the target, a photon may be absorbed by the conduction band or core atomic shells with ionization potentials lower than or equal to the photon energy. The photon attenuation length in Ru for the case of normal incidence as a function of the photon energy is shown in Fig. 3.1. The figure compares photon attenuation lengths from Refs. [28–30]. The referenced datasets agree for photon energies above ~ 200 eV, but in the range from ~ 50 eV to 200 eV there is some uncertainty in the data. At lower energies the data from Refs. [28, 29], calculated within the atomic approximation, qualitatively diverge from the experimental data on solid Ru from Ref. [30]. This indicates that at lower energies less then 50 eV collective effects such as the band structure of Ru and plasmon excitations start to play an important role. In this work we focus on the photon energy of 92 eV, as was used in experiments at FLASH (see Ref. [13]). At this photon energy there is almost no difference between experimental data and data from Ref. [29], so either of them can be used, although one has to keep in mind that the photon attenuation length is only known with some uncertainty for this energy. At photon energies where there is a significant difference, the experimental data from Ref. [30] must be taken.

As was shown in previous studies, an electronic system of a solid under femtosecond FEL irradiation follows the so called “bump-on-hot-tail” distribution [31, 32]: the majority of low-energy electrons is almost in thermal equilibrium, with the minority of the highly excited electrons forming the high-energy out-of-equilibrium tail of the distribution. This typical shape allows one to split the electron distribution into the high-energy and low-energy fractions, and treat each of them individually with appropriate methods. Note that a proper interconnection between the fractions (and, correspondingly, the methods) must be made in order to obtain reliable results.

3.2.1. XCASCADE(3D)

The absorption of XUV photons and the non-equilibrium high-energy electron kinetics induced as a result of photoabsorption is simulated with an event-by-event MC code XCASCADE(3D) [24, 25]. The code models a target as a homogeneous arrangement of atoms (atomic approximation) with a density corresponding to the chosen material. The photoabsorption cross sections and the ionization potentials of the target are also described in the atomic approximation. The model applicability is limited to a particular range of photon energies. The lower limit of 50 eV is due to solid state effects, whereas the upper limit is defined by relativistic effects, which give an error of ~ 10% at the energy of 40 keV, or ~ 20% at the energy of 100 keV.

The code accounts for the following processes: photoabsorption by deep-shell levels, Auger recombination of created holes with release of an Auger electron, propagation of photo- and secondary electrons, inelastic (impact ionization) and elastic scattering of electrons on neutral atoms [24, 25]. Within the MC event-by-event simulation model, both ballistic and diffusive regimes of electron transport appear naturally, and the transition between the two is automatically accounted for based on the kinetic energy of the electrons [25]. All photo- as well as secondary electrons are traced until their energy falls below a predefined cutoff energy. Electrons with energies below this cutoff, as well as holes created in the valence atomic levels, are considered as thermalized and belonging to the bath of the conduction band electrons. Their energy is treated as the energy of the conduction band electrons, as will be discussed below in more detail.

XCASCADE(3D) takes advantage of the approximation of non-interacting electrons. The free electron-electron scattering is neglected, so the cascades develop independently. Such an approximation is valid if the density of high-energy electrons participating in the cascading process is significantly smaller than the atomic density, thereby making impact ionization and elastic scattering the dominant processes of electron interaction [33, 34]. In other words, it means that the fluence of an incident laser pulse must not be too high to produce a density of excited electrons comparable to or higher than atomic density of a target.

Within the XCASCADE(3D) code we also assume that the material properties are not affected during the electron cascading, i.e. the photoionization, impact ionization and elastic scattering cross sections do not change significantly due to excitation of the target. Consequently, the cross sections for the unexcited material are applied. This approximation implies that all processes that significantly change the material electronic or atomic structure, such as melting or vaporization, must occur after the electron cascading is finished. In case of femtosecond FEL pulses, this assumption is consistent with the low-fluence approximation made above.

The inelastic scattering resulting in impact ionization is modeled with the binary-encounter-Bethe (BEB) cross section [35], whereas for the elastic scattering the Mott's cross-section with Moliere screening parameter is employed [34], both valid within the atomic approximation. The cross sections neglect collective effects within the target, which play a role at electron energies below ~ 50 eV. Although we use the same cross sections for electrons with lower energies, this should not influence the kinetics much, since electrons with such energies reach the cutoff after only few collisions [36].

When all photo- and secondary electrons lose their energy to a level below the cutoff energy, the cascading stops. At this point we consider the electronic system to be ther-

malized to the Fermi-Dirac distribution. A possible deviation of the low-energy electrons from the Fermi-Dirac distribution is not taken into account. It would require dedicated simulations with, e.g., the Boltzmann equation [37, 38]. It is expected that within the bump-on-hot-tail distribution, such deviations are small.

To calculate the number and energy density depth profiles we perform the simulation in two steps: first, we perform simulations for bulk material assuming all photons are absorbed at z = 0 ("surface"). Then, the realistic absorption positions are taken into account by applying a convolution with the Lambert-Beer's law. Here we treat the region z ≥ 0 as irradiated material, while region z < 0 is considered as vacuum above the surface. This approach enables one to estimate the total energy emitted from the sample, but not the actual distribution of energy above the surface. The units of energy density, eV/atom, are used for the vacuum region to be compared with the energy density inside the material, although there are no atoms in vacuum; it should only be used to estimate the total emitted energy, and can be converted into the energy density units of, e.g., eV/cm^3 by multiplying with the target atomic density under normal conditions.

3.2.2. TWO TEMPERATURE MODEL

The low-energy electrons are used as the energy source in the TTM. The transport of energy within this formalism is diffusive in nature since the standard Fourier law of heat conduction is used. Such an assumption breaks when the typical size of a system becomes comparable with the mean free path of the heat carriers [39]. We assume that all ballistic transport effects were captured by the MC modeling of the high-energy electrons described above, and the low-energy electrons only exhibit the diffusive behavior. When this is not the case, a more general approach should be used, such as the ballistic-diffusive equation [39], which is beyond the scope of the present paper.

The TTM is a set of two coupled nonlinear differential equations, which describe the evolution of electron (T_e) and lattice (T_l) temperatures as functions of depth (z) and time (t) induced by absorption of an ultrashort laser pulse:

$$\begin{cases} C_e \dfrac{\partial T_e}{\partial t} = \dfrac{\partial}{\partial \mathrm{z}}\left(k_e \dfrac{\partial T_e}{\partial \mathrm{z}}\right) - G(T_e - T_l) + S(\mathrm{z}, t) \\ \\ C_l \dfrac{\partial T_l}{\partial t} = G(T_e - T_l). \end{cases} \tag{3.1}$$

C_e and C_l are the electron and lattice heat capacities, respectively; k_e is the electron thermal conductivity; G is the electron-phonon coupling factor. The lattice thermal conductivity is usually neglected for metals since it is typically much smaller than the electron thermal conductivity. $S(\mathrm{z}, t)$ is the heat source, which is obtained from XCASCADE(3D) as the derivative of the energy density $U(\mathrm{z}, t)$ of low-energy electrons and valence holes:

$$S(\mathrm{z}, t) = \frac{\partial U(\mathrm{z}, t)}{\partial t}, \qquad \mathrm{z} \in [0, L], \tag{3.2}$$

where L is the film thickness. The problem is formulated in only one, in-depth, dimension z, since the typical laser spot size (~ μm, see Ref. [13]) is much larger than the penetration depth of the radiation (~nm), which makes the temperature gradients in lateral direction much smaller than in the in-depth direction.

The TTM assumes that the atomic lattice can be described in terms of phonons, the collective harmonic oscillators. This approximation requires that (i) the crystal has a perfect periodic structure that is undamaged during the simulation; (ii) the interatomic potential can be approximated as harmonic and does not change in time (due to, e.g., nonthermal effects); and (iii) the characteristic times of the studied processes are larger than the characteristic phonon time (inverse phonon frequency). Strictly speaking, these conditions may not be satisfied under femtosecond FEL pulse irradiation, however, more general approaches to electron-ion energy exchange are computationally much more demanding and will not be used in this work [40, 41].

The TTM formulated above is solved numerically using a finite difference method. The initial and boundary conditions are the following:

$$T_e(\mathrm{z}, -2\tau_p) = T_l(\mathrm{z}, -2\tau_p) = 300\,\mathrm{K}, \qquad \mathrm{z} \in [0, L], \tag{3.3}$$

$$\left.\frac{\partial T_e}{\partial \mathrm{z}}\right|_{\mathrm{z}=0} = \left.\frac{\partial T_l}{\partial \mathrm{z}}\right|_{\mathrm{z}=0} = \left.\frac{\partial T_e}{\partial \mathrm{z}}\right|_{\mathrm{z}=L} = \left.\frac{\partial T_l}{\partial \mathrm{z}}\right|_{\mathrm{z}=L} = 0, \tag{3.4}$$

where τ_p is the pulse duration. As one can see, thermally isolated boundaries are used during the entire simulation, which corresponds to a free-standing film. For this approximation to be accurate, the thickness of the film should be large enough to make sure that the supporting substrate does not affect the thermal evolution of the film near the irradiated boundary.

The enthalpy approach [42] is used in order to take melting into account. The difference in thermal properties between the liquid and the solid phase is neglected for simplicity. The lattice heat capacity dependence on the lattice temperature is extracted from the relationship between the enthalpy and the lattice temperature taken from Ref. [43].

The results of the TTM calculations strongly depend on the choice of the thermal parameters for a particular material of interest. Generally, all parameters are temperature dependent. In the regime of high fluences, the electron temperature can reach high values in the order of the Fermi temperature or higher. In such a regime, thermal parameters may differ significantly from their room temperature values. In this work, we study various approximations for the model parameters of Ru, their applicability and influence on the behavior of electron and lattice temperatures, with the latter being crucial for understanding the mechanisms of laser-induced damage in metals.

3.3. RESULTS AND DISCUSSION

3.3.1. MODEL PARAMETERS OF RU

In this section we describe the different approximations for the following model parameters of Ru: photoelectron velocity distribution (due to the photon polarization), electron cutoff energy (separating high-energy from low-energy electrons in the MC scheme), electron heat capacity, electron thermal conductivity and electron-phonon coupling factor.

PHOTOELECTRON VELOCITY DISTRIBUTION

In a single-shot damage experiment reported in Ref. [13], authors used p-polarized light with respect to the sample surface. Generally, polarization influences the direction of

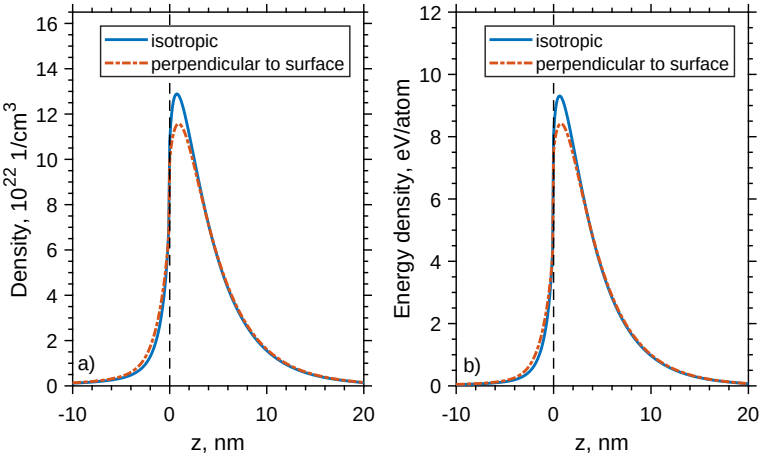

Figure 3.2: Depth profiles of total number density (a) and energy density (b) of thermalized electrons and valence holes at $t = 200$ fs, calculated with the XCASCADE(3D) code for an incident fluence $F = 200\,\mathrm{mJ/cm^2}$. Solid lines are results of calculations with isotropic directions of photoelectrons, while dash-dot lines – with directions of photoelectrons perpendicular to the surface. The cutoff energy is 6.38 eV. Vertical dashed lines mark the surface of Ru with z < 0 region treated as vacuum.

photoelectrons emitted after absorption of the photons. In order to study the effect of polarization on the final energy and density distributions of thermalized electrons and valence holes, we consider two limiting cases. In the first case, we assume random directions of photoelectrons (isotropic), as if the polarization had no effect. In the other limiting case, we allow photoelectrons to travel only perpendicular to the surface (up and down), mimicking p-polarization of a pulse under grazing incidence conditions. In that case, the effect of polarization is most pronounced: more electrons and energy are expected to be emitted from the surface on the one hand, and more electrons will propagate deeper into Ru on the other hand.

The comparison between these two limiting cases is shown in Fig. 3.2. The total density profiles of thermalized electrons (those with energy below the cutoff of 6.38 eV) and valence holes at time $t = 200$ fs are plotted in Fig. 3.2 (a). Fig. 3.2 (b) shows the total energy density. The results demonstrate only minor differences: the peaks are reduced by about 10% for the polarized case, while the tails of the distributions practically coincide. The time $t = 200$ fs corresponds to the moment when all electron cascades are already finished.

We conclude that at the photon energy of 92 eV, the polarization does not affect the electronic transport significantly. We expect, however, that the effects will be more pronounced for higher photon energies. For all further calculations in this work we choose the initial velocities of the photoelectrons to be perpendicular to the surface, since this case is closer to the experimental conditions used in Ref. [13]

CUTOFF ENERGY OF CASCADING ELECTRONS

We perform a similar comparison to the one described above, but vary the energy cutoff in the MC scheme, which separates the cascading electrons from the thermalized ones. Two values are considered: 10 eV, which is a standard cutoff energy used in previous

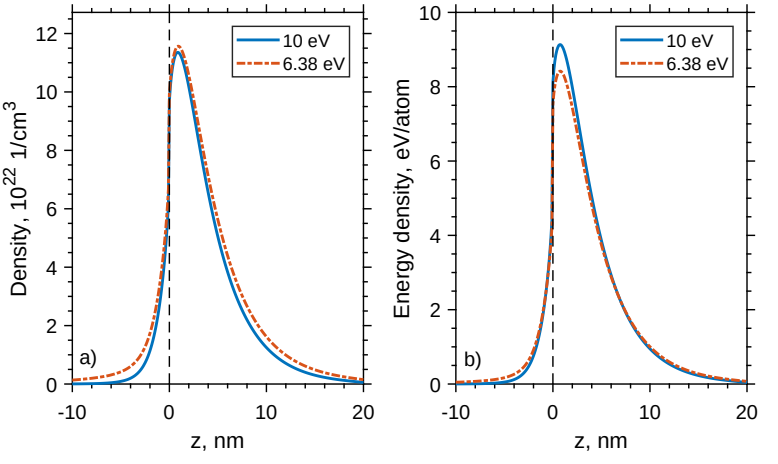

Figure 3.3: Depth profiles of total number density (a) and energy density (b) of thermalized electrons and valence holes at $t = 200$ fs, calculated with the XCASCADE(3D) code for an incident fluence $F = 200\,\mathrm{mJ/cm^2}$. Solid lines are the results of calculations with 10 eV cutoff energy, dash-dot lines with 6.38 eV. The velocities of photoelectrons are perpendicular to the surface. Vertical dashed lines mark the surface of Ru with the z < 0 region treated as vacuum.

studies of electron cascading [25, 31], and 6.38 eV, which corresponds to the ionization potential of the outermost shell (5s) of the Ru atom [44]. By the ionization potential we mean the energy necessary to promote an electron from the 5s state into the unoccupied delocalized states of the conduction band. In the case of 6.38 eV cutoff energy electrons have additional freedom for the final impact ionization of 5s shell before their motion is stopped and they are considered as thermalized. The comparison is presented in Fig. 3.3.

The total density, Fig. 3.3 (a), is slightly higher in the case of 6.38 eV cutoff energy, since an additional impact ionization event of 5s shell leads to higher number of thermalized electrons and valence 5s holes at the end of cascading process. The energy density, Fig. 3.3 (b), in that case is slightly more spread in space, since a lower cutoff energy allows the electrons to travel slightly further. However, the total energy of the system is the same for both cases.

Our results show that the choice of the cutoff energy (within a few eV margin) hardly affects the spatial energy distribution or the duration of electron cascading (not shown). Indeed, the number of escaping electrons and the amount of energy they carry away are only changed by 4% and 2%, respectively. The electronic number and energy densities never differ by more than 9% for the two considered cases. In all further calculations 6.38 eV cutoff energy is used.

ELECTRON HEAT CAPACITY

The linear approximation for the electron heat capacity derived within the Sommerfeld model (free electron gas approximation) is typically used for metals in the regime of relatively low electron temperatures: $C_e(T_e) = \gamma T_e$, where γ is the electron specific heat constant. In order to go beyond the free electron gas approximation and take into account a realistic density of states (DOS) of a material, we perform calculations of the

electron heat capacity dependence on the electron temperature, using the formalism described in [45]. The Ru DOS is taken from Ref. [46]. The results are shown in the previous Chapter, Fig. 2.10 (a). Dashed and solid lines are the electron heat capacity in the free electron gas approximation and calculated with the DOS of Ru, respectively. The results are close to each other up to ~ 6000 K, after which the increase of C_e calculated with with DOS becomes more gradual compared to the free electron gas approximation.

ELECTRON-PHONON COUPLING FACTOR

The temperature dependence of the electron-phonon coupling factor is calculated using the formalism described in Refs. [45, 47]. The results are shown in the previous Chapter, Fig. 2.10 (b). The strong enhancement is followed by a decrease with a maximum value reached at $T_e \sim 1.2 \cdot 10^4$ K. A similar behavior of G with increasing electron temperature was previously reported for titanium [6]. Both metals have an hcp crystal structure and relatively low DOS at the Fermi level, which may explain the similar behavior. Note that at low temperatures the calculated values agree reasonably well with the experimental data from Refs. [48, 49] (marked in Fig. 2.10 (b) with dashed lines).

ELECTRON THERMAL CONDUCTIVITY

Different approximations for the electron thermal conductivity k_e are available in the literature [50]. In the regime of low electron temperatures the following approximation is typically used:

$$k_e^{\text{linear}}(T_e, T_l) = k_0 \frac{T_e}{T_l}, \tag{3.5}$$

where k_0 is the room temperature equilibrium thermal conductivity. It is assumed here that electron-phonon scattering is the dominant scattering process. For higher electron temperatures, both electron-electron and electron-phonon scattering processes play a role, and a more general approximation for k_e must be used [50]:

$$k_e^{\text{A,B}}(T_e, T_l) = \frac{1}{3} v_F \gamma \frac{T_e}{A T_e^2 + B T_l}, \tag{3.6}$$

where v_F is the Fermi velocity and A and B are material dependent constants which are determined by the electron-electron and electron-phonon collision frequencies, respectively. Eq. 3.6 is only valid for electron temperatures considerably smaller than the Fermi temperature, otherwise a more general expression should be used [50, 51]:

$$k_e^{\text{K,b}}(T_e, T_l) = K \cdot \frac{(\vartheta^2 + 0.16)^{5/4}\,(\vartheta^2 + 0.44)\vartheta}{(\vartheta^2 + 0.092)^{1/2}\,(\vartheta^2 + b\vartheta_l)}. \tag{3.7}$$

Here $\vartheta = k_B T_e / E_F$ and $\vartheta_l = k_B T_l / E_F$, where k_B is the Boltzmann constant and E_f is the Fermi energy. K and b are material dependent constants.

Although the approximations described above are known and widely applied, the constants A and B or K and b are unknown for most materials. We propose a way of determining the corresponding constants based on a measured temperature dependence of the thermal conductivity, taken from Ref. [52]. Eq. 3.6 and 3.7 can be fitted to the experimental data with A and B, or K and b, as fitting parameters, respectively, taking $T_e = T_l = T$, since experimental values of the thermal conductivity are measured

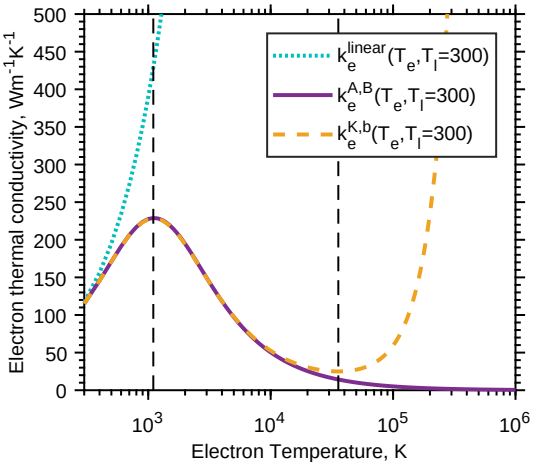

Figure 3.4: Electron temperature dependence of the electron thermal conductivity in three different approximations (Eqs. 3.5, 3.6, 3.7) plotted for a fixed lattice temperature $T_l = 300$K. Dashed vertical lines schematically divide the whole electron temperature range into three characteristic regions.

in the regime of thermal equilibrium between electrons and the lattice. Following this procedure for Ru, we find $A = 7.82 \cdot 10^8\,\mathrm{s^{-1}K^{-2}}$, $B = 3.24 \cdot 10^{12}\,\mathrm{s^{-1}K^{-1}}$ (for Eq. 3.6), and $K = 34.98\,\mathrm{Wm^{-1}K^{-1}}$ and $b = 0.0416$ (for Eq. 3.7). In the fitting procedure the data from Ref. [52] are taken only up to the melting point of Ru which means that the influence of melting on the thermal conductivity coefficient is not taken into account.

The three approximations for electron thermal conductivity are compared in Fig. 3.4. The dependence on electron temperature is shown with the lattice temperature fixed at room temperature, $T_l = 300$K. The first approximation (Eq. 3.5), which we will refer to as the linear approximation, results in a rapid increase of the electron thermal conductivity. The two other approximations (Eq. 3.6 and 3.7) exhibit a qualitatively different behavior. The initial increase up to ~ 1100K is followed by a significant drop of k_e. Eq. 3.6 tends to zero with further increasing electron temperature, while Eq. 3.7 exhibits a second sharp increase for $T_e \geq 36000$K as expected in the plasma limit [50].

Based on that behavior, the electron temperature range can be approximately divided into three characteristic regions: (i) "low" temperatures, $T_e < 1100$K, (ii) "intermediate" temperatures, $1100 \leq T_e \leq 36000$K, and (iii) "high" temperatures, $T_e > 36000$K. The vertical dashed lines in Fig. 3.4 mark these three regions. Although k_e in all three approximations is qualitatively similar in region (i), a significant quantitative difference is reached with increasing T_e (almost a factor of 2 difference at $T_e = 1100$K). This fact makes the linear approximation questionable to use for all temperature ranges.

The results for Eq. 3.6 and 3.7 almost coincide in regions (i) and (ii), but differ strongly in region (iii). From this analysis we conclude that Eq. 3.6 is valid in regions (i) and (ii), while the most general approximation, Eq. 3.7, should be valid for all electron temperatures considered here.

3.3.2. INFLUENCE OF THERMAL PARAMETERS ON DAMAGE CHARACTERISTICS

In our recent study [13] we showed that the nature of single-shot damage of a 50 nm Ru film induced by a 100 fs XUV (92 eV) FEL pulse is thermo-mechanical ablation in the stress confinement regime. The phenomenon of ablation was extensively studied both experimentally and theoretically in the field of interaction of optical and XUV lasers with matter [14–23]. The mechanism behind laser-induced ablation in metals is the following. The laser energy is firstly absorbed by the electrons in the near surface layer of a metal. Then, the excited electrons propagate into the depth of the target, simultaneously heating the lattice due to electron-phonon interaction. If the heating of the lattice by the hot electrons occurs faster than mechanical relaxation of the system, the heating is almost isochoric. As a result, large compressive stresses are generated. The compressive component of a stress wave is followed by a tensile component due to the existence of a free surface. The amplitude of a tensile stress propagating into the depth of the material is increasing until the threshold value is reached at some depth, which leads to ablation.

The condition of the stress confinement regime can be formulated in a following way [14, 15, 19]: $\tau_{\text{e-ph}} \leq \tau_a$, where $\tau_{\text{e-ph}}$ is the electron-phonon thermalization time and τ_a is the acoustic relaxation time. The latter can be calculated as $\tau_a = L_c/C_s$, where L_c is the electron diffusion length and C_s is bulk speed of sound. Therefore, one needs to know the characteristic thermal time ($\tau_{\text{e-ph}}$) and length (L_c) scales of the problem in order to find out whether the regime of stress confinement is realized.

Another key process playing a role in the single-shot damage mechanism is melting. It was shown that for metals melting typically occurs before the ablation, so that ablation starts in a liquid material [15, 19]. The calculated depth of melting can be compared with the experimentally observed depth of the damaged crater in order to check whether the latter is smaller than the first.

In this section we study the influence of the particular choice of thermal parameters of Ru on the electron and lattice temperatures behavior and on the characteristic values playing a role in the damage process, such as the electron-phonon thermalization time, the electron diffusion length and the melted depth. The analysis is performed in a way that each parameter (C_e, G and k_e) is varied, fixing the choice of the approximations for the other two.

Combined XCASCADE(3D) and TTM calculations are performed in the same way as was described above and, in more detail, in Ref. [13]. All parameters used in the simulations are for bulk Ru and are summarized in Table 3.1. The incident fluence level used in all the simulations is chosen to be $F = 200\,\text{mJ/cm}^2$, which is the experimentally determined ablation threshold of Ru [13]. The corresponding absorbed fluence is calculated as $F_{\text{abs}} = F(1-R)(1-\alpha)$, where R is surface reflectivity and α is the fraction of the energy that escapes from the surface due to electron emission. The latter is estimated to be $\sim 12\%$ for the case of 6.38 eV cutoff energy and velocities of photoelectrons perpendicular to the surface (extracted from Fig. 3.2 (b)). The thickness of the film L is taken to be 200 nm. In that way we make sure that the increase of the rear surface temperature of the film is negligible compared to the changes of the front surface temperatures, so that the Si substrate can be excluded from the calculations.

Table 3.1: Model parameters.

Film thickness	$L = 200$ nm
Photon energy	92 eV
Grazing incidence angle	20°
Fermi energy[a]	$E_F = 8.5$ eV
Pulse duration	$\tau_p = 100$ fs
Surface reflectivity[b]	$R = 0.68$
Electron emission coefficient[c]	$\alpha = 0.12$
Incident fluence	$F = 200$ mJ/cm^2
Absorbed fluence	$F_{\text{abs}} = 56$ mJ/cm^2
Photon attenuation length[b]	$\delta = 3.5$ nm
Electron specific heat constant[d]	$\gamma = 400$ J/m^3/K^2
Electron-phonon coupling factor[e]	$G^{\text{const}} = 18.5 \cdot 10^{17}$ W/m^3/K
Equilibrium thermal conductivity[f]	$k_0 = 117$ W/m/K
Latent heat of melting[g]	$H_m = 4.7 \cdot 10^9$ J/m^3
Bulk modulus[h]	$B = 310$ GPa
Density[g]	$\rho = 12.3$ g/cm^3

[a] Ref. [46]

[b] Ref. [29], at 92 eV photon energy, 20° grazing incidence

[c] Extracted from Fig. 3.2 (b)

[d] Ref. [53]

[e] Ref. [49]

[f] Ref. [52]

[g] Ref. [43]

[h] Ref. [54]

INFLUENCE OF PARAMETERS ON ELECTRON AND LATTICE TEMPERATURES

Fig. 3.5 (a) compares the temporal evolution of electron and lattice surface temperatures for different electron heat capacities. Calculations with C_e^{DOS} result into a much higher electron temperature peak value, since C_e^{DOS} is significantly lower than C_e^{linear} at electron temperatures in the order of $2-3 \cdot 10^4$ K (see Fig. 2.10 (a)). Although the initial difference in temperatures (both electron and lattice) between calculations with C_e^{linear} and C_e^{DOS} is noticeable, the strong electron-phonon coupling factor of Ru (see Fig. 2.10 (b)) results in rapidly reaching thermal equilibrium between electrons and the lattice, after which the difference in temperatures is negligible. This is confirmed with electron temperature depth profiles plotted at different moments of time, shown in Fig. 3.5 (b). The small difference in temperatures in the near surface region before electron-phonon thermalization ($t = 0.5$ ps) vanishes at later times. The fact that k_e and G dependencies are fixed results in almost identical depth profiles for the entire thickness of the film. Note that here and further only top 50 nm of the total 200 nm thickness are shown.

A similar analysis is performed for two other thermal parameters: G and k_e. Fig. 3.6 compares calculations performed for a constant value of G (measured at room temperature, see Ref. [49]) and for electron temperature dependent $G(T_e)$ obtained with the DOS taken into account, Fig. 2.10 (b). In contrast to the variation of C_e described above,

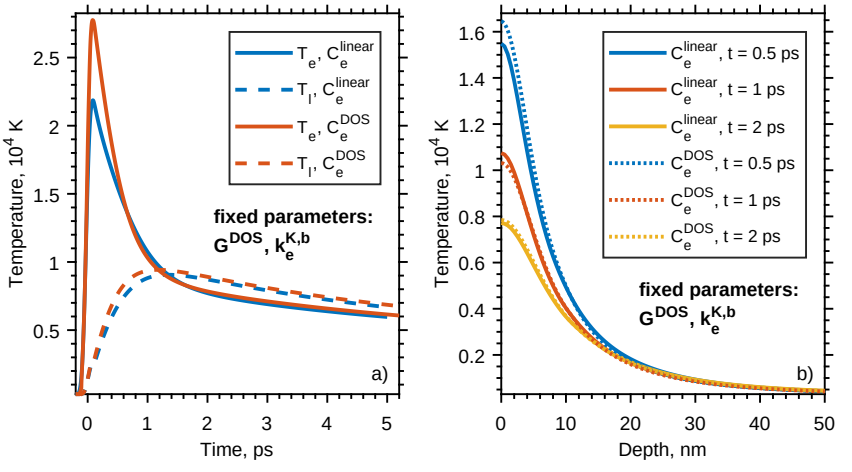

Figure 3.5: (a) Calculated temporal evolution of electron (T_e, solid lines) and lattice (T_l, dashed lines) surface temperatures of a 200 nm Ru film irradiated by a 100 fs XUV pulse. Absorbed fluence is $F_{\text{abs}} = 56$ mJ/cm^2. Electron heat capacity C_e is a varied parameter, and electron-phonon coupling factor and electron thermal conductivity are fixed at G^{DOS}, $k_e^{\text{K,b}}$ values. (b) Electron temperature depth profiles at different times calculated under the same conditions.

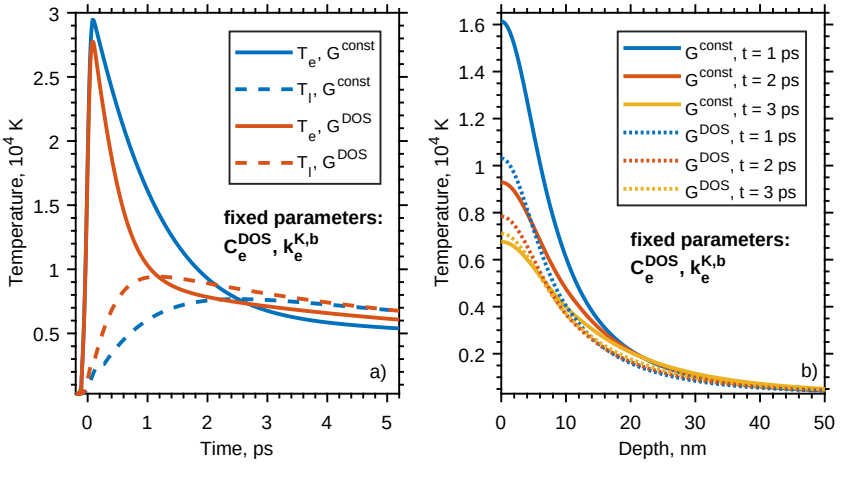

Figure 3.6: Same as Fig. 3.5 but for electron-phonon coupling factor as a varied parameter, and electron heat capacity and electron thermal conductivity fixed at C_e^{DOS}, $k_e^{\text{K,b}}$ values.

different G functions almost do not affect the electron temperature peak value, while the dynamics of electron-phonon thermalization is different, as could be expected, Fig. 3.6 (a). Stronger electron-phonon coupling (G^{DOS}, see Fig. 2.10 (b)) results in earlier thermal equilibrium compared to a constant value of G. Electron temperature depth profiles, Fig. 3.6 (b), demonstrate a significant difference in temperatures in the top ~ 20 nm of Ru at early times ($t = 1, 2$ ps), although the difference decreases with time ($t = 3$ ps). No significant difference in temperatures profiles is found for deeper parts of Ru.

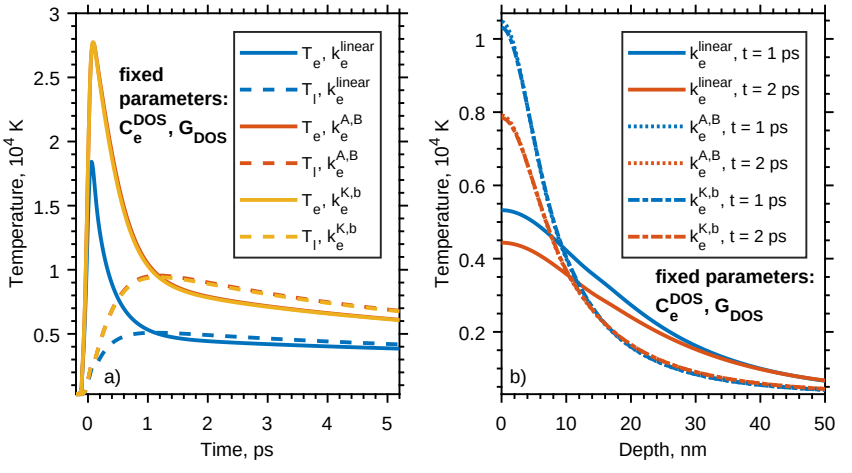

Figure 3.7: Same as Fig. 3.5 but for electron thermal conductivity as a varied parameter, and electron heat capacity and electron-phonon coupling factor fixed at C_e^{DOS}, G^{DOS} values.

Fig. 3.7 compares the calculations performed with different approximations for the electron thermal conductivity k_e. There is almost no difference in temperatures behavior between calculations with $k_e^{\mathrm{A,B}}$ (Eq. 3.6) and $k_e^{\mathrm{K,b}}$ (Eq. 3.7), which is not surprising, since these approximations are almost identical for the electron temperature range in the simulations (see Fig. 3.4). However, a larger difference is expected for higher fluences. A dramatic difference is observed when comparing $k_e^{\mathrm{A,B}}$ or $k_e^{\mathrm{K,b}}$ with the linear approximation. A much higher k_e^{linear} leads to much faster heat transport from the surface into the depth of the Ru film. As a result, the model gives significantly lower surface temperatures, Fig. 3.7 (a). The electron thermal conductivity significantly affects the distribution of the absorbed energy in the Ru film. A lower k_e in Eq. 3.6 and Eq. 3.7 approximations results in confinement of heat in the top ~ 20 nm during the first few ps after the pulse, while for a higher k_e in the linear approximation, the heat propagates much deeper. This indicates that the simple linear approximation may result in significant underestimation of the temperatures.

Summarizing the performed analysis, we found that the electron thermal conductivity has the most significant impact on electron and lattice temperatures evolution in irradiated Ru.

Finally, to emphasize the importance of a proper choice of thermal parameters, we compare calculations of temperatures evolution for two sets of parameters: the simplest set (C_e^{linear}, G^{const}, k_e^{linear}) and (presumably) the most accurate one (C_e^{DOS}, G^{DOS}, $k_e^{\mathrm{K,b}}$). The results are shown in Fig. 3.8 illustrating the dramatic qualitative and quantitative difference in temperatures behavior.

INFLUENCE OF PARAMETERS ON THE MELTING DYNAMICS

As was described above, melting plays an important role in laser-induced damage of metals. We demonstrate the influence of thermal parameters on the melting dynamics on the example of varying electron thermal conductivity, since we showed above that this parameter has the strongest impact on the temperature behavior. No significant

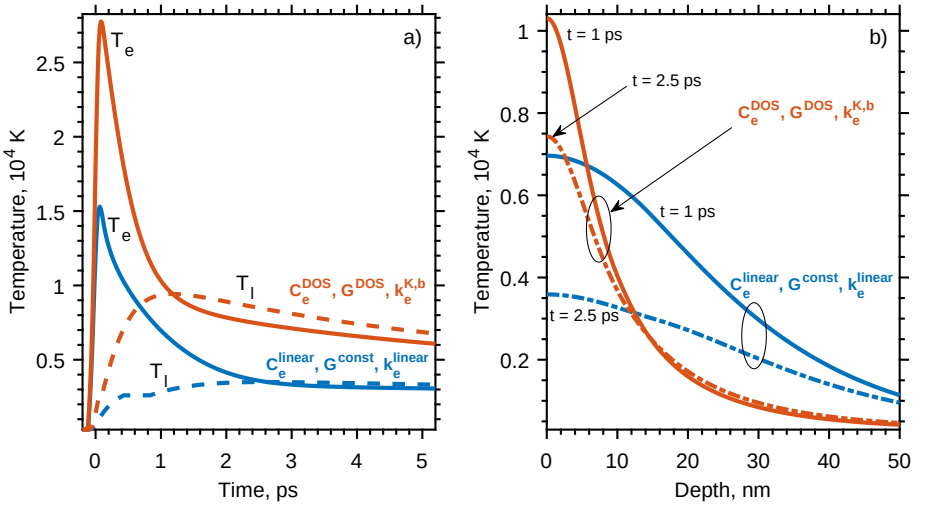

Figure 3.8: Same as Fig. 3.5 but the following sets of thermal parameters are compared: (C_e^{linear}, G^{const}, k_e^{linear}) and (C_e^{DOS}, G^{DOS}, $k_e^{\text{K,b}}$).

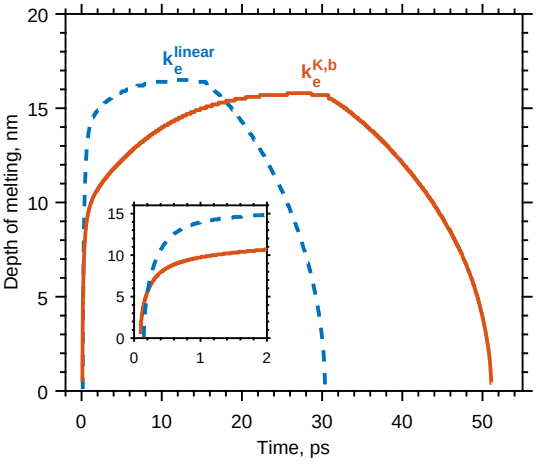

Figure 3.9: Calculated transient depth of melting in 200 nm Ru film irradiated by a 100 fs XUV pulse. The absorbed fluence is $F_{\text{abs}} = 56$ mJ/cm^2. Calculations with two approximations for the electron thermal conductivity are compared: k_e^{linear} (dashed line) and $k_e^{\text{K,b}}$ (solid line). The initial stage of melting is shown in the inset.

difference was found between Eq. 3.6 and 3.7 for the temperature range obtained in the simulations, therefore we will focus on comparing the linear approximation with the most accurate one, Eq. 3.7. The other two thermal parameters are chosen as those with the DOS taken into account (C_e^{DOS}, G^{DOS}).

Fig. 3.9 shows such a comparison for the calculated depth of melting changing with time. Both curves exhibit a similar behavior: (i) fast melting of the top 10 – 15 nm of Ru during the first 2 ps in the regime of thermal non-equilibrium between electrons

Table 3.2: Calculated thermal and mechanical characteristics of Ru irradiated by a 100 fs XUV laser pulse. The absorbed fluence is F_{abs}.

	C_e^{linear}, G^{const}, k_e^{linear}	C_e^{DOS}, G^{DOS}, $k_e^{\text{K,b}}$
$\tau_{\text{e-ph}}$ [ps]	0.82	0.48
L_c [nm]	38	11
τ_a [ps]	7.6	2.2
$T_e^{\max}$ [10^4 K]	1.53	2.78
$T_l^{\max}$ [10^4 K]	0.35	0.94

and lattice, (ii) slower propagation of the melting front in the equilibrium regime before the maximum depth of melting is reached, and (iii) cooling down and recrystallization. Although the general behavior is similar, the dynamics of melting and recrystallization is different. Higher thermal conductivity in the linear approximation makes the heat diffusion from the surface into the depth of the material much faster. As a result, melting starts slightly later, but propagates faster.

The maximum depth of melting L_{melt} is almost the same for the two approximations (L_{melt} = 16.5 and 15.8 nm for k_e^{linear} and $k_e^{\text{K,b}}$, respectively), but is reached at different times: at ~ 13 ps for k_e^{linear} and at ~ 27 ps for $k_e^{\text{K,b}}$. Both values of L_{melt} are larger than or equal to the experimentally determined thickness of the ablated layer at the ablation threshold (5−16 nm, see Ref. [13]), which is consistent with the assumption that ablation starts in a melted material.

The same value of L_{melt} for different k_e approximations can be explained by the fact that the total amount of melted material after irradiation with a femtosecond pulse is mostly determined by the absorbed fluence, the heat capacity and the latent heat of melting H_m as $L_{\text{melt}} \sim F_{\text{abs}}/(C_l(T_{\text{melt}} - T_0) + H_m)$. The thermal conductivity only has a strong effect on how fast L_{melt} is reached. Slightly larger value of L_{melt} in case of calculations with k_e^{linear} is due to the fact that for a higher thermal conductivity, a larger amount of energy diffuses away from the melted region before L_{melt} is reached. Cooling and ensuing recrystallization is also faster for a higher k_e^{linear}.

INFLUENCE OF PARAMETERS ON THE STRESS CONFINEMENT CONDITION

To check whether the condition of stress confinement is satisfied, one needs to know thermal and mechanical characteristic time scales, $\tau_{\text{e-ph}}$ and τ_a, respectively. The electron-phonon thermalization time $\tau_{\text{e-ph}}$ is defined as the time when the normalized difference between the electron and the lattice surface temperatures decreases to the $1/e$ level. To determine τ_a, the electron diffusion length L_c is extracted from the electron temperature depth profile at $t = \tau_{\text{e-ph}}$ as the depth where the normalized temperature decreases to $1/e$ level. The bulk speed of sound C_s is calculated as $C_s = \sqrt{B/\rho} \sim 5000$ m/sec, where B is the bulk modulus and ρ is the density.

We found that the condition of stress confinement is satisfied for all possible parameter combinations, although the particular values of $\tau_{\text{e-ph}}$ and L_c vary significantly. This is illustrated in Table 3.2, where $\tau_{\text{e-ph}}$ and L_c (and corresponding τ_a) together with the maximum values of the electron and the lattice temperatures are shown for two sets of thermal parameters, namely (C_e^{linear}, G^{const}, k_e^{linear}) and (C_e^{DOS}, G^{DOS}, $k_e^{\text{K,b}}$), the same as

in Fig. 3.8.

As one can see from Table 3.2 and Fig. 3.8, different k_e strongly affect the electron diffusion length L_c and, as a result, the maximum values of both the electron and lattice temperatures. In the case of irradiation of a Ru film with a femtosecond XUV laser pulse considered in this work, the stress confinement regime is satisfied for any set of available thermal parameters. Hence, the mechanism of damage does not depend on the particular choice. However, the quantitative description of the processes differs significantly. Moreover, for other materials or laser pulse parameters, inaccurate choice of the thermal parameters may lead to unreliable conclusions about the nature of laser-induced damage, and its kinetic pathways. Dedicated experimental studies are required to validate thermal parameters in the regime of high electron temperatures reached during the laser ablation of metals.

3.4. CONCLUSIONS

We performed the analysis of model parameters used in simulations of interaction of a high fluence femtosecond XUV FEL pulse with a Ru target. For simulations we used a combined approach, where photoabsorption and non-equilibrium electron kinetics were modeled with the Monte Carlo code XCASCADE(3D), and the electron and lattice temperatures evolution was described with the TTM. Variation of parameters used in the XCASCADE(3D) part of the simulations (photoelectron velocity distribution and energy cutoff) showed no significant difference in the description of electron cascades, although larger differences are expected for higher photon energies.

The following thermal parameters were varied within the TTM part of the simulations: the electron heat capacity, the electron-phonon coupling factor and the electron thermal conductivity. The latter was found to have a major impact on temperatures behavior and, hence, on the description of single-shot damage processes. Although we found that the condition of stress confinement, proposed as the key mechanism responsible for damage, is fulfilled for all possible parameter combinations in our particular case, it may not hold universally for other materials or laser parameters. Moreover, the choice of model parameters considerably affects the temporal kinetics of heating and relaxation of the target. Therefore, the proper choice of model parameters, especially the electronic thermal conductivity in the regime of high electron temperatures, is important.

ACKNOWLEDGEMENTS

I acknowledge helpful discussions with Beata Ziaja (Center for Free-Electron Laser Science, Deutsches Elektronen-Synchrotron DESY) as well as her contribution to the development of the XCASCADE(3D) code.

REFERENCES

[1] S. Schreiber and B. Faatz, *The free-electron laser FLASH,* High Power Laser Sci. **3** (2015).

[2] C. Bostedt, S. Boutet, D. M. Fritz, Z. Huang, H. J. Lee, H. T. Lemke, A. Robert, W. F.

Schlotter, J. J. Turner, and G. J. Williams, *Linac coherent light source: The first five years,* Rev. Mod. Phys. **88**, 015007 (2016).

[3] C. J. Milne *et al.*, *SwissFEL: The Swiss X-ray free electron laser,* Appl. Sci. **7**, 720 (2017).

[4] D. Pile, *X-rays: First light from SACLA,* Nat. Photonics **5**, 456 (2011).

[5] E. Allaria, C. Callegari, D. Cocco, W. M. Fawley, M. Kiskinova, C. Masciovecchio, and F. Parmigiani, *The FERMI@Elettra free-electron-laser source for coherent X-ray physics: photon properties, beam transport system and applications,* New J. Phys. **12**, 075002 (2010).

[6] Z. Lin, L. V. Zhigilei, and V. Celli, *Electron-phonon coupling and electron heat capacity of metals under conditions of strong electron-phonon nonequilibrium,* Phys. Rev. B **77**, 075133 (2008).

[7] X. Wang, D. M. Riffe, Y.-S. Lee, and M. Downer, *Time-resolved electron-temperature measurement in a highly excited gold target using femtosecond thermionic emission,* Phys. Rev. B **50**, 8016 (1994).

[8] W.-L. Chan, R. S. Averback, D. G. Cahill, and A. Lagoutchev, *Dynamics of femtosecond laser-induced melting of silver,* Phys. Rev. B **78**, 214107 (2008).

[9] I. A. Makhotkin, R. Sobierajski, J. Chalupský, K. Tiedtke, G. de Vries, M. Störmer, F. Scholze, F. Siewert, R. W. E. van de Kruijs, I. Milov, E. Louis, I. Jacyna, M. Jurek, D. Klinger, L. Nittler, Y. Syryanyy, L. Juha, V. Hájková, V. Vozda, T. Burian, K. Saksl, B. Faatz, B. Keitel, E. Plönjes, S. Schreiber, S. Toleikis, R. Loch, M. Hermann, S. Strobel, H.-K. Nienhuys, G. Gwalt, T. Mey, and H. Enkisch, *Experimental study of EUV mirror radiation damage resistance under long-term free-electron laser exposures below the single-shot damage threshold,* J. Synchrotron Radiat. **25**, 77 (2018).

[10] A. Aquila, R. Sobierajski, C. Ozkan, V. Hájková, T. Burian, J. Chalupský, L. Juha, M. Störmer, S. Bajt, M. T. Klepka, P. Dłużewski, K. Morawiec, H. Ohashi, T. Koyama, K. Tono, Y. Inubushi, M. Yabashi, H. Sinn, T. Tschentscher, a. P. Mancuso, and J. Gaudin, *Fluence thresholds for grazing incidence hard X-ray mirrors,* Appl. Phys. Lett. **106**, 241905 (2015).

[11] T. Koyama, H. Yumoto, K. Tono, T. Sato, T. Togashi, Y. Inubushi, T. Katayama, J. Kim, S. Matsuyama, H. Mimura, M. Yabashi, K. Yamauchi, and H. Ohashi, *Damage threshold investigation using grazing incidence irradiation by hard X-ray free electron laser,* Proceed. SPIE, Advances in X-ray/EUV Optics and Components VIII **8848**, 88480T (2013).

[12] O. Peyrusse, J.-M. André, P. Jonnard, and J. Gaudin, *Modeling of the interaction of an X-ray free-electron laser with large finite samples,* Phys. Rev. E **96**, 043205 (2017).

[13] I. Milov, I. A. Makhotkin, R. Sobierajski, N. Medvedev, V. Lipp, J. Chalupskỳ, J. M. Sturm, K. Tiedtke, G. de Vries, M. Störmer, *et al.*, *Mechanism of single-shot damage of Ru thin films irradiated by femtosecond extreme UV free-electron laser,* Opt. Express **26**, 19665 (2018).

[14] E. Leveugle, D. Ivanov, and L. Zhigilei, *Photomechanical spallation of molecular and metal targets: molecular dynamics study,* Appl. Phys. A **79**, 1643 (2004).

[15] B. J. Demaske, V. V. Zhakhovsky, N. A. Inogamov, and I. I. Oleynik, *Ablation and spallation of gold films irradiated by ultrashort laser pulses,* Phys. Rev. B **82**, 064113 (2010).

[16] J.-M. Savolainen, M. S. Christensen, and P. Balling, *Material swelling as the first step in the ablation of metals by ultrashort laser pulses,* Phys. Rev. B **84**, 193410 (2011).

[17] S. I. Ashitkov, N. a. Inogamov, V. V. Zhakhovskii, Y. N. Emirov, M. B. Agranat, I. I. Oleinik, S. I. Anisimov, and V. E. Fortov, *Formation of nanocavities in the surface layer of an aluminum target irradiated by a femtosecond laser pulse,* JETP Lett. **95**, 176 (2012).

[18] C. Wu and L. V. Zhigilei, *Microscopic mechanisms of laser spallation and ablation of metal targets from large-scale molecular dynamics simulations,* Appl. Phys. A **114**, 11 (2014).

[19] L. V. Zhigilei, Z. Lin, and D. S. Ivanov, *Atomistic Modeling of Short Pulse Laser Ablation of Metals: Connections between Melting, Spallation, and Phase Explosion,* J. Phys. Chem. C **113**, 11892 (2009).

[20] A. Y. Faenov, N. Inogamov, V. Zhakhovskii, V. Khokhlov, K. Nishihara, Y. Kato, M. Tanaka, T. Pikuz, M. Kishimoto, M. Ishino, *et al.*, *Low-threshold ablation of dielectrics irradiated by picosecond soft X-ray laser pulses,* Appl. Phys. Lett. **94**, 231107 (2009).

[21] M. Ishino, A. Y. Faenov, M. Tanaka, N. Hasegawa, M. Nishikino, S. Tamotsu, T. A. Pikuz, N. A. Inogamov, V. V. Zhakhovsky, I. Y. Skobelev, *et al.*, *Nanoscale surface modifications and formation of conical structures at aluminum surface induced by single shot exposure of soft X-ray laser pulse,* J. Appl. Phys. **109**, 013504 (2011).

[22] G. Norman, S. Starikov, V. Stegailov, V. Fortov, I. Skobelev, T. Pikuz, A. Faenov, S. Tamotsu, Y. Kato, M. Ishino, *et al.*, *Nanomodification of gold surface by picosecond soft X-ray laser pulse,* J. Appl. Phys. **112**, 013104 (2012).

[23] N. Medvedev, V. Tkachenko, V. Lipp, Z. Li, and B. Ziaja, *Various damage mechanisms in carbon and silicon materials under femtosecond X-ray irradiation,* 4open **1**, 3 (2018).

[24] N. Medvedev, *Femtosecond X-ray induced electron kinetics in dielectrics: application for FEL-pulse-duration monitor,* Appl. Phys. B **118**, 417 (2015).

[25] V. Lipp, N. Medvedev, and B. Ziaja, *Classical Monte-Carlo simulations of X-ray induced electron cascades in various materials,* Proc. SPIE, Damage to VUV, EUV, and X-ray Optics VI **10236**, 102360H (2017).

[26] M. Kaganov, I. Lifshitz, and L. Tanatarov, *Relaxation between electrons and crystalline lattice,* Sov. Phys. JETP **4**, 173 (1957).

[27] S. Anisimov, B. Kapeliovich, and T. Perelman, *Electron emission from metal surfaces exposed to ultrashort laser pulses,* Zh. Eksp. Teor. Fiz **66**, 776 (1974).

[28] D. E. Cullen, J. H. Hubbell, and L. Kissel, *EPDL97: the Evaluated Photon Data Library, '97 version*, Tech. Rep. UCRL–50400, Vol. 6, Rev. 5 (Lawrence Livermore National Lab., CA, 1997).

[29] B. Henke, E. Gullikson, and J. Davis, *X-ray Interactions: Photoabsorption, Scattering, Transmission, and Reflection at E = 50-30,000 eV, Z = 1-92*, Atom. Data Nucl. Data **54**, 181 (1993).

[30] E. D. Palik, *Handbook of Optical Constants of Solids*, Academic Press Handbook Series, Vol. 1 (Academic Press, 1985).

[31] N. Medvedev, A. Volkov, and B. Ziaja, *Electronic and atomic kinetics in solids irradiated with free-electron lasers or swift-heavy ions,* Nucl. Instrum. Meth. B **365**, 437 (2015).

[32] D. A. Chapman and D. O. Gericke, *Analysis of Thomson Scattering from Nonequilibrium Plasmas,* Phys. Rev. Lett. **107**, 165004 (2011).

[33] C. Jacoboni and L. Reggiani, *The Monte Carlo method for the solution of charge transport in semiconductors with applications to covalent materials,* Rev. Mod. Phys. **55**, 645 (1983).

[34] T. M. Jenkins, W. R. Nelson, and A. Rindi, eds., *Monte Carlo Transport of Electrons and Photons* (Springer US, Boston, 1988).

[35] Y.-K. Kim and M. E. Rudd, *Binary-encounter-dipole model for electron-impact ionization,* Phys. Rev. A **50**, 3954 (1994).

[36] N. Medvedev, *X-ray-induced electron cascades in dielectrics modeled with XCASCADE code: Effect of impact ionization cross sections,* Proceed. SPIE, Damage to VUV, EUV, and X-ray Optics V **9511**, 95110M (2015).

[37] B. Rethfeld, A. Kaiser, M. Vicanek, and G. Simon, *Ultrafast dynamics of nonequilibrium electrons in metals under femtosecond laser irradiation,* Phys. Rev. B **65**, 214303 (2002).

[38] R. R. Fäustlin, T. Bornath, T. Döppner, S. Düsterer, E. Förster, C. Fortmann, S. Glenzer, S. Göde, G. Gregori, R. Irsig, *et al.*, *Observation of ultrafast nonequilibrium collective dynamics in warm dense hydrogen,* Phys. Rev. letters **104**, 125002 (2010).

[39] G. Chen, *Ballistic-diffusive heat-conduction equations,* Phys. Rev. Lett. **86**, 2297 (2001).

[40] N. Medvedev, Z. Li, V. Tkachenko, and B. Ziaja, *Electron-ion coupling in semiconductors beyond Fermi's golden rule,* Phys. Rev. B **95**, 014309 (2017).

[41] C. Lian, S. Zhang, and S. Meng, *Ab initio evidence for nonthermal characteristics in ultrafast laser melting,* Phys. Rev. B **94**, 184310 (2016).

[42] H. Hu and S. A. Argyropoulos, *Mathematical modelling of solidification and melting: a review,* Model. Simul. Mater. Sc. **4**, 371 (1996).

[43] A. E. Morris, H. A. Fine, and G. Geiger, *Handbook on Material and Energy Balance Calculations in Material Processing* (John Wiley Sons, 2011).

[44] S. Perkins, D. Cullen, M. Chen, J. Rathkopf, J. Scofield, and J. Hubbell, *Tables and graphs of atomic subshell and relaxation data derived from the LLNL Evaluated Atomic Data Library (EADL), Z= 1–100*, Tech. Rep. (Lawrence Livermore National Lab., CA (United States), 1991).

[45] S. Gorbunov, N. Medvedev, P. Terekhin, and A. Volkov, *Electron–lattice coupling after high-energy deposition in aluminum,* Nucl. Instrum. Meth. B **354**, 220 (2015).

[46] D. A. Papaconstantopoulos, *Handbook of the Band Structure of Elemental Solids: From Z=1 To Z=112* (Springer, 2016).

[47] B. Mueller and B. Rethfeld, *Relaxation dynamics in laser-excited metals under nonequilibrium conditions,* Phys. Rev. B **87**, 035139 (2013).

[48] J. Hohlfeld, S.-S. Wellershoff, J. Güdde, U. Conrad, V. Jähnke, and E. Matthias, *Electron and lattice dynamics following optical excitation of metals,* Chem. Phys. **251**, 237 (2000).

[49] M. Bonn, D. N. Denzler, S. Funk, M. Wolf, S.-S. Wellershoff, and J. Hohlfeld, *Ultrafast electron dynamics at metal surfaces: Competition between electron-phonon coupling and hot-electron transport,* Phys. Rev. B **61**, 1101 (2000).

[50] B. Rethfeld, D. S. Ivanov, M. E. Garcia, and S. I. Anisimov, *Modelling ultrafast laser ablation,* J. Phys. D: Appl. Phys. **50**, 193001 (2017).

[51] S. I. Anisimov and B. Rethfeld, *Theory of ultrashort laser pulse interaction with a metal,* in *Nonresonant Laser-Matter Interaction (NLMI-9)*, Vol. 3093 (International Society for Optics and Photonics, 1997) pp. 192–204.

[52] C. Y. Ho, R. W. Powell, and P. E. Liley, *Thermal conductivity of the elements,* J. Phys. Chem. Ref. Data **1**, 279 (1972).

[53] C. Kittel and P. McEuen, *Introduction to solid state physics*, Vol. 8 (Wiley New York, 1996).

[54] R. Ramji Rao and A. Ramanand, *Lattice dynamics, thermal expansion, and bulk modulus of ruthenium,* J. Low Temp. Phys. **27**, 837 (1977).

4

SIMILARITY IN RUTHENIUM DAMAGE INDUCED BY PHOTONS WITH DIFFERENT ENERGIES: FROM VISIBLE LIGHT TO HARD X-RAYS

We performed combined experimental and computational research on damage processes in ruthenium thin films induced by femtosecond lasers with various photon energies. We present an experiment with an optical laser at normal incidence conditions and compare it with previously reported experiments at grazing incidence conditions with XUV and hard X-ray photons, covering a large range of photon energies. Analysis of ablation craters in Ru shows very similar crater morphology and depth of about 10-20 nm for all considered irradiation conditions. Simulations of light-matter interactions are performed with our combined Monte Carlo and two-temperature hydrodynamics approach. The simulation results show that the primal cause of eventual ablation is Auger decay of core-shell holes created after absorption of XUV and hard X-ray photons in the vicinity of ruthenium surface. They lead to the creation of many low-energy electrons which consequently release the absorbed energy near the surface, resembling the optical irradiation case. Similar absorbed energy distributions in the top part of ruthenium induce a similar thermo-mechanical response and, therefore, similar ablation process. Our results suggest that such mechanism is universal in a wide range of photon energies at grazing incidence conditions, when the photon absorption depth is smaller than the photoelectrons range.

4.1. INTRODUCTION

Interaction of femtosecond laser pulses with matter is a complex multi-physical and multi-scale process, which strongly depends on the irradiation conditions and the target properties. Understanding the mechanisms that govern such interactions is of crucial importance in both fundamental and applied science. Absorption of intense femtosecond laser pulses can bring material into an excited non-equilibrium state at considerably high temperature (up to several eV), but still at solid state density. The theoretical description of such a state, also referred to as warm dense matter [1, 2], is challenging, since neither standard solid state nor semi-classical plasma formalisms can be directly applied [3, 4]. Relaxation of such an excited system may lead to strong changes in the lattice structure of the irradiated target and eventually to severe damage. Identifying and controlling such processes is necessary, e.g., to manufacture long lasting reflective optics for the rapidly developing X-ray free-electron lasers (XFELs).

A typical damage phenomenon that occurs after irradiation of a target with intense femtosecond laser pulses is ablation of the top surface material. Many studies of laser ablation in solids with optical lasers were performed in the past [5–10]. Damage tests of different materials such as multilayer mirrors [11–13], thick substrates [14–16] and thin films [12, 14–19] at extreme ultraviolet (XUV) and X-ray free-electron laser light sources were also reported. Although such experiments at XFELs are becoming more and more accessible, there is still a lack of detailed understanding of the nature of the observed damage phenomena. Moreover, scalability of already known results to different materials and irradiation conditions is of high demand in order to avoid numerous experimental tests.

Thin metal films are commonly used as grazing incidence mirrors at XFEL facilities to ensure high reflectivity. At such conditions light is absorbed in the thin (several nm) top layer of the target, which is similar to the well-studied optical case, where absorption occurs within the skin depth of about 10 nm. Despite that similarity in the photoabsorption depth, the following evolution of excited electrons strongly depends on the incident photon energy. In a metal, an optical laser only probes conduction band electrons due to low energy of the incident photons. Excitation of core electrons is possible only via multi-photon absorption which requires extremely high intensities. Contrarily, in the X-rays regime the photons are predominantly absorbed by core-shell electrons. As a result, secondary electrons with various kinetic energies are created, which can play a role in the damage processes in the target [20–22].

In the present paper, we perform an experimental and theoretical comparative study of single-shot damage produced in ruthenium (Ru) films by femtosecond laser pulses in a wide photon energy range, from the optical to the hard X-ray regime. Ru is chosen as a relevant material to be used as a grazing incidence reflective mirror at XFEL facilities [15, 21, 23]. Four different photon energies are compared, namely 1.5 eV (optical), 92 eV (XUV), 7 and 12 keV (hard X-rays). The XUV single-shot damage experiment was reported by Milov et al. in previous work [23], while for 7 and 12 keV we analyze the data from the work by Aquila et al. [21, 24]. The optical damage experiment is performed in the present work.

The complex nature of light-matter interaction dictates the necessity to use a combination of different models to describe various physical aspects involved in such interaction. For example, a combination of the two-temperature-based models with classical

molecular dynamics is frequently used to describe the interaction of the optical lasers with the targets [25, 26]. In the Ref. [22] an approach of combining hydrodynamics simulations with calculations of the radiation field in the material was applied to model the XFEL-matter interaction.

In our work, the experimental results are analyzed using a two-temperature hydrodynamics (2T-HD) model [27], which simulates material response to ultrafast energy deposition. The latter is obtained with the Monte Carlo code XCASCADE(3D) [28], which models the photoabsorption and subsequent non-equilibrium electron kinetics. Such an approach combining the Monte Carlo and 2T-HD methods provides insights into the spatial distributions of material characteristics inside a heated sample during its evolution, starting from photoabsorption and non-equilibrium electron cascades, up to the lattice response and damage formation.

To successfully apply the 2T-HD model, the equation of state (EOS) of the material under investigation is required. Ru is still poorly studied in the two-temperature (2T) regime of thermal non-equilibrium between electrons and ions, which is realized after the absorption of a femtosecond laser pulse. In a separate paper [29] we obtain the 2T EOS that govern the thermodynamics of Ru in a wide range of temperatures and pressures using *ab initio* density functional theory (DFT) calculations. The kinetic coefficients (2T thermal conductivity and electron-phonon coupling factor) are also calculated in [29].

4.2. EXPERIMENT

Optical single-shot damage experiments were performed using a femtosecond regenerative amplifier system (Spectra Physics Spitfire, 800 nm wavelength, maximum energy of 2.2 mJ at 1 kHz, ~ 90 fs FWHM pulse length) under atmospheric conditions. For the damage experiment the laser system was operated in single-shot mode, which allows only one laser pulse to be released after the trigger event. For beam characterization, the laser system was operated in multi-shot mode, where pulses were released at 1 kHz repetition rate.

The p-polarized laser beam was focused on a sample into a spot of ~ 42 μm radius (radius at $1/e^2$). The beam radius was characterized by the knife edge method along the horizontal direction. The sample was positioned slightly before the focal spot to avoid possible ionization of air and, therefore, disturbance of the beam quality at the sample. The angle of incidence (AOI) was set close to normal (~10° off-normal). To continuously control the laser fluence we used an attenuator comprising a half-wave plate and a polarizer. We characterized the laser pulse duration by locating an autocorrelator just before the sample, with typical measured values to be ~ 90 fs (FWHM).

A Ru polycrystalline film of 50 nm thickness was used as a target. The sample was prepared by depositing Ru on a naturally oxidized super-polished silicon substrate using the magnetron sputtering technique. Irradiations were performed varying the incident fluence. For each fluence a pristine surface was irradiated.

Ex situ analysis was performed by means of scanning electron microscopy (SEM) and transmission electron microscopy (TEM). Fig. 4.1 (a) shows a SEM image of a typical damage crater produced during the experiment described above. Ablation, also referred to as thermo-(photo-) mechanical spallation, of the top part of Ru is observed, which

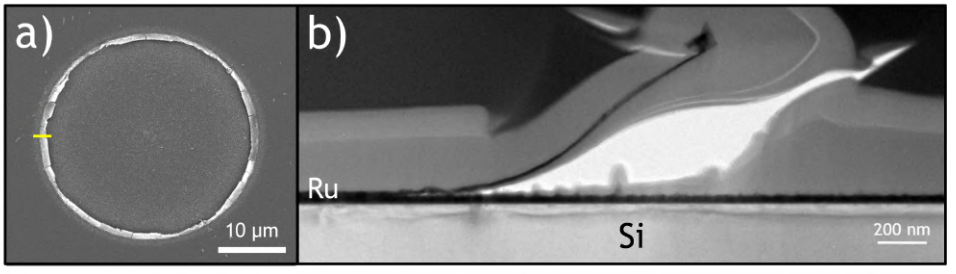

Figure 4.1: (a) SEM image of Ru damage crater produced by a 90 fs 1.5 eV (800 nm) laser pulse with an incident peak fluence $F = 500\,\mathrm{mJ/cm^2}$. The yellow line indicates where the TEM cross-section is made. (b) TEM cross-section image taken at the edge of the damage crater, illustrating ablation of the top 15 – 20 nm of Ru.

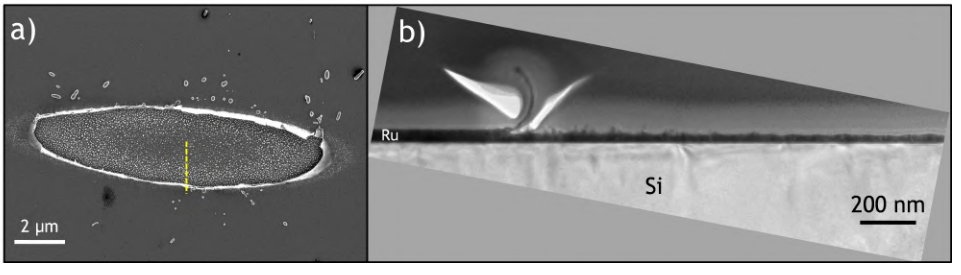

Figure 4.2: (a) SEM image of Ru damage crater produced by a 100 fs 92 eV (13.5 nm) laser pulse with an incident peak fluence $F = 300\,\mathrm{mJ/cm^2}$. The yellow line indicates where the TEM cross-section is made. (b) TEM cross-section image taken along the short axis at the edge of the damage crater, illustrating ablation of the top 18 – 22 nm of Ru.

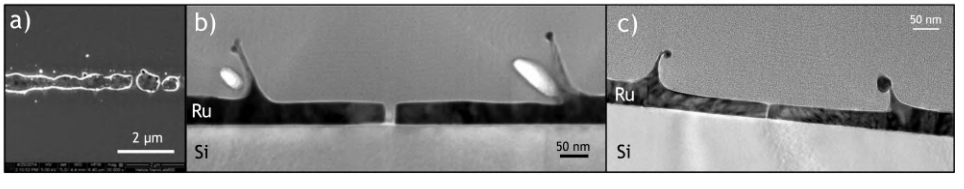

Figure 4.3: (a) SEM image of Ru damage crater produced by a 20 fs 7 keV laser pulse near the ablation threshold fluence. (b) TEM cross-section image at the edge of the damage crater produced by the 20 fs 7 keV laser pulse, illustrating ablation of the top 10 – 20 nm of Ru. (c) TEM cross-section image at the edge of the damage crater produced by a 20 fs 12 keV laser pulse, illustrating ablation of the top 15 – 20 nm of Ru. All images are taken from Ref. [21, 24].

is typical for metals irradiated with high fluence femtosecond optical lasers [9, 26, 30–33]. The remaining part of the ablated Ru forms the edge of the crater. The surface at the bottom of the crater appears to be much rougher, compared to the non-irradiated surface. The fact that only the top part of the Ru layer is ablated is confirmed by TEM measurements. Fig. 4.1 (b) shows a TEM cross-section image taken at the edge of the crater. The depth of the crater was found to be ~ 15 – 20 nm by measuring the thickness of the remaining Ru inside the crater and subtracting it from the initial 50 nm thickness.

We compare the results of the optical laser damage experiment described above with three other single-shot damage experiments previously performed at XFEL facilities, where light with different photon energies was used. Identical samples were irradiated, namely 50 nm thick Ru films on Si substrates prepared with magnetron sputtering.

In the first experiment performed at the Free-electron LASer in Hamburg [34]), femtosecond XUV pulses with 92 eV photon energy (13.5 nm wavelength) were used [23]. Exposures were performed in a high-vacuum chamber at grazing incidence conditions (20° grazing angle) mimicking the operation conditions for Ru thin film as an X-ray reflective mirror. The details of the experiment can be found in Refs. [12, 23]. A SEM image of a typical damage crater produced in this experiment is shown in Fig. 4.2 (a). The crater is similar to the one obtained after irradiation with the optical laser (see Fig. 4.1). Similar ablation of the top Ru layer is observed (see TEM image at the edge of the crater shown in Fig. 4.2 (b)). The crater depth is measured in the same way as described above and is about 18-22 nm. We observe similar surface morphology inside the crater for optical and XUV cases: the roughness decreases from the edge towards the center of the crater.

Two other experiments, reported by Aquila et al. [21, 24], were performed at SPring-8 Angstrom Compact free-electron LAser (SACLA [35]). Ru films were exposed to single-shot femtosecond XFEL pulses with 7 and 12 keV photon energy (0.177 and 0.103 nm wavelength, respectively). Due to the much higher photon energy compared to the experiments described above, extremely grazing incidence conditions (0.26° and 0.17°, respectively) were applied to guarantee high reflectivity of Ru. The SEM and TEM images of the damage crater for the 7 keV case, together with the TEM image of the 12 keV crater are shown in Fig. 4.3. The craters are strongly elongated in one direction due to the extremely grazing AOI. Only a part of the crater is shown in Fig. 4.3 (a). Similar to the experiments described above, ablation of the top Ru layer is observed for both the 7 and the 12keV cases, with the reported value of the crater depth to be 10 - 20 nm. The bottom of the craters for the 7 and 12keV exposures are considerably smoother, compared to the optical and XUV cases. Cracks inside the crater are observed on the SEM image, and the ones that spread through the entire Ru layer in the center of the crater are detected on the TEM images.

In all the described experiments, single-shot ablation thresholds were determined with the Liu method [36]. Crater areas were measured using optical microscopy. The spatial shape of the beam at XFEL facilities is typically non-Gaussian. For that reason, in XUV and hard X-ray experiments a fluence scan method [37, 38] was used to characterize the spatial beam shape and effective beam area prior to the damage experiments.

Table 4.1 summarizes the main results and parameters of the described experiments. Note that the threshold fluences reported in [21] should be scaled by a $\sin(\theta)$ factor, in order to obtain the incident threshold fluence at the sample surface, F^{th}, where θ is the AOI measured from the sample surface. For better comparison of all four experiments, the single-shot ablation threshold values, F^{th}, are recalculated into the absorbed fluence $F^{\text{th}}_{\text{abs}} = F^{\text{th}}(1-R)(1-\xi)$ taking into account surface reflectivity, R, and the fraction of energy that escapes from Ru due to electron emission from the front surface, ξ. The latter is determined by the XCASCADE(3D) simulations reported below. In our assumption of instant electron thermalization, the electron emission in the optical case can only occur due to the tail of the Fermi-Dirac distribution, which is exponentially small at our calculated electron temperatures.

Table 4.1: Summary of experimental conditions to determine single-shot ablation thresholds at four different photon energies: 1.5, 92, 7000 and 12000 eV. The threshold value F^{th} and crater depth are measured in the present work for the 1.5 eV case, while for the XUV (92 eV) and hard X-ray (7 and 12 keV) cases the values are taken from Refs. [23] and [21], respectively. The absorbed threshold fluence $F^{\text{th}}_{\text{abs}}$ is calculated taking into account the surface reflectivity, R, and the fraction of energy that escapes from Ru due to electron emission, ξ. The latter is determined in the XCASCADE(3D) simulations.

Photon energy [eV]	1.5	92	7000	12000
Environment	atmosphere	high vacuum		
AOI[a], θ [deg]	~80	20	0.26	0.17
Photon penetration depth, δ [nm]	12.8	3.5	1.8	1.9
Surface reflectivity, R [%]	67	68	89.9	95
Pulse duration (FWHM), τ_p [fs]	90	100	20	20
Exp. dam. threshold, F^{th} [mJ/cm^2]	367 ± 66	200 ± 40	1395	14100
Fraction of escaped energy[b], ξ [%]	0	9	47	48
$F^{\text{th}}_{\text{abs}} = F^{\text{th}}(1-R)(1-\xi)$ [mJ/cm^2]	121 ± 22	58 ± 12	75	367
Abs. dose, $D = F^{\text{th}}_{\text{abs}}/\delta$ [eV/atom]	8	14	35	162
Crater depth [nm]	15-20	18-22	10-20	15-20

[a]Measured from the sample surface

[b]Calculated with XCASCADE(3D)

It is known that the surface roughness can increase the X-ray absorption at extremely small grazing angles [39], but for our conditions such an effect on absorbed fluence is estimated to be insignificant.

An increase of the threshold fluence value with increasing photon energy is observed, although the case of 1.5 eV deviates from that trend, having a higher threshold value compared to 92 and 7000 eV, see Table 4.1 The deviation of the 1.5 eV case can be explained by a larger penetration depth of the optical light compared to XUV and hard X-rays at the considered experimental conditions (12.8 nm vs 3.5 and 1.8 nm, respectively). But different photon penetration depth alone cannot explain the full trend in the ablation threshold behavior. Moreover, the opposite trend could have been expected, since the photon penetration depth is the smallest for hard X-rays at our conditions. It is known from the literature [21, 40, 41] that X-ray photons are capable of creating significant electron cascades that can influence the absorbed energy distribution in the irradiated target and, hence, the damage processes. The effect of such electron cascading should be included in the analysis of X-ray matter interaction, especially in the high fluence regime. It becomes clear, if one calculates the absorbed dose without taking the transport of non-equilibrium electrons into account (see Table 4.1 and Ref. [21]). Another interesting observation is that despite orders of magnitude difference in the incident photon energy, all examined damage spots exhibit comparable crater depth, which indicates that the mechanisms responsible for damage may be similar.

The main goal of the present work is to study the effect of electron cascades created by photons with different energy on single-shot ablation in Ru films. To better understand the experimental results presented above, we perform simulations of laser pulse interaction with Ru at different irradiation conditions using our combined Monte Carlo-

hydrodynamics approach that is described in the next section. With our simulations we aim to explain the similarities in the observed damage for considerably different irradiation conditions.

4.3. MODEL

The photoabsorption and non-equilibrium electron kinetics induced by incident photons are simulated with the classical Monte-Carlo (MC) code XCASCADE(3D) [28]. Cascading electrons with kinetic energy below a certain threshold (equal to the outermost ionization potential of the target atom, which is 8.12 eV for Ru) are considered as thermalized and provide a heat source for the 2T-HD model [27]. This model takes into account thermal diffusion of thermalized (equilibrium) electrons into the depth (in 1d) of the irradiated material, energy transfer from electronic into the ionic system and hydrodynamic evolution of the material due to thermo-induced stresses. As a result of such simulations, internal energy and temperature of both electrons and ions together with density, pressure and mass velocity can be obtained as functions of the depth and time.

In case of visible light, the energy of incident photons is not sufficient to induce electron cascades. For that reason, a standard heat source in the form of a temporally Gaussian laser pulse with exponential decay of the absorbed energy in depth is used as a heat source for the 2T-HD instead of the output of the XCASCADE(3D) code.

4.3.1. XCASCADE(3D)

The XCASCADE(3D) is an asymptotic trajectory event-by-event classical MC code that models X-ray-induced non-equilibrium electron transport in a target within the atomic approximation [28]. The target is represented as an infinite homogeneous arrangement of atoms with a density corresponding to the chosen material. The photoabsorption cross sections, parameters for the electron scattering cross sections and the ionization potentials of the target taken from the EPICS2017 databases [42] are also described in the atomic approximation.

The code accounts for the following processes: photoabsorption by core-shell levels, Auger recombination of created holes with release of Auger electrons, propagation of photo- and secondary electrons, and inelastic and elastic scattering of electrons on neutral atoms. All photo- as well as secondary electrons are traced until their energy falls below the predefined cutoff energy. Electrons with energies below this cutoff, as well as holes created in the valence atomic levels, are considered as thermalized. Their energy is treated as the energy of the conduction band electrons, forming a time- and space-dependent source term for further 2T-HD simulations as described below.

The inelastic scattering resulting in impact ionization is modeled with the binary-encounter-Bethe (BEB) cross sections [43], whereas for the elastic scattering, the Mott's cross section with the modified Moliere screening parameter is employed [44], both valid within the atomic approximation. The anisotropic scheme of electron-atom scattering is used [28].

The XCASCADE(3D) simulations are performed in two steps: first, we simulate a bulk material assuming all photons are absorbed at z = 0 ("surface"). Then, the realistic absorption profiles are taken into account by applying a convolution with the Lambert-Beer's law with the characteristic penetration depth, which depends on the

target density, photon energy and the angle of incidence. This approach, previously utilized in [23, 45], also enables one to estimate the total energy emitted from the sample by escaping electrons, but not the actual distribution of the energy above the surface.

In all experiments described above the authors used p-polarized light. In case of very small grazing incidence angles (7 and 12 keV), the polarization vector then is almost perpendicularly to Ru surface. We take the effect of polarization into account by allowing photoelectrons to travel only perpendicular to the surface (up and down) until their first scattering event. For simplicity, we use the same approximation for 92 eV photons, although the AOI is no longer small. It was shown that for 92 eV the effect of polarization is negligible due to small cascade ranges and quick randomization of the electron motion [45].

The applicability of the XCASCADE(3D) code is limited to the fluence regime when the density of cascading electrons is considerably lower than the atomic density. In that case the electron-atom scattering is dominant, while electron-electron interaction can be neglected. We checked that this condition was fulfilled in all the simulations presented in this work.

This limitation also allows to always use the cross sections of unmodified, unexcited material. As we show below, the cascade duration in Ru is short at the considered irradiation conditions. The material properties that can influence the cascading process do not change significantly during this time due to the excitation of the target. That justifies the application of the XCASCADE(3D) code to model the cascading process in Ru for fluences at which damage is expected on later timescale. In terms of incident photon energy, the code is applicable in a wide range from ~50 eV up to a few tens of keV.

An a-posteriori analysis of our results suggests that during the cascading time (few tens of fs), the irradiated material properties used in the XCASCADE(3D) simulations do not significantly change. That justifies a coupling between XCASCADE(3D) and 2T-HD using a scheme without feedback, when the output data from MC simulations are passed one-way into the 2T-HD model as the input.

4.3.2. TWO-TEMPERATURE HYDRODYNAMICS AND EQUATION OF STATE

The energy distribution of thermalized conduction band electrons, $U(z,t)$, obtained with the XCASCADE(3D) code is used to form a heat source in the 2T-HD model [27]. The 2T-HD equations in Lagrangian mass coordinates take the following form:

$$\frac{\partial}{\partial t}\left(\frac{1}{\rho}\right) = \frac{\partial u}{\partial m}, \tag{4.1}$$

$$\frac{\partial u}{\partial t} + \frac{\partial P}{\partial m} = 0, \tag{4.2}$$

$$\frac{\partial \varepsilon_e}{\partial t} + P_e \frac{\partial u}{\partial m} = \frac{\partial}{\partial m}\left(k_e \rho \frac{\partial T_e}{\partial m}\right) - \frac{\alpha}{\rho}\,(T_e - T_i) + S, \tag{4.3}$$

$$\frac{\partial \varepsilon_i}{\partial t} + P_i \frac{\partial u}{\partial m} = \frac{\alpha}{\rho}\,(T_e - T_i). \tag{4.4}$$

Here m is Lagrangian mass coordinate:

$$dm = \rho dz, \;\; m = \int_{z_0}^{z} \rho dz, \tag{4.5}$$

$\rho(z,t)$ is the material density, z is the depth Cartesian variable, z_0 is the Cartesian coordinate of the material surface and $u = dz/dt$ is the velocity of a Lagrangian particle. Eqs. (4.1) and (4.2) represent the conservation of mass and momentum, respectively. The conservation of energy is written separately for electronic and ionic subsystems, accounting for energy exchange between them, Eqs. (4.3) and (4.4), respectively. Such a separation is valid in the two-temperature (2T) approximation, when $T_e \neq T_i$, with T_e and T_i being electron and ion temperatures, respectively. The specific internal energies per unit mass of the electronic and ionic subsystems are ε_e and ε_i, respectively.

The energy exchange between electrons and ions is governed by the term $(\alpha/\rho)(T_e - T_i)$, where $\alpha = \alpha(T_e)$ is the electron temperature dependent electron-phonon coupling factor. The heat diffusion is assumed to be in the Fourier form defined by the heat flux $k_e\rho(\partial T_e/\partial m)$, where $k_e = k_e(\rho, T_e, T_i)$ is the density and temperature dependent electron thermal conductivity. The terms $P_e(\partial u/\partial m)$ and $P_i(\partial u/\partial m)$ in the energy conservation law equations define the work performed by electronic and ionic subsystems, respectively.

The heat source $S(z,t)$ is obtained from the XCASCADE(3D) calculations as the time derivative of the energy density of thermalized electrons:

$$S(z,t) = \frac{\partial U(z,t)}{\partial t}. \tag{4.6}$$

In the case of optical excitation, where there is no cascading effect, we use the standard heat source, representing heating of the electronic system with a temporally Gaussian laser pulse with exponential decay of absorbed energy in depth:

$$S(z,t) = \sqrt{\frac{4\ln 2}{\pi}} \frac{F_{\text{abs}}}{\delta \tau_p \rho} \exp\left(-4\ln 2\left(t/\tau_p\right)^2\right) \exp\left(-\frac{z(m,t) - z(m_0,t)}{\delta}\right), \tag{4.7}$$

where F_{abs} is the absorbed fluence, δ is the photon penetration depth, τ_p is the laser pulse duration, $z(m,t)$ is the trajectory of a Lagrangian particle with a coordinate m and m_0 is the Lagrangian coordinate of the irradiated target surface.

The system of equations (4.1) - (4.4) has to be completed with the equations of state (EOS), which describe pressure and internal energy of the material as functions of density, electron and ion temperatures. These equations govern the thermodynamics of the material in the two- and one-temperature states. The physics of the 2T states of metals is studied in detail [46–49]. However, for each particular metal the corresponding parameters are unique and must be obtained separately. In this work, the 2T EOS for single crystal hexagonal close-packed Ru are obtained and are applicable in a wide range of densities, temperatures and pressures that can be realized after irradiation of Ru with femtosecond high fluence laser pulses.

The idea of an analytical approximation of the 2T states of metals is to present the internal energy and pressure as a sum of electronic and ionic components [50]: $P = P_i + P_e$ and $\varepsilon = \varepsilon_i + \varepsilon_e$. In the framework of the Mie-Grüneisen approximation [50] the

ionic components can be presented as a sum of cold and thermal parts. So for the total internal energy and pressure we have:

$$\varepsilon(\rho, T_e, T_i) = \varepsilon_i^{cold}(\rho) + \varepsilon_i^T(T_i) + \varepsilon_e(\rho, T_e), \tag{4.8}$$

$$P(\rho, T_e, T_i) = P_i^{cold}(\rho) + P_i^T(\rho, T_i) + P_e(\rho, T_e). \tag{4.9}$$

The procedures of obtaining analytical approximations for each term in Eqs. (4.8) and (4.9) is described in [29]. Calculations of the electron-phonon coupling factor $\alpha(T_e)$ and the electron thermal conductivity $k_e(\rho, T_e, T_i)$ are also described in [29].

The system of equations (4.1,4.2,4.3,4.4) completed with the EOS (4.9) and (4.8) is solved using the implicit finite-difference method. The artificial viscosity is introduced to suppress non-physical oscillations in the obtained solutions [51].

4.4. RESULTS

In this section we present the results of the simulations with our combined approach in two fluence regimes. First, a relatively low fluence is applied in order to stay below the melting point in simulations for all four photon energies. In that regime we stay strictly within the applicability of the 2T-HD part of our model for Ru, which currently does not take into account the melting. A second set of simulations is performed in a high fluence regime corresponding to the ablation threshold values obtained in the experiments (see Table 1). In such a regime of high fluences, we expect melting of Ru to occur. The fact that melting is not simulated, due to the lack of knowledge of the EOS for liquid Ru, may influence the accuracy of our calculations. Therefore, we only aim to provide a qualitative analysis of the damage processes, which enables us to explain the trends observed in the experiment.

4.4.1. THE FLUENCE REGIME BELOW MELTING

We perform simulations of a thick Ru target exposed to single femtosecond laser pulses with four photon energies: 1.5, 92, 7000 and 12000 eV. For a clean comparison, the thickness of the Ru layer in each simulation is chosen large enough to mimic a bulk sample and eliminate possible substrate effects. For the case of optical excitation (1.5 eV) we consider no electron cascading and assume instantaneous electron thermalization. We perform XCASCADE(3D) calculations only for the XUV (92 eV) and hard X-ray (7 and 12 keV) cases.

First, we study the effect of different incident photon energies on the cascading kinetics and the final distribution of the absorbed energy stored in low-energy (thermalized) conduction band electrons. For pure theoretical comparison, we set the irradiation conditions such that the total absorbed volumetric energy density is identical for all photon energies. To achieve that, we set the values of the absorbed fluence and photon penetration depth to be the same for all photon energies. The crucial difference will be in how the absorbed energy is transported into the depth of Ru by cascading electrons. The photon penetration depth in all the cases is chosen to be equal to the optical (1.5 eV) skin depth of Ru, δ = 12.8 nm. We set the value of F_{abs} = 20 mJ/cm^2 in order to stay below melting in all four simulations, which guarantees the applicability of the

Table 4.2: Summary of irradiation conditions used in the simulations in the fluence regime below melting. Irradiation conditions are chosen to have equal volumetric absorbed energy density (dose), F_{abs}/δ, for all considered photon energies. Cascade durations are calculated for the 92, 7000 and 12000 eV cases. No cascading is considered for the 1.5 eV case.

Photon energy [eV]	1.5	92	7000	12000
Pulse duration (FWHM), τ_p [fs]			20	
AOI*, θ [deg]	80	29.2	0.59	0.32
Photon penetration depth, δ [nm]			12.8	
Surface reflectivity, R [%]	67	14.6	20.6	53.2
Fraction of escaped energy, ξ [%]	0	3	38	44
Incident fluence, F [mJ/cm^2]	61	24	41	76
Abs. fluence, $F_{\text{abs}} = F(1-R)(1-\xi)$ [mJ/cm^2]			20	
Cascade duration [fs]	-	0.2	4.4	9.9

*Measured from the sample surface

whole model. The absorbed fluence is calculated taking into account the surface reflectivity, R, and a fraction of the energy that escapes from Ru due to electron emission, ξ: $F_{\text{abs}} = F(1-R)(1-\xi)$. Table 4.2 summarizes the irradiation parameters used in the simulations together with the most important results.

The values of ξ are extracted from XCASCADE(3D) calculations by integrating the energy distribution above the surface of Ru and are equal to 3, 38 and 44% for 92, 7000 and 12000 eV, respectively. Only a small portion of the energy carried by the cascading electrons is released from the surface in the 92 eV case due to the low energy of the particles. A minority of electrons is able to reach the surface and overcome the work function of Ru (4.71 eV [52]). Contrarily, a considerable part of the energy leaves the target in the case of hard X-rays due to the higher energy of the cascading electrons. The value is lower than 50%, since photoelectrons that travel up perpendicular to the surface before leaving the material can lose energy by creating secondary electrons. The value of ξ is higher for 12 keV, because the probability for a photoelectron to create a secondary electron while travelling from the point of photoabsorption to the surface is lower for higher energy of a photoelectron.

In the calculations of ξ we do not take into account the surface charging effect, therefore the obtained values can be considered as the upper limit. The effect is expected to be insignificant for the considered irradiation conditions. For the 92 eV case, the electron emission is already negligible. For the hard X-ray cases a major part of the energy is escaping via photoelectrons with high kinetic energy, which should enable them to travel a sufficient distance from the sample surface without being attracted back.

The distribution of the absorbed energy density stored in low-energy (thermalized) electrons, $U(z,t)$, at the moment of time when the cascading is finished (defined as the time when density of cascading electrons decreases below 1% of its maximum value) is shown in Fig. 4.4 for 92, 7000 and 12000 eV photons. The top 50 nm of Ru are shown in Fig. 4.4 (a), while Fig. 4.4 (b) focuses on the deeper part of Ru with long energy tails in the 7 and 12 keV cases.

As discussed above, since the absolute majority of excited electrons in the optical

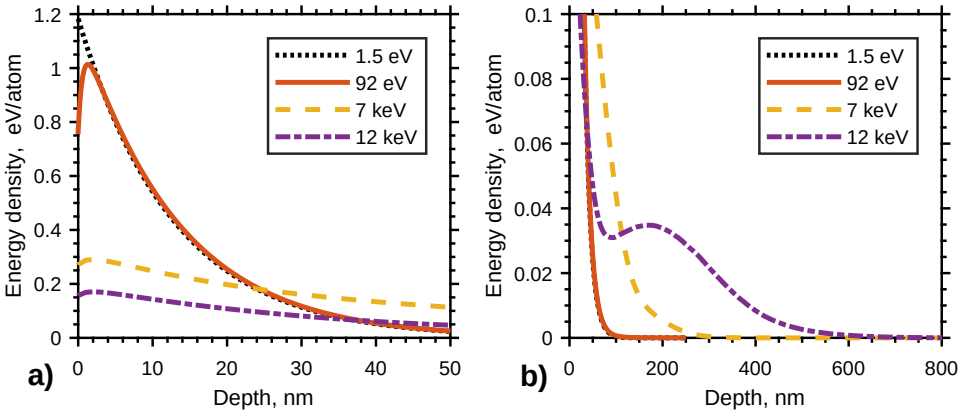

Figure 4.4: (a) Distribution of energy density $U(z, t)$ in the top 50 nm of irradiated Ru at the end of the cascading process, calculated with the XCASCADE(3D) code for different photon energies in the fluence regime below melting. The irradiation parameters are listed in Table 4.2. Since there is no cascading in the 1.5 eV case, the distribution of energy is represented with the Lambert–Beer's law (dotted line). (b) The same distribution shown in the entire Ru to emphasize the long energy tails in 7 and 12 keV cases.

irradiation case (1.5 eV) has energy below 8.12 eV cutoff, there is no cascading in such a case by our definition. Therefore, the absorbed energy density can be represented with the Lambert–Beer's law as $(F_{\text{abs}}/\delta)\exp(-z/\delta)$. Photons with 92 eV energy are capable of ionizing 4s, 4p, 4d and 5s electrons in atomic Ru, with 4d and 5s valence levels representing the conduction band of the material in our atomic approximation, as we discussed in [23, 45]. Photoelectrons with relatively low kinetic energy (~10-40 eV) are thus created, which results in a very short cascading range, since these electrons lose the energy below the cutoff after only a few collisions. Only a slightly deeper spread of the energy is observed for the 92 eV case compared to 1.5 eV, which demonstrates a small effect of electron cascading in Ru for 92 eV photons.

Photons with 7 and 12 keV energies are capable of ionizing core-shell electrons down to the 2s level of Ru, creating a majority of photoelectrons with energy of ~3800 and 8800 eV, respectively. Their cascading ranges are considerably larger than those in the XUV case. A much deeper spread of energy for hard X-rays, having the same total amount of absorbed energy, results in a much lower energy density in the near surface region compared to the XUV and optical cases, see Fig. 4.4 (a). In Fig. 4.4 (b), the peak at 170 nm depth on the 12 keV curve corresponds to the average photoelectron range for that photon energy. The peak is separated from the contribution of secondary electrons which have lower energy and, hence, travel a shorter distance. For the 7 keV curve, the contributions from photo- and secondary electrons happen to be mostly overlapping, therefore no separate photoelectron peak is observed.

An average single (produced by one photon) cascade duration is determined as the FWHM of the energy density time derivative [53]. The results are 0.2, 4.4 and 9.9 fs for 92, 7000 and 12000 eV, respectively. Such extremely short times justify our approximation that during the cascading, the material is considered as undamaged within the MC scheme.

The 2T-HD calculations are performed using the power densities $\partial U(z, t)/\partial t$ as heat

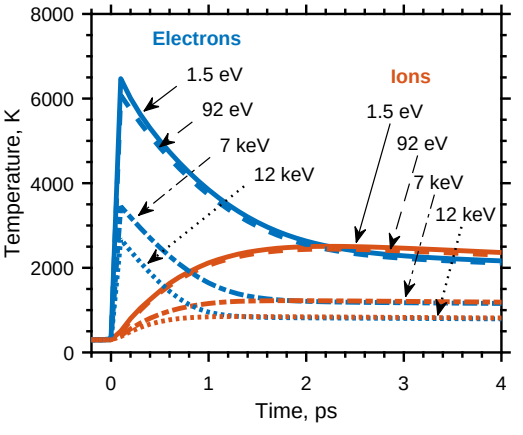

Figure 4.5: Time dependence of electron and ion surface temperatures, calculated with the 2T-HD code for different photon energies in the fluence regime below melting. The irradiation parameters are listed in Table 4.2.

sources. For 1.5 eV the standard heat source, Eq. (4.7), is used. Fig. 4.5 shows the time dependence of electron and ion surface temperatures. All four cases exhibit thermal non-equilibrium between electrons and ions during the first ~1-2 ps. Although the qualitative behavior of the surface temperatures is similar for all photon energies, the reached temperatures differ considerably. The higher the photon energy, the deeper electrons transfer an equal amount of absorbed energy (cf. Fig. 4.4), which results in a lower surface temperature. Note, that T_i stays below the melting temperature $T_m = 2607$ K in all the calculations.

The depth profiles of ion temperature T_i and total pressure P at $t = 5$ ps for different photon energies are shown in Fig. 4.6 (a) and (b), respectively. The time $t = 5$ ps is chosen as the time when the tensile pressure wave is already formed and reached an amplitude close to the maximum value (see description below). A much deeper distribution of absorbed energy by cascading electrons for the 7 and 12 keV cases results in a more gradual change of ion temperature with depth compared to a steep decrease in the cases of 1.5 and 92 eV photons. The small peak in the ion temperature profiles at the depth of ~10 nm is due to the compression of material in that region.

Ultrafast almost isochoric heating of a target by a femtosecond laser pulse results in generation of thermo-induced stress. Such a situation is referred to as the stress confinement regime [23, 26, 33] and is realized when the heating time is shorter than the acoustic relaxation time. The latter can be determined as the heated depth divided by the speed of sound. For Ru at the considered irradiation conditions the acoustic time is ~10 ps, while the heating time is ~1 ps (see Fig. 4.5). Therefore, the material is in the stress confinement regime.

The compressive wave created at the surface propagates into the depth of the irradiated material and is followed by the tensile wave, Fig. 4.6 (b), due to the existence of a free surface. The fracture typically occurs when the amplitude of a tensile wave overcomes the spall strength of the material [26]. The spall strength of Ru at ultra-high strain rates of about 10^{10} s^{-1} that are typically realized during the ablation process is unknown.

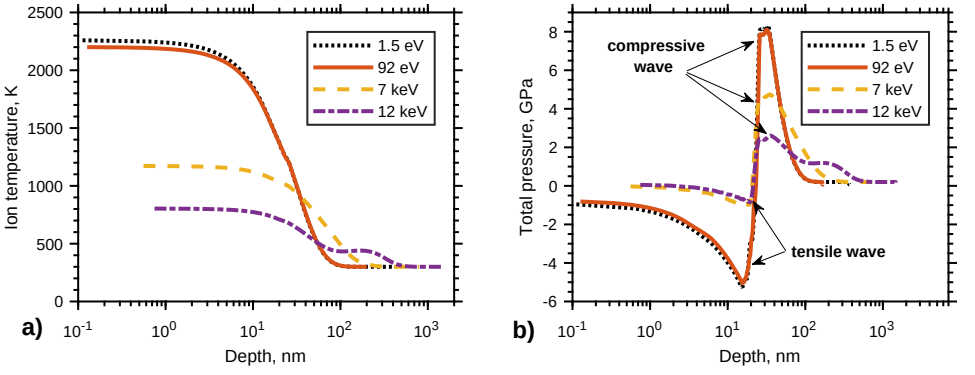

Figure 4.6: (a) Ion temperature and (b) total pressure depth profiles at $t = 5$ ps, calculated with 2T-HD code for different photon energies in the fluence regime below melting. The irradiation parameters are listed in Table 4.2.

For solid iron the spall strength at 10^9 s^{-1} strain rate is 15 GPa [54]. The spall strength of Ru must be even higher, judging from the comparison of cold curves for these two metals (a cold curve, which is the dependence of pressure on volume/density at absolute zero temperature, can be extracted from [55]). In the studied cases, the tensile pressure in Ru stays above -7 GPa, therefore no fracture of material is expected.

The general behavior of pressure profiles in Fig. 4.6 (b) is similar for all photon energies, but the amplitudes of the pressure waves are considerably different. Stronger temperature gradients in the cases of 1.5 and 92 eV result in stronger pressures compared to the 7 and 12 keV case.

The performed analysis demonstrates that the electron cascading effect in the 7 and 12 keV cases plays an essential role in the distribution of the absorbed energy in Ru, making the hard X-ray case considerably different from the 1.5 and 92 eV cases. Despite the fact that the energy is transferred much deeper for 7 and 12 keV, which results into a lower energy distribution in the top 50 nm of Ru, there are still temperature gradients that induce pressure waves. The amplitudes of those pressure waves are much smaller than in the 1.5 and 92 eV cases. Based on our analysis, one can expect higher amplitudes of pressure waves for higher fluences, which can result into damage. We investigate the evolution of the Ru target irradiated with fluences corresponding to the measured damage threshold values in more details in the next section.

4.4.2. THE FLUENCE REGIME AT THE ABLATION THRESHOLD LEVEL

In this section we perform similar simulations as the ones described above, but for the irradiation conditions used in the experiments (see Table 4.1). The absorbed fluences are chosen to be 121, 58, 75 and 367 mJ/cm^2 for 1.5, 92, 7000 and 12000eV photon energy, respectively, which correspond to the measured single-shot ablation thresholds, $F_{\text{abs}}^{\text{th}}$. The values of ξ calculated for the irradiation conditions considered here are 9, 47 and 48% in the 92, 7000 and 12000 eV cases, respectively. The values are higher, compared to the ones reported in the previous section, because the photon penetration depth is now smaller (see Table 4.1).

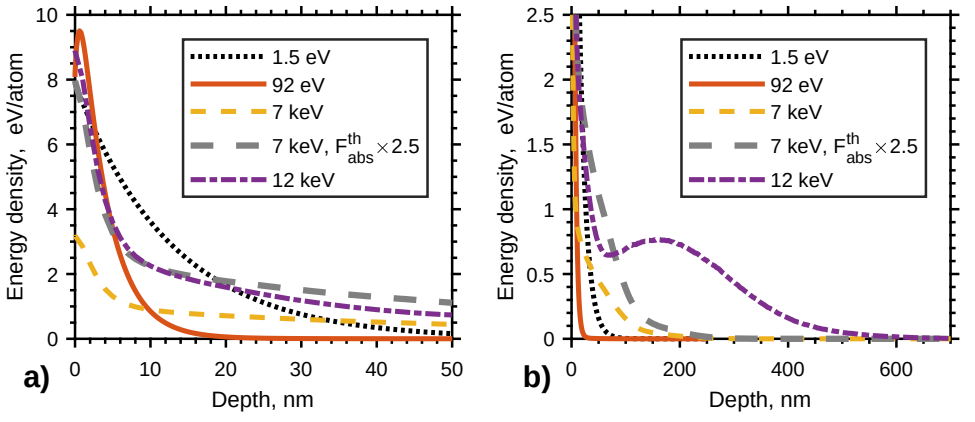

Figure 4.7: (a) Distribution of energy density $U(z,t)$ in the top 50 nm of irradiated Ru at the end of the cascading process, calculated with the XCASCADE(3D) code for different photon energies in the fluence regime corresponding to the measured ablation threshold. The irradiation parameters are listed in Table 4.1. Since there is no cascading in the 1.5 eV case, the distribution of energy is represented with the Lambert–Beer's law (dotted line). The thick dashed grey line shows the 7 keV case calculated with a fluence 2.5 times higher than the measured ablation threshold. The fluence has to be increased in order to achieve a similar distribution of energy density in the top 50 nm for all considered photon energies (see discussion in the text). (b) The same distribution shown in the entire Ru to emphasize the long energy tails in 7 and 12 keV cases.

To significantly simplify the simulation, all calculations are again performed for the thick Ru sample, with a thicknesses large enough to mimic bulk material for each particular photon energy, whereas the thin Ru films with a thickness of 50 nm on Si substrates were used in the experiment. It will be shown below that the prime mechanism of damage with the fluences near the ablation threshold does not involve a major role of the substrate. The fact that the crater depth measured in all considered experiments is smaller than half of the film thickness also supports that assumption (see Discussion).

Fig. 4.7 shows the distribution of the absorbed energy density at the end of the cascading process for 92, 7000 and 12000 eV. Again, the exponential decay of the absorbed energy for the optical case corresponds to the Lambert–Beer's law with the photon penetration depth $\delta = 12.8$ nm. Fig. 4.7 (a) shows the distribution of the energy in the top 50 nm of Ru, while Fig. 4.7 (b) shows the depth up to 700 nm focusing on the long energy tails for the 7 and 12 keV cases. The dose of several eV/atom is achieved at the near surface region in all four simulations. Such doses are considerably higher than that required for melting of Ru (~1 eV/atom, see Fig. 4.4 (a) and Ref. [56]). This indicates that stronger damage is expected, which is confirmed in the experiments. Similar energy density distributions in the top 50 nm are observed in Fig. 4.7 (a) for the cases of 1.5, 92 and 12000 eV, while the 7000 eV curve lies considerably lower. We will discuss the distinction of the 7 keV case below.

The long range behavior, Fig. 4.7 (b), is different for the cases of 92, 7000 and 12000 eV photons due to different impact of the cascading effect: cascading electrons propagate deeper for higher photon energy as discussed above. Let us recall that calculations are performed for thick Ru, while according to the experiment the region $z > 50$ nm should correspond to the Si substrate. The electron range in Si is approximately 4.5 and 5.5

times larger than in Ru for the incident photon energy of 7 and 12 keV, respectively. Based on that rough estimation, the tails of the energy distribution, Fig. 4.7 (a), should be stretched in the region z > 50 nm with corresponding factors (not shown here), which will result in the dose in that region being lower than 0.25 eV/atom. Such dose is considerably lower than the melting dose for Si, ~0.65 eV/atom [57, 58], which guaranties that the Si substrate is not damaged at the given irradiation conditions. This conclusion is also supported by the experimental evidence of no visible damage in the substrate.

Similar to Fig. 4.4, the peak at 160 nm in the 12 keV case in Fig. 4.7 is due to photoelectrons, while the near surface peak is the contribution from secondary electrons. More specifically, the peak-like distribution of energy in the top 10 nm of Ru for all three photon energies (92, 7000 and 12000 eV) is caused by Auger electrons produced during many-step decay of core-shell holes created after release of a photoelectron. The average kinetic energy of such Auger electrons is relatively small, so they do not travel far and stay in the near surface region. In the 92 eV case Auger electrons have a higher energy than photoelectrons, and the entire energy distribution is dominated by the former.

Similar energy distributions in the top part of Ru should induce similar hydrodynamic evolution and eventually lead to similar damage phenomena observed in the experiment (ablation of the top 10-20 nm). The long range energy tails in the spatial energy distribution are not expected to play a major role at our fluences, apart from being the energy sink from the near surface region. The temperature gradients are low in the deeper region compared to those in the top 20 nm of Ru. Hence, no strong pressure waves are generated there. The tails therefore act as an almost uniform mild heating source for the deep parts of the sample. That can potentially influence later stages of material evolution, playing a role in the recrystallization process and the formation of the final structure that is observed post mortem in the experiment.

According to our hypothesis that the distribution of the absorbed energy in the near surface region of Ru plays the dominant role in the ablation process detected in the experiment, one should expect similar energy profiles in that region for all considered photon energies. However our calculations show that the 7 keV profile differs from the others at the considered experimental conditions (see Fig. 4.7 (a), thin dashed line). Only if we increase the fluence by 2.5 times, the profile becomes very similar to the other ones (thick dashed line).

We justify the need of introducing a fluence correction factor with the following argument. Sophisticated geometry conditions in the reported experiment for 7 and 12 keV cases [21], namely the extremely grazing AOI, makes the procedure of accurate determination of the damage threshold values very challenging. The complicated shape of the damaged craters (very stretched thin lines of about $100 \times 1\mu$m size [21]) may introduce additional large errors into the procedure of measuring the area of such craters, and consequently into the damage threshold values.

To study how the cascading processes at different photon energies influence the hydrodynamic evolution of Ru, we perform 2T-HD calculations with heat sources obtained with the XCASCADE(3D) simulations (except for the optical case in which eq. (4.7) is used). In the case of 7 keV we show results obtained with the fluence 2.5 times higher than the measured ablation threshold.

The ion temperature evolution in Ru during the first 8 ps is shown in Fig. 4.8 for 1.5, 92, 7000 and 12000 eV photon energies. As one can see, all four cases exhibit strong

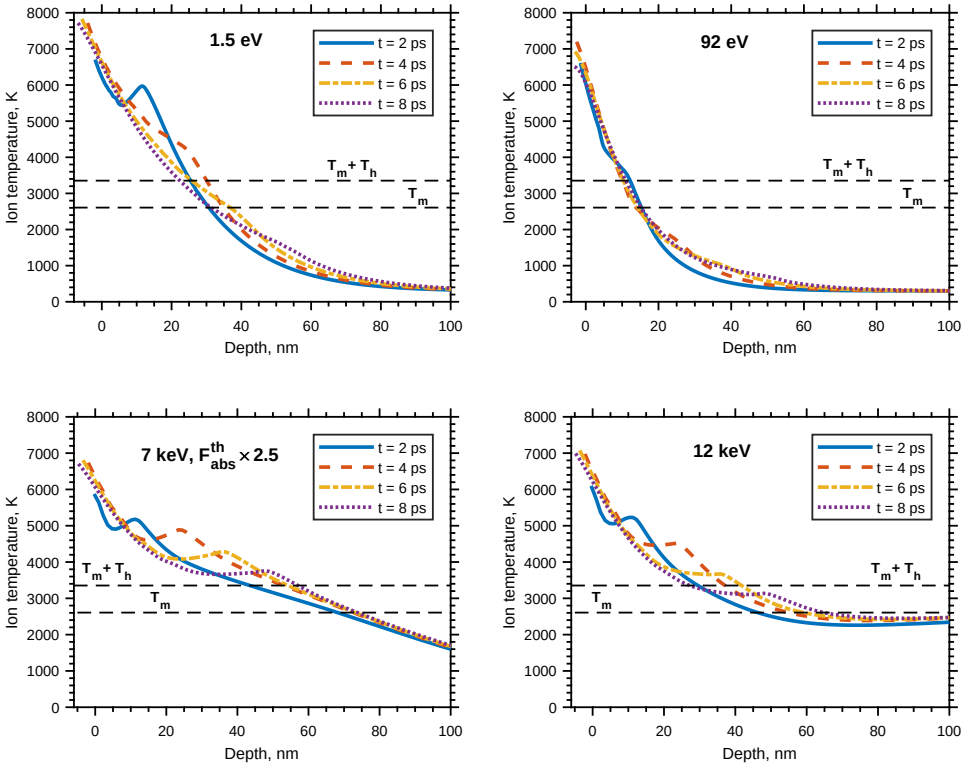

Figure 4.8: Ion temperature depth profiles evolution in Ru calculated with the 2T-HD code for different photon energies and fluences corresponding to the measured ablation thresholds. The values of the absorbed fluence (with surface reflectivity and energy escape from the sample via energetic electrons taken into account) are 120, 55, 185 and 364 mJ/cm^2 for the 1.5, 92, 7000 and 12000 eV photons, respectively. Other irradiation parameters are listed in Table 4.1. Note that for 7 keV we show the results of calculations with 2.5 times higher fluence than the measured ablation threshold. The black dashed lines show the melting temperature of Ru $T_m = 2607$ K and the value $T_m + T_h = 3353$ K, where the latent heat of melting is taken into account.

heating of the ions near the surface considerably above the melting temperature of Ru, $T_m = 2607$ K. The peaks on the ion temperature profiles that propagate into the depth of the sample with time are, as already mentioned above, due to strong compression of the material in that region (see pressure profiles below). Most of the heat is confined in the top 20-40 nm of Ru in the cases of 1.5 and 92 eV. For 7 and 12 keV the heat is spread over a larger region in accordance with the energy profiles shown in Fig. 4.7.

The maximum depth of melting during the considered 8 ps timescale is estimated to be 30, 12, 57 and 42 nm for 1.5, 92, 7000 and 12000 eV, respectively. These values are obtained by comparing the temperature profiles with the value $T_m + T_h$, where $T_h = H_m/C_i = 746$ K. Here $H_m = 4.7 \cdot 10^9$ J/m^3 is the latent heat of melting and $C_i = 6.3 \cdot 10^6$ J/m^3/K is the ion heat capacity at the melting temperature [59]. Note, that the melting depth in the 7keV case would expand into the substrate in the experiments. However, as we mentioned earlier, the actual absorbed dose in the substrate is much lower due to a large spread of the photoelectrons, therefore no melting is actually expected at those

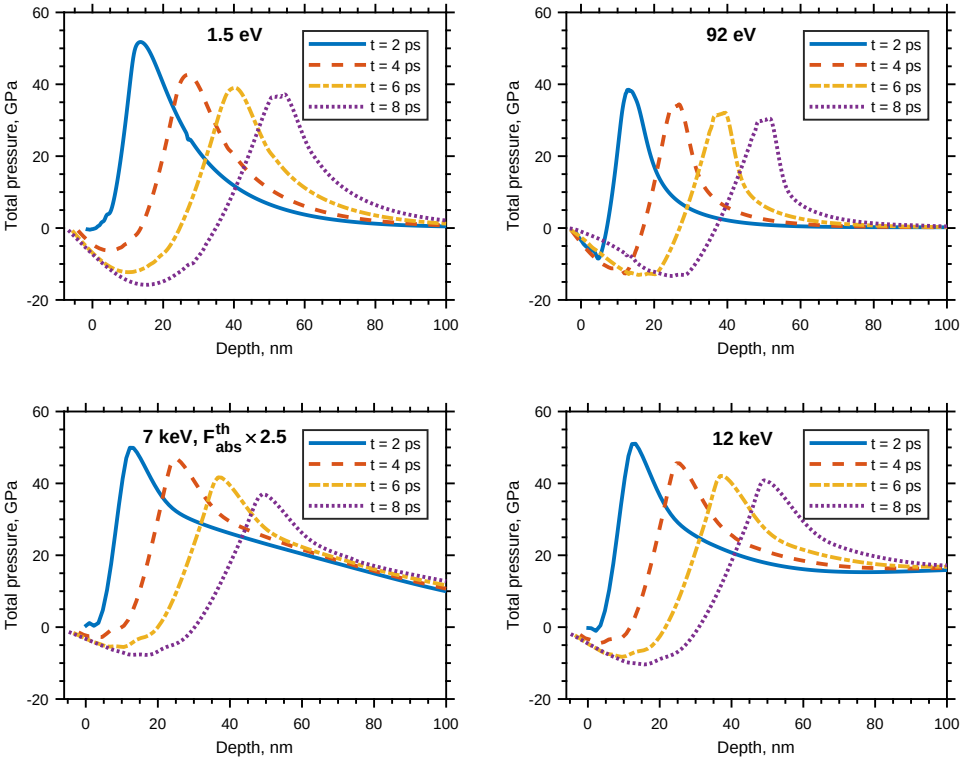

Figure 4.9: Total pressure depth profiles evolution in Ru calculated with the 2T-HD code for different photon energies and fluences corresponding to the measured ablation threshold. The values of the absorbed fluence (with surface reflectivity and energy escape from the sample via energetic electrons taken into account) are 120, 55, 185 and 364 mJ/cm^2 for the 1.5, 92, 7000 and 12000 eV photons, respectively. Other irradiation parameters are listed in Table 4.1. Note that for 7 keV we show the results of calculations with 2.5 times higher fluence than the measured ablation threshold.

depths.

The corresponding total pressure profiles are shown in Fig. 4.9. Strong compression waves with maximum amplitudes of ~40-50 GPa are followed by rarefaction tensile waves. For accurate analysis of the strength of the tensile wave in the context of damage, one needs to know the spall strength of liquid Ru at high strain rates of $\sim 10^{10}$ s^{-1} that are realized during the ablation processes. Unfortunately, very limited data on spall strength of metallic melts are available in the literature [60–63], with Ru not being studied at all in this respect. Due to that reason we use the experimental knowledge of the crater depth (10-20 nm) as an indication where the fracture of the material occurs. The maximum amplitude of the tensile wave reached at the depth of 10-20 nm lies in the range of $10-15$ GPa for all photon energies. These values can be considered as our model prediction of the spall strength of Ru at high strain rates. For comparison, the spall strength of solid iron at 10^9 s^{-1} strain rate is 15 GPa [54]; the spall strength of liquid aluminum at $\sim 10^9$ s^{-1} strain rate is 3.2 GPa at $T = 1100$ K and is decreasing with temperature [62].

Similar amplitudes of the tensile pressure reached in the top 20 nm region for all

photon energies explain the observed similarities in the crater depths.

4.5. DISCUSSION

4.5.1. PHYSICAL REASONS FOR ENERGY CONFINEMENT

A comparison of ablation craters in Ru obtained in the experiments demonstrates that at threshold fluences damage occurs in the top 10-20 nm for all considered irradiation conditions. Our theoretical analysis shows a similar distribution of the absorbed energy after the cascading process in the top 10-20 nm of Ru for all four photon energies, if for the 7 keV case one increases the absorbed fluence by a factor of 2.5. A similar energy distribution in the top 20 nm induces a similar hydrodynamical evolution and, hence, similar ablation craters.

Separate XCASCADE(3D) calculations show that for hard X-rays (7 and 12 keV), the peaks in the local energy density in the top 10 nm, see Fig. 4.7 (a), are primarily caused by the Auger electrons created at the positions of the photoabsorption due to many-step decays of core-shell holes. For both considered hard X-ray energies, the electron ranges of those Auger electrons are around 8 nm, leading to the accumulation of the energy in a small volume and resulting in damage. This number is calculated taking into account the spectrum of Auger electrons created by the incoming X-ray photon and their corresponding electron ranges, all obtained using the XCASCADE(3D) code. It has also been independently verified using the Auger spectra from the ab initio code XATOM [64–66], based on the Hartree-Fock-Slater approximation. Although such electrons possess less than half of the absorbed energy and the rest is brought deeper by the energetic photoelectrons, the latter spread the energy over a larger volume, thus decreasing the effective local absorbed dose in the depth. Only in the vicinity of the surface the energy density is sufficient to cause damage under our conditions.

This simulation result can be understood by considering the involved cross sections. First of all, the probability for a hard X-ray photon to create a core-shell hole is more than 100 times higher than that to create a valence hole [42]. It means that absorbed photons predominantly initiate Auger cascades at the positions of their absorption. Auger electrons have relatively low kinetic energies, which confines them to the proximity of their creation – the photoabsorption site. In contrast, the photoelectrons on their paths predominantly excite valence electrons. Only very few core-shell holes are created by the cascading electrons [42]. The corresponding energy loss of the photoelectrons is around 10 eV/nm, thus the photoelectrons typically spread the energy over a large depth.

The fact that Auger electrons may play a role in bulk materials evolution after irradiation with X-rays was discussed in [67]. An importance of Auger electrons was shown for small clusters irradiated with X-rays [68]. Since energetic photoelectrons can leave a cluster thus bringing out most of the absorbed energy from it, the remaining Auger electrons and Coulomb repulsion lead to the subsequent damage. However, for our case of metals, no Coulomb repulsion is expected and therefore one can see the pure effect of Auger electrons. To our knowledge, no corresponding studies have been published for bulk solids.

In case of 92 eV photons the photoabsorption also mostly results in the creation of the core-shell holes, which however possess a major part of the photon energy. The corresponding Auger cascades thus, again, become the main cause of the eventual damage.

For the low energy photons the localization of absorbed energy in the vicinity of the surface always occurs due to the absence of energetic electrons. For the high energy photons the localization of energy is due to the Auger electrons. Therefore, a similar spatial energy distribution near the surface leads to a very similar hydrodynamical evolution of the target and eventual damage *independently of the photon energy*. We expect that such a mechanism is universal in a wide range of photon energies and in various materials, however a rigorous verification is outside of the scope of this paper.

4.5.2. THE 7 keV CASE

Without the correction factor of 2.5 in the absorbed fluence, the maximum amplitude of the tensile pressure at the depth of 20 nm for the 7 keV case reaches only 5.7 GPa. This value is too low to expect damage and takes the 7 keV out of the trend when compared to other considered photon energies.

Another indication that the damage threshold for the 7 keV case has to be higher follows from the analysis of the damage threshold values for all considered cases (see Table 4.1). Simulation results presented in Fig. 4.4 show that the deeper penetration of the absorbed energy results in a lower energy density in the surface region. Therefore, one expects the damage threshold value to increase with increasing energy penetration depth. Then, as it follows from Fig. 4.7, the considered photon energies should be listed in the order of the threshold fluence increase in the following way: 92, 1.5, 7000 and 12000 eV. One can see from Table 4.1 that this is only possible if the threshold fluence for the 7 keV case is increased. A factor of 2.5 increase results in a reasonable trend.

We believe that the discrepancy between the experiment and our calculations for the 7 keV case can only be completely resolved with more experimental data.

4.5.3. MELTING

The 2T EOS obtained in [29] do not take into account the phase transitions, i.e. are valid only for solid Ru. Construction of a wide range EOS (with different phases included) for Ru requires a separate dedicated study and is beyond the scope of the present work. Our 2T-HD calculations show that the top part of the sample is subjected to melting in all considered irradiation conditions (see Fig. 4.8). Melting can influence the pressure profiles in the molten region of the sample. It can be shown, for example, that for Au and Al the influence of melting is small if one compares the wide range EOS [69] with the solid phase EOS in the Mie-Grüneisen approximation [50] for these two metals. The Grüneisen parameter should be taken as 3.1 and 2.1 for Au and Al, respectively. With a separate classical molecular dynamics simulation [32, 70–72] we checked that the effect of melting on the resulting pressure profiles during the first several ps is small for Ru as well (results will be reported elsewhere). Such a verification is obtained by comparing the pressure profile at $t = 2$ ps for the XUV case, calculated with molecular dynamics (melting is naturally included) and with the present 2T-HD code. The difference in the amplitude of the tensile wave is about 1 GPa, which is small compared to the maximum amplitude of 10-15 GPa obtained in our simulations (see Fig. 4.9).

4.5.4. SUBSTRATE

There are two possible thermo-mechanical damage scenarios in a thin film on a substrate. In the first one, the frontal tensile wave is sufficiently strong to cause material rapture, before the superposition with the pressure wave coming from the Ru-Si interface occurs. In the second scenario the frontal tensile wave is too weak to cause damage, but after the superposition with a rear-side wave, the resulting tensile stress can be sufficiently high. In that case damage starts in the region deeper than the middle of the film thickness [26]. Therefore, experimentally determined crater depths, defined by the energy localization, indicate that the first scenario is realized, making the role of a substrate negligible on the timescale before the material rapture occurs.

4.6. CONCLUSIONS

We performed a comparative study of ablation in Ru thin films irradiated with single-shot femtosecond laser pulses at various photon energies: 1.5 eV (optical), 92 eV (XUV), 7 and 12 keV (hard X-rays). Optical irradiation was set at normal incidence conditions, while grazing incidence conditions were applied in the XUV and hard X-ray cases. The ablation threshold is found to increase with increasing energy penetration depth. Despite the wide range of experimental irradiation conditions, the ablation craters appear to be very similar with approximately the same depth of 10-20 nm.

Such unexpected similarity in the ablation crater depth and the trend in the ablation threshold are explained with our theoretical analysis using the combination of Monte-Carlo simulations of electron transport and two-temperature hydrodynamics. The non-equilibrium electron cascading processes induced after absorption of XUV and hard X-ray photons play an essential role in spreading the absorbed laser energy in the sample: the higher the photon energy, the deeper the absorbed energy is transported by cascading electrons. In order to achieve the same absorbed dose in the top part of the sample, where the damage occurs, one needs a higher fluence for higher photon energy.

Although, after the cascading is finished, the deep parts of absorbed energy distribution are different and strongly depend on the photon energy, the energy distributions in the top 10-20 nm are similar for all considered photon energies. We found that the same process determines the near-surface absorbed energy profile for the XUV and hard X-rays cases, namely the many-step decay of the core-shell hole with a release of numerous low-energy Auger electrons. Such Auger electrons can only travel a short distance of less than 10 nm, confining the energy in the vicinity of the surface. One should note that such a mechanism is dominant only for grazing incidence conditions, when the photon absorption depth is smaller than the photoelectron range. Nevertheless, our model, in general, is not restricted only to the grazing incidence of X-rays, and can be applied to normal incident conditions, for example to study interaction of XFEL pulses with transmissive optics or filters.

A similar distribution of the absorbed energy in the top 10-20 nm of Ru induces a similar hydrodynamical evolution. With our 2T-HD simulations we show that the thermo-induced pressure waves are generated in the surface region and propagate into the depth of the material. The tensile part of the pressure wave is responsible for the material rapture. The maximum amplitude of the tensile wave reached at the depth of 10-20 nm (where ablation occurs according to the experiment) is similar for all photon

energies and equals to 10-15 GPa. That gives us an estimation of the spall strength of Ru at ultra-high strain rates of 10^{10}s^{-1}.

ACKNOWLEDGEMENTS

I thank Ryszard Sobierajski, Jaromir Chalupsky and Andrew Aquila for the useful discussions and for providing additional information regarding the experiments at SACLA. I thank Ludger Inhester for the help with the XATOM simulations.

REFERENCES

[1] R. Ernstorfer, M. Harb, C. T. Hebeisen, G. Sciaini, T. Dartigalongue, and R. D. Miller, *The formation of warm dense matter: experimental evidence for electronic bond hardening in gold,* Science **323**, 1033 (2009).

[2] E. García Saiz, G. Gregori, D. O. Gericke, J. Vorberger, B. Barbrel, R. J. Clarke, R. R. Freeman, S. H. Glenzer, F. Y. Khattak, M. Koenig, O. L. Landen, D. Neely, P. Neumayer, M. M. Notley, A. Pelka, D. Price, M. Roth, M. Schollmeier, C. Spindloe, R. L. Weber, L. van Woerkom, K. Wünsch, and D. Riley, *Probing warm dense lithium by inelastic X-ray scattering,* Nat. Phys. **4**, 940 (2008).

[3] N. Medvedev and B. Ziaja, *Multistep transition of diamond to warm dense matter state revealed by femtosecond X-ray diffraction,* Sci. Rep. **8**, 5284 (2018).

[4] F. Graziani, M. P. Desjarlais, R. Redmer, and S. B. Trickey, *Frontiers and challenges in warm dense matter*, Vol. 96 (Springer Science & Business, 2014).

[5] B. N. Chichkov, C. Momma, S. Nolte, F. Von Alvensleben, and A. Tünnermann, *Femtosecond, picosecond and nanosecond laser ablation of solids,* Appl. Phys. A **63**, 109 (1996).

[6] X. Liu, D. Du, and G. Mourou, *Laser ablation and micromachining with ultrashort laser pulses,* IEEE J. Quant. Electron. **33**, 1706 (1997).

[7] J. Hermann, M. Benfarah, G. Coustillier, S. Bruneau, E. Axente, J.-F. Guillemoles, M. Sentis, P. Alloncle, and T. Itina, *Selective ablation of thin films with short and ultrashort laser pulses,* Appl. Surf. Sci. **252**, 4814 (2006).

[8] S. I. Ashitkov, N. Inogamov, V. V. Zhakhovskii, Y. N. Emirov, M. B. Agranat, I. Oleinik, S. I. Anisimov, and V. E. Fortov, *Formation of nanocavities in the surface layer of an aluminum target irradiated by a femtosecond laser pulse,* JETP Lett. **95**, 176 (2012).

[9] M. V. Shugaev, C. Wu, O. Armbruster, A. Naghilou, N. Brouwer, D. S. Ivanov, T. J. Derrien, N. M. Bulgakova, W. Kautek, B. Rethfeld, and L. V. Zhigilei, *Fundamentals of ultrafast laser–material interaction,* MRS Bull. **41**, 960 (2016).

[10] M. V. Shugaev, I. Gnilitskyi, N. M. Bulgakova, and L. V. Zhigilei, *Mechanism of single-pulse ablative generation of laser-induced periodic surface structures,* Phys. Rev. B **96**, 205429 (2017).

[11] A. R. Khorsand, R. Sobierajski, E. Louis, S. Bruijn, E. D. van Hattum, R. W. E. van de Kruijs, M. Jurek, D. Klinger, J. B. Pelka, L. Juha, T. Burian, J. Chalupsky, J. Cihelka, V. Hajkova, L. Vysin, U. Jastrow, N. Stojanovic, S. Toleikis, H. Wabnitz, K. Tiedtke, K. Sokolowski-Tinten, U. Shymanovich, J. Krzywinski, S. Hau-Riege, R. London, A. Gleeson, E. M. Gullikson, and F. Bijkerk, *Single shot damage mechanism of Mo/Si multilayer optics under intense pulsed XUV-exposure,* Opt. Express **18**, 700 (2010).

[12] I. A. Makhotkin, R. Sobierajski, J. Chalupský, K. Tiedtke, G. de Vries, M. Störmer, F. Scholze, F. Siewert, R. W. E. van de Kruijs, I. Milov, E. Louis, I. Jacyna, M. Jurek, D. Klinger, L. Nittler, Y. Syryanyy, L. Juha, V. Hájková, V. Vozda, T. Burian, K. Saksl, B. Faatz, B. Keitel, E. Plönjes, S. Schreiber, S. Toleikis, R. Loch, M. Hermann, S. Strobel, H.-K. Nienhuys, G. Gwalt, T. Mey, and H. Enkisch, *Experimental study of EUV mirror radiation damage resistance under long-term free-electron laser exposures below the single-shot damage threshold,* J. Synchrotron Radiat. **25**, 77 (2018).

[13] R. Follath, T. Koyama, V. Lipp, N. Medvedev, K. Tono, H. Ohashi, L. Patthey, M. Yabashi, and B. Ziaja, *X-ray induced damage of B4C-coated bilayer materials under various irradiation conditions,* Sci. Rep. **9**, 2029 (2019).

[14] J. Pelka, R. Sobierajski, D. Klinger, W. Paszkowicz, J. Krzywinski, M. Jurek, D. Zymierska, A. Wawro, A. Petroutchik, L. Juha, V. Hajkova, J. Cihelka, J. Chalupsky, T. Burian, L. Vysin, S. Toleikis, K. Sokolowski-Tinten, N. Stojanovic, U. Zastrau, R. London, S. Hau-Riege, C. Riekel, R. Davies, M. Burghammer, E. Dynowska, W. Szuszkiewicz, W. Caliebe, and R. Nietubyc, *Damage in solids irradiated by a single shot of XUV free-electron laser: Irreversible changes investigated using X-ray microdiffraction, atomic force microscopy and nomarski optical microscopy,* Radiat. Phys. Chem. **78**, S46 (2009).

[15] T. Koyama, H. Yumoto, T. Miura, K. Tono, T. Togashi, Y. Inubushi, T. Katayama, J. Kim, S. Matsuyama, M. Yabashi, K. Yamauchi, and H. Ohashi, *Damage threshold of coating materials on X-ray mirror for X-ray free electron laser,* Rev. Sci. Instrum. **87**, 051801 (2016).

[16] T. Koyama, H. Yumoto, Y. Senba, K. Tono, T. Sato, T. Togashi, Y. Inubushi, T. Katayama, J. Kim, S. Matsuyama, H. Mimura, M. Yabashi, K. Yamauchi, H. Ohashi, and T. Ishikawa, *Investigation of ablation thresholds of optical materials using 1-µm-focusing beam at hard X-ray free electron laser,* Opt. Express **21**, 15382 (2013).

[17] S. Dastjani Farahani, J. Chalupsky, T. Burian, H. Chapman, A. Gleeson, V. Hajkoya, L. Juha, M. Jurek, D. Klinger, H. Sinn, R. Sobierajski, M. Störmer, K. Tiedtke, S. Toleikis, T. Tschentscher, H. Wabnitz, and J. Gaudin, *Damage threshold of amorphous carbon mirror for 177 eV FEL radiation,* Nucl. Instrum. Meth. A **635**, S39 (2011).

[18] J. Krzywinski, D. Cocco, S. Moeller, and D. Ratner, *Damage threshold of platinum coating used for optics for self-seeding of soft X-ray free electron laser,* Opt. Express **23**, 5397 (2015).

[19] I. A. Makhotkin, I. Milov, J. Chalupský, K. Tiedtke, H. Enkisch, G. de Vries, F. Scholze, F. Siewert, J. M. Sturm, K. V. Nikolaev, R. W. E. van de Kruijs, M. A. Smithers, H. A. G. M. van Wolferen, E. G. Keim, E. Louis, I. Jacyna, M. Jurek, D. Klinger, J. B. Pelka, L. Juha, V. Hájková, V. Vozda, T. Burian, K. Saksl, B. Faatz, B. Keitel, E. Plönjes, S. Schreiber, S. Toleikis, R. Loch, M. Hermann, S. Strobel, R. Donker, T. Mey, and R. Sobierajski, *Damage accumulation in thin ruthenium films induced by repetitive exposure to femtosecond XUV pulses below the single-shot ablation threshold,* J. Opt. Soc. Am. B **35**, 2799 (2018).

[20] U. Zastrau, T. Burian, J. Chalupsky, T. Döppner, T. Dzelzainis, R. Fäustlin, C. Fortmann, E. Galtier, S. Glenzer, G. Gregori, L. Juha, H. Lee, R. Lee, C. Lewis, N. Medvedev, B. Nagler, A. Nelson, D. Riley, F. Rosmej, S. Toleikis, T. Tschentscher, I. Uschmann, S. Vinko, J. Wark, T. Whitcher, and E. Förster, *XUV spectroscopic characterization of warm dense aluminum plasmas generated by the free-electron-laser FLASH,* Laser Part. Beams **30**, 45 (2012).

[21] A. Aquila, R. Sobierajski, C. Ozkan, V. Hájková, T. Burian, J. Chalupský, L. Juha, M. Störmer, S. Bajt, M. T. Klepka, P. Dłużewski, K. Morawiec, H. Ohashi, T. Koyama, K. Tono, Y. Inubushi, M. Yabashi, H. Sinn, T. Tschentscher, A. P. Mancuso, and J. Gaudin, *Fluence thresholds for grazing incidence hard X-ray mirrors,* Appl. Phys. Lett. **106**, 241905 (2015).

[22] O. Peyrusse, J.-M. André, P. Jonnard, and J. Gaudin, *Modeling of the interaction of an X-ray free-electron laser with large finite samples,* Phys. Rev. E **96**, 043205 (2017).

[23] I. Milov, I. A. Makhotkin, R. Sobierajski, N. Medvedev, V. Lipp, J. Chalupský, J. M. Sturm, K. Tiedtke, G. de Vries, M. Störmer, F. Siewert, R. van de Kruijs, E. Louis, I. Jacyna, M. Jurek, L. Juha, V. Hájková, V. Vozda, T. Burian, K. Saksl, B. Faatz, B. Keitel, E. Plönjes, S. Schreiber, S. Toleikis, R. Loch, M. Hermann, S. Strobel, H.-K. Nienhuys, G. Gwalt, T. Mey, H. Enkisch, and F. Bijkerk, *Mechanism of single-shot damage of Ru thin films irradiated by femtosecond extreme UV free-electron laser,* Opt. Express **26**, 19665 (2018).

[24] A. Aquila, R. Sobierajski, C. Ozkan, V. Hájková, T. Burian, J. Chalupský, L. Juha, M. Störmer, S. Bajt, M. T. Klepka, P. Dłużewski, K. Morawiec, H. Ohashi, T. Koyama, K. Tono, Y. Inubushi, M. Yabashi, H. Sinn, T. Tschentscher, A. P. Mancuso, and J. Gaudin, *Erratum: "Fluence thresholds for grazing incidence hard X-ray mirrors" [appl. phys. lett. 106, 241905 (2015)],* Appl. Phys. Lett. **115**, 059901 (2019).

[25] D. S. Ivanov and L. V. Zhigilei, *Combined atomistic-continuum modeling of short-pulse laser melting and disintegration of metal films,* Phys. Rev. B **68**, 064114 (2003).

[26] B. J. Demaske, V. V. Zhakhovsky, N. A. Inogamov, and I. I. Oleynik, *Ablation and spallation of gold films irradiated by ultrashort laser pulses,* Phys. Rev. B **82**, 064113 (2010).

[27] S. Anisimov, N. Inogamov, Y. V. Petrov, V. Khokhlov, V. Zhakhovskii, K. Nishihara, M. Agranat, S. Ashitkov, and P. Komarov, *Interaction of short laser pulses with metals at moderate intensities,* Appl. Phys. A **92**, 939 (2008).

[28] V. Lipp, N. Medvedev, and B. Ziaja, *Classical Monte-Carlo simulations of X-ray induced electron cascades in various materials,* Proc. SPIE, Damage to VUV, EUV, and X-ray Optics VI **10236**, 102360H (2017).

[29] Y. Petrov, K. Migdal, N. Inogamov, V. Khokhlov, D. Ilnitsky, I. Milov, N. Medvedev, V. Lipp, and V. Zhakhovsky, *Ruthenium under ultrafast laser excitation: Model and dataset for equation of state, conductivity, and electron-ion coupling,* Data Brief **28**, 104980 (2020).

[30] S. Nolte, C. Momma, H. Jacobs, A. Tünnermann, B. N. Chichkov, B. Wellegehausen, and H. Welling, *Ablation of metals by ultrashort laser pulses,* J. Opt. Soc. Am. B **14**, 2716 (1997).

[31] K. Sokolowski-Tinten, J. Bialkowski, A. Cavalleri, D. von der Linde, A. Oparin, J. Meyer-ter Vehn, and S. I. Anisimov, *Transient States of Matter during Short Pulse Laser Ablation,* Phys. Rev. Lett. **81**, 224 (1998).

[32] V. Zhakhovskii, N. Inogamov, Y. Petrov, S. Ashitkov, and K. Nishihara, *Molecular dynamics simulation of femtosecond ablation and spallation with different interatomic potentials,* Appl. Surf. Sci. **255**, 9592 (2009).

[33] L. V. Zhigilei, Z. Lin, and D. S. Ivanov, *Atomistic Modeling of Short Pulse Laser Ablation of Metals: Connections between Melting, Spallation, and Phase Explosion,* J. Phys. Chem. C **113**, 11892 (2009).

[34] W. Ackermann *et al.*, *Operation of a free-electron laser from the extreme ultraviolet to the water window,* Nat. Photonics **1**, 336 (2007).

[35] D. Pile, *X-rays: First light from Sacla,* Nat. Photonics **5**, 456 (2011).

[36] J. M. Liu, *Simple technique for measurements of pulsed Gaussian-beam spot sizes,* Opt. Lett. **7**, 196 (1982).

[37] J. Chalupský, J. Krzywinski, L. Juha, V. Hájková, J. Cihelka, T. Burian, L. Vyšín, J. Gaudin, A. Gleeson, M. Jurek, A. R. Khorsand, D. Klinger, H. Wabnitz, R. Sobierajski, M. Störmer, K. Tiedtke, and S. Toleikis, *Spot size characterization of focused non-Gaussian X-ray laser beams,* Opt. Express **18**, 27836 (2010).

[38] J. Chalupský, T. Burian, V. Hájková, L. Juha, T. Polcar, J. Gaudin, M. Nagasono, R. Sobierajski, M. Yabashi, and J. Krzywinski, *Fluence scan: an unexplored property of a laser beam,* Opt. Express **21**, 26363 (2013).

[39] M. Wen, I. V. Kozhevnikov, F. Siewert, A. V. Buzmakov, C. Xie, Q. Huang, Z. Wang, L. Samoylova, and H. Sinn, *Effect of the surface roughness on X-ray absorption by mirrors operating at extremely small grazing angles,* Opt. Express **26**, 21003 (2018).

[40] B. Ziaja, R. A. London, and J. Hajdu, *Unified model of secondary electron cascades in diamond,* J. Appl. Phys. **97**, 064905 (2005).

[41] K. Mecseki, H. Höppner, M. Büscher, V. Tkachenko, N. Medvedev, J. J. Bekx, V. Lipp, P. Piekarz, M. Windeler, J. W. G. Tisch, D. J. Walke, M. Nakatsutsumi, M. J. Prandolini, J. M. Glownia, T. Sato, M. Sikorski, M. Chollet, U. Teubner, J. Robinson, S. Toleikis, B. Ziaja, and F. Tavella, *Hard X-ray induced fast secondary electron cascading processes in solids,* Appl. Phys. Lett. **113**, 114102 (2018).

[42] D. Cullen, *A Survey of Atomic Binding Energies for use in EPICS2017*, Tech. Rep. (Vienna, 2018).

[43] Y.-K. Kim and M. E. Rudd, *Binary-encounter-dipole model for electron-impact ionization,* Phys. Rev. A **50**, 3954 (1994).

[44] T. M. Jenkins, W. R. Nelson, and A. Rindi, *Monte Carlo transport of electrons and photons*, Vol. 38 (Springer Science & Business Media, 2012).

[45] I. Milov, V. Lipp, N. Medvedev, I. A. Makhotkin, E. Louis, and F. Bijkerk, *Modeling of XUV-induced damage in Ru films: the role of model parameters,* J. Opt. Soc. Am. B **35**, B43 (2018).

[46] S. Anisimov, B. Kapeliovich, and T. Perelman, *Electron emission from metal surfaces exposed to ultrashort laser pulses,* Zh. Eksp. Teor. Fiz **66**, 776 (1974).

[47] Y. V. Petrov, N. A. Inogamov, and K. P. Migdal, *Thermal conductivity and the electron-ion heat transfer coefficient in condensed media with a strongly excited electron subsystem,* JETP Lett. **97**, 20 (2013).

[48] N. A. Inogamov, Y. V. Petrov, V. V. Zhakhovsky, V. A. Khokhlov, B. J. Demaske, S. I. Ashitkov, K. V. Khishchenko, K. P. Migdal, M. B. Agranat, S. I. .Anisimov, and V. E. Fortov, *Two-temperature thermodynamic and kinetic proporties of transition metals irradiated by femtosecond lasers,* AIP Conf. Proc. **1464**, 593 (2012).

[49] B. Rethfeld, D. S. Ivanov, M. E. Garcia, and S. I. Anisimov, *Modelling ultrafast laser ablation,* J. Phys. D **50**, 193001 (2017).

[50] Y. B. Zel'dovich and Y. P. Raizer, *Physics of shock waves and high-temperature hydrodynamic phenomena*, edited by N. Academic Press (NY: Academic Press, 1967).

[51] M. L. Wilkins, *Computer simulation of dynamic phenomena* (Springer Science & Business Media, 2013).

[52] H. B. Michaelson, *The work function of the elements and its periodicity,* J. Appl. Phys. **48**, 4729 (1977).

[53] N. Medvedev, *Femtosecond X-ray induced electron kinetics in dielectrics: application for FEL-pulse-duration monitor,* Appl. Phys. B **118**, 417 (2015).

[54] S. Ashitkov, V. Zhakhovsky, N. Inogamov, P. Komarov, M. Agranat, and G. Kanel, *The behavior of iron under ultrafast shock loading driven by a femtosecond laser,* in *AIP Conf. Proc.*, Vol. 1793 (AIP Publishing, 2017) p. 100035.

[55] J. H. Rose, J. R. Smith, F. Guinea, and J. Ferrante, *Universal features of the equation of state of metals,* Phys. Rev. B **29**, 2963 (1984).

[56] E. Cordfunke and R. Konings, *The high temperature thermophysical properties of ruthenium and palladium,* Thermochim. Acta **139**, 99 (1989).

[57] N. Medvedev, Z. Li, and B. Ziaja, *Thermal and nonthermal melting of silicon under femtosecond X-ray irradiation,* Phys. Rev. B **91**, 054113 (2015).

[58] N. Medvedev, V. Tkachenko, V. Lipp, Z. Li, and B. Ziaja, *Various damage mechanisms in carbon and silicon materials under femtosecond X-ray irradiation,* 4open **1**, 3 (2018).

[59] A. E. Morris, H. A. Fine, and G. Geiger, *Handbook on Material and Energy Balance Calculations in Material Processing* (John Wiley Sons, 2011).

[60] G. Kanel, S. Razorenov, A. Bogatch, A. Utkin, V. Fortov, and D. Grady, *Spall fracture properties of aluminum and magnesium at high temperatures,* J. Appl. Phys. **79**, 8310 (1996).

[61] T. De Rességuier, L. Signor, A. Dragon, P. Severin, and M. Boustie, *Spallation in laser shock-loaded tin below and just above melting on release,* J. Appl. Phys. **102**, 073535 (2007).

[62] M. B. Agranat, S. I. Anisimov, S. I. Ashitkov, V. V. Zhakhovskii, N. Inogamov, P. S. Komarov, A. V. Ovchinnikov, V. E. Fortov, V. A. Khokhlov, and V. V. Shepelev, *Strength properties of an aluminum melt at extremely high tension rates under the action of femtosecond laser pulses,* JETP Lett. **91**, 471 (2010).

[63] Y. Cai, H. Wu, and S. Luo, *Spall strength of liquid copper and accuracy of the acoustic method,* J. Appl. Phys. **121**, 105901 (2017).

[64] S.-K. Son, L. Young, R. Santra, *et al.*, *Impact of hollow-atom formation on coherent X-ray scattering at high intensity,* Phys. Rev. A **83**, 033402 (2011).

[65] S.-K. Son and R. Santra, *Monte Carlo calculation of ion, electron, and photon spectra of xenon atoms in X-ray free-electron laser pulses,* Phys. Rev. A **85**, 063415 (2012).

[66] K. Toyota, S.-K. Son, and R. Santra, *Interplay between relativistic energy corrections and resonant excitations in X-ray multiphoton ionization dynamics of Xe atoms,* Phys. Rev. A **95**, 043412 (2017).

[67] B. Ziaja, D. van der Spoel, A. Szöke, and J. Hajdu, *Auger-electron cascades in diamond and amorphous carbon,* Phys. Rev. B **64**, 214104 (2001).

[68] T. Tachibana, Z. Jurek, H. Fukuzawa, K. Motomura, K. Nagaya, S. Wada, P. Johnsson, M. Siano, S. Mondal, Y. Ito, M. Kimura, T. Sakai, K. Matsunami, H. Hayashita, J. Kajikawa, X.-J. Liu, E. Robert, C. Miron, R. Feifel, J. P. Marangos, K. Tono, Y. Inubushi, M. Yabashi, S.-K. Son, B. Ziaja, M. Yao, R. Santra, and K. Ueda, *Nanoplasma formation by high intensity hard X-rays,* Sci. Rep. **5**, 10977 (2015).

[69] N. A. Inogamov, V. V. Zhakhovsky, S. I. Ashitkov, V. A. Khokhlov, V. V. Shepelev, P. S. Komarov, A. V. Ovchinnikov, D. S. Sitnikov, Y. V. Petrov, M. B. Agranat, S. I. Anisimov, and V. E. Fortov, *Laser acoustic probing of two-temperature zone created by femtosecond pulse,* Contrib. Plasm. Phys. **51**, 367 (2011).

[70] V. Zhakhovskii, K. Nishihara, Y. Fukuda, S. Shimojo, T. Akiyama, S. Miyanaga, H. Sone, H. Kobayashi, E. Ito, Y. Seo, M. Tamura, and Y. Ueshima, *A new dynamical domain decomposition method for parallel molecular dynamics simulation,* in *IEEE International Symposium on Cluster Computing and the Grid*, Vol. 2 (2005) pp. 848–854.

[71] V. Zhakhovsky, K. Migdal, N. Inogamov, and S. Anisimov, *MD simulation of steady shock-wave fronts with phase transition in single-crystal iron,* in *AIP Conf. Proc.*, Vol. 1793 (AIP Publishing, 2017) p. 070003.

[72] I. Milov, V. Zhakhovsky, D. Ilnitsky, K. Migdal, V. Khokhlov, Y. Petrov, N. Inogamov, V. Lipp, N. Medvedev, B. Ziaja, V. Medvedev, I. Makhotkin, E. Louis, and F. Bijkerk, *Two-level ablation and damage morphology of Ru films under femtosecond extreme UV irradiation,* Appl. Surf. Sci. , 146952 (2020).

5

TWO-LEVEL ABLATION AND DAMAGE MORPHOLOGY OF RU FILMS UNDER FEMTOSECOND EXTREME UV IRRADIATION

The dynamics of a thin ruthenium film irradiated by femtosecond extreme UV laser pulses is studied with a hybrid computational approach, which includes Monte Carlo, two-temperature hydrodynamics and molecular dynamics models. This approach is capable of accurate simulations of all stages of material evolution induced by extreme UV or X-ray photons: from nonequilibrium electron kinetics till complete lattice relaxation. We found that fast energy deposition in a subsurface layer leads to a two-level ablation: the top thin layer is ablated as a gas-liquid mixture due to expansion of overheated material at near and above critical conditions, whereas a thicker liquid layer below is ablated via a cavitation process. The latter occurs due to a thermo-mechanically induced tensile pressure wave. The liquid ablating layer exhibits unstable behaviour and disintegrates into droplets soon after detachment from the rest of the target. Our simulations reveal basic processes leading to formation of specific surface morphologies outside and inside the damage craters. The calculated ablation threshold, crater depth and morphological features are in quantitative agreement with the experimental data, which justifies the applicability of our hybrid model to study laser-induced material damage.

5.1. INTRODUCTION

The rapid development of free electron lasers (FELs) leads to a continuous increase of the pulse intensity at such facilities. Recent reports claim the achievement of submicron focusing of the light down to a 50 nm spot size, which will result in an on-target peak intensity above 10^{20} W/cm^2 [1, 2]. Such an extreme intensity can transfer irradiated materials into highly excited non-equilibrium states that are still not fully understood [3]. Apart from the target itself, the optical elements at the FEL facilities can be illuminated with high radiation doses as well, which can lead to irreversible changes and degrade their performance. Numerous experimental studies of damage of the materials relevant to the extreme ultraviolet (XUV) and X-ray optics were performed to determine failure conditions of the optical elements [4–14].

One of the common damage mechanisms occurring after irradiating matter with ultrashort pulses of moderate to high intensity is laser ablation [15]. Apart from the fundamental interest in the context of warm dense matter studies [3, 16–18], the phenomenon of laser ablation has been widely utilized in many applications such as pulsed laser deposition [19], laser-induced breakdown spectroscopy [20], laser propulsion [21], laser printing [22], surface micromachining [23] and nanoparticles production [24]. The latter includes applications in plasmonics [25], catalysis [26] and biomedicine [27].

Different applications of laser ablation require a different final outcome of the ablation process, for example, different size, shape and structure of the produced nanoparticles, or different morphology of the surface nanostructures. Such a sensitive control of the ablation process can only be achieved if all physical mechanisms involved in the interaction of high intensity ultrashort laser pulses with matter are quantitatively understood. For that, the dedicated experimental studies should be supplemented with reliable computational models.

The complex nature of light-matter interaction involves various physical processes occurring on a broad temporal scale. In order to describe the full timescale of material evolution under laser irradiation, from the initial excitation to the final material removal during the ablation process and relaxation of the irradiated target, one typically has to apply hybrid computational schemes. Hybrid simulation techniques combine several models into a unified approach to efficiently describe various sub-problems within the complex problem studied. They include, for example, multiscale techniques [28, 29], and similar approaches [30].

Combinations of two-temperature-based models (TTM [31–33] or two-temperature hydrodynamics [34]) with the molecular dynamics (MD) method are commonly used to describe ultrafast laser ablation of metals [35–38]. For semiconductors, a modification of the classical two-temperature model has been applied to take into account the non-constant density of conduction band electrons and valence band holes [39, 40]. The combination of such a density dependent TTM with the MD was used to study the interaction of femtosecond laser pulses with Si targets [41, 42]. Another approach which combines a Monte Carlo (MC) method with MD was applied to simulate melting, ablation, and solidification in Si induced by laser pulses with different duration [43].

Hybrid schemes that include two-temperature-based parts usually consider the electronic system to always be in a thermodynamic equilibrium, so that it can be described with an electronic temperature. In case of metals, such an approximation is typically valid if the photon energy is low (infrared and optical range), so that only the con-

duction band electrons are excited, and their thermalization is fast (on the femtosecond timescale). However, it was experimentally shown [44, 45] and theoretically verified [46, 47] that the electron gas in a metal excited with an optical or infrared femtosecond lasers can stay out of equilibrium for a few hundred fs up to the picosecond timescale. Such behaviour of the excited electronic system can limit the applicability of the two-temperature-based models to timescales above ~ 1 ps only. In order to overcome this limitation, a full Boltzmann collision integral approach can be used to investigate a transient evolution of a non-equilibrium electron distribution function [48], which demonstrates that, generally, equilibration within the electronic system of a metal occurs faster when increasing the fluence of a femtosecond optical pulse.

Absorption of higher energy XUV or X-ray photons (~ 10 eV and higher) results in a non-equilibrium electron kinetics that cannot be neglected. The X-ray induced electron cascades in matter can be efficiently simulated with Monte-Carlo-based (MC) models [49–51].

To have a more complete understanding of how X-ray irradiated materials evolve, including both electronic and atomic systems, one may use hybrid approaches. For instance, in the work [52] the authors used the X-RIM code to model the X-ray FEL (XFEL) interaction with ruthenium and silicon at the damage threshold intensity. The code links the calculations of the radiation field in the material with the hydrodynamics (HD) simulations. One should note that the HD part of the model limits it to the elastoplastic regime only. As another example, a hybrid approach XTANT (X-ray-induced Thermal And Non-thermal Transition) [30] simulates material evolution taking into account non-equilibrium electron distribution, non-adiabatic electron-ion energy exchange, transient electron band structure, atomic potential energy surface evolution, and atomic motion, within one interconnected model. The complexity of parallel calculations of various physical processes restricts the model to a timescale up to ~ 100 ps and system size up to ~ 1000 atoms.

In our previous work [53], focused on the effect of different energy of the incident photons on the early stage of ruthenium (Ru) target evolution, we reported on our combined MC-HD approach. This approach was capable of reliable simulations of material evolution only during the early picosecond stage after irradiation, but was not able to simulate significant lattice modifications on a longer timescale. A combination of HD with MD was also developed previously (see Ref. [34] for example), but it did not take into account nonequilibrium electron kinetics, hence was not applicable in case of photon energies sufficiently high to induce electron cascades.

In this work, to overcome these limitations and to cover all stages of material response to irradiation, we combine the mentioned approaches together. Thus, a new hybrid model with a significantly extended applicability is implemented, which is a combination of Monte Carlo, hydrodynamics and molecular dynamics. This model simulates the material evolution from photoabsorption (~ 100 fs) to complete relaxation and formation of the final damage morphologies (~ 1-10 ns). The in-house parallel MD code with the highly adaptive load balancing algorithm [54, 55] allows to consider large systems with a highly nonuniform mass distribution and a number of atoms above 10^8.

The model is applicable in a wide range of photon energies from XUV to hard X-rays. An extension down to optical or NIR photon energies is possible with a replacement of the MC module with a TTM-based approach if applicable, or with a Boltzmann kinetic

equation in a general case. The applicability of the MC-HD part of the model in the case of 800 nm laser light was demonstrated in [53]. Any metal can be considered if the required parameters that describe the physical properties of a metal in the one- and two-temperature states are known.

We apply our model to study the dynamics of a Ru thin film under femtosecond extreme UV laser irradiation in the intensity regime below and above the ablation threshold. Ru is chosen as a material that can be used as a grazing incidence mirror in the XUV and hard X-ray regimes [8, 9, 11]. We focus on the atomistic picture of material evolution, because it provides us with the detailed understanding of physical processes responsible for material damage, and gives us access to the direct comparison of simulation results with the experiment. The specific irradiation conditions that we use to verify our model are dictated by the single-shot damage experiment performed at the femtosecond XUV free-electron laser in Hamburg (FLASH [56]) that was reported in Refs. [11, 57].

The parameterization of the model to be applied for a particular material (Ru in our case) is based on reproducing the known mechanical and thermophysical properties of the material, as will be discussed below in detail. No knowledge of the results of the light-matter interaction experiments is required as input data. Therefore, our model can be used not only to describe the existing experiments, but also to predict the results of the future ones.

5.2. HYBRID COMPUTATIONAL MODEL

The femtosecond duration of the laser pulses allows one to separate the physical processes involved in the light-metal interaction in time [58]. Three characteristic stages can be identified. (i) Absorption of light and the following non-equilibrium electron kinetics. During that stage, if the photon energy is sufficiently high, photo- and secondary electrons created upon photoabsorption propagate in a metal and create electron cascades [50]. The cascading process depends on the photon energy and material properties and continues until all excited electrons become slow and can be considered as thermalized in the conduction band [53]. At the end of this stage electrons are at high temperature, while ions are still cold. (ii) Two-temperature (2T) state of the irradiated metal. At this stage the target can be represented as consisting of electronic and ionic subsystems, both in local thermal equilibrium, with the corresponding individual temperatures T_e and T_i. The 2T stage lasts as long as T_e is considerably different from T_i. During that stage, the absorbed laser energy, stored in the thermalized electrons, diffuses into the depth of the material, while simultaneously interacting with the ionic subsystem, which results in heating of the latter. If the characteristic heating time is faster than the time required for a material to mechanically react to it by expanding, the heating is effectively isochoric. This situation is usually referred to as stress confinement regime [36, 59]. As a result, thermo-induced stresses are generated. (iii) The 2T stage proceeds into the one-temperature (1T) stage after thermal equilibrium between electrons and ions is reached ($T_e \approx T_i$). The evolution of the material, started in the 2T stage, continues. If the laser fluence is sufficiently high, such evolution typically includes melting, cavitation, ablation and recrystallization processes. Electrostatic processes such as Coulomb explosion are unlikely to occur in metals at moderate fluences [60] and therefore are not considered in this work.

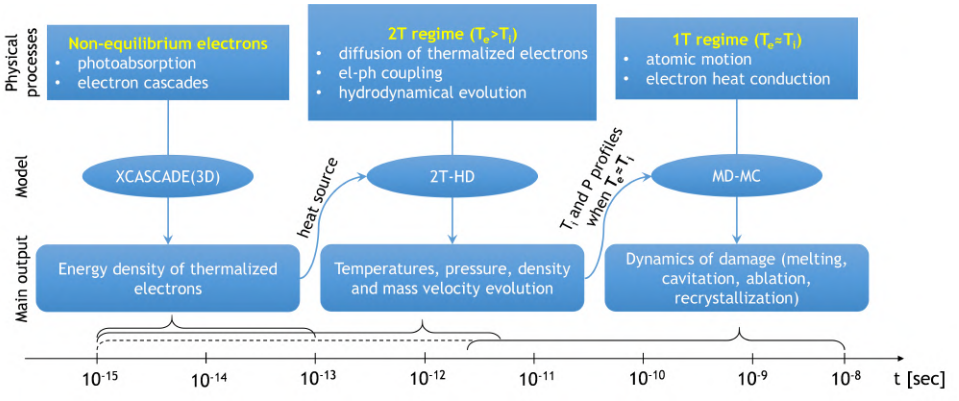

Figure 5.1: Basic processes and corresponding simulation techniques used in our hybrid model.

Developing a model to describe laser pulse interaction with a metal, we exploit the time separation of the whole process into three distinct stages, determined by fast electron response to an ultrashort laser pulse irradiation, then by electron diffusion and electron-ion energy exchange, and finally by slow evolution of the ionic system, respectively. We use three different models, one for each stage, and combine them into one hybrid approach. Due to the femtosecond duration of the laser pulse, it is possible to model the physical processes at each stage sequentially [58]. The model scheme is presented in Fig. 5.1 and will be described below in more detail.

5.2.1. XCASCADE(3D)

The photoabsorption and the following non-equilibrium electron kinetics are modeled with the asymptotic trajectory classical MC code XCASCADE(3D) [51]. The target is represented as a homogeneous arrangement of atoms with a density corresponding to the chosen material. The photoabsorption cross sections, electron scattering cross sections and the ionization potentials of the target, taken from the EPICS2017 databases [61], are described in the atomic approximation.

The MC code accounts for the following processes: photoabsorption by valence and core-shell electrons, Auger recombination of created deep holes with release of Auger electrons, propagation of photo- and secondary electrons, and both inelastic (impact ionization) and elastic scattering of electrons on neutral atoms. All photo- as well as secondary electrons are traced until their energy falls below a predefined cutoff energy. Electrons with energies below this cutoff, as well as holes created in the valence atomic levels, are considered as thermalized electrons in the conduction band of the metal. The spatio-temporal energy density of these thermalized electrons forms a heat source for the two-temperature hydrodynamics (2T-HD) code [53].

As it was shown in previous studies, an electronic system of a solid under femtosecond XFEL irradiation follows the so called “bump-on-hot-tail” distribution [62, 63]: the majority of low-energy electrons is almost in thermal equilibrium, with the minority of the highly excited electrons forming the high-energy out-of-equilibrium tail of the distribution. In our approach, the nonequilibrium cascading of high-energy electrons

is modeled with the XCASCADE(3D) code, whereas the low-energy (thermalized) electrons are treated with the 2T-HD code. A possible deviation of the low-energy electrons from the Fermi-Dirac distribution is not taken into account. This would require dedicated simulations with, e.g., the Boltzmann equation [48]. It is expected that within the bump-on-hot-tail distribution, such deviations are small [63].

The applicability of the XCASCADE(3D) code is limited to the fluence regime when the density of cascading electrons is considerably lower than the atomic density. In that case, the electron-atom scattering is dominant, while scattering among excited electrons can be neglected. We checked that this condition was fulfilled for all the fluences considered in this work: the electron density does not exceed 1% of the atomic density. There are no plasma effects at the level of excitation considered here. All electron cascades evolve in solid state Ru, and they finish long before any phase transition occurs.

An *a posteriori* analysis of our results suggests that during the cascading time, the irradiated material properties used in the XCASCADE(3D) simulations do not significantly change. That justifies a coupling between XCASCADE(3D) and 2T-HD within a scheme without feedback, when the output data from the MC simulations are passed one-way into the 2T-HD model as the input (source term), see Fig. 5.1. Therefore, the XCASCADE(3D) code can be applied to model the cascading processes in the irradiated target even at high fluences at which structural damage is expected on a later timescale, if the cascading time is sufficiently short.

5.2.2. TWO-TEMPERATURE HYDRODYNAMICS AND EQUATION OF STATE

The hydrodynamic behaviour of the material in the 2T stage is modeled with our Lagrangian 2T-HD code [34, 53]. The code simulates the evolution of material properties, namely density, pressure, mass velocity, and electron and ion temperatures, induced by the heat source obtained with the XCASCADE(3D) calculations.

The 2T equations of state that govern the thermodynamics of Ru, together with the 2T thermal conductivity and the electron-phonon coupling factor, are taken from our previous work [64], where these properties were obtained from *ab initio* calculations. The equations of state are currently obtained only for the solid phase of Ru, which means that melting and evaporation are not taken into account in the 2T stage. These processes are naturally described with the MD code, although we cannot guarantee completely reliable simulation of them during the 2T stage. However, this stage in Ru lasts for a relatively short time (2-3 ps), ending before significant melting and material ejection occur, so the possible inaccuracy in the description of the 2T stage is insignificant. More details on that are described in Section 5.3.2.

We include electron pressure P_e into the 2T-HD code. The total pressure $P = P_i + P_e$ is responsible for material movement. At the border with vacuum, according to our boundary conditions the total pressure is always zero, so $P_e = -P_i$ at the Ru-vacuum interface. This means that the outermost Lagrangian particle (LP) at any moment of time has to adjust so that this boundary conditions is fulfilled. Typically, the outermost LP stretches significantly into vacuum to guarantee zero total pressure at the boundary. Such a boundary condition is realistic at moderate fluences, when the formation of dense plasma and vapour can be neglected during the time when the electron pressure is strong.

We carry out the 2T-HD calculations until the end of the 2T stage when the ther-

mal equilibrium between the electronic and ionic systems is reached: $T_e \approx T_i$ within the entire Ru thickness. The total pressure and the ion temperature depth profiles at the end of the 2T-HD simulation are stored. After that, we run the MD code starting again from the absorption of a laser pulse. The initial conditions of the MD code and the parameters simulating Monte Carlo pseudo-electrons (MD-MC approach [54]) are adjusted to reproduce the stored hydrodynamic profiles at the end of the 2T stage. With such a scheme, we guarantee that with the MD simulations we arrive at the correct state of excited material predicted with the 2T-HD. Synchronized with the 2T-HD after the electron-ion equilibration is reached, the MD-MC code continues alone and describes further material evolution until complete relaxation. The details of this scheme applied to Ru are described in Section 5.3.2 and Appendix 5.7.

The subsequent material evolution in the 1T regime is modeled with our classical MD code that simulates atomic motion, while the electronic heat conductivity is taken into account within the Monte Carlo formalism (MD-MC approach) [54].

5.2.3. MOLECULAR DYNAMICS COMBINED WITH MC ELECTRONS

Material evolution in the 1T state is modeled with the classical MD method [54, 55]. Classical MD by default takes into account only the atomic system, whereas free electrons are not considered. Electron heat conductivity plays a very important role in the context of laser damage of metals, and thus has to be included into the model. Combination of continuous TTM with MD is one of the ways to do that [35]. In our work we use a different approach to include electron heat conductivity into the classical MD scheme, namely the MC method described in detail in Ref. [65].

Instead of real quantum electrons we introduce classical pseudo-particles with a mass (not related to the effective electron mass in the material) that can "hop" between moving neighbouring atoms, whose motion is simulated with the MD method. For simplicity, we will refer to these particles as "pseudo-electrons", although they are not real electrons and are introduced solely as a method to solve heat transfer in a complex 3D geometry of the evolving target. Each host atom has one MC pseudo-electron, which has its own momentum, but its position is always allocated on its host atom. It guarantees the charge neutrality in the combined electron-atom system at any conditions, simplifying the simulations. A randomly chosen pair of pseudo-electrons allocated at neighbouring atoms swaps over their hosts with a certain rate, which is a free MC parameter that has to be defined in order to reproduce the experimental thermal conductivity. Such swapping of pseudo-electron momenta results in a diffusion of thermal energy on a mobile atomic network, which can reproduce heat conduction in a moving material having a complex geometry with voids. After each hop, a pseudo-electron exchanges energy with its new host atom via a collision, enabling electron-atom energy coupling.

Our MC model is parameterized with two fitting parameters: the mass of pseudo-electrons and the exchange rate. The latter is used for both swapping and electron-ion collision rates. The details of the parametrization procedure are described in Appendix 5.7.

To reliably simulate the atomic motion, one has to use the MD interatomic potential most suitable for the problem under investigation. In the context of light-matter interaction at high intensities, the interatomic potential must properly reproduce the material properties at extreme conditions, namely at high temperatures and under strong pres-

sures. For that purpose, we developed the Ru interatomic potential in the framework of the embedded atom model (EAM) using the stress-matching method [66, 67]. The procedure is described in Appendix 5.8, and the interatomic potential itself is available in the Supplementary Material of Ref. [68].

Post-mortem analysis of the experimental ablation craters in the Ru/Si target showed that the damage is confined to the Ru layer, with no visible damage to the Si substrate at the studied fluences [57]. To avoid unnecessary difficulties when using separate interatomic potentials for Si atoms and for Ru-Si interaction at the interface, we model the Si substrate with a layer composed of Ru pseudo-atoms, which are arranged in the same crystal structure as the original Ru film. The mass of the Ru pseudo-atoms is modified to reproduce the acoustic impedance of the Si substrate. This technique provides a correct description of the pressure wave reflection from the Ru-substrate interface (the mechanical properties of Si are reproduced), although the thermal properties of our model Si, which we will refer to as a "substrate", should be adjusted separately. A similar approach was successfully used to model the Ni-on-glass system [69]. The correct thermal conductivity in the substrate is achieved by adjusting the MC pseudo-electron exchange rate parameter in the MD box region that corresponds to the substrate.

The effect of thermal boundary resistance of the Ru-substrate interface was tested by changing the probability of MC pseudo-electrons exchange through the interface. We found no significant effect of the heat transfer through the interface on the dynamics of material evolution.

The MD-MC calculations are performed for a system of 50 nm thick hexagonal close-packed (*hcp*) Ru on a substrate, composed of Ru pseudo-atoms. The periodic boundary conditions are applied in two lateral directions (x and y). The in-depth size L_z of the MD simulation box is taken to be 150 nm (50 nm Ru and 100 nm substrate). Non-reflecting boundary conditions at the bottom of the substrate are applied, which means that the pressure wave that arrives at the bottom of the simulation box is completely absorbed by the boundary to mimic bulk material.

The following additional procedure is introduced in order to accurately simulate the thermal conductivity in the finite size substrate. First, we perform a calculation with a simulation box of small lateral sizes L_x and L_y and large in-depth size L_z: $8\times8\times650\,\mathrm{nm}^3$. The periodic boundary conditions are applied in x and y lateral directions. The velocity $u(t)$ and temperature $T(t)$ history of a Lagrangian particle (LP) in the layer $150-152$ nm is recorded. After that, we perform a new calculation with an $8\times8\times150\,\mathrm{nm}^3$ box, where the LP history from the previous step is used for the bottom boundary. We check that the temperature and pressure depth profiles in the top 150 nm are the same in these two calculations. Finally, a calculation with desired L_x and L_y and with $L_z = 150$ nm is performed using the LP time history. With such an approach we ensure that we can mimic a thick Si substrate. Not only the pressure wave is absorbed at the bottom of the simulation box, but also the thermal conductivity in a large system ($L_z = 650$ nm) is properly reproduced using a smaller system ($L_z = 150$ nm).

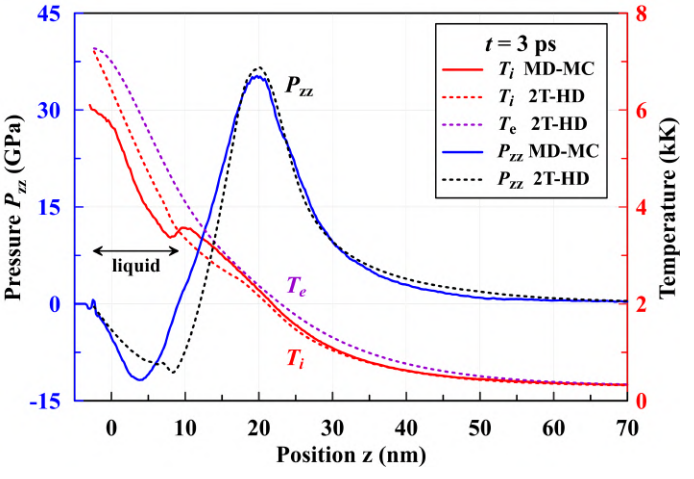

Figure 5.2: Comparison of temperature and pressure profiles calculated with the 2T-HD and the MD-MC methods, which illustrates the procedure of linking these two methods in our hybrid scheme. The absorbed fluence is $F_{\text{abs}} = 40\,\text{mJ/cm}^2$.

5.3. SIMULATION RESULTS

5.3.1. NON-EQUILIBRIUM ELECTRON KINETICS

We performed simulations of XUV (92 eV or 13.5 nm), 100 fs FWHM laser pulses interaction with the Ru-on-substrate target using our hybrid model. We considered grazing incidence of the XUV pulses (20° with respect to the surface), since this condition was used in the experiment [57] that we aim to compare our results with, see Section 5.4. The corresponding photon penetration depth is 3.5 nm, and the surface reflectivity is 68%.

First, the photoabsorption and the electron cascades kinetics are simulated with the XCASCADE(3D) code. In previous papers [53, 57, 70] we studied the spatio-temporal characteristics of electrons in XUV-irradiated Ru at the ablation threshold fluence. In particular, it was shown, that the cascading process in Ru induced by 92 eV photons was extremely fast (< 1 fs) and the cascading electrons on average travel a very short distance of about 1 – 2 nm before the thermalization, see Figs. 5 and 6 in Ref. [57]. The amount of energy that escapes from the surface via photo- and secondary electrons was calculated to be ~ 9%. Therefore, the cascading process in the 92 eV case is not significant, although for higher photon energies the non-equilibrium electrons can play a crucial role in the damage processes [53].

5.3.2. TWO-TEMPERATURE HYDRODYNAMIC EVOLUTION

The 2T evolution of Ru is simulated with our 2T-HD code. We run the 2T-HD code until the end of the 2T stage when the thermal equilibrium between electrons and ions is reached. After that, the MD-MC simulation takes over, ensured that its state at the end of the 2T stage corresponds to the state predicted with the 2T-HD. Adjusting the MD-MC parameters it is crucial to reproduce the *shape* of the 2T-HD profiles. The amplitudes of the profiles are determined by the absorbed fluence.

In general, the procedure of adjusting the initial conditions and the MC parameters

(see Appendix 5.7) of the MD-MC code to match the output of the 2T-HD should be performed for all considered fluences. However, in the case of Ru, the shape of the 2T-HD profiles weakly depends on fluence. This is due to the fact that the thermal diffusivity k_e/C_e of Ru is almost constant at high electron temperatures (electron thermal conductivity k_e and heat capacity C_e both linearly increase with electron temperature in high temperature region, see Ref. [64]). Additionally, the electron-phonon coupling factor weakly depends on electron temperature [64].

The weak dependence of the shape of the 2T-HD profiles on fluence is also supported by the experiment, where the crater depth (which is connected to the heat affected zone and pressure profile) is constant in a large central region of the damage crater (see Fig. 5.12 below). This fact allows us to perform the procedure of fitting the shape of the MD-MC temperature and pressure profiles to the 2T-HD ones only once. Obtained for one fluence, the same parameters are used for all MD-MC calculations in this work. To minimize the effect of melting, which is not taken into account in the 2T-HD code, we use the lowest considered fluence of $F_{\text{abs}} = 40\,\text{mJ/cm}^2$ for the fitting procedure. The time $\tau = 3\,\text{ps}$, when the two codes are linked, is chosen as the time when thermal equilibrium is reached, $T_e(\text{z}) \approx T_i(\text{z})$.

The 2T-HD profiles $T_i(\text{z})$ and $P_{zz}(\text{z})$ at $t = 3\,\text{ps}$ are shown in Fig. 5.2, where they are compared with the same profiles obtained with the MD-MC code. The 2T-HD electronic and ionic temperature profiles are close to each other along the entire Ru thickness, which demonstrates the establishment of thermal equilibrium. In the fitting procedure of the MD-MC profiles to the 2T-HD ones, we used only the region $\text{z} \geq 10\,\text{nm}$. That is because the top part of Ru $\text{z} < 10\,\text{nm}$ is considered as molten: $T_i > T_m + T_h$ in that region, $T_h = H_m/C_i = 746\,\text{K}$. Here $H_m = 4.7 \cdot 10^9\,\text{J/m}^3$ is the latent heat of melting and $C_i = 6.3 \cdot 10^6\,\text{J/m}^3/\text{K}$ is the ion heat capacity at the melting temperature [71]. Since melting is not included in the 2T-HD, the temperature and pressure profiles in the liquid region may contain inaccuracies, therefore we do not use this region in the fitting procedure.

There is a good agreement between the 2T-HD and the MD-MC profiles in the region $\text{z} \geq 15\,\text{nm}$. The difference in the top region $\text{z} < 15\,\text{nm}$ can be due to the following reasons. As just mentioned above, melting is not taken into account in the 2T-HD, but is naturally included in the MD-MC code. It is known, that melting can influence the amplitude of the pressure wave, but as one can see, this effect is small in Ru. The speed of sound is higher in the solid phase, which can explain the deeper position of the 2T-HD pressure minimum compared to the MD-MC one. Another reason for the different positions of the pressure minima can be due to the electron pressure, which is taken into account in the 2T-HD, but is not included in the MD-MC calculations. The existence of a strong electron pressure in the 2T-HD approach due to the high electron temperature during the first $1-2\,\text{ps}$ can result in the formation of a tensile wave (negative pressure) sooner than in the MD-MC code.

Overall, the difference between the 2T-HD and the MD-MC profiles is small, which demonstrates a successful linking of the two codes. A possible inaccuracy, resulting from the fact that (i) phase transitions are not included into the 2T-HD code and (ii) electronic pressure is not included into the MD-MC code, is minimized with our fitting procedure; so it should not affect the following long-time scale material evolution that we focus on in this work.

The XCASCADE(3D) and 2T-HD calculations at the ablation threshold are used to

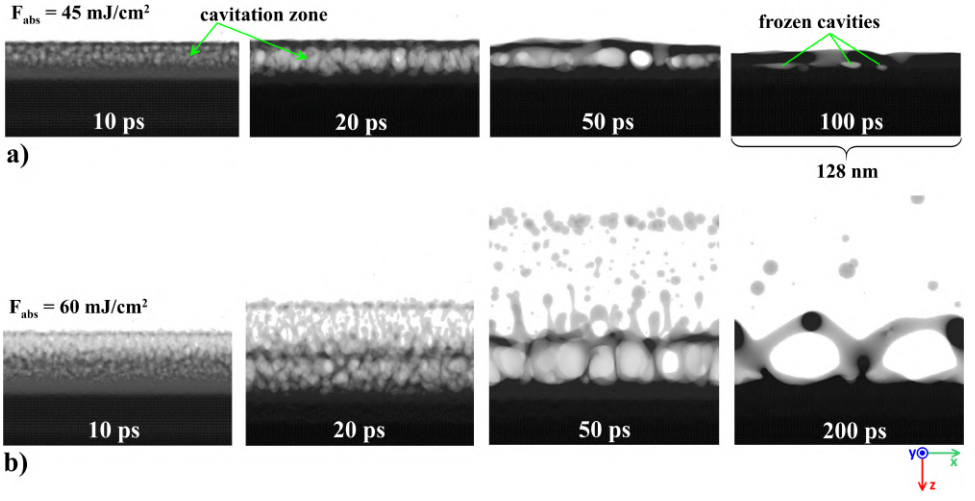

Figure 5.3: Mass distributions obtained with the MD-MC calculations. The evolution of the Ru-on-substrate target irradiated with a 100 fs XUV laser pulse is shown for the absorbed fluences of (a) $F_{\text{abs}} = 45\,\text{mJ/cm}^2$ and (b) $F_{\text{abs}} = 60\,\text{mJ/cm}^2$. Only the top parts of Ru that are subjected to structural modifications are shown.

tune the parameters of the MD-MC code, so that with the MD-MC calculations we enter the 1T stage of material evolution in a correct way.

Below we present the results of a series of MD-MC calculations for different fluences in the pre- and above ablation regimes in order to study the evolution of the Ru target on an atomistic level. We aim to identify and describe the physical processes responsible for different regimes of Ru laser-induced damage.

5.3.3. FLUENCE DEPENDENT ATOMISTIC PICTURE OF MATERIAL EVOLUTION

In this section we report the results of our MD-MC simulations on the dynamics of a 50 nm Ru film exposed to single 100 fs FWHM XUV laser pulses of various fluences. The size of the MD box used is $128 \times 32 \times 150\,\text{nm}^3$. It contains ~ 46 million atoms. The lateral dimensions $128 \times 32\,\text{nm}^2$ are chosen to be sufficiently large, so that the maximum size of the features that we obtain in our simulations for all considered fluences is smaller than the size of the box. The procedure of mimicking a thick Si substrate in the depth direction (via Ru pseudo-atoms) was described above. The periodic boundary conditions are applied in x and y lateral directions. Each simulation is performed with a top-hat shape of the laser pulse.

We start with a relatively low absorbed fluence of $45\,\text{mJ/cm}^2$. The corresponding mass distributions at different times are shown in Fig. 5.3 (a). The laser pulse comes from the top. The time $t = 0.5\,\text{ps}$ corresponds to the moment when the maximum inten-

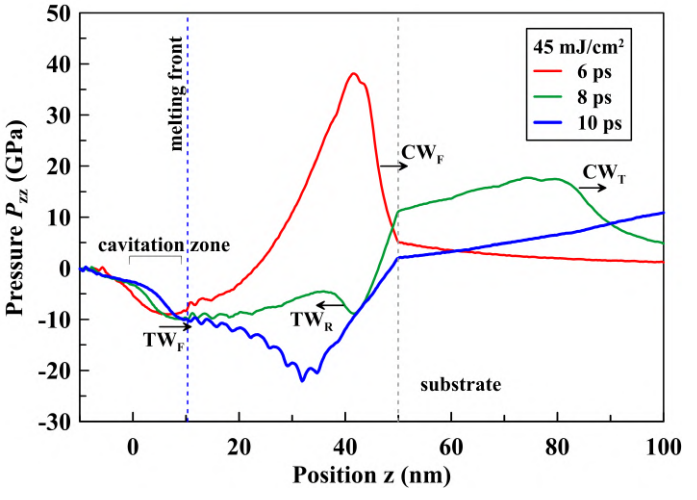

Figure 5.4: Evolution of pressure in the Ru-on-substrate target irradiated with a 100 fs XUV laser pulse. The absorbed fluence is $F_{\text{abs}} = 45\,\text{mJ/cm}^2$. The blue dashed line indicates the position of the melting front at $t = 10\,\text{ps}$.

sity of the laser pulse is at the Ru surface.

The transfer of the absorbed energy from the electronic system to the lattice results in ultrafast melting of the top Ru layer. The maximum molten depth of 14 nm is reached at $t = 20\,\text{ps}$. The ultrafast heating in the stress-confinement regime induces a strong compressive pressure wave at the front Ru surface. The time evolution of the thermo-induced pressure wave is shown in Fig. 5.4. The frontal compressive wave CW_F propagates into the depth of the target and is followed by a tensile wave TW_F. It propagates in the molten Ru with an increasing amplitude. A rupture occurs when the amplitude of this tensile wave is sufficient to overcome the tensile strength of the material. Comparing the mass distributions with the pressure profiles, one can see that a cavitation zone is created in liquid Ru as a result of propagation of the frontal tensile wave TW_F. The cavitation threshold, i.e. the minimum fluence required to produce a cavity, is found with separate MD-MC calculations to be $\sim 30\,\text{mJ/cm}^2$.

When the compressive wave CW_F reaches the Ru-substrate interface, it is partially transmitted through the interface (CW_T wave) and is partially reflected back with a sign change (TW_R wave), see Fig. 5.4. Although large in amplitude, this reflected wave does not cause damage, as one can see from the mass distributions in Fig. 5.3 (a), since it propagates in the solid material, which has a higher strength than a liquid. There is no experimental data on the tensile strength of Ru at high strain rates, but our simulations indicate that it is above 20 GPa for solid Ru. The tensile strength of liquid Ru can be estimated from the pressure profiles in Fig. 5.4 and is about $5-10\,\text{GPa}$ at a temperature of $\sim 5000\,\text{K}$ and a strain rate $\sim 8\cdot 10^{10}\,1/\text{s}$. Identification of the exact value of the tensile strength is beyond the scope of the present work, since it is difficult to trace at which conditions the first cavity is formed.

One can see from the mass distributions in Fig. 5.3 (a) that the fluence of 45mJ/cm^2 is not sufficient to cause ablation. The cavitation zone collapses due to the surface tension,

which is strong in Ru (see Ref. [72] and Appendix 5.8). The resolidification front that arrives from the depth freezes the target with small subsurface cavities at about 160 ps.

Fig. 5.3 (b) shows simulation results at the absorbed fluence of 60 mJ/cm^2. Unlike the previous case, ablation of the top thin layer of Ru is observed. It is important to note that ablation starts at the fluence twice higher than the cavitation threshold (see Discussion 5.5). The higher fluence creates a stronger pressure gradient and, hence, higher velocity of the top liquid layer – sufficient to cause ablation. Another factor in favour of ablation is a higher temperature of the top layer, which reduces the tensile strength. The propagation of the tensile wave into the depth causes a cavitation zone below the ablated thin layer. The produced cavities emerge during the stretching of the cavitation zone. At a time of about 200 ps only two large cavities remain and start to collapse (not shown).

Ablation of a larger amount of material occurs at higher fluences, as shown with the mass distributions in Fig. 5.5. At 90mJ/cm^2 the early stage of material evolution is similar to the previous case of 60 mJ/cm^2: ablation of the top thin layer and the formation and stretching of the cavitation zone below. The difference to the previous case is that now the cavitation zone does not collapse, but is stretched significantly until the binding material between the ablating layer and the remaining target breaks at about 300 ps. The ablated liquid layer disintegrates into two large droplets of about 25 – 30 nm size.

The pressure evolution in the target during the first 13 ps after the absorption of 90 mJ/cm^2 is shown in Fig. 5.6. The amplitude of the frontal tensile wave TW_F decreases with increasing temperature and, hence, is lower compared to the case of 60 mJ/cm^2. The tensile strength of the material also decreases with temperature. So, although the tensile pressure is weaker, it is sufficiently strong to create a cavitation zone in the near surface region below the ablated top layer. This cavitation zone is labeled C_1 on the density map at $t = 15$ ps, shown in the inset in Fig. 5.6.

As discussed above, the compressive wave partially reflects from the mechanically softer substrate (the acoustic impedance of Si is smaller than that of Ru) and, as a result, the reflected tensile wave TW_R propagates from the interface back to the surface. The superposition of the two tensile waves, $TW_F + TW_R$ creates a second cavitation zone C_2 deeper than the first one. Both cavitation zones are clearly observed on the density profile at $t = 15$ ps, shown in Fig. 5.6 with a dashed line. Further material evolution results in stretching of the first cavitation zone and collapse of the second one. The density map at $t = 50$ ps in Fig. 5.5 (a) shows the stretched cavitation zone C_1 and the remainders of the cavitation zone C_2 in the form of a few small cavities.

A similar pressure evolution (not shown) and, hence, similar ablation process occurs in the case of 120mJ/cm^2 of absorbed fluence, see the mass distributions in Fig. 5.5 (b). A minor difference between the 90mJ/cm^2 and the 120mJ/cm^2 is that in the latter case the cavitation zone gradually grows into the depth of the sample following the propagation of the frontal tensile wave. No distinct two layers of cavitation are observed. Another difference between these two cases is that the ablating layer does not disintegrates into droplets in the case of 120 mJ/cm^2, but stays intact. That may be an effect of periodic boundary conditions that can stabilize the ablating layer. We investigate the behaviour of the ablating layer in Section 5.3.4.

A different situation is realized at the highest considered fluence of 225 mJ/cm^2, Fig. 5.5 (c). Due to the extremely high atomic temperature of 20 – 30 kK reached in

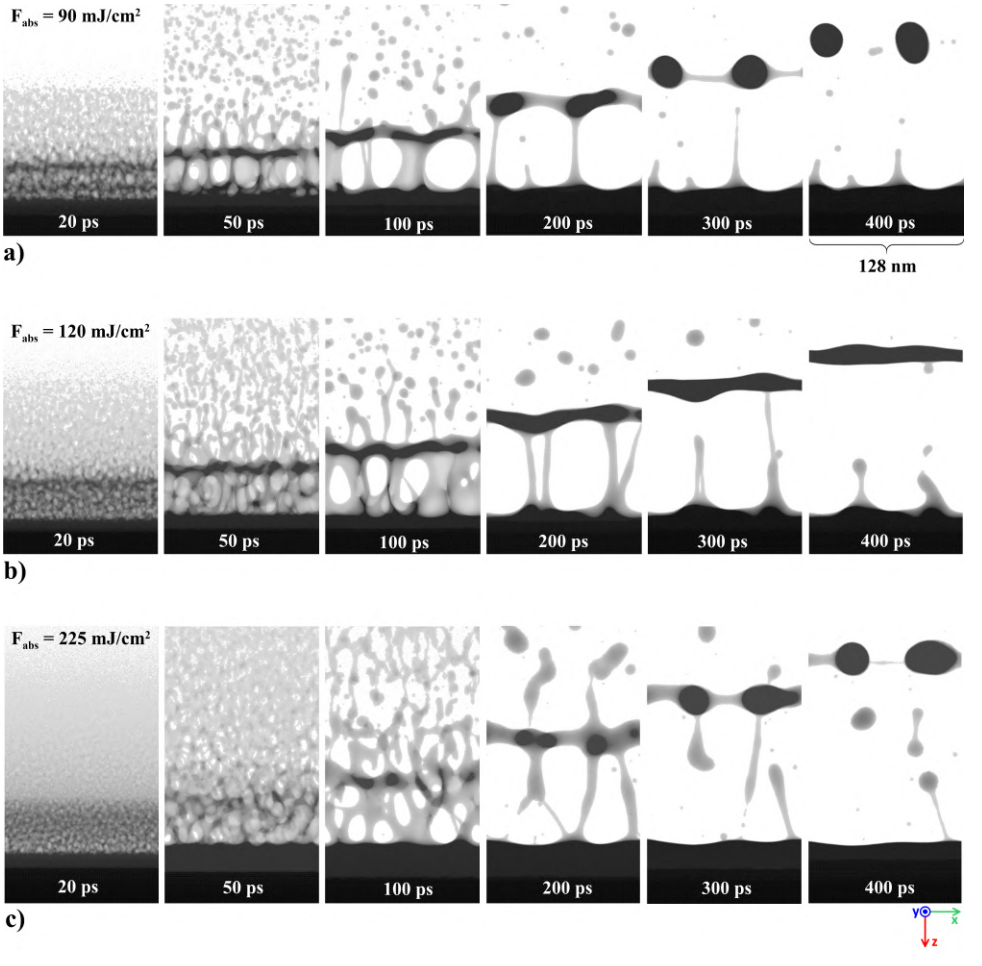

Figure 5.5: Mass distributions obtained with the MD-MC calculations. Evolution of the Ru-on-substrate target irradiated with a 100 fs XUV laser pulse is shown for the absorbed fluences of (a) $F_{\text{abs}} = 90\,\text{mJ/cm}^2$, (b) $F_{\text{abs}} = 120\,\text{mJ/cm}^2$ and (c) $F_{\text{abs}} = 225\,\text{mJ/cm}^2$. Only the top parts of Ru that are subjected to structural modifications are shown. Movies of mass distribution and symmetry parameter evolution from these simulations can be found in the Supplementary Material of Ref. [68]. The symmetry parameter distinguishes between solid and liquid phases, so melting and recrystallization dynamics can be traced.

the thin subsurface region of Ru during the first few ps after absorption, the pressure remains strictly positive until the frontal compressive wave is reflected from the Ru-substrate interface, see the pressure profiles in Fig. 5.7. The superposition of the waves $\text{TW}_\text{F} + \text{TW}_\text{R}$ creates sufficiently strong tensile pressure and the cavitation zone is formed at a depth of about 20 nm. This cavitation zone is clearly observed on the density map shown in the inset of Fig. 5.7. The cavitation zone grows in the direction shown with a white arrow.

As one can see from Fig. 5.5, Ru under femtosecond XUV exposure exhibits two-level ablation in a wide range of fluences near and well above the ablation threshold. The top

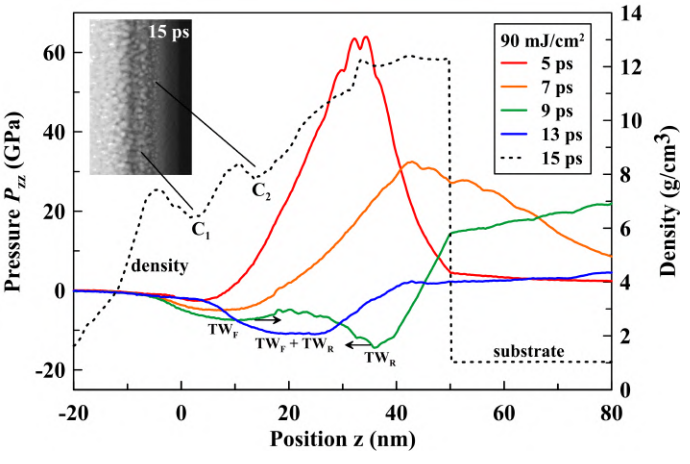

Figure 5.6: Evolution of pressure in the Ru-on-substrate target irradiated with a 100 fs XUV laser pulse. The absorbed fluence is $F_{abs} = 90\,mJ/cm^2$. The density profile at $t = 15$ ps is shown with the dashed line on the same graph. The density map at $t = 15$ ps is shown in the inset. The two cavitation zones, C_1 and C_2, are clearly visible and are formed with the frontal tensile wave TW_F and with the superposition of the frontal and the reflected waves $TW_F + TW_R$, respectively

few nm layer ablation is followed by ablation of a thicker layer. As shown above, the latter occurs due to the tensile wave, either purely by the frontal one or by the superposition of the frontal and the reflected one.

The mechanism responsible for the thin top layer ablation depends on the fluence. For low fluences $60-90\,mJ/cm^2$ the frontal tensile wave results in cavitation and ablation of the top material. Even low stresses produced by the tensile wave are sufficient for rupture, since the significantly heated liquid has a low tensile strength. For higher fluences, the pressure is strictly positive during the first few ps, whereas the ejection of material has already begun. This means that ablation of the top thin layer occurs not via thermo-mechanical cavitation, but due to the expansion of the liquid which phase state runs from an initial high-temperature state towards the subcritical or supercritical thermodynamic state. Expansion to a subcritical condition may result in the formation of gas-liquid mixture ejecta via overheating and fast explosive boiling of the hot liquid [73]. The supercritical ablation consists in a continuous formation of hot gas ejecta without phase separation into vapour and liquid [74].

To illustrate different mechanisms of top layer ablation we show the atomistic configuration of the top Ru part at $t = 20$ ps in case of $F_{abs} = 120\,mJ/cm^2$, see Fig. 5.8. Three characteristic regions can be identified: hot gas of Ru atoms in the top part (supercritical ablation), hot gas-liquid mixture (subcritical ablation), and cavitation zone created by the tensile wave. The corresponding temperature and density profiles are also shown. It is worth to note that the negative pressure is generated only in the cavitation zone and causes the deceleration of material there.

The critical parameters of Ru modeled with the EAM interatomic potential are extracted from separate MD-MC calculations using the phase coexistence method. The results are $T_c = 14500\,K$, $P_c = 0.19\,GPa$ and $\rho_c = 1.1\,g/cm^3$. The atomic temperature

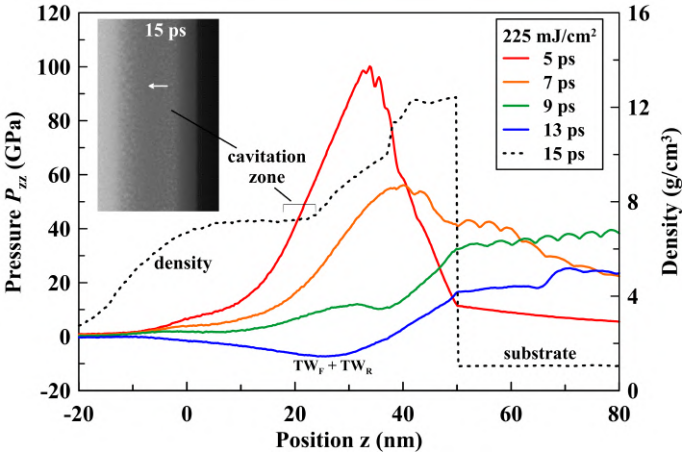

Figure 5.7: Evolution of pressure in the Ru-on-substrate target irradiated by a 100 fs XUV laser pulse. The absorbed fluence is $F_{abs} = 225\,mJ/cm^2$. The density profile at $t = 15$ ps is shown with the dashed line on the same graph. The density map at $t = 15$ ps is shown in the inset. The cavitation zone is formed with the superposition of the frontal and the reflected waves $TW_F + TW_R$. The white arrow shows the direction of the expansion of the cavitation zone with time.

of the Ru top surface rises above 16 kK during the first few ps after the absorption of $120\,mJ/cm^2$, while the density drops below $2\,g/cm^3$, which confirms that both subcritical and supercritical ablation mechanisms are possible. A similar situation is realized for higher fluences.

5.3.4. DYNAMICS OF ABLATING LAYER

Fig. 5.5 suggests that the thick ablating layer exhibits inconsistent behaviour with increasing fluence. With our MD-MC simulations we found that the layer stays stable at fluences of 120 and $150\,mJ/cm^2$, whereas for other considered fluences (lower as well as higher) it disintegrates into liquid droplets. In this section we investigate possible reasons of unstable evolution of the ablating layer.

RAYLEIGH-TAYLOR INSTABILITY

It is known that development of Rayleigh-Taylor instability (RTI) can induce fragmentation of ablating material [75]. Such a phenomenon may occur when a more dense liquid (Ru in our case) is expanding into a less dense environment (vacuum or vapour in our case) and is being affected by a strong deceleration. The deceleration of the target surface is produced by a subsurface pressure gradient directed towards the vacuum, which generates a corresponding force directed to the bulk of the target. Just after absorption of a laser pulse, the pressure under the surface has a large positive value which produces the pressure gradient directed to the target, and thus this gradient causes expansion of the material and acceleration of the surface. Then, the subsurface pressure decreases, and if it drops below the vapour pressure above the surface, the pressure gradient changes its sign and begins decelerating the target surface. The sign change of the subsurface pressure gradient is clearly visible in Fig. 5.7, where it happens after 9 ps.

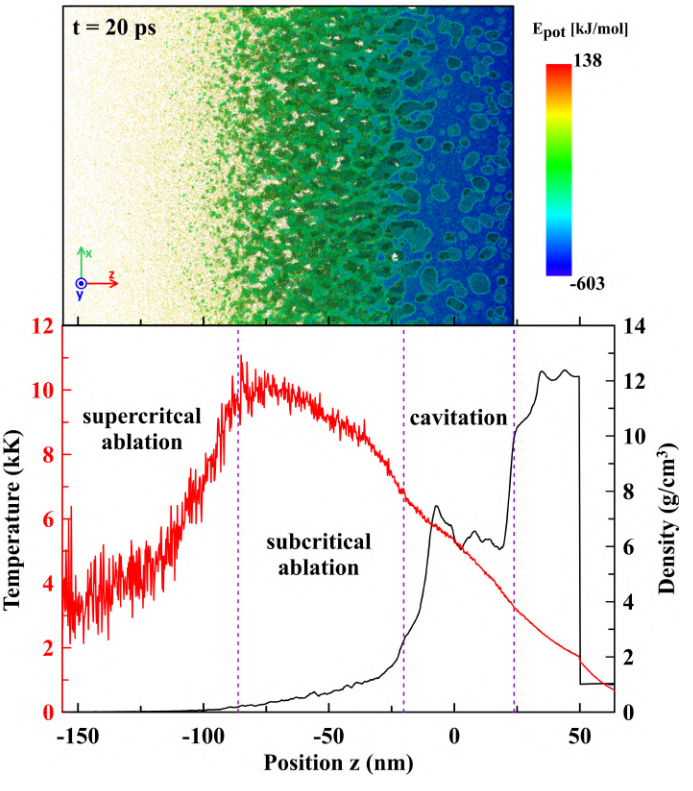

Figure 5.8: Top panel: phase structure of material flow at $t = 20$ ps induced by $F_{abs} = 120\,mJ/cm^2$. The atoms are coloured according to their potential energy. The leading expanding gas on the left is produced in supercritical expansion of a top hot layer with a thickness of $1-2$ nm. It follows by a two-phase gas-liquid zone formed via fragmentation of a hot liquid expanding along a subcritical adiabat. This zone is followed by a dense foam-like material formed via cavitation of relatively cold liquid stretched by the negative pressure. Only the last zone is subjected to deceleration and a Rayleigh-Taylor instability may develop here, see Section 5.3.4. Bottom panel: the corresponding temperature and density profiles.

Such a decelerating pressure gradient results from two sources. First, it is a result of stretching of a continuous subsurface material at an early stage of the expansion. Then, after cavitation of the stretched liquid, it also results from the tension of the foam-like material in the cavitation zone that may pull the ablating layer back to the target during a long time until the foam ruptures. It is clear that the cohesive forces of continuous liquid are much stronger than the capillary forces in the foam, which results in a huge deceleration at the early stage of expansion and a relatively small deceleration after cavitation.

To investigate whether the RTI plays a role in Ru ablation, we analyze the velocity of the ablating layer in the case of $F_{abs} = 120\,mJ/cm^2$. At each time step we record the velocity of the top material at a density level of $6\,g/cm^3$, which is an average density in the ablating layer. Knowing the velocity, we calculate the deceleration of the layer. The results are shown in Fig. 5.9. Please note that z axis is directed in the depth of Ru, hence

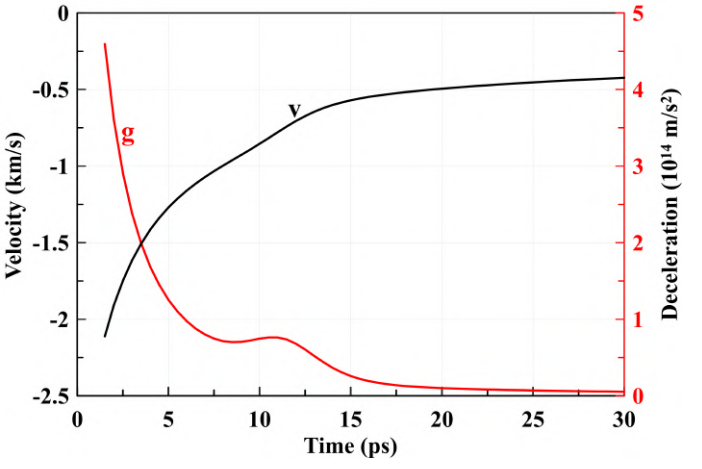

Figure 5.9: The time dependence of the velocity and deceleration of the ablating liquid layer calculated for the case of $F_{\text{abs}} = 120\,\text{mJ/cm}^2$, see Fig. 5.5 (b).

the negative sign of velocity directed to the vacuum. An enormously strong deceleration of the top material is observed during the first 15−20ps. Further stretching of the cavitation zone weakens the force that pulls the ablating layer back, since the net cross-section surface line of cavities in the binding foam-like material decreases due to the reduction of the number of cavities and increase of their sizes.

To check if such a large deceleration acting on the ablating layer over a short timescale is sufficient to cause the RTI development, we calculate the characteristic RTI growth rate γ:

$$\gamma(t) = \sqrt{\text{At}g(t)k - k^3\sigma/\rho}. \tag{5.1}$$

Here $g(t)$ is deceleration, $k = 2\pi/\lambda$ is the wave number of the surface profile perturbation with wavelength λ that may develop due to the deceleration, At is an Atwood number, which is equal to 1 in the case of vacuum, σ is the surface tension, and ρ is the density of the liquid Ru layer. The expression (5.1) is taken from [76] with the viscosity of liquid Ru ν not taken into account ($\nu = 0$). Here we only aim to get an estimation of γ and obtain a qualitative criterion for the RTI development. The average density of the ablating layer is $6\,\text{g/cm}^3$. For the surface tension we take $\sigma = 1.6\,\text{J/m}^2$ at $T = 5000\,\text{K}$, see Appendix 5.8. The latter is the average temperature of the ablated layer at the considered timescale.

As a criterion of the RTI strength we use exponential amplification in the linear perturbation amplitude in the quasi-classical approximation [75]:

$$a(t)/a(t_0) = \exp\left(\int_{t_1}^{t} \gamma(t')dt'\right). \tag{5.2}$$

Here $a(t_0)$ is a small nanometer-scaled amplitude of the initial perturbations, and integration starts from the onset time t_1 when the boundary between the subcritical and

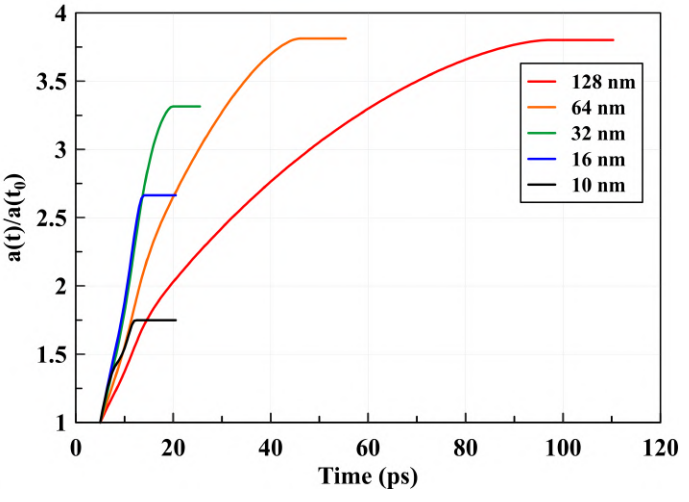

Figure 5.10: RTI amplifications of small perturbations with different wavelengths. Amplifications are saturated after the deceleration drops below $g = k^2\sigma/\rho$/At.

cavitation zone is formed, see Fig. 5.8. In our case it is around 5 ps. Only starting from this time the RTI can develop. The amplification is calculated for different perturbation wavelengths λ and is shown in Fig. 5.10. The maximum allowed wavelength is equal to the largest MD box dimension, 128 nm in our case. The amplification stops to increase at the moment when the surface tension σ dampens the perturbation for the considered λ (root expression in (5.1) becomes zero). One can see that for all considered λ the amplification of the initial perturbations with nano-scaled amplitudes is below a factor of 4, which is not sufficiently large to cause fragmentation of the ablating layer.

The perturbation $\lambda = 10$ nm is considered with the aim to explain the development of liquid jets at the border of the ablating surface at the early stage of ablation, see, for example, Fig. 5.5 (a) at $t = 50$ ps. Such stretched liquid jets is not a typical feature of explosive boiling. The lateral size of these jets is around 10 nm. As one can see from Fig. 5.10, such a perturbation is short-lived and is damped by the surface tension after 12 ps. The value of surface tension is taken to be $\sigma = 1.03\,\mathrm{J/m^2}$, which corresponds to $T = 7000$ K. The resulting amplification is below a factor of 2, which is insignificant.

The stretching of the liquid jets at the border of the ablating surface can be explained by the difference in the velocity between the ablating surface, which is strongly decelerated, and the velocity of the jet attached to it.

In the study of gold ablation into water, for example, amplification of 50 and higher was required for the RTI to play a noticeable role, see Fig. 31 at $t = 297.6$ ps and corresponding amplification in Fig. 30 in the Ref. [75]. Such a large amplification is achieved because of a long action of deceleration onto the gold-water boundary. In contrast, stronger deceleration of Ru ablating into vacuum, considered in this work, acts over a very short time, not sufficient for the RTI to develop. When gold ablates into vacuum, which is also considered in Ref. [75], the RTI does not develop due to a large thickness (large inertia) of the ablating layer and a low surface tension of gold (low tensile strength

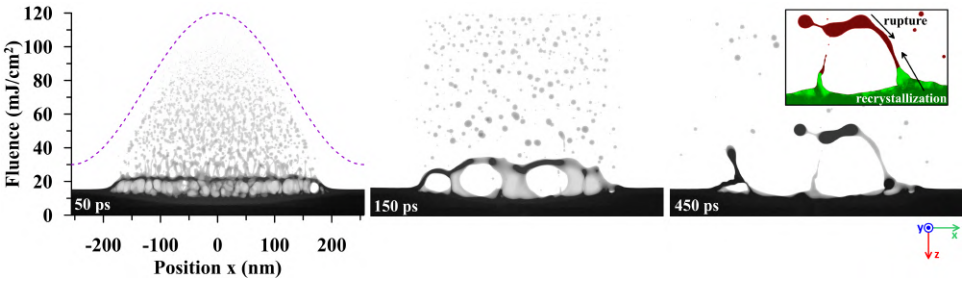

Figure 5.11: Maps with mass distributions illustrating the ablation of Ru obtained with a large-scale MD-MC simulation. The fluence profile of an XUV 100 fs laser pulse is taken according to expression (5.3) and is shown with a dashed line. The inset shows a symmetry parameter distribution with green colour corresponding to a solid phase and red colour to a liquid phase. The bottom arrow shows the direction of the recrystallization front propagation. The top arrow illustrates that the rupture of the liquid ablating layer propagates from the center towards the edge. The dynamics of these processes defines the final structure of the crater edge.

of binding foam). But in the case of Ru, even with the factors favourable for the RTI development, namely small thickness of the ablating layer and high surface tension, the effect of the RTI is insignificant. Other possible reasons of layer disintegration will be discussed in the next section.

NONUNIFORM FLUENCE PROFILE

As was already mentioned, the periodic boundary conditions applied in lateral directions can affect the evolution of the ablating layer by stabilizing it. To reduce a possible size effect, we performed a calculation with an increased MD box size. We increase L_x to 512 nm, so the resulting MD box has a size of $512 \times 32 \times 150\,\text{nm}^3$ and contains ~ 183 million atoms.

Moreover, instead of a top-hat fluence profile we use

$$F(x) = F_e + (F_p - F_e)\cos^2(\pi x / L_x). \tag{5.3}$$

Such a profile provides a peak fluence F_p in the center of the MD box and F_e fluence at the edges. A $\cos^2(\pi x/L_x)$ function is chosen due to its periodicity, which is dictated by the periodic boundary conditions, and due to its similarity to a Gaussian function, which realistically represents a spatial energy distribution in a laser pulse. With this simulation we aim to investigate how a nonuniform fluence distribution would affect the dynamics of the ablating layer.

Such a more realistic representation of a laser pulse in our simulations comes at the expense of losing accuracy in modeling non-reflecting boundary condition and in mimicking heat conduction in a thick substrate. Due to a nonuniform fluence distribution, the history of a LP will be different for different x coordinates. For simplicity, we use the history of a Lagrangian particle (LP) at the averaged fluence for the entire length of the simulation box. Since with this simulation we are interested in the short-term dynamics of the ablating layer and not in the recrystallization process, our simplified one-dimensional LP formalism should be sufficiently accurate to provide a reliable qualitative picture of the ablation dynamics. The LP formalism is described above in Section 5.2.3.

The mass distributions obtained with the MD-MC calculations using the fluence profile according to expression (5.3) are shown in Fig. 5.11. For the peak and edge fluences we used $F_p = 120\,\mathrm{mJ/cm^2}$ and $F_e = 30\,\mathrm{mJ/cm^2}$, respectively. The fluence range is chosen such that the lower fluence is equal to the cavitation threshold and the peak fluence corresponds to the regime where we observed a stable ablating layer in case of a top-hat fluence distribution, see Fig. 5.5 (b). At the early stage of material evolution, $t = 50\,\mathrm{ps}$, we see the ablated plume formed by the material ejected from the top thin layer of Ru, a liquid ablation layer and a cavitation zone below it. Evolution of the cavitation zone results in the formation of larger cavities. The ablated layer exhibits unstable behaviour and disintegrates into droplets.

The disintegration of the ablated layer can be a result of the interplay between various factors, such as surface tension and its temperature dependence, parameters of the cavitation zone, and thickness of the ablating layer. The mass distribution at 150 ps shown in Fig. 5.11 illustrates that the ablating layer is pulled back nonuniformly by the remaining material in the cavitation zone, which is a possible source of instability. Another possible explanation of the fragmentation into droplets is the existence of cavities in the ablating layer.

With the simulations presented in Fig. 5.11 it is possible to get insights into another important process – formation of the crater edge. The evolution of the ablating layer can be described with the following stages: (i) formation of the layer, (ii) expanding of the layer into vacuum, (iii) fragmentation that starts in the center and propagates towards the edge, and (iv) recrystallization of the remaining part at the edge. The interplay between the last two processes defines the final structure of the crater edge, see the inset in Fig. 5.11 at $t = 450\,\mathrm{ps}$. Although, as mentioned above, the process of recrystallization is not modeled quantitatively accurate, this calculation provides us with a qualitative description of the key processes leading to crater edge formation.

In the following section we compare the results of our simulations with the available experimental data obtained in single-shot damage threshold experiments.

5.4. DAMAGE THRESHOLDS AND FINAL SURFACE MORPHOLOGY

The single-shot damage experiments were performed at the free electron laser in Hamburg (FLASH), where Ru polycrystalline films of 50 nm thickness on a single-crystal Si substrate were exposed to 100 fs FWHM, XUV (92 eV or 13.5 nm) laser pulses with various fluence. The detailed description of this experiment together with the *post-mortem* analysis of damage craters is reported in [57]. The goal of this section is a detailed explanation of the existing experimental data using our simulations. First, we briefly recall the main experimental results.

The development of the damage morphology with increasing fluence can be studied within a single damage spot. A high-resolution scanning electron microscopy (HR-SEM) image of a typical crater produced in Ru is shown in Fig. 5.12 (a). Visible damage starts with increased surface roughness near the edge of the crater (area 1). Inside the crater, where ablation of material occurs, there are two characteristic zones: a rough periphery (area 2) and a flat central part (area 3), separated by a distinct crack. The roughness in area 2 gradually decreases towards the center of the crater, which is illustrated with an

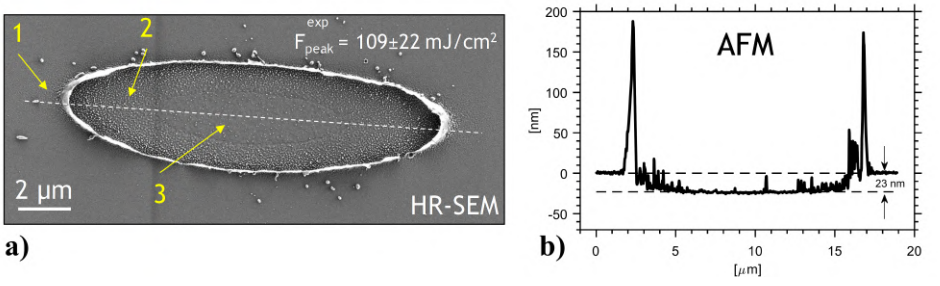

Figure 5.12: (a) HR-SEM image of a single-shot damage spot produced in Ru with a 100 fs XUV FEL pulse. The peak absorbed fluence is $F_p = 109 \pm 22\,\mathrm{mJ/cm^2}$. The labels 1,2 and 3 indicate the characteristic damage morphologies: increased roughness outside the crater, rough periphery and flat center inside the crater, respectively. The dashed line indicates where the AFM line profile was measured. (b) AFM line profile illustrating the decrease of the surface roughness at the bottom of the crater from the edge towards the center.

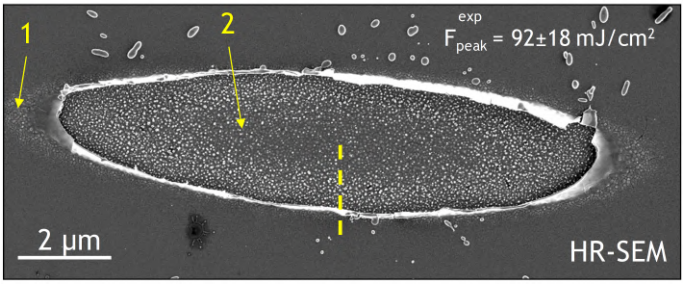

Figure 5.13: HR-SEM image of a single-shot damage spot produced in Ru with a 100fs XUV FEL pulse. The peak absorbed fluence is $F_p = 92 \pm 18\,\mathrm{mJ/cm^2}$. The labels 1 and 2 indicate the characteristic damage morphologies: increased roughness outside the crater and rough surface inside the crater, respectively. No distinct flat area in the center is detected. A dashed line indicates where the TEM analysis is performed, see Fig. 5.14.

AFM line profile, Fig. 5.12 (b), taken through the center of the damage spot as indicated with a dashed line in Fig. 5.12 (a).

The peak incident fluence of the laser pulse that produced this crater was measured to be $374 \pm 75\,\mathrm{mJ/cm^2}$, which corresponds to $109 \pm 22\,\mathrm{mJ/cm^2}$ of absorbed fluence, if one takes into account the surface reflectivity (68%) and a calculated fraction of energy that escapes from the surface via photo- and secondary electrons (~ 9%) [57]. For convenience we continue our analysis only in terms of the absorbed fluence. The ablation threshold was determined by Liu's plot method [77] to be $F_{\mathrm{abl}}^{\mathrm{exp}} = 58 \pm 12\,\mathrm{mJ/cm^2}$. The flattening phenomenon in the center also exhibits a threshold behaviour with a threshold fluence $F_{\mathrm{flat}}^{\mathrm{exp}} = 91 \pm 18\,\mathrm{mJ/cm^2}$. The crater depth in the flat area is constant and is equal to 23 nm, see Fig. 5.12 (b).

A HR-SEM image of a damage spot produced with a peak fluence $92 \pm 18\,\mathrm{mJ/cm^2}$, which is just at the flattening threshold, is shown in Fig. 5.13. As one can see, no distinct flat area in the center of the crater has developed yet.

In order to reveal the in-depth structure of a damage crater a transmission electron microscopy (TEM) cross section is taken in the area indicated with a dashed yellow line

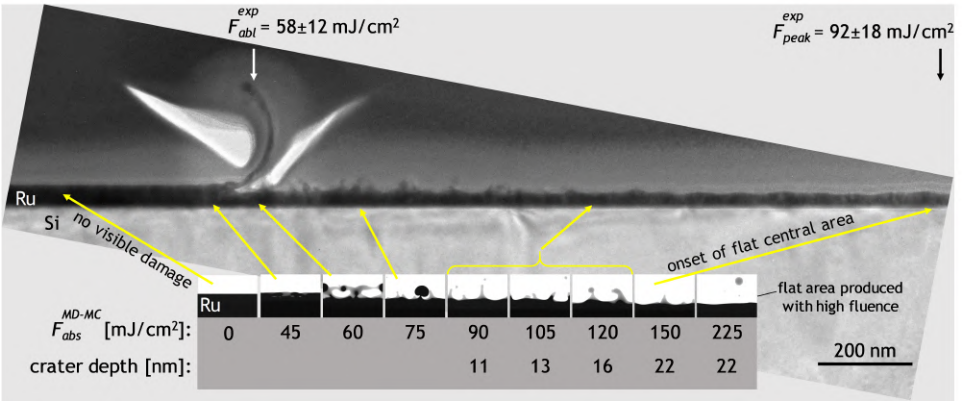

Figure 5.14: Comparison of the MD-MC simulations with the experimental damage morphology obtained with a TEM cross-section. TEM image shows the vicinity of the crater edge and the morphology inside the crater. The MD-MC results are shown below and represent the mass distributions of Ru at the end of the simulations, i.e. when Ru is totally recrystallized. The substrate is shown schematically with a grey rectangle. The scale of the TEM image and the MD-MC results is the same, enabling one-to-one comparison.

in Fig. 5.13. The TEM image is shown in Fig. 5.14. One can see the undamaged part of the Ru film, the edge of the crater, and the morphology inside the crater. The edge of the crater is formed during the process of recrystallization of the remaining part of the ablating layer, see Fig. 5.11. The roughness of the surface inside the crater decreases towards the center, where the local fluence is higher, which is consistent with the AFM cross section in Fig. 5.12 (b).

The results of the MD-MC simulations are shown in Fig. 5.14 together with the TEM image in the same scale for a one-to-one comparison. Note, that the simulations with the top-hat fluence profile and various fluence levels are considered in this section, same as in Section 5.3.3. In such a way we probe different positions along the damage crater, corresponding to a different locally absorbed fluence. Computation of the whole damage spot of several μm size is, of course, not possible to accomplish in reasonable time with the available computer power.

The end results of the simulations are shown in Fig. 5.14, namely completely recrystallized targets after the irradiation procedure. Only the Ru part of the sample is shown with the MD-MC mass distributions, the substrate is schematically shown with a grey rectangle. No visible damage to the substrate was detected in all performed simulations. The arrows approximately indicate the correspondence between the simulation results and the experimentally determined morphology. The result with the highest considered fluence of 225 mJ/cm^2 is shown for a complete picture of the surface morphology evolution with increasing fluence, but significantly exceeds the experimental fluence.

The pre-ablation regime with cavitation, F_{abs} = 45 mJ/cm^2, see Fig. 5.3 (a), results in the formation of the surface with increased roughness after the complete resolidification. The roughness and insignificant swelling of the surface are caused by the small subsurface cavities that got frozen by the resolidification front. That explains the surface morphology outside the damage crater (area 1 in Figs. 5.12 and 5.13). The existence of the frozen subsurface cavities after the irradiation of the targets with a laser was also

reported for other metals [78–80].

In the case of $F_{\text{abs}} = 60\,\text{mJ/cm}^2$ no significant ablation occurs, only a thin top layer is removed, see Fig. 5.3 (b). That case can be considered as just slightly below the experimentally detected ablation threshold. We suppose that ablation of a thin few nm layer via sub- and supercritical mechanisms discussed above is another contribution to the formation of a rough surface outside the experimental crater.

The onset of the ablation of a thicker layer is detected for a fluence $F_{\text{abs}} = 75\,\text{mJ/cm}^2$. The final frozen Ru surface for that case is shown in Fig. 5.14. While a part of the material was ablated, the other part did not overcome the surface tension, got pulled back to the surface and remained frozen in the form of a large droplet with a size of about 30 nm. Therefore, with our MD-MC simulations we define the ablation threshold to be around $F_{\text{abl}}^{\text{MD-MC}} = 60 - 75\,\text{mJ/cm}^2$, which is in a very good agreement with the experiment.

A series of simulations with a fluence $F_{\text{abs}} = 90 - 150\,\text{mJ/cm}^2$ demonstrates the decrease of the frozen surface roughness with increasing fluence. The average crater depth, extracted from the calculation of the amount of removed material, increases from 11 nm for $F_{\text{abs}} = 90\,\text{mJ/cm}^2$ to 22 nm for $F_{\text{abs}} = 150\,\text{mJ/cm}^2$, which is also in a very good agreement with the experiment. The case of $F_{\text{abs}} = 150\text{mJ/cm}^2$ can be considered as the onset of the flat central area (area 3 in Fig. 5.12), which serves as our model estimation of the flattening threshold.

As one can see, our model overestimates the flattening threshold, but provides an accurate description of the surface morphology trend with increasing fluence. The deviation from the experiment in the limit of high fluence may result from the lack of reliable knowledge of the Ru parameters at sub- and supercritical conditions. Calculations made with the EAM potential of Ru developed in this work (see Appendix 5.8) may overestimate the critical parameters of Ru, which, unfortunately, are not known.

The highest considered fluence of $F_{\text{abs}} = 225\,\text{mJ/cm}^2$ demonstrates the flat frozen surface. The crater depth of 22 nm agrees well with the experimental value of 23 nm in the central part of the crater, see Fig. 5.12 (b).

The morphology of the bottom of the crater is determined by a local absorbed fluence. Two key processes play a crucial role here: the hydrodynamic evolution of the top molten material and the rate of the heat dissipation from the top hot region to the deeper cold part of the material. For relatively low fluences, the characteristic time of hydrodynamic motion of ablating material is longer than the characteristic time of its resolidification, which leads to the formation of the rough bottom of the crater. For higher fluences, the characteristic time of material ablation and smoothing of the remaining molten material by surface tension is shorter than the characteristic resolidification time, which leads to the formation of the flat frozen surface in the central part of the crater. Dynamics of melting, ablation and recrystallization for fluences $F_{\text{abs}} = 90$, 120 and $225\,\text{mJ/cm}^2$ is illustrated with the movies, that can be found in the Supplementary Material of Ref. [68].

5.5. DISCUSSION

We reported simulation results on the dynamics of the Ru damage in pre- and above ablation regimes induced by femtosecond XUV laser pulses. The simulations were performed with our new hybrid computational scheme that overcomes several limits of the

previous models and is applicable in a wide range of irradiation parameters and materials:

- In principle, there is no restriction on the **angle of incidence** in our model. However, angles above the critical angle in the XUV and X-ray regime would result in a large photon penetration depth. The necessity to simulate a thick sample in that case may significantly increase the total computation time, mainly in the MD part of the model.

- **Photon energy** from XUV to hard X-rays. Relativistic effects restrict the photon energy to $\sim 10^5$ eV. To consider optical photon energy and below, the initial MC part of our model must be replaced with a Boltzmann kinetic equation, or a TTM-based approach if applicable.

- **Fluence** is restricted to a maximum value in the following way. First, the fluence must not be too high, otherwise the density of the excited electrons will become comparable to or higher than the atomic density of the target, and XCASCADE(3D) will not be applicable. Second, in the HD and MD parts of the model, the equation of state and interatomic potential, respectively, should properly reproduce the material properties at sub- and supercritical conditions when the fluence becomes considerably high, otherwise unrealistic results can be obtained. Third, the fluence should stay below the threshold for plasma formation. In this work, the highest fluence $F_{\text{abs}} = 225\,\text{mJ/cm}^2$ can be considered at the limit of the model applicability, since it already brings Ru to a supercritical state. Further increase of the fluence requires dedicated studies.

- **Pulse duration** should be sufficiently short, so one can assume that absorption of all the photons in a laser pulse occurs in the unmodified target. The particular applicable values of the pulse duration depend on the fluence. The higher the fluence, the sooner the material is modified, the shorter the pulse duration should be. For metals in the fluence regime near the ablation it is typically restricted to ~ 1 ps.

- **Any metal** can be considered, as long as its 2T equation of state, 2T thermal conductivity, electron-phonon coupling factor and interatomic potential are known in a wide range of density, temperature and pressure. In the context of ablation, the following properties are important to reproduce with the MD interatomic potential: melting temperature, stress-strain curve, surface tension and its dependence on temperature (see Appendix 5.8).

The main novelty of our model is the ability to simulate interaction of high energy photons with matter, preserving a large spatiotemporal scale of the simulations. The applicability of the Monte Carlo and hydrodynamics parts of the model to the cases of much higher photon energy was demonstrated in the previous work [53].

The disadvantage of our approach is a lack of completely reliable description of lattice evolution on an atomistic level during the first 3 ps (as described in Sections 5.2.2 and 5.3.2). However, there are no significant 3D spatial and phase modifications in the material during that time, so the applicability of the 2T-HD model to describe that stage

of material evolution is justified. Improving this part of the model may be considered as a next step in our hybrid model development. As an alternative, the TTM-MD method (with the electronic pressure included [37]) could be used, provided with the heat source from the XCASCADE(3D). This method, although different in technical details, takes into account the same physical processes, so similar results are expected.

Taking into account possible nonequilibrium behaviour of the ionic system would require a different, significantly more complex approach (such as e.g. Boltzmann kinetic equations) instead of two-temperature-based formalisms, which would have a larger computational cost. It is beyond the scope of the present work, since here we are mostly interested in the process of ablation and formation of the final frozen surface structures.

The model was applied to the XUV irradiated Ru with the focus on an atomistic picture of damage development, since such details of femtosecond ablation dynamics of Ru were never studied before. The parametrization of Ru in the 2T state [64] used in this work was obtained via ab-initio calculations and, to the best of our knowledge, is the most accurate theoretical data on Ru in the studied context. The electron-phonon coupling factor exhibits a decrease with an increasing electron temperature [64], similar to some other transition metals such as iron, nickel and platinum [81]. The decrease is not significant compared to a constant coupling factor (taken at $T_e = 0$, for example), and can only slightly influence the quantitative characteristics of the ablation process. A reliable interatomic potential for Ru applicable for various high-energy high-pressure studies was developed for the first time (see Appendix 5.8) and can be found in the Supplementary Material of Ref. [68].

General mechanisms of femtosecond ablation that are common for various metals were found to be responsible for XUV induced damage in Ru, although with several non typical effects. We found that ablation threshold is twice higher than the cavitation threshold, which is not typical compared to the previously studied optically excited metals such as Au [36] and Al [82]. For these metals with a large heat affected zone and a thick ablation layer the cavitation and ablation thresholds are close to each other. We interpret the large difference between the two thresholds in our case as a result of a large surface tension of Ru and a small heat affected zone (thin ablation layer).

According to our simulations, a two-level ablation occurs in Ru in a wide range of fluences near and well above the ablation threshold. For lower fluences in that range both levels are ablated due to a tensile component of the generated pressure wave, whereas for higher fluences the top thin layer is ablated via sub- and supercritical decomposition into a gas-liquid mixture. Other studied metals typically exhibit ablation of a relatively thick single layer via a thermo-mechanical mechanism (tensile wave) [36, 59], whereas complex ablation of the top material involving sub- and supercritical decomposition, also referred to as phase explosion, with simultaneous cavitation in the deeper parts is found only at fluences significantly higher than the ablation threshold [82, 83].

The two-level ablation in Ru even at relatively low fluence near the ablation threshold occurs due to the high density of the absorbed energy in the surface layer during the initial stage of the Ru evolution. Such confinement of energy transferred to the ionic subsystem of the surface layer is realized due to (i) the irradiation conditions, namely absorption of XUV light at 20° grazing incidence, which occurs in the top 3.5 nm layer, (ii) the XUV induced electron cascades spreading the energy only insignificantly, and (iii) the Ru thermal properties, namely a relatively low electron thermal conductivity and

a strong electron-phonon coupling factor, which provides the transfer of energy from electrons to the ions faster than the stress relaxation via expansion of heated material. Altogether it creates a small heat affected zone with a high temperature and pressure even at relatively low fluence near the ablation threshold. One would need a considerably higher fluence to reach a similar two-level ablation in materials where the heat affected zone is large, such as Au or Al.

We showed that disintegration of the ablating layer is unlikely to be caused by the development of a Rayleigh-Taylor instability, but is rather a result of a large surface tension of Ru, see Fig. 5.11. To get more insight into this process, the dynamics of the ablation process can be investigated with pump-probe experiments. It is known that one can observe the transient Newton's rings (NRs) during the ablation process by using the time-resolved microscopy technique [84]. The NRs result from the interference of light reflected from the ablating layer and the remaining part of the target [85]. The existence of the NRs on a long nanosecond timescale, known for example for such metals as Al, Au, Ti, Ni [84, 86], means that the ablating layer stays stable during that time. On the other hand, the short lifetime of the NRs observed using a soft x-ray probe was reported for W and Pt, and was attributed to the rapid growth of the surface roughness of the ablating layer [87]. MD simulations of Pt ablation showed disintegration of the ablating layer into droplets [88], confirming the experimental findings. We suppose that high surface tension in combination with small thickness of the liquid ablating layer are necessary conditions for layer disintegration.

Dedicated experimental studies are required to complement the simulation results presented in this work in order to get more insight into the transient evolution of the ablating layer. Such pump-probe experiments are outside the scope of the present paper.

The rigorousness of our simulations is illustrated with a quantitative agreement with the previously reported experimental results [57] on ablation threshold fluence, crater depth and fine details of the crater damage morphology. For the first time, frozen (i.e. final) structures at the bottom of the crater and their dependence on the absorbed fluence level were described. It was shown that heat removal plays a key role in the formation of these structures. Namely, in the case when heat removal is hindered and Ru is in a melted state for a relatively long time, there are no frozen structures at the bottom of the crater - the bottom is smooth.

Our simulation with a nonuniform fluence profile explains the mechanism of the crater edge formation. The edge which appears as a rim around ablation craters is observed practically in all laser ablation experiments (see, for example, Fig. 5.12 (b) and Refs. [5, 78, 79]). Previous explanation of the edge formation as a result of frozen subsurface cavities is complemented with our analysis presented in Fig. 5.11. We show that the edge can be formed during the recrystallization of the remaining part of the ablated layer, after a detachment of a central part of the layer. The mechanism of the crater edge formation defines its position, which is important for quantitative measurements of the ablation threshold by Liu's plot method [77].

The results obtained in this work are of course sensitive to a particular choice of the thermo-mechanical parametrization of Ru in the two- and one-temperature stage. The parameters used in the 2T-HD calculations (the most important ones are temperature dependent heat capacity, electron thermal conductivity and electron-phonon coupling, see Ref. [64]) and the interatomic potential (see Appendix 5.8) were obtained from first-

principal calculations, and, to the best of our knowledge, are the most accurate data on Ru in the context of femtosecond laser ablation. A good agreement of our simulations with the ablation experiment validates the parametrization used.

5.6. CONCLUSIONS

A new hybrid computational approach that combines Monte Carlo, hydrodynamic and molecular dynamic models was developed and applied to study the dynamics of femtosecond XUV laser damage in Ru thin films. The model is based on previously reported solutions and extends its applicability to a wide range of irradiation conditions covering the full timescale of material evolution.

The studied irradiation parameters were chosen in accordance with the previously reported single-shot damage experiments. Due to the grazing incidence of the XUV laser pulses (small photon penetration depth), insignificant XUV-induced electron cascading and Ru thermal properties (low thermal conductivity and large electron-phonon coupling factor) the heat affected zone is small, resulting in a high energy density in the surface region even for relatively low fluences. Such a distribution of the absorbed energy results in a two-level ablation in a wide range of fluence near and well above the ablation threshold.

Large scale atomistic simulations were carried out until a complete resolidification of Ru is reached, which opens up a possibility of a direct one-to-one comparison with the experimental results on damage crater morphology. We achieved a quantitative agreement between the simulations and the experiment in ablation threshold fluence, crater depth and frozen structures on the bottom of the crater, and explained the responsible damage mechanisms.

5.7. APPENDIX A: HEAT CONDUCTION WITH MONTE CARLO PSEUDO-ELECTRONS

We simulate electron heat conduction using the MC approach combined with the classical MD model. The MC model is parameterized with two fitting parameters: the mass of pseudo-electrons (see description in Section 5.2.3) and the exchange rate determining both the pseudo-electron swapping between neighbouring atoms and pseudo-electron-ion collision rates.

To define the pseudo-electron exchange rate, prior to the main simulations, the problem of heat transfer between two surfaces with different constant temperatures $T_1 > T_2$ is simulated with the MD-MC method. Such a problem has a steady-state solution $T(z) = T_1 - z(T_1 - T_2)/L$, where L is the distance between the two surfaces. Since the solution is time independent, the pseudo-electron mass and pseudo-electron-ion collision rate can be arbitrary. Thus, the required experimental heat flux can be obtained by adjusting the single MC parameter of pseudo-electron exchange rate, which fits the experimental thermal conductivity precisely at the given conditions. As was demonstrated in earlier works, such a method can efficiently treat electronic heat conduction [54].

With the procedure described above we aim to reproduce the experimental thermal conductivity of Ru at the temperature close to the melting point $T_m = 2607$ K. That provides us with an accurate description of the melting and recrystallization front propa-

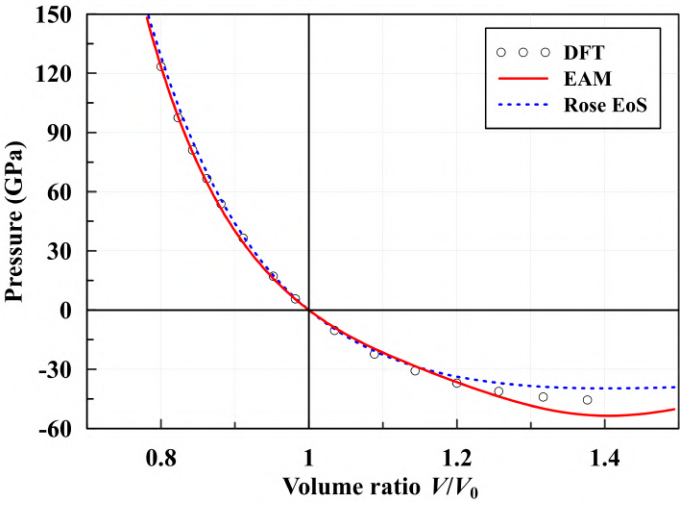

Figure 5.15: Two EAM potentials give almost identical cold pressure curves in bulk compression of Ru. Fitting of the pressure was bounded by $V/V_0 < 1.2$. Dotted line shows $P(V)$ at $T = 0$ K from the universal Rose's equation of states [90].

gation, which is essential in order to obtain the realistic final frozen surface structures in long timescale simulations. The experimental data available in the literature give the value $k_e = 79.6$ W/m/K at $T = 2500$ K [89]. We choose the values for T_1 and T_2 to be 2600 and 2500 K, respectively, and L is 100 nm. The heat flux of $8 \cdot 10^{10}$ W/m^2 for the given temperature gradient can be established by the pseudo-electron exchange rate of 1.8 fs^{-1}.

The pseudo-electron mass m_e^* can be fitted after finding the exchange rate described above. This second MC parameter determines the energy transfer between a pseudo-electron and an atom via their collision governed by the following expressions:

$$\begin{aligned} \boldsymbol{v}_e' &= (m_e^* \boldsymbol{v}_e + m_a \boldsymbol{v}_a + m_a v \boldsymbol{n})/(m_e^* + m_a), \\ \boldsymbol{v}_a' &= (m_e^* \boldsymbol{v}_e + m_a \boldsymbol{v}_a - m_e^* v \boldsymbol{n})/(m_e^* + m_a), \end{aligned} \tag{5.4}$$

where $\boldsymbol{v}_e$, $\boldsymbol{v}_a$ and $\boldsymbol{v}_e'$, $\boldsymbol{v}_a'$ are pseudo-electron and atom velocities in the laboratory system before and after an exchange event, respectively, and v is the pseudo-electron-atom relative speed. The scattering unit vector $\boldsymbol{n}$ is assumed to be distributed isotropically and is provided by a uniform random generator of directions. Such energy exchange conserves the total energy and momentum of the entire pseudo-electron-atom system.

The pseudo-electron mass is obtained within the procedure of linking the 2T-HD code with the MD-MC. The 2T-HD part describes the 2T regime of material evolution, whereas classical MD is only applicable in the 1T regime. For that reason, we link the two parts of our hybrid scheme at the moment of time $\tau = 3$ ps, when the thermal equilibrium between electrons and atoms is reached ($T_e \approx T_i$). The 2T-HD calculations are performed prior to the MD-MC ones to obtain the ion temperature $T_i(z)$ and total pressure $P_{zz}(z)$ depth profiles at $t = \tau$. In the MD-MC code the mass of the pseudo-electrons and the initial heating profile (that mimics the distribution of absorbed laser energy) are

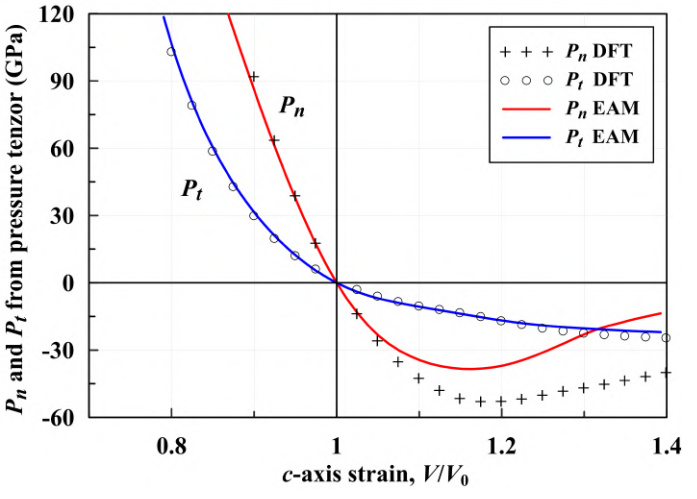

Figure 5.16: Normal P_n and tangential P_t components of the pressure tensor obtained in uniaxial deformation along the c-axis using EAM potential. Fitting was bounded by strains $V/V_0 < 1.1$.

adjusted in order to reproduce the T_i(z) and P_{zz}(z) profiles obtained with the 2T-HD (see Fig. 5.2).

The resulting mass is $m_e^* = 150\ m_e$, where m_e is the free electron mass. Please note that the obtained mass does not have the physical meaning of the effective electron mass, since our MC pseudo-particles should not be considered as real electrons, as explained in Section 5.2.3. We also remind here that the MC pseudo-electrons provide reliable description of the electron heat conductivity only during the 1T stage. The nonequilibrium electron cascade stage is modeled with the XCASCADE(3D) code, while the electronic system in the 2T regime is accurately described with the 2T-HD equations, where the band structure effects, such as different effective masses of s- and d-electrons are taken into account based on ab initio calculations of thermal parameters described in Ref. [64].

Although, technically speaking, with the MD-MC code we obtain results in both time domains, 2T and 1T, the MD-MC code can provide a reliable description of the material evolution only for $t \geq \tau$ (see Fig. 5.1). Thus, from this time onward, the MD code replaces the 2T-HD in our simulation scheme.

5.8. APPENDIX B: EMBEDDED ATOM MODEL POTENTIAL FOR RUTHENIUM

The stress-matching method [66, 67] was used to develop an interatomic embedded atom model (EAM) potential for Ru which is capable to reproduce correctly the response of a crystal to compression and stretching in a wide range of strains. The fitting database is built of the stress tensor components $\sigma_{\alpha\beta}(V) = -P_{\alpha\beta}(V)$ calculated with the density functional theory (DFT) method in a cold *hcp* lattice under continuous bulk and uniaxial deformation along the c-axis.

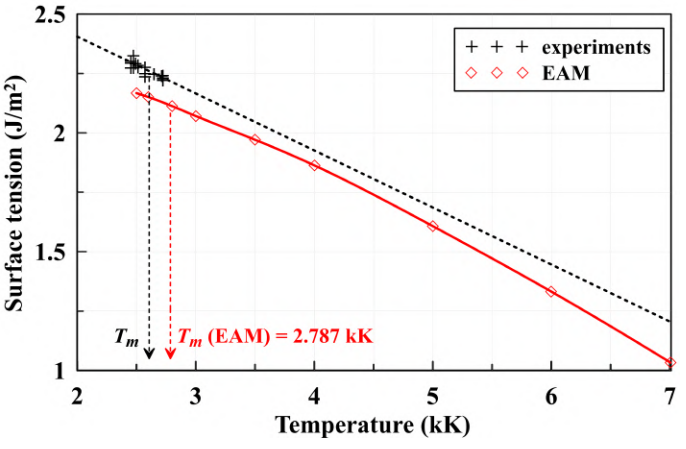

Figure 5.17: Dependence of the Ru surface tension on temperature. Dotted line shows a linear fit of experimental data [97]. Red diamonds show the result of our calculation with the Ru EAM potential.

To obtain the first-principles cold pressure curves of Ru and its c/a ratio, DFT calculations were performed using the projector augmented wave (PAW) method [91] with the Vienna *ab initio* simulation package (VASP) [92, 93]. The PAW pseudopotential of "sv" type from the standard VASP library, which takes into account two semicore electron bands $4s^2$ and $4p^6$ in addition to the valence electrons, was utilized with the Perdew-Burke-Ernzerhof functional for VASP 5.4, see details and the calculated density of states in [64].

The highly accurate DFT calculations were performed with an energy cutoff of 800 eV and number of k-points $21 \times 21 \times Y$ generated according to the Monkhorst-Pack scheme for sampling the Brillouin zone. Here the number Y takes values from 13 for the maximal ratio $c/a = 2.57$ to $Y = 28$ for the minimal ratio $c/a = 1.18$ in order to keep a constant grid step in the reciprocal space. The number of unoccupied levels was 18 per atom. The *hcp*-lattice cell with two Ru atoms in periodical boundary conditions was used in the DFT calculations. To calculate the uniaxial pressure components, a series of stepwise static calculations were performed for uniaxial strains along the c-axis. Figures 5.15 and 5.16 show the obtained DFT data for bulk and c-axis deformations.

The experimental bulk modulus of 310.9GPa [94], equilibrium density of $12.45 \mathrm{g/cm^3}$ with the lattice parameters of $c = 0.4273$ nm and $a = 0.27003$ nm [95], and the cohesive energy 6.74 eV [96] of ruthenium were also included in the database. The fitting procedure involves also the ratio c/a as a function of the compression ratio.

The constraints of the monotonic behaviour of $P_{\alpha\alpha}(V)$, including the requirement of an increase of the speed of sound with compression, as well as the absence of solid-solid phase transitions from the stable *hcp* phase of Ru in a wide range of deformation were also applied in the fitting.

The high-order rational functions were used to represent the EAM potential consisting of a pairwise energy, charge density and embedding energy. Fitting of potential coefficients was performed by minimization of a target function with the use of a downhill simplex algorithm combined with a random walk in a multidimensional space of the

fitting coefficients [67]. Figures 5.15 and 5.16 show the cold pressure curves calculated by our new EAM potential. It shows good agreement with the cold stress-strain curves from DFT in the wide range of deformations, and provides the melting points close to the experimental one $T_m = 2607$ K, see Fig. 5.17.

Figure 5.17 shows the experimental data [97] on the Ru surface tension dependence on temperature in the vicinity of the melting point and a linear extrapolation to higher temperatures. The same dependence is calculated with our EAM potential, demonstrating a good agreement with the experiment.

The obtained EAM potential does not depend on the electron temperature, i.e., a possible influence of the excited electronic system on the interatomic potential is not taken into account. Development of a temperature-dependent potential is challenging [98], and can be considered as a possible future improvement of our model.

ACKNOWLEDGEMENTS

Most of the MD simulations in this work were carried out on the Dutch national e-infrastructure with the support of SURF Cooperative.

REFERENCES

[1] M. Yabashi, H. Tanaka, and T. Ishikawa, *Overview of the SACLA facility,* J. Synchrotron Radiat. **22**, 477 (2015).

[2] T. Tschentscher, C. Bressler, J. Grünert, A. Madsen, A. Mancuso, M. Meyer, A. Scherz, H. Sinn, and U. Zastrau, *Photon beam transport and scientific instruments at the european XFEL,* Appl. Sci. **7**, 592 (2017).

[3] F. Graziani, M. P. Desjarlais, R. Redmer, and S. B. Trickey, *Frontiers and challenges in warm dense matter*, Vol. 96 (Springer Science & Business, 2014).

[4] S. P. Hau-Riege, R. A. London, R. M. Bionta, R. Soufli, D. Ryutov, M. Shirk, S. L. Baker, P. M. Smith, and P. Nataraj, *Multiple pulse thermal damage thresholds of materials for X-ray free electron laser optics investigated with an ultraviolet laser,* Appl. Phys. Lett. **93**, 201105 (2008).

[5] J. Pelka, R. Sobierajski, D. Klinger, W. Paszkowicz, J. Krzywinski, M. Jurek, D. Zymierska, A. Wawro, A. Petroutchik, L. Juha, V. Hajkova, J. Cihelka, J. Chalupsky, T. Burian, L. Vysin, S. Toleikis, K. Sokolowski-Tinten, N. Stojanovic, U. Zastrau, R. London, S. Hau-Riege, C. Riekel, R. Davies, M. Burghammer, E. Dynowska, W. Szuszkiewicz, W. Caliebe, and R. Nietubyc, *Damage in solids irradiated by a single shot of XUV free-electron laser: Irreversible changes investigated using X-ray microdiffraction, atomic force microscopy and Nomarski optical microscopy,* Radiat. Phys. Chem. **78**, S46 (2009).

[6] A. R. Khorsand, R. Sobierajski, E. Louis, S. Bruijn, E. D. van Hattum, R. W. E. van de Kruijs, M. Jurek, D. Klinger, J. B. Pelka, L. Juha, T. Burian, J. Chalupsky, J. Cihelka, V. Hajkova, L. Vysin, U. Jastrow, N. Stojanovic, S. Toleikis, H. Wabnitz, K. Tiedtke, K. Sokolowski-Tinten, U. Shymanovich, J. Krzywinski, S. Hau-Riege, R. London,

A. Gleeson, E. M. Gullikson, and F. Bijkerk, *Single shot damage mechanism of Mo/Si multilayer optics under intense pulsed XUV-exposure,* Opt. Express **18**, 700 (2010).

[7] S. Dastjani Farahani, J. Chalupsky, T. Burian, H. Chapman, A. Gleeson, V. Hajkoya, L. Juha, M. Jurek, D. Klinger, H. Sinn, R. Sobierajski, M. Störmer, K. Tiedtke, S. Toleikis, T. Tschentscher, H. Wabnitz, and J. Gaudin, *Damage threshold of amorphous carbon mirror for 177 eV FEL radiation,* Nucl. Instrum. Meth. A **635**, S39 (2011).

[8] A. Aquila, R. Sobierajski, C. Ozkan, V. Hájková, T. Burian, J. Chalupský, L. Juha, M. Störmer, S. Bajt, M. T. Klepka, P. Dłużewski, K. Morawiec, H. Ohashi, T. Koyama, K. Tono, Y. Inubushi, M. Yabashi, H. Sinn, T. Tschentscher, A. P. Mancuso, and J. Gaudin, *Fluence thresholds for grazing incidence hard X-ray mirrors,* Appl. Phys. Lett. **106**, 241905 (2015).

[9] T. Koyama, H. Yumoto, T. Miura, K. Tono, T. Togashi, Y. Inubushi, T. Katayama, J. Kim, S. Matsuyama, M. Yabashi, K. Yamauchi, and H. Ohashi, *Damage threshold of coating materials on X-ray mirror for X-ray free electron laser,* Rev. Sci. Instrum. **87**, 051801 (2016).

[10] R. Sobierajski, I. Jacyna, P. Dłużewski, M. T. Klepka, D. Klinger, J. B. Pełka, T. Burian, V. Hájková, L. Juha, K. Saksl, V. Vozda, I. Makhotkin, E. Louis, B. Faatz, K. Tiedtke, S. Toleikis, H. Enkisch, M. Hermann, S. Strobel, R. A. Loch, and J. Chalupsky, *Role of heat accumulation in the multi-shot damage of silicon irradiated with femtosecond XUV pulses at a 1 MHz repetition rate,* Opt. Express **24**, 15468 (2016).

[11] I. A. Makhotkin, R. Sobierajski, J. Chalupský, K. Tiedtke, G. de Vries, M. Störmer, F. Scholze, F. Siewert, R. W. E. van de Kruijs, I. Milov, E. Louis, I. Jacyna, M. Jurek, D. Klinger, L. Nittler, Y. Syryanyy, L. Juha, V. Hájková, V. Vozda, T. Burian, K. Saksl, B. Faatz, B. Keitel, E. Plönjes, S. Schreiber, S. Toleikis, R. Loch, M. Hermann, S. Strobel, H.-K. Nienhuys, G. Gwalt, T. Mey, and H. Enkisch, *Experimental study of EUV mirror radiation damage resistance under long-term free-electron laser exposures below the single-shot damage threshold,* J. Synchrotron Radiat. **25**, 77 (2018).

[12] I. A. Makhotkin, I. Milov, J. Chalupský, K. Tiedtke, H. Enkisch, G. de Vries, F. Scholze, F. Siewert, J. M. Sturm, K. V. Nikolaev, R. W. E. van de Kruijs, M. A. Smithers, H. A. G. M. van Wolferen, E. G. Keim, E. Louis, I. Jacyna, M. Jurek, D. Klinger, J. B. Pelka, L. Juha, V. Hájková, V. Vozda, T. Burian, K. Saksl, B. Faatz, B. Keitel, E. Plönjes, S. Schreiber, S. Toleikis, R. Loch, M. Hermann, S. Strobel, R. Donker, T. Mey, and R. Sobierajski, *Damage accumulation in thin ruthenium films induced by repetitive exposure to femtosecond XUV pulses below the single-shot ablation threshold,* J. Opt. Soc. Am. B **35**, 2799 (2018).

[13] J. Krzywinski, R. Conley, S. Moeller, G. Gwalt, F. Siewert, C. Waberski, T. Zeschke, and D. Cocco, *Damage thresholds for blaze diffraction gratings and grazing incidence optics at an X-ray free-electron laser,* J. Synchrotron Radiat. **25**, 85 (2018).

[14] R. Follath, T. Koyama, V. Lipp, N. Medvedev, K. Tono, H. Ohashi, L. Patthey, M. Yabashi, and B. Ziaja, *X-ray induced damage of B4C-coated bilayer materials under various irradiation conditions,* Sci. Rep. **9**, 2029 (2019).

[15] B. N. Chichkov, C. Momma, S. Nolte, F. Von Alvensleben, and A. Tünnermann, *Femtosecond, picosecond and nanosecond laser ablation of solids,* Appl. Phys. A **63**, 109 (1996).

[16] R. Ernstorfer, M. Harb, C. T. Hebeisen, G. Sciaini, T. Dartigalongue, and R. D. Miller, *The formation of warm dense matter: experimental evidence for electronic bond hardening in gold,* Science **323**, 1033 (2009).

[17] E. García Saiz, G. Gregori, D. O. Gericke, J. Vorberger, B. Barbrel, R. J. Clarke, R. R. Freeman, S. H. Glenzer, F. Y. Khattak, M. Koenig, O. L. Landen, D. Neely, P. Neumayer, M. M. Notley, A. Pelka, D. Price, M. Roth, M. Schollmeier, C. Spindloe, R. L. Weber, L. van Woerkom, K. Wünsch, and D. Riley, *Probing warm dense lithium by inelastic X-ray scattering,* Nat. Phys. **4**, 940 (2008).

[18] N. Medvedev and B. Ziaja, *Multistep transition of diamond to warm dense matter state revealed by femtosecond X-ray diffraction,* Sci. Rep. **8**, 5284 (2018).

[19] M. N. Ashfold, F. Claeyssens, G. M. Fuge, and S. J. Henley, *Pulsed laser ablation and deposition of thin films,* Chem. Soc. Rev. **33**, 23 (2004).

[20] T. A. Labutin, V. N. Lednev, A. A. Ilyin, and A. M. Popov, *Femtosecond laser-induced breakdown spectroscopy,* J. Anal. At. Spectrom. **31**, 90 (2016).

[21] C. Phipps, C. Bonnal, F. Masson, and P. Musumeci, *Launching swarms of microsatellites using a 100 kW average power pulsed laser,* J. Opt. Soc. Am. B **35**, B20 (2018).

[22] L. Koch, S. Kuhn, H. Sorg, M. Gruene, S. Schlie, R. Gaebel, B. Polchow, K. Reimers, S. Stoelting, N. Ma, P. M. Vogt, G. Steinhoff, and B. Chichkov, *Laser printing of skin cells and human stem cells,* Tissue Eng. Part C: Methods **16**, 847 (2009).

[23] R. R. Gattass and E. Mazur, *Femtosecond laser micromachining in transparent materials,* Nat. Photonics **2**, 219 (2008).

[24] H. Zeng, X.-W. Du, S. C. Singh, S. A. Kulinich, S. Yang, J. He, and W. Cai, *Nanomaterials via laser ablation/irradiation in liquid: a review,* Adv. Funct. Mater. **22**, 1333 (2012).

[25] E. Messina, E. Cavallaro, A. Cacciola, M. A. Iatì, P. G. Gucciardi, F. Borghese, P. Denti, R. Saija, G. Compagnini, M. Meneghetti, V. Amendola, and O. M. Maragò, *Plasmon-enhanced optical trapping of gold nanoaggregates with selected optical properties,* ACS Nano **5**, 905 (2011).

[26] W. Dong, S. Reichenberger, S. Chu, P. Weide, H. Ruland, S. Barcikowski, P. Wagener, and M. Muhler, *The effect of the Au loading on the liquid-phase aerobic oxidation of ethanol over Au/TiO2 catalysts prepared by pulsed laser ablation,* J. Catal. **330**, 497 (2015).

[27] T. Baati, A. Al-Kattan, M.-A. Esteve, L. Njim, Y. Ryabchikov, F. Chaspoul, M. Hammami, M. Sentis, A. V. Kabashin, and D. Braguer, *Ultrapure laser-synthesized Si-based nanomaterials for biomedical applications: in vivo assessment of safety and biodistribution,* Sci. Rep. **6**, 25400 (2016).

[28] K. Nordlund, C. Björkas, T. Ahlgren, A. Lasa, and A. E. Sand, *Multiscale modelling of plasma–wall interactions in fusion reactor conditions,* J. Phys. D: Appl. Phys. , 224018.

[29] Y. Rong, P. Ji, M. He, Y. Zhang, and Y. Tang, *Multiscale investigation of femtosecond laser pulses processing aluminum in burst mode,* Nanosc. Microsc. Therm. **22**, 324 (2018).

[30] N. Medvedev, V. Tkachenko, V. Lipp, Z. Li, and B. Ziaja, *Various damage mechanisms in carbon and silicon materials under femtosecond X-ray irradiation,* 4open **1**, 3 (2018).

[31] M. Kaganov, I. Lifshitz, and L. Tanatarov, *Relaxation between electrons and crystalline lattice,* Sov. Phys. JETP **4**, 173 (1957).

[32] S. Anisimov, A. Bonch-Bruevich, M. El'yashevich, Y. Imas, N. Pavlenko, and G. Romanov, *Effect of powerful light (laser) fluxes on metals,* Zh. Tekh. Fiz **36**, 1273 (1966).

[33] S. Anisimov, B. Kapeliovich, and T. Perelman, *Electron emission from metal surfaces exposed to ultrashort laser pulses,* Zh. Eksp. Teor. Fiz **66**, 776 (1974).

[34] S. Anisimov, N. Inogamov, Y. V. Petrov, V. Khokhlov, V. Zhakhovskii, K. Nishihara, M. Agranat, S. Ashitkov, and P. Komarov, *Interaction of short laser pulses with metals at moderate intensities,* Appl. Phys. A **92**, 939 (2008).

[35] D. S. Ivanov and L. V. Zhigilei, *Combined atomistic-continuum modeling of short-pulse laser melting and disintegration of metal films,* Phys. Rev. B **68**, 064114 (2003).

[36] B. J. Demaske, V. V. Zhakhovsky, N. A. Inogamov, and I. I. Oleynik, *Ablation and spallation of gold films irradiated by ultrashort laser pulses,* Phys. Rev. B **82**, 064113 (2010).

[37] S. V. Starikov and V. V. Pisarev, *Atomistic simulation of laser-pulse surface modification: predictions of models with various length and time scales,* J. Appl. Phys. **117**, 135901 (2015).

[38] N. A. Inogamov, V. V. Zhakhovsky, V. A. Khokhlov, Y. V. Petrov, and K. P. Migdal, *Solitary nanostructures produced by ultrashort laser pulse,* Nanoscale Res. Lett. **11**, 177 (2016).

[39] H. M. van Driel, *Kinetics of high-density plasmas generated in Si by 1.06- and 0.53-μm picosecond laser pulses,* Phys. Rev. B **35**, 8166 (1987).

[40] J. Chen, D. Tzou, and J. Beraun, *Numerical investigation of ultrashort laser damage in semiconductors,* Int. J. Heat Mass Tran. **48**, 501 (2005).

[41] Y. Gan and J. Chen, *Combined continuum-atomistic modeling of ultrashort-pulsed laser irradiation of silicon,* Appl. Phys. A **105**, 427 (2011).

[42] V. P. Lipp, B. Rethfeld, M. E. Garcia, and D. S. Ivanov, *Atomistic-continuum modeling of short laser pulse melting of Si targets,* Phys. Rev. B **90**, 245306 (2014).

[43] P. Lorazo, L. J. Lewis, and M. Meunier, *Thermodynamic pathways to melting, ablation, and solidification in absorbing solids under pulsed laser irradiation,* Phys. Rev. B **73**, 134108 (2006).

[44] W. S. Fann, R. Storz, H. W. K. Tom, and J. Bokor, *Electron thermalization in gold,* Phys. Rev. B **46**, 13592 (1992).

[45] C.-K. Sun, F. Vallée, L. H. Acioli, E. P. Ippen, and J. G. Fujimoto, *Femtosecond-tunable measurement of electron thermalization in gold,* Phys. Rev. B **50**, 15337 (1994).

[46] D. Bejan and G. Raşeev, *Nonequilibrium electron distribution in metals,* Phys. Rev. B **55**, 4250 (1997).

[47] A. V. Lugovskoy and I. Bray, *Ultrafast electron dynamics in metals under laser irradiation,* Phys. Rev. B **60**, 3279 (1999).

[48] B. Rethfeld, A. Kaiser, M. Vicanek, and G. Simon, *Ultrafast dynamics of nonequilibrium electrons in metals under femtosecond laser irradiation,* Phys. Rev. B **65**, 214303 (2002).

[49] J. Sempau, E. Acosta, J. Baro, J. Fernández-Varea, and F. Salvat, *An algorithm for Monte Carlo simulation of coupled electron-photon transport,* Nucl. Instrum. Meth. B **132**, 377 (1997).

[50] N. Medvedev, *Femtosecond X-ray induced electron kinetics in dielectrics: application for FEL-pulse-duration monitor,* Appl. Phys. B **118**, 417 (2015).

[51] V. Lipp, N. Medvedev, and B. Ziaja, *Classical Monte-Carlo simulations of X-ray induced electron cascades in various materials,* Proc. SPIE **10236**, 102360H (2017).

[52] O. Peyrusse, J.-M. André, P. Jonnard, and J. Gaudin, *Modeling of the interaction of an X-ray free-electron laser with large finite samples,* Phys. Rev. E **96**, 043205 (2017).

[53] I. Milov, V. Lipp, D. Ilnitsky, N. Medvedev, K. Migdal, V. Zhakhovsky, V. Khokhlov, Y. Petrov, N. Inogamov, S. Semin, A. Kimel, B. Ziaja, I. Makhotkin, E. Louis, and F. Bijkerk, *Similarity in ruthenium damage induced by photons with different energies: From visible light to hard x-rays,* Appl. Surf. Sci. **501**, 143973 (2020).

[54] V. Zhakhovskii, K. Nishihara, Y. Fukuda, S. Shimojo, T. Akiyama, S. Miyanaga, H. Sone, H. Kobayashi, E. Ito, Y. Seo, M. Tamura, and Y. Ueshima, *A new dynamical domain decomposition method for parallel molecular dynamics simulation,* in *IEEE International Symposium on Cluster Computing and the Grid*, Vol. 2 (2005) pp. 848–854.

[55] M. Egorova, S. Dyachkov, A. Parshikov, and V. Zhakhovsky, *Parallel SPH modeling using dynamic domain decomposition and load balancing displacement of voronoi subdomains,* Comput. Phys. Commun. **234**, 112 (2019).

[56] W. Ackermann *et al.*, *Operation of a free-electron laser from the extreme ultraviolet to the water window,* Nat. Photonics **1**, 336 (2007).

[57] I. Milov, I. A. Makhotkin, R. Sobierajski, N. Medvedev, V. Lipp, J. Chalupský, J. M. Sturm, K. Tiedtke, G. de Vries, M. Störmer, F. Siewert, R. van de Kruijs, E. Louis, I. Jacyna, M. Jurek, L. Juha, V. Hájková, V. Vozda, T. Burian, K. Saksl, B. Faatz, B. Keitel, E. Plönjes, S. Schreiber, S. Toleikis, R. Loch, M. Hermann, S. Strobel, H.-K. Nienhuys, G. Gwalt, T. Mey, H. Enkisch, and F. Bijkerk, *Mechanism of single-shot damage of Ru thin films irradiated by femtosecond extreme UV free-electron laser,* Opt. Express **26**, 19665 (2018).

[58] B. Rethfeld, D. S. Ivanov, M. E. Garcia, and S. I. Anisimov, *Modelling ultrafast laser ablation,* J. Phys. D Appl. Phys. **50**, 193001 (2017).

[59] L. V. Zhigilei, Z. Lin, and D. S. Ivanov, *Atomistic modeling of short pulse laser ablation of metals: Connections between melting, spallation, and phase explosion,* J. Phys. Chem. C **113**, 11892 (2009).

[60] N. M. Bulgakova, R. Stoian, A. Rosenfeld, I. Hertel, W. Marine, and E. Campbell, *A general continuum approach to describe fast electronic transport in pulsed laser irradiated materials: The problem of Coulomb explosion,* Appl. Phys. A **81**, 345 (2005).

[61] D. Cullen, *A Survey of Atomic Binding Energies for use in EPICS2017,* Tech. Rep. (Vienna, 2018).

[62] D. A. Chapman and D. O. Gericke, *Analysis of thomson scattering from nonequilibrium plasmas,* Phys. Rev. Lett. **107**, 165004 (2011).

[63] N. Medvedev, A. Volkov, and B. Ziaja, *Electronic and atomic kinetics in solids irradiated with free-electron lasers or swift-heavy ions,* Nucl. Instrum. Meth. B **365**, 437 (2015).

[64] Y. Petrov, K. Migdal, N. Inogamov, V. Khokhlov, D. Ilnitsky, I. Milov, N. Medvedev, V. Lipp, and V. Zhakhovsky, *Ruthenium under ultrafast laser excitation: Model and dataset for equation of state, conductivity, and electron-ion coupling,* Data Brief **28**, 104980 (2020).

[65] N. A. Inogamov and V. V. Zhakhovsky, *Surface 3D nanostructuring by tightly focused laser pulse: simulations by Lagrangian code and molecular dynamics,* J. Phys. Conf. Ser. **681**, 012001 (2016).

[66] V. Zhakhovskii, N. Inogamov, Y. Petrov, S. Ashitkov, and K. Nishihara, *Molecular dynamics simulation of femtosecond ablation and spallation with different interatomic potentials,* Appl. Surf. Sci. **255**, 9592 (2009).

[67] V. V. Zhakhovsky, K. P. Migdal, N. A. Inogamov, and S. I. Anisimov, *MD simulation of steady shock-wave fronts with phase transition in single-crystal iron,* in *AIP Conf. Proc.*, January, p. 070003.

[68] I. Milov, V. Zhakhovsky, D. Ilnitsky, K. Migdal, V. Khokhlov, Y. Petrov, N. Inogamov, V. Lipp, N. Medvedev, B. Ziaja, V. Medvedev, I. Makhotkin, E. Louis, and F. Bijkerk, *Two-level ablation and damage morphology of Ru films under femtosecond extreme UV irradiation,* Appl. Surf. Sci. , 146952 (2020).

[69] B. J. Demaske, V. V. Zhakhovsky, N. A. Inogamov, and I. I. Oleynik, *Ultrashort shock waves in nickel induced by femtosecond laser pulses,* Phys. Rev. B **87**, 054109 (2013).

[70] I. Milov, V. Lipp, N. Medvedev, I. A. Makhotkin, E. Louis, and F. Bijkerk, *Modeling of XUV-induced damage in Ru films: the role of model parameters,* J. Opt. Soc. Am. B **35**, B43 (2018).

[71] A. E. Morris, H. A. Fine, and G. Geiger, *Handbook on Material and Energy Balance Calculations in Material Processing* (John Wiley Sons, 2011).

[72] B. Keene, *Review of data for the surface tension of pure metals,* International Materials Reviews **38**, 157 (1993).

[73] V. P. Skripov, *Metastable liquids* (Wiley, New York, 1974).

[74] M. M. Basko, M. S. Krivokorytov, A. Y. Vinokhodov, Y. V. Sidelnikov, V. M. Krivtsun, V. V. Medvedev, D. A. Kim, V. O. Kompanets, A. A. Lash, and K. N. Koshelev, *Fragmentation dynamics of liquid-metal droplets under ultra-short laser pulses,* Laser Phys. Lett. **14**, 036001.

[75] N. A. Inogamov, V. V. Zhakhovskii, and V. A. Khokhlov, *Dynamics of gold ablation into water,* JETP **127**, 79 (2018).

[76] K. O. Mikaelian, *Rayleigh-Taylor instability in finite-thickness fluids with viscosity and surface tension,* Phys. Rev. E **54**, 3676 (1996).

[77] J. M. Liu, *Simple technique for measurements of pulsed Gaussian-beam spot sizes,* Opt. Lett. **7**, 196 (1982).

[78] J.-M. Savolainen, M. S. Christensen, and P. Balling, *Material swelling as the first step in the ablation of metals by ultrashort laser pulses,* Phys. Rev. B **84**, 193410 (2011).

[79] S. I. Ashitkov, N. Inogamov, V. V. Zhakhovskii, Y. N. Emirov, M. B. Agranat, I. Oleinik, S. I. Anisimov, and V. E. Fortov, *Formation of nanocavities in the surface layer of an aluminum target irradiated by a femtosecond laser pulse,* JETP Lett. **95**, 176 (2012).

[80] C. Wu, M. S. Christensen, J.-M. Savolainen, P. Balling, and L. V. Zhigilei, *Generation of subsurface voids and a nanocrystalline surface layer in femtosecond laser irradiation of a single-crystal Ag target,* Phys. Rev. B **91**, 035413 (2015).

[81] Z. Lin, L. V. Zhigilei, and V. Celli, *Electron-phonon coupling and electron heat capacity of metals under conditions of strong electron-phonon nonequilibrium,* Phys. Rev. B **77**, 075133 (2008).

[82] C. Wu and L. V. Zhigilei, *Microscopic mechanisms of laser spallation and ablation of metal targets from large-scale molecular dynamics simulations,* Appl.Phys. A **114**, 11 (2014).

[83] C.-Y. Shih, M. V. Shugaev, C. Wu, and L. V. Zhigilei, *Generation of subsurface voids, incubation effect, and formation of nanoparticles in short pulse laser interactions with bulk metal targets in liquid: Molecular dynamics study,* J. Phys. Chem. C **121**, 16549 (2017).

[84] K. Sokolowski-Tinten, J. Bialkowski, A. Cavalleri, D. von der Linde, A. Oparin, J. Meyer-ter Vehn, and S. Anisimov, *Transient states of matter during short pulse laser ablation,* Phys. Rev. Lett. **81**, 224 (1998).

[85] N. Inogamov, Y. V. Petrov, S. Anisimov, A. Oparin, N. Shaposhnikov, D. Von der Linde, and J. Meyer-ter Vehn, *Expansion of matter heated by an ultrashort laser pulse,* JETP Lett. **69**, 310 (1999).

[86] K. J. Schrider, B. Torralva, and S. M. Yalisove, *The dynamics of femtosecond pulsed laser removal of 20 nm Ni films from an interface,* Appl. Phys. Lett. **107**, 124101 (2015).

[87] M. Nishikino, N. Hasegawa, T. Tomita, Y. Minami, T. Eyama, N. Kakimoto, R. Izutsu, M. Baba, T. Kawachi, and T. Suemoto, *Formation of X-ray Newton's rings from nano-scale spallation shells of metals in laser ablation,* AIP Adv. **7**, 015311 (2017).

[88] C. M. Rouleau, C.-Y. Shih, C. Wu, L. V. Zhigilei, A. A. Puretzky, and D. B. Geohegan, *Nanoparticle generation and transport resulting from femtosecond laser ablation of ultrathin metal films: Time-resolved measurements and molecular dynamics simulations,* Appl. Phys. Lett. **104**, 193106 (2014).

[89] C. Y. Ho, R. W. Powell, and P. E. Liley, *Thermal conductivity of the elements,* J. Phys. Chem. Ref. Data **1**, 279 (1972).

[90] J. H. Rose, J. R. Smith, F. Guinea, and J. Ferrante, *Universal features of the equation of state of metals,* Phys. Rev. B **29**, 2963 (1984).

[91] P. E. Blöchl, *Projector augmented-wave method,* Phys. Rev. B **50**, 17953 (1994).

[92] G. Kresse and J. Hafner, *Ab initio molecular dynamics for liquid metals,* PPhys. Rev. B. **47**, 558 (1993).

[93] G. Kresse and J. Furthmüller, *Efficient iterative schemes for ab initio total-energy calculations using a plane-wave basis set,* Phys. Rev. B **54**, 11169 (1996).

[94] R. O. Simmons and H. Wang, *Single Crystal Elastic Constants and Calculated Aggregate Properties: A Handbook* (MIT Press, Cambridge, 1991).

[95] W. B. Pearson, *Handbook of Lattice Spacings and Structure of Metals and Alloys* (Pergamon, Oxford, 1967).

[96] C. Kittel, *Introduction to Solid State Physics; 8th Edition* (John Wiley & Sons, Inc, 2005).

[97] P. Paradis, T. Ishikawa, and S. Yoda, *Thermophysical properties of liquid and supercooled ruthenium measured by noncontact methods,* J. Mater. Res. **19**, 590 (2004).

[98] B. Bauerhenne, V. P. Lipp, T. Zier, E. S. Zijlstra, and M. E. Garcia, *Self-learning method for construction of analytical interatomic potentials to describe laser-excited materials,* Phys. Rev. Lett. **124**, 085501 (2020).

6

DAMAGE ACCUMULATION IN THIN RUTHENIUM FILMS INDUCED BY REPETITIVE EXPOSURE TO FEMTOSECOND XUV PULSES BELOW THE SINGLE-SHOT ABLATION THRESHOLD

The process of damage accumulation in thin ruthenium films exposed to multiple femtosecond XUV free-electron laser (FEL) pulses below the critical angle of reflectance was experimentally analyzed at the Free electron LASer facility in Hamburg (FLASH). The multi-shot damage threshold is found to be lower than the single-shot damage threshold. Detailed analysis of the damage morphology and its dependence on irradiation conditions justifies the assumption that cavitation induced by the FEL pulse is the prime mechanism responsible for multi-shot damage in optical coatings.

6.1. INTRODUCTION

The development of high peak brilliance, high repetition rate free-electron laser (FEL) light sources operating in the XUV and X-ray spectral regime such as FLASH [1], European XFEL [2] and LCLS [3] leads to increased interest in the durability of thin films exposed to a large number of pulses. FEL optical elements such as mirrors or beam-stoppers should be designed considering the limitation on durability to FEL radiation together with the requirements on high optical performance of the materials. Avoiding FEL-induced damage is also critical when long exposures of thin film samples are foreseen during FEL experiments. Examples of such experiments can be found in time resolved studies of surface chemical reactions with pump-probe X-ray diffraction techniques [4].

Only recently the first papers on the resistivity of metal films to multi-shot X-ray radiation were published [5, 6]. Earlier, Hau-Riege et.al. [7] investigated B4C coatings. In both cases it was observed that the multi-shot damage threshold is slightly lower than the single-shot one, but no detailed analysis of the nature of multi-shot damage was yet reported. Within the extreme ultraviolet (XUV) wavelength range multi-shot damage studies of bulk Si samples were reported by Sobierajski et al. [8]. The prime damage mechanism was identified as crossing the melting threshold due to heat accumulation in the vicinity of the Si surface.

In this work we investigate the multi-shot damage effect in Ru coatings exposed to various numbers of 100 fs (FWHM) pulses at 13.5 nm wavelength generated with various repetition rates. The influence of the irradiation conditions, namely the number of pulses and the grazing angle of incidence (AOI), on the morphology of the damaged spots is studied. Mechanisms responsible for the observed damage phenomena are suggested, although detailed atomistic simulations are required to confirm the proposed mechanisms.

Understanding the multi-shot damage of Ru films has a practical relevance. Since Ru has a high reflection coefficient for the extreme ultraviolet and soft X-ray wavelength ranges, and has a low oxidation rate, it is a very attractive material for reflective coatings. This work is a continuation of a series of studies of optics durability exposed to FEL radiation below the single-shot damage threshold [9].

6.2. EXPERIMENT

For this study, polycrystalline Ru coatings of 50 nm thickness were deposited on super-polished silicon substrates using magnetron sputtering in Ar atmosphere. The thickness of the Ru layer was determined by X-ray reflectivity measurements. Exposure of the Ru films was performed at the BL2 beamline of the FLASH facility [1]. Details of the experiment can be found elsewhere [9, 10]. For irradiations we used 100 fs (FWHM) XUV pulses with a wavelength of 13.5 nm. The light was p-polarized with respect to the sample surface. We used the multi-shot irradiation mode where FLASH generated one bunch of pulses per 0.1 second [11]. The maximum duration of a bunch was 400 μs and the maximum repetition rate of pulses within one bunch was 1 MHz. During the experiment we tuned the number of pulses within a bunch either by reducing the duration of the bunch, or by reducing the repetition rate while keeping the bunch duration constant.

The determination of the multi-shot damage threshold (MSDT) was performed us-

Table 6.1: Summary of the irradiation conditions. Exposures at 3.17° aimed to measure the damage threshold values and study its dependence on the number of pulses in a bunch at a fixed repetition rate, and on the pulse repetition rate at a fixed number of pulses in a bunch. The development of damage morphologies with the increasing number of pulses at fixed average fluence per pulse is studied with the irradiations performed at 20°.

AOI[a] [deg]	N of bunches	N of pulses in a bunch	Bunch rep. rate [Hz]	Pulse rep. rate [MHz]	Average abs. fluence [mJ/cm^2]
3.17	1	1, 50[b], 100, 200, 400	-	1	Variable
		100	-	0.25, 0.5, 1	
20	4	400[c]	10	1	12.5
	23	400[c]	10	1	
	209	400[b]	10	1	
	209	1[c]	5	-	

[a]Measured from the sample surface

[b]see Fig. 6.1

[c]see Fig. 6.2

ing Liu's method [12–14] and the fluence scan method [10, 15] based on measuring damaged areas with differential image contrast (also referred to as Nomarski) microscopy. The dependence of the damage threshold on the repetition rate and the number of pulses was studied using irradiations at 3.17° grazing incidence with an effective area of the beam [15, 16] on the sample surface of 40500 ± 2000 μm^2. The development of the damage morphology was studied by analysis of damage craters caused by different numbers of pulses arriving at 20° grazing incidence at a fixed average fluence per pulse using a focused beam with an effective area on the sample surface of 120 μm^2. The XUV reflectivity values at 3.17° and 20° degrees were measured to be 95.5% and 68%, respectively [17]. In both cases only the evanescence wave penetrates into the film resulting in a comparable penetration depth for these two angles of incidence, namely 2.5 nm and 3.5 nm, respectively. For Ru, the critical angle of reflection for XUV radiation at a wavelength of 13.5 nm is 27°.

For a consistent comparison of the damage threshold values at different irradiation conditions, all analysis is performed in terms of absorbed fluence. It is calculated according to the formula $F_{\text{abs}} = (1-R)E/A$, where E is the total energy of the pulse, A is the effective area of the beam on the sample surface determined according to [16], and R is the reflectivity coefficient at the corresponding exposure conditions. The total energy of the pulse E was measured with a gas monitor detector described by Tiedtke et.al. [18]. The experimental conditions at which the exposures were performed are summarized in Table 6.1.

6.3. RESULTS AND DISCUSSION

First, we present the results of multi-shot damage experiments of 50 nm Ru films performed at a grazing incidence of 3.17°. One set of exposures was performed for a fixed number of pulses in a bunch (100 pulses), but varying the pulse repetition rate (time interval between pulses in a bunch). In another experiment the Ru films were exposed

Table 6.2: Dependence of the multi-shot damage threshold on the pulse repetition rate for exposure at 3.17° grazing incidence. The number of pulses is fixed at 100. The threshold values are given in terms of absorbed fluence. The error in the threshold determination is approximately 20%.

Repetition rate [MHz]	0.25	0.5	1
Damage threshold [mJ/cm^2]	7.5	8.3	8.3

Table 6.3: Dependence of the multi-shot damage threshold on the number of pulses for exposure at 3.17° grazing incidence and 1 MHz pulse repetition rate. The threshold values are given in terms of absorbed fluence. The error in the threshold determination is approximately 20%.

Number of pulses	1	50	100	200	400
Damage threshold [mJ/cm^2]	26.1	13.3	8.3	5.8	6.7

to single bunches, consisting of a different number of pulses from 1 to 400 at a fixed repetition rate of 1 MHz. The measured damage threshold values of these two sets of exposures are summarized in Tables 6.2 and 6.3, respectively. The damage was determined as any visible surface modification observed with Nomarski microscopy.

As one can see from Table 6.2, the MSDT does not depend on the repetition rate up to 1 MHz within the error margin which in our case was approximately 20%. This value represents a combined error of pulse energy measurements and determination of the effective area of the beam. The data in Table 6.2 suggest that heat accumulation is unlikely to be the damage mechanism for the given experimental conditions. This is in contrast to the previously reported work of Sobierajski et al. [8], where heat accumulation in bulk Si exposed to similar radiation conditions but at normal incidence was found to be the main mechanism responsible for multi-shot damage caused by XUV femtosecond FLASH laser pulses. Ru however, being a metal, has a high thermal conductivity, which guarantees that the energy that is absorbed at the surface, diffuses through the entire Ru layer into the Si substrate mostly before the next pulse in a bunch arrives.

Another observation is the decrease of the damage threshold upon increasing the number of pulses at a fixed repetition rate of 1 MHz (see Table 6.3). The decrease continues up to 200 pulses and seems to saturate at that level. This result, together with the independence of the MSDT on the repetition rate described above, suggests that there is an accumulation of an irreversible process. From simulations of the dynamics of Ru single-shot ablation (see, for example, Chapter 5) we know that the complete relaxation of the target occurs in $\sim 1-10$ ns. It means that during the 1 MHz repetition rate exposures (1 μs between the pulses) the target has sufficient time to relax, including the cooling down of Ru back to room temperature. Therefore, damage at the fluence level below the single-shot damage threshold can only occur if individual pulses in a bunch cause irreversible structural changes, such as melting with or without cavitation (see Chapter 5) and recrystallization into a structure modified compared to the pristine material.

In order to better understand the processes responsible for the multi-shot damage of Ru, we performed *ex-situ* analysis of the damage morphology by means of high-resolution scanning electron microscopy (HR-SEM), atomic force microscopy (AFM) and transmission electron microscopy (TEM). Additionally, we compared the damage

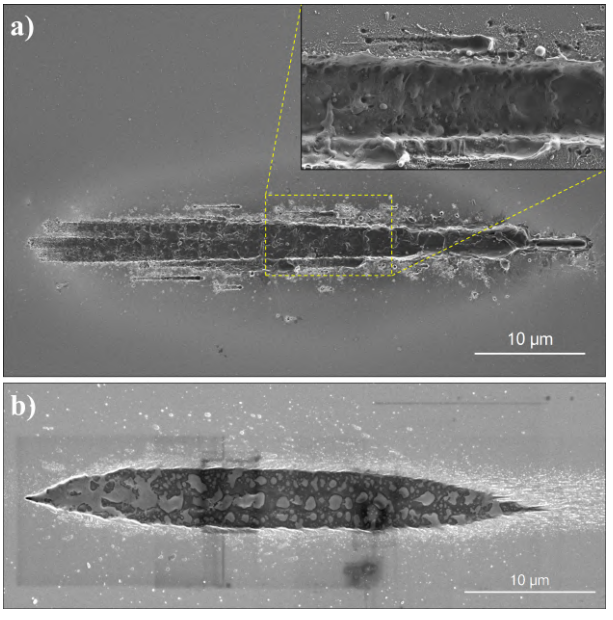

Figure 6.1: HR-SEM image of a damaged spot produced with a) single bunch consisting of 50 pulses with 1 MHz repetition rate at 3.17° grazing incidence angle and average absorbed fluence of 15 mJ/cm^2 per pulse, and b) 209 bunches each consisting of 400 pulses at 20° grazing incidence angle and average absorbed fluence of 12.5 mJ/cm^2 per pulse. The bunch repetition rate was 10 Hz, while the pulse repetition rate within a bunch was 1 MHz. The grey rectangular shadows visible in b) are the traces of electron-induced carbon growth originating from SEM measurements carried out before the one showed in the image.

morphologies obtained at 3.17° and 20° grazing incidence to study the influence of different angles of incidence. The HR-SEM image of a damaged spot exposed to a single bunch that consisted of 50 pulses with 1 MHz repetition rate at 3.17° grazing incidence is shown in Fig. 6.1 (a). The mean value of the fluence per pulse was 15 mJ/cm^2, which is close to the measured damage threshold value in Table 6.3, which is 13.3 mJ/cm^2. The damaged spot has a total area of ~ 320 μm^2 and can be characterized as a deep crater penetrating through the Ru layer into the Si substrate. The fact that the crater depth exceeds the thickness of the Ru layer is verified using an energy selective backscattered (ESB) detector (image is not shown), which is sensitive to elemental composition of the surface, confirming that Si is at the bottom of the crater. No other significant surface modifications around the craters, such as increased roughness or cracks, were detected by means of HR-SEM.

Fig. 6.1 (b) shows a crater resulting from irradiation of the Ru film with a much larger number of pulses, namely ~ 80 thousand (209 bunches of 400 pulses), but performed at 20° grazing incidence and a mean value of absorbed fluence per pulse of 12.5 mJ/cm^2. This fluence level is close to the one used for 3.17° exposure. From the measurements of the ESB detector (not shown) we concluded that the bottom of the crater shown in Fig. 6.1 (b) consists of silicon with Ru droplets on top (dark grey - Si and light grey - Ru). Fig. 6.1 shows that, although both exposures were carried out with a similar average fluence close to the damage threshold, a much smaller number of pulses arriving at 3.17°

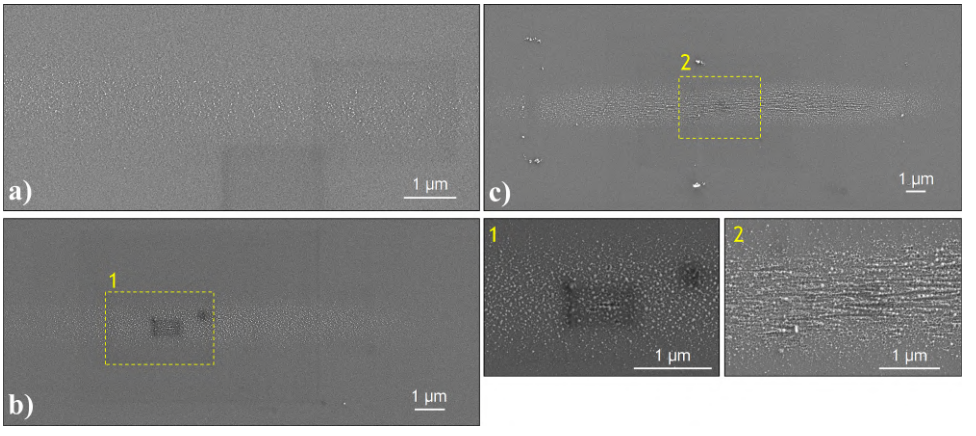

Figure 6.2: HR-SEM images of damage morphologies caused by a) 1600 b) 209 and c) 9200 femtosecond XUV pulses at 20° grazing incidence condition. The mean value of the absorbed fluence per pulse was 12.5 mJ/cm^2

causes comparable damage to the one caused by the large number of pulses arriving at 20° grazing incidence.

To elaborate on the mechanism of accumulation of damage we study the development of damage morphology with increasing number of pulses for irradiation at 20° grazing incidence angle. The following exposures were analyzed: 209 individual pulses generated at 5 Hz repetition rate, together with 4 and 23 bunches, generated with 10 Hz repetition rate. Each bunch in this experiment consisted of 400 pulses generated with 1 MHz repetition rate. The damage threshold value, determined by Liu's method, for a single bunch was 14 ± 3 mJ/cm^2.

The mean value of the fluence per pulse in the irradiation was 12.5 mJ/cm^2, which is slightly below the single-bunch damage threshold. Only surface modifications of the Ru layer were detected (see Fig. 6.2). TEM and AFM measurements of the damaged spots (not shown) confirmed that only the Ru layer is modified. All three damaged spots presented in Fig. 6.2 can be characterized as increased surface roughness, although the degree of roughening is different. Surprisingly, the surface roughness is considerably lower after irradiation with 1600 pulses (4×400), than after 209 individual pulses, whereas the opposite is expected.

The possible explanation of this contradiction is the random character of the pulse fluences within the irradiation. We should note that because of the self-amplified spontaneous emission (SASE) operation of the FEL, the fluences of individual pulses varied from 1 to 30 mJ/cm^2. The histograms of absorbed fluences per pulse for irradiations with 209, 1600 and 9200 (23×400) pulses are shown in Fig. 6.3. One can see, that although the average fluence was aimed to be 12.5 mJ/cm^2, there is a large spread in the fluence values and, most importantly, a considerable number of pulses had relatively high fluences.

The solid lines in Fig. 6.3 show the number of pulses within the exposure sequence that has a fluence equal to or higher than the x-axis coordinate value. Based on such analysis one can see that there are more high-fluence pulses (more than 20 mJ/cm^2 of

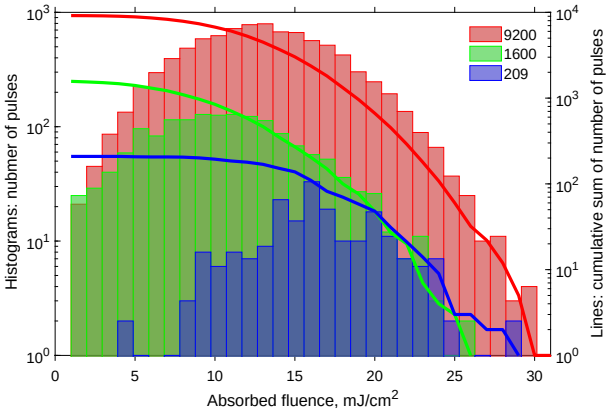

Figure 6.3: Histograms of fluence for irradiation containing 209 (blue), 1600 (green) and 9200 (red) pulses at 20° grazing incidence angle. The solid lines correspond to the cumulative sum of the number of pulses for each absorbed fluence value. The y-axis coordinate of each point on a line corresponds to the total number of pulses that has a fluence equal to or higher than the corresponding x-axis coordinate.

absorbed fluence) in the case of irradiation with 209 pulses than in the case of 1600 pulses. If we assume that there is a process that causes significant irreversible structural changes in the range of 20-25 mJ/cm^2, it can explain the more severe damage with 209 pulses, since the Ru film was exposed to a larger number of such high-fluence pulses compared to the 1600 pulses case. More dedicated experiments are required to check this assumption.

In previous chapters we showed that the nature of single-shot XUV-induced damage of Ru is thermo-mechanical ablation in the stress confinement regime. The latter means that heating of the lattice is faster than the acoustic relaxation time, which results in a situation that heating occurs at effectively isochoric conditions. It was shown in damage studies of metals induced with optical lasers [19–21] that this situation leads to the generation of large thermo-induced stresses and, as a result, to ablation of the top part of the metal (see the details in Chapter 5). The single-shot ablation threshold at 20° grazing incidence was measured to be $F_{\text{abl}} = 58 \pm 12$ mJ/cm^2 of absorbed fluence, while the melting threshold was calculated to be $F_{\text{melt}} = 13$ mJ/cm^2 [22]. It is known from literature [19] and also shown in Chapter 5) with molecular dynamics (MD) calculations, that ablation starts with nucleation of subsurface voids or cavities in a melted layer of irradiated metal, created as a result of propagation of a tensile stress wave. In a particular fluence range high enough to cause cavitation, but not sufficient to induce complete ablation, the cavities can remain frozen below the surface, which was proven experimentally [20, 21, 23] and with MD simulations [20]. Therefore, for metals there is a cavitation threshold that is lower than the ablation threshold.

Within this damage mechanism, we suggest that individual pulses with the highest fluence in a bunch are capable of not only melting the surface of Ru, but causing cavitation below the surface, as described above. The existence of subsurface cavities can create significant roughness and swelling of the surface [20, 21, 23], see also Fig. 5.3 in Chapter 5. The cavitation threshold for Ru was found with separate MD calcula-

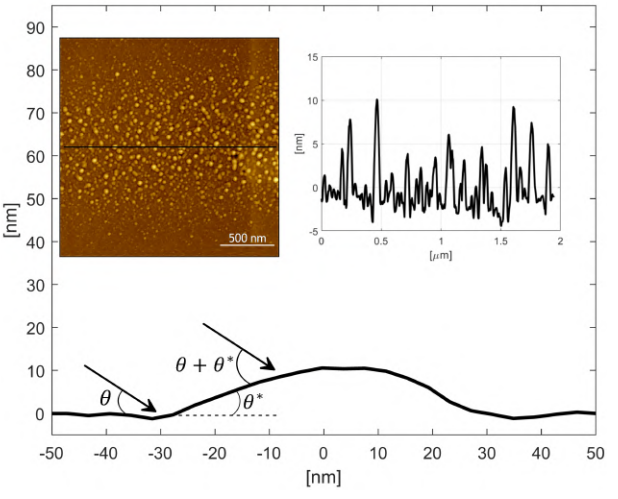

Figure 6.4: The AFM image of damage caused by 209 pulses. The black line on the AFM image (top left) indicates the cross-section of entire scan shown in top right corner. The magnified cross-section of the height of one swollen region (bottom plot) shows that due to swelling the incidence angle θ can be increased by $\theta^* = 20°$.

tions to be $\sim 30\,\mathrm{mJ/cm^2}$ (see Chapter 5), which is close to the experimental fluence of $20-25\,\mathrm{mJ/cm^2}$ at which, as we suggest, individual pulses can start damaging the Ru surface.

The fact that cavitation causes surface swelling and increased roughness can be used to explain the effect of different angles of incidence on the damage accumulation process described above and demonstrated with Fig. 6.1. The difference in the multi-shot damage caused at very grazing and close to critical angles of incidence, 3.17° and 20°, respectively, can be explained assuming the increased surface roughness to be the onset of damage. As an example, we consider the case of irradiation with 209 pulses from Fig. 6.2 (b). The corresponding atomic force microscopy (AFM) image of the surface is shown in Fig. 6.4. The surface appears as a collection of nanometer-scale bumps, with one typical bump shown at the bottom of Fig. 6.4 with an AFM line profile.

The roughness observed in Fig. 6.4, can approximately be considered as surface areas inclined at a certain angle θ^* to the initial surface. Therefore, the incident angle locally increases to the value $\theta+\theta^*$. To illustrate how the locally absorbed dose D depends on the angle of incidence we plot the following expression as a function of an arbitrary incident angle θ:

$$D(\theta) = \frac{(1-R(\theta))\sin(\theta)}{\delta(\theta)}, \tag{6.1}$$

where $R(\theta)$ and $\delta(\theta)$ are surface reflectivity and light attenuation length, respectively. For simplicity, these values are taken from [24], with $R(\theta)$ and $\delta(\theta)$ calculated for thick Ru without primary roughness for p-polarized light which was used in the experiments. The resulting curve $D(\theta)$ normalized to its value at 90° (normal incidence) and the absorption coefficient curve $1-R(\theta)$ are shown in Fig. 6.5 (left y axis). The $\delta(\theta)$ curve is

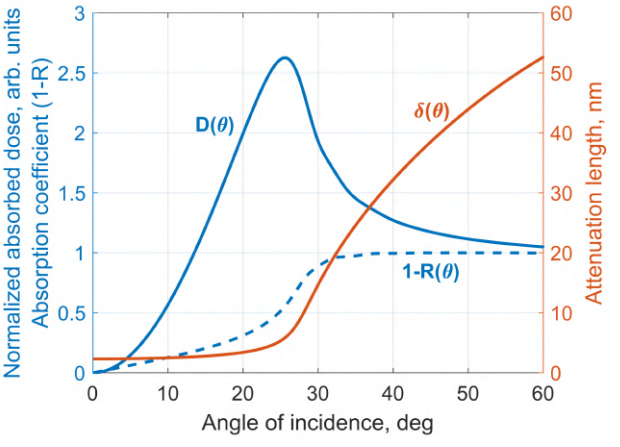

Figure 6.5: Surface absorption coefficient, light attenuation length and effective absorbed dose in Ru calculated according to 6.1 as functions of the grazing angle of incidence of 13.5 nm wavelength light.

shown using a right y axes. A sharp increase in the absorbed dose with increasing AOI up to the critical angle value is due to an increase of the absorption coefficient, whereas a decrease for higher AOI is due to a sharp increase of the attenuation length $\delta(\theta)$, which increases the absorption volume dramatically.

In the case of irradiation with 3.17° grazing incidence, a local change in the AOI by, for example, 20° due to laser-induced roughness (see Fig. 6.4) will result in a factor of 40 increase in the locally absorbed dose. Contrarily, when irradiating a sample with 20° grazing incidence, an increase of local AOI by 20° will result to a small decrease of the absorbed dose due to a large increase of the absorption volume. Such a qualitative analysis illustrates the effect of local laser-induced roughness development during a multi-shot exposure on the locally absorbed dose to be more significant for small grazing incidence angles. That can potentially explain the difference in damage between exposures with 3.17° and 20° angles presented in Fig. 6.1, although more experiments are required to verify this conclusion.

6.4. CONCLUSIONS

We present an experimental study of the damage caused by multiple femtosecond XUV pulses in Ru coatings at two different grazing angles of incidence, 3.17° and 20°. By comparing damage threshold values obtained for 100 pulses arriving at 3.17° we found that the multi-shot damage threshold does not depend on the repetition rate in the range from 0.25 to 1 MHz. In another set of measurements we found a decrease of the damage threshold with increasing number of pulses from 1 to 200 at a fixed repetition rate of 1 MHz. Further increase of the number of pulses to 400 did not change the damage threshold value. Altogether these results suggest that there is an accumulation of irreversible structural changes that eventually cause detectable damage. Such irreversible changes can be a result of melting, cavitation and recrystallization induced by individual laser pulses.

Based on the analysis of damage morphology development caused by an increase in the number of pulses arriving at 20° grazing angle and with a fluence near the damage threshold, we suggest that the prime cause of the multi-shot damage is roughening of the Ru surface induced by melting and cavitation processes. An increased surface roughness can cause a significant increase of the locally absorbed radiation dose in the case of irradiation at a small grazing angle of incidence (3.17°), whereas for a larger angle (20°), the effect of the increased roughness is less pronounced. Thus, the onset to multiple damage, at the fluences investigated here, is damage created by a single pulse, resulting in an enhanced roughness of the surface that makes the surface more vulnerable to damage caused by the next pulse.

The complex problem of multi-shot laser-matter interaction in the context of material damage requires further systematic experiments with well-controlled conditions. Such experiments supported with detailed numerical simulations should provide more insight in the mechanisms of damage accumulation.

ACKNOWLEDGEMENTS

Support from the operators of the FLASH facility is gratefully acknowledged. Furthermore, I acknowledge the help of Jana Buchheim and Klaus Mann.

REFERENCES

[1] W. Ackermann *et al., Operation of a free-electron laser from the extreme ultraviolet to the water window,* Nat. Photonics **1**, 336 (2007).

[2] T. Tschentscher, C. Bressler, J. Grünert, A. Madsen, A. Mancuso, M. Meyer, A. Scherz, H. Sinn, and U. Zastrau, *Photon Beam Transport and Scientific Instruments at the European XFEL,* Appl. Sci. **7**, 592 (2017).

[3] R. Schoenlein, S. Boutet, M. Minitti, and A. Dunne, *The linac coherent light source: recent developments and future plans,* Appl. Sci. **7**, 850 (2017).

[4] I. Inoue, Y. Inubushi, T. Sato, K. Tono, T. Katayama, T. Kameshima, K. Ogawa, T. Togashi, S. Owada, Y. Amemiya, T. Tanaka, T. Hara, and M. Yabashi, *Observation of femtosecond X-ray interactions with matter using an X-ray–X-ray pump–probe scheme,* P. Natl. Acad. Sci. USA **113**, 1492 (2016).

[5] J. Krzywinski, D. Cocco, S. Moeller, and D. Ratner, *Damage threshold of platinum coating used for optics for self-seeding of soft X-ray free electron laser,* Opt. Express **23**, 5397 (2015).

[6] J. Krzywinski, R. Conley, S. Moeller, G. Gwalt, F. Siewert, C. Waberski, T. Zeschke, and D. Cocco, *Damage thresholds for blaze diffraction gratings and grazing incidence optics at an X-ray free-electron laser,* J. Synchrotron Radiat. **25**, 85 (2018).

[7] S. P. Hau-Riege, R. A. London, A. Graf, S. L. Baker, R. Soufli, R. Sobierajski, T. Burian, J. Chalupsky, L. Juha, J. Gaudin, J. Krzywinski, S. Moeller, M. Messerschmidt, J. Bozek, and C. Bostedt, *Interaction of short X-ray pulses with low-Z X-ray optics materials at the LCLS free-electron laser,* Opt. Express **18**, 23933 (2010).

[8] R. Sobierajski, I. Jacyna, P. Dłużewski, M. T. Klepka, D. Klinger, J. B. Pełka, T. Burian, V. Hájková, L. Juha, K. Saksl, V. Vozda, I. Makhotkin, E. Louis, B. Faatz, K. Tiedtke, S. Toleikis, H. Enkisch, M. Hermann, S. Strobel, R. A. Loch, and J. Chalupsky, *Role of heat accumulation in the multi-shot damage of silicon irradiated with femtosecond XUV pulses at a 1 MHz repetition rate,* Opt. Express **24**, 15468 (2016).

[9] I. A. Makhotkin, R. Sobierajski, J. Chalupský, K. Tiedtke, G. de Vries, M. Störmer, F. Scholze, F. Siewert, R. W. E. van de Kruijs, I. Milov, E. Louis, I. Jacyna, M. Jurek, D. Klinger, L. Nittler, Y. Syryanyy, L. Juha, V. Hájková, V. Vozda, T. Burian, K. Saksl, B. Faatz, B. Keitel, E. Plönjes, S. Schreiber, S. Toleikis, R. Loch, M. Hermann, S. Strobel, H.-K. Nienhuys, G. Gwalt, T. Mey, and H. Enkisch, *Experimental study of EUV mirror radiation damage resistance under long-term free-electron laser exposures below the single-shot damage threshold,* J. Synchrotron Radiat. **25**, 77 (2018).

[10] R. Sobierajski, M. Jurek, J. Chalupský, J. Krzywinski, T. Burian, S. Dastjani Farahani, V. Hájková, M. Harmand, L. Juha, D. Klinger, R. A. Loch, C. Ozkan, J. B. Pełka, K. Sokolowski-Tinten, H. Sinn, S. Toleikis, K. Tiedtke, T. Tschentscher, H. Wabnitz, and J. Gaudin, *Experimental set-up and procedures for the investigation of XUV free electron laser interactions with solids,* J. Instrum. **8** (2013), 10.1088/1748-0221/8/02/P02010.

[11] K. Tiedtke, A. Azima, N. Von Bargen, L. Bittner, S. Bonfigt, S. Düsterer, B. Faatz, U. Frühling, M. Gensch, C. Gerth, N. Guerassimova, U. Hahn, T. Hans, M. Hesse, K. Honkavaar, U. Jastrow, P. Juranic, S. Kapitzki, B. Keitel, T. Kracht, M. Kuhlmann, W. B. Li, M. Martins, T. Núñez, E. Plönjes, H. Redlin, E. L. Saldin, E. A. Schneidmiller, J. R. Schneider, S. Schreiber, N. Stojanovic, F. Tavella, S. Toleikis, R. Treusch, H. Weigelt, M. Wellhöfer, H. Wabnitz, M. V. Yurkov, and J. Feldhaus, *The soft X-ray free-electron laser FLASH at DESY: Beamlines, diagnostics and end-stations,* New J. Phys. **11** (2009), 10.1088/1367-2630/11/2/023029.

[12] A. Aquila, R. Sobierajski, C. Ozkan, V. Hájková, T. Burian, J. Chalupský, L. Juha, M. Störmer, S. Bajt, M. T. Klepka, P. Dłuzewski, K. Morawiec, H. Ohashi, T. Koyama, K. Tono, Y. Inubushi, M. Yabashi, H. Sinn, T. Tschentscher, A. P. Mancuso, and J. Gaudin, *Fluence thresholds for grazing incidence hard X-ray mirrors,* Appl. Phys. Lett. **106** (2015), 10.1063/1.4922380.

[13] J. Liu, *Simple technique for measurements of pulsed gaussian-beam spot sizes,* Opt. Lett. **7**, 196 (1982).

[14] J. Chalupský, L. Juha, J. Kuba, J. Cihelka, V. Hájková, S. Koptyaev, J. Krása, A. Velyhan, M. Bergh, C. Caleman, J. Hajdu, R. M. Bionta, H. Chapman, S. P. Hau-Riege, R. A. London, M. Jurek, J. Krzywinski, R. Nietubyc, J. B. Pelka, R. Sobierajski, J. Meyer-ter Vehn, A. Tronnier, K. Sokolowski-Tinten, N. Stojanovic, K. Tiedtke, S. Toleikis, T. Tschentscher, H. Wabnitz, and U. Zastrau, *Characteristics of focused soft X-ray free-electron laser beam determined by ablation of organic molecular solids,* Opt. Express **15**, 6036 (2007).

[15] J. Chalupský, T. Burian, V. Hájková, L. Juha, T. Polcar, J. Gaudin, M. Nagasono, R. Sobierajski, M. Yabashi, and J. Krzywinski, *Fluence scan: an unexplored property of a laser beam,* Opt. Express **21**, 26363 (2013).

[16] J. Chalupský, J. Krzywinski, L. Juha, V. Hájková, J. Cihelka, T. Burian, L. Vyšín, J. Gaudin, A. Gleeson, M. Jurek, A. R. Khorsand, D. Klinger, H. Wabnitz, R. Sobierajski, M. Störmer, K. Tiedtke, and S. Toleikis, *Spot size characterization of focused non-Gaussian X-ray laser beams,* Opt. Express **18**, 27836 (2010).

[17] F. Scholze, C. Laubis, C. Buchholz, A. Fischer, S. Ploeger, F. Scholz, H. Wagner, and G. Ulm, *Status of EUV reflectometry at PTB,* Emerging Lithographic Technologies IX **5751**, 749 (2005).

[18] K. Tiedtke, J. Feldhaus, U. Hahn, U. Jastrow, T. Nunez, T. Tschentscher, S. V. Bobashev, A. A. Sorokin, J. B. Hastings, S. Möller, L. Cibik, A. Gottwald, A. Hoehl, U. Kroth, M. Krumrey, H. Schöppe, G. Ulm, and M. Richter, *Gas detectors for X-ray lasers,* J. Appl. Phys. **103** (2008), 10.1063/1.2913328.

[19] V. V. Zhakhovskii, N. A. Inogamov, and K. Nishihara, *New mechanism of the formation of the nanorelief on a surface irradiated by a femtosecond laser pulse,* JETP Lett. **87**, 423 (2008).

[20] C. Wu, M. S. Christensen, J.-M. Savolainen, P. Balling, and L. V. Zhigilei, *Generation of subsurface voids and a nanocrystalline surface layer in femtosecond laser irradiation of a single-crystal Ag target,* Phys. Rev. B **91**, 035413 (2015).

[21] S. I. Ashitkov, N. a. Inogamov, V. V. Zhakhovskii, Y. N. Emirov, M. B. Agranat, I. I. Oleinik, S. I. Anisimov, and V. E. Fortov, *Formation of nanocavities in the surface layer of an aluminum target irradiated by a femtosecond laser pulse,* JETP Lett. **95**, 176 (2012).

[22] I. Milov, I. A. Makhotkin, R. Sobierajski, N. Medvedev, V. Lipp, J. Chalupský, J. M. Sturm, K. Tiedtke, G. de Vries, M. Störmer, F. Siewert, R. van de Kruijs, E. Louis, I. Jacyna, M. Jurek, L. Juha, V. Hájková, V. Vozda, T. Burian, K. Saksl, B. Faatz, B. Keitel, E. Plönjes, S. Schreiber, S. Toleikis, R. Loch, M. Hermann, S. Strobel, H.-K. Nienhuys, G. Gwalt, T. Mey, H. Enkisch, and F. Bijkerk, *Mechanism of single-shot damage of Ru thin films irradiated by femtosecond extreme UV free-electron laser,* Opt. Express **26**, 19665 (2018).

[23] J.-M. Savolainen, M. S. Christensen, and P. Balling, *Material swelling as the first step in the ablation of metals by ultrashort laser pulses,* Phys. Rev. B **84**, 193410 (2011).

[24] B. Henke, E. Gullikson, and J. Davis, *X-ray Interactions: Photoabsorption, Scattering, Transmission, and Reflection at E = 50-30,000 eV, Z = 1-92,* Atom. Data Nucl. Data **54**, 181 (1993).

SUMMARY

The research performed in this thesis aims to understand the fundamental processes occurring in matter exposed to high doses of laser radiation on ultrashort time scale, and eventually leading to severe material damage. More specifically, ruthenium (Ru) thin films irradiated with femtosecond optical, XUV and hard X-ray laser pulses were studied. An experimental as well as a theoretical analysis were performed with the focus on the latter. A comprehensive hybrid modeling scheme has been developed, enabling simulations of the full timescale evolution of a metal exposed to ultrashort pulses in a wide range of fluence and energy of the incident photons.

The model developed consists of three major parts. The Monte Carlo code XCASCADE(3D) simulates the photoabsorption processes and the resulting non-equilibrium electron cascades. When the cascading is finished and the electrons can be considered as hot and thermalized in the conduction band of a metal, their diffusive transport, the transfer of their energy to the lattice ions and the resulting material movement are modeled with two-temperature hydrodynamics. Evolution of a material on an atomistic scale includes such processes as melting, cavitation, ablation and recrystallization and is simulated with molecular dynamics. Although separate parts of the model were developed prior to this work, the combination of them into a full hybrid scheme and applying it to study Ru damage at different conditions is the novel outcome of this work.

Most of the effort was dedicated to study single-shot XUV induced damage in Ru. Extensive post-mortem microscopy analysis revealed different damage morphologies: from minor surface roughening to crater formation with various structures at its bottom. Simulations performed with the hybrid approach explained the mechanisms responsible for these different types of morphology. Minor surface modifications are caused by melting, cavitation and recrystallization, leading to the formation of frozen subsurface voids. The existence of such voids below the surface results in surface roughening. Ablation of the material from the top surface results in crater formation. The interplay between ablation and recrystallization processes leads to different final structures inside the crater: a rough periphery and a smooth centre. The local absorbed fluence level is found to be the dominant factor. At the edge of the crater, where the fluence is lower, recrystallization takes less time than in the centre, where fluence is higher. As a result, after ablation, the remaining liquid material in the centre has more time to smooth out before the recrystallization front arrives, compared to the periphery.

The hybrid simulations provided detailed information about the dynamics of damage processes. Different regimes of ablation were identified depending on the fluence. For relatively low fluence a standard thermo-mechanical ablation via a tensile wave, formed as a response to ultrafast heating, is responsible for material ejection. For higher fluences Ru exhibits a two-level ablation. Overheating and significant expansion of the top thin layer result in critical-point phase separation and ejection of a hot gas-liquid mixture. A thicker layer below is ablated thermo-mechanically, and disintegrates into liquid droplets soon after separation from the target. Such a two-level ablation is not

typical for metals and is found to be the result of the combination of the Ru thermo-mechanical properties and irradiation conditions.

With the XUV case studied in detail, the research was extended to a broad range of incident light wavelength (photon energy). Damage to Ru with optical, XUV and hard X-ray femtosecond lasers was compared. Surprising similarity in ablation craters was discovered and explained with simulations. The important parameter in the context of damage is the photon penetration depth, which was small compared to the film thickness in all cases considered. Whereas in the optical case the penetration depth is defined by a skin depth of ~ 10 nm for metals, in the XUV and hard X-ray case it depends on the angle of incidence. Grazing incidence conditions mimicking the practical use of a Ru thin film as a reflective mirror were applied and provided a small photon penetration depth of few nanometres.

Electron cascades induced after photoabsorption played a key role in explaining the similarity in damage. The absence of cascades in the optical case and an insignificant effect of it in the XUV case confine the absorbed energy in the vicinity of the Ru surface at the initial stage of material evolution. Significant cascading in the hard X-ray regime separates the energy stored in the electronic system into two parts: energetic photoelectrons spread the absorbed energy deep into the sample, whereas Auger recombination of deep-shell holes created after release of photoelectrons keeps the rest of the energy in the vicinity of the surface. It was found that this latter part of the absorbed energy distribution causes the ablation. Therefore, all cases considered exhibit a similar absorbed energy distribution in the top part of Ru, which leads to a similar hydrodynamic evolution and eventually to similar damage processes. Such an important finding enables one to build a bridge between damage processes induced by different laser sources.

An experimental study was performed in order to make a step towards understanding a possible damage accumulation problem, when multiple pulses, each with a fluence below the ablation threshold, are used. It was found that although each laser pulse in multi-shot exposures separately could not induce ablation in Ru, the fluence in some of the pulses was sufficiently high to induce pre-ablation processes such as melting and even cavitation. These processes lead to surface roughening and a local increase of the absorption for the next incoming pulses. It continues until the locally increased absorption overcomes the ablation threshold and severe damage is produced in Ru. The effect is more pronounced at smaller grazing incidence angles. Further steps have to be done to study the multi-shot regime in more detail.

SAMENVATTING

Het doel van het in dit proefschrift beschreven onderzoek is het op atomair niveau begrijpen van wat er in een materiaal gebeurt wanneer het aan zeer intense, ultrakorte pulsen laserlicht wordt blootgesteld. In het bijzonder zijn dunne lagen ruthenium (Ru) op silicium substraten bestraald met femtoseconde pulsen in het zichtbare, extreem ultraviolette (XUV) en harde röntgen golflengtegebied en de resultaten zijn zowel experimenteel als theoretisch bestudeerd waarbij de theoretische benadering het grootste deel van dit proefschrift vormt. Het beschrijft de ontwikkeling van een allesomvattend hybride model dat het tijdverloop van het gehele proces van absorptie en energiedissipatie beschrijft voor een reeks van fotonenergieën en doses van de invallende fotonen.

Dit model bestaat uit drie componenten. Te beginnen met de "Monte Carlo" code XCASCADE(3D) die het absorptieproces en de daaropvolgende cascade van elektron excitaties en emissies berekent. Nadat deze cascade is beëindigd en de "hete" elektronen zich in thermisch evenwicht in de geleidingsband van het metaal bevinden, wordt een twee-temperaturen (elektron- en roostertemperatuur apart) hydrodynamisch model toegepast om het energietransport middels elektronen-diffusie en elektron-fonon energie-uitwisseling en de daarbij behorende beweging van de roosteratomen te berekenen. De evolutie van het materiaal op atomair niveau wordt vervolgens berekend met een "Moleculaire Dynamica" model dat rekening houdt met fenomenen als smelten, cavitatie, ablatie en rekristallisatie bij het stollen. De afzonderlijke modellen zijn reeds eerder ontwikkeld, maar de combinatie ervan, toegepast op het metaal ruthenium, is nooit eerder gedaan en het is deze gecombineerde toepassing die diep inzicht geeft in wat er werkelijk gebeurt in het materiaal.

Het grootste deel van dit proefschrift is gewijd aan de studie van de schademechanismen bij zogenaamde 'single shot' belichting van Ru met licht in het Extreem Ultraviolette deel van het spectrum. Na de belichtingen zijn de samples microscopisch onderzocht waarbij schade in verschillende vormen is waargenomen: van lichte verruwing van het oppervlak tot kratervorming met een verscheidenheid aan structuren op de bodem van de kraters. De met het bovengenoemde hybride model uitgevoerde simulaties kunnen de verschillende vormen van schade goed verklaren. De verruwing is het resultaat van het smelten van het Ru, de vorming van kleine belletjes of holtes (cavitatie) en rekristallisatie tijdens het stollingsproces waarbij de holtes in het stollende materiaal aanwezig blijven en het oppervlak ruw wordt. Bij een hogere dosis leidt de combinatie van ablatie en rekristallisatieprocessen tot verschillende structuren in de uiteindelijke krater, van een ruwe periferie tot een glad centrum. De lokaal geabsorbeerde dosis blijkt hier de bepalende factor. In de periferie, waar de dosis niet zo hoog is, vindt rekristallisatie vrij snel plaats en blijft een ruw oppervlak over. In het centrum, bij de hoge dosis, duurt het langer voor er rekristallisatie optreedt en kan het vloeibare Ru eerst vlak trekken, wat tot een glad oppervlak leidt.

De hybride simulaties geven een duidelijk beeld van de dynamica van de beschadigende processen in Ru. De verschillende regimes van ablatie, als functie van de stra-

lingsdosis, worden duidelijk geïdentificeerd. Bij een relatief lage dosis is er ultrasnelle verhitting, waarbij het materiaal niet snel genoeg mechanisch kan reageren en er treedt een drukgolf op die het materiaal uiteen doet spatten, een fenomeen dat bekend staat als thermomechanische ablatie. Bij een hogere dosis vertoont Ru ablatie in twee fasen. Oververhitting en een flinke uitzetting van het bovenste deel van de Ru-laag resulteren in een kritische fasescheiding en een heet mengsel van gas en vloeistof wordt uitgestoten. Een dikkere laag eronder wordt dan via de eerder genoemde thermomechanische ablatie uitgestoten en zal kort na het verlaten van de Ru laag uiteenvallen in druppeltjes. Een dergelijke twee-fase ablatie is ongewoon voor metalen en is in dit geval het gevolg van de combinatie van specifieke thermomechanische eigenschappen van Ru en de belichtingsomstandigheden.

Vervolgens is de kennis, opgedaan bij het bestuderen van bestraling met XUV licht, gebruikt om experimentele resultaten van belichtingen met andere golflengtes te analyseren. Daarbij hebben we bestralingen met zichtbaar licht, XUV en harde röntgenstraling (twee golflengtes) met elkaar vergeleken. De afwezigheid van elektronische excitatie en dus de cascade van elektronen in het geval van zichtbaar licht, en het geringe bereik van dit proces bij XUV bestraling, zorgen ervoor dat de geabsorbeerde energie tijdens de initiële evolutie van het materiaal in een dunne laag vlak onder het oppervlak blijft. In het geval van harde röntgenstraling wordt de geabsorbeerde energie op twee verschillende manieren in het elektronische systeem opgeslagen: energetische foto-elektronen dringen diep door in de laag en verspreiden de energie over het materiaal, terwijl de energie van Auger-recombinatie van diep in het atoom gelegen gaten gelokaliseerd blijft vlak onder het oppervlak. Uit de berekeningen blijkt, dat met name dit laatste deel van de opgeslagen energie verantwoordelijk is voor de ablatie van de toplaag. We zien voor alle bestudeerde golflengtes een vergelijkbare geabsorbeerde energiedistributie onder het Ru oppervlak, en dus een vergelijkbare hydrodynamische ontwikkeling van het materiaal en uiteindelijk dezelfde schade processen. Deze belangrijke conclusie stelt ons in staat om het verband te begrijpen tussen schade ontstaan door sterk verschillende laser pulsen en daarmee ook te kunnen voorspellen hoe Ru zal reageren op andere straling met een andere golflengte.

Tot slot is een begin gemaakt met het bestuderen van mogelijke cumulatieve effecten wanneer een Ru-laag door meerdere pulsen, elk met een dosis beneden de drempelwaarde voor beschadiging door een enkele puls, wordt belicht. Bij de experimenten werd gevonden dat, hoewel elke puls onder de ablatie-drempel bleef, sommige pulsen toch voldoende intens waren om het Ru lokaal te laten smelten waardoor cavitatie kon ontstaan. Deze processen leidden lokaal tot verruwing en daardoor tot verhoogde absorptie van de volgende pulsen, tot er uiteindelijk toch zoveel straling werd geabsorbeerd dat ablatie plaatsvond en ernstige schade ontstond. Dit effect bleek sterker bij meer scherende hoeken van inval. Vervolgonderzoek is zeker nodig om schade door meerdere pulsen in kaart te brengen en te begrijpen.

OUTLOOK AND VALORIZATION

The necessity of having optical elements tolerant to damage is crucial not only for the optics at X-ray free-electron lasers, synchrotron beamlines, and other sources like high harmonic generation and laser produced plasmas, but also for product alignment sensors in photolithography, different types of photodetectors and generally in any laboratory that deals with intensive radiation. The main outcome of this thesis is a hybrid computational model that can predict single-shot damage thresholds such as melting, cavitation or ablation (and explain the mechanisms behind them) of metallic coatings exposed to ultrashort pulses over a wide range of photon energies. Altogether, this enables a diverse community of optics users, either at visible, XUV or X-ray range, to select the right damage resistant components for their set-ups without having to carry out an extensive series of costly and time consuming experiments.

The detailed analysis of XUV-induced single-shot damage and the first steps performed in the direction of multi-shot damage revealed the complexity of the physical mechanisms involved. The importance of surface damage phenomena less severe than ablation, such as cavitation, melting and even minor surface chemistry effects is emphasized. It deepens and supplements the accumulated knowledge on the materials damage phenomena in the XUV and X-ray regimes. The similarity in damage found for a wide range of photon energies from visible to hard X-ray radiation bridges the gaps between these domains, making the understanding of the processes involved more universal.

Several directions of further research in the direction of optics lifetime are foreseen. One of them is a continuation of damage accumulation studies, when each pulse in a multi-pulse exposure situation is below the single-shot ablation, cavitation or melting thresholds. Such regimes are close to real conditions in various applications of ultrashort laser pulses, hence are very relevant for industry. When the pulse fluence becomes even lower than the melting threshold, mechanical fatigue or accumulation of various point defects can start to play a role. Photo-induced surface chemistry can change the optical properties of the target and lead to problems in long-term exposures. Therefore, one will have to consider using different types of protective capping layers and their interaction with the target environment.

Applying the computational model developed in this thesis to other metals, but also expanding it to treat other types of materials such as semiconductors and dielectrics is another expected future step. The photoabsorption mechanisms and the resulting electron-hole kinetics are different for band gap materials compared to metals. Therefore, the corresponding modules in our computational scheme must be modified. The generalization of the model in the direction of treating different types of radiation (not only photons, but also electron and ion beams) is also foreseen.

Another fundamental improvement of the hybrid model developed would be substitution of the two-temperature hydrodynamics part, which assumes electron and ion

systems to be individually at thermodynamic equilibrium, with essentially nonthermodynamic models, such as Boltzmann transport equation. It was shown that at particular irradiation conditions the excited electrons in a metal can stay out of equilibrium for up to a picosecond timescale [1]. Therefore, accurate description of the early-stage non-equilibrium dynamics of irradiated targets requires application of models that go beyond the two-temperature approach.

A detailed description of Ru properties and behaviour under extreme conditions, together with the corresponding methodology, can be of high interest for the high temperature and high pressure community studying the properties of warm dense matter, hydro- and thermodynamics of different cosmic objects, or shock wave phenomena. The computational tools developed in this thesis can be combined with recent fundamental experiments [2] on ultrafast phase transitions in matter under laser irradiation, performed at X-ray free electron lasers.

One of the main physical processes studied in this thesis is laser ablation. As was written in the introduction, laser ablation is a vast field containing many different and sometimes exotic applications. Femtosecond lasers are used in surface micromachining and nanostructuring, thin film deposition and eye surgery. Another example is nanoparticles (NPs) generation using laser ablation. NPs are being used in many applications such as plasmonics, catalysis and biomedicine. Depending on the application, different size, shape and structure of the NPs is required. The efficiency of NPs generation is also an important factor for mass production. Getting a full control on the products of the ablation process by tuning the laser parameters and ambient environment is crucial and can only be achieved if one understands the fundamental processes that govern the whole procedure. Such a desire of deep understanding of the mechanisms involved in light-matter interaction at high intensity was the driving force of the research performed in this thesis, and it will stay the same way in possible future steps.

REFERENCES

[1] W. S. Fann, R. Storz, H. W. K. Tom, and J. Bokor, *Electron thermalization in gold,* Phys. Rev. B **46**, 13592 (1992).

[2] M. Z. Mo, Z. Chen, R. K. Li, M. Dunning, B. B. L. Witte, J. K. Baldwin, L. B. Fletcher, J. B. Kim, A. Ng, R. Redmer, A. H. Reid, P. Shekhar, X. Z. Shen, M. Shen, K. Sokolowski-Tinten, Y. Y. Tsui, Y. Q. Wang, Q. Zheng, X. J. Wang, and S. H. Glenzer, *Heterogeneous to homogeneous melting transition visualized with ultrafast electron diffraction,* Science **360**, 1451 (2018).

ACKNOWLEDGEMENTS

I am very grateful to Fred Bijkerk for giving me the opportunity and sufficient freedom to perform quite theoretical fundamental research in the Industrial Focus Group. Carefully applied time pressure stimulated me to overcome my excessive perfectionism and finish everything in a reasonable time without sacrificing the quality of my work. I'm thankful to my daily supervisors Igor Makhotkin and Eric Louis for always being by my side, ready to help in any situation, either work related or not. They gave me many life lessons and developed my confidence as a scientist. I acknowledge the help and support from the rest of the XUV Optics senior staff, and especially from Marko Sturm for performing AFM measurements. I am very thankful to Jacqueline Emmerich and Carin Krijnen, without whose administrative work neither my PhD nor any other essential activity in our group would be possible. I appreciate the help from our MESA+ colleagues Mark Smithers, Henk van Wolferen and Rico Keim for performing SEM, FIB and TEM measurements and for very useful discussions.

I acknowledge the great support from a vast network of external colleagues and collaborators that has been developed over the course of my PhD. I would like to express huge thanks to Nikita Medvedev and Vasily Zhakhovsky, who practically became remote supervisors of a theoretical part of my work. Their strong involvement into the project, professionalism and gratuitous readiness to teach and help me were at many times crucial to successfully complete this thesis. I'm thankful to Ryszard Sobierajski for guiding me in the two-temperature world in the beginning of my project and providing help in the analysis of experimentally observed damage phenomena; to Slava Medvedev for initiating a collaboration with colleagues from Moscow that positively changed the course of my PhD with the possibility to run complex atomistic simulations of the ablation process; to Alexey Kimel for being open to our scientific interests and giving the opportunity to perform pump-probe measurements in his lab at the Radboud University, and to Sergey Semin for his willingness to teach me the basics of a laser experiment and to participate in it; to Vladimir Lipp, Beata Ziaja, Nail Inogamov, Denis Ilnitsky, Kirill Migdal and all other external colleagues for a very fruitful collaboration; to our industrial partners Carl Zeiss SMT and ASML, and especially to Hartmut Enkisch and Gosse de Vries for being truly interested in the fundamental aspects of my work.

Looking back to almost 5 years spent in the group I'm happy to realize that I was surrounded by colleagues who became my true friends outside office hours. With a smile on my face I will always remember our shashlik and singing evenings with Konstantin Nikolaev and Dmitry Kuznetsov, board games with Andrey Zameshin, dancing parties with Cristiane Vilas Boas and Parikshit Phadke, jamming in a studio with Roman Medvedev, and nights out in the beautiful city of Enschede with Airat Shafikov, Theo van Oijen and Dennis IJpes. I'm thankful to all former and current colleagues of the XUV Optics Group for providing a friendly and motivating environment.

I would like to thank my friends outside the academic world, Yelizaveta Gasyuk for being very supportive in difficult times, and the members of Phoenix Lacrosse Enschede

for providing a perfect way to switch off from work and vent my mind on and off a lacrosse field. I'm thankful to my Russian friends Ilya Klimovskih, Maria Kutmerova, Gleb Sarapin, Ilya Filippov, Dmitry Bit-Rigu, Alexey Matveev, Stanislav Bodnar, Ekaterina Ananina, Anton Kononov and Dmitry Raev for staying in touch, for our rare but priceless meetings.

Finally, I'm endlessly grateful to my parents for their love and support. They gave me everything I needed to reach the goals that I set for myself.